Measuring permeability vs depth in the unlined section of a wellbore using the descent of a fluid column made of two distinct fluids : inversion workflow, laboratory & in-situ tests

Sivaprasath Manivannan

Thèse de doctorat

Measuring permeability vs depth in the unlined section of a wellbore using the descent of a fluid column made of two distinct fluids: inversion workflow, laboratory & in-situ tests

Thèse de doctorat de l'Université Paris-Saclay
préparée à l'Ecole Polytechnique

École doctorale n°579 Sciences mécanique et énergetiques,
matériaux, géosciences: Mécanique des solides

Soutenue à Palaiseau, 27/11/2018, par

Sivaprasath MANIVANNAN

Composition du Jury :

Amade POUYA	
Professeur, Université Paris-Est (Laboratoire Navier - UMR 8205)	Rapporteur
Marc FLEURY	
Ingénieur de recherche, IFP Energies Nouvelles	Rapporteur
Jean-François SEMBLAT	
Professeur, ENSTA Paris Tech	Président du jury
Alain C. GRINGARTEN	
Professeur Emérite, Imperial College London	Examinateur
Bertrand THEUVENY	
Reservoir domain head, Schlumberger (Testing services)	Examinateur
Vincent JAFFREZIC	
Reservoir engineer, TOTAL SA	Examinateur
Antoine JACQUES	
Reservoir engineer, TOTAL SA	Examinateur
Pierre Bérest	
Professeur Emérite, Ecole Polytechnique	Directeur de thèse
(Laboratoire de mécanique des solides - UMR 7469)	
Benoît Brouard	
Président, Brouard Consulting SAS	Invité

Dedicated to my parents

Alamelumangai & Manivannan

Acknowledgements

Abstract

In wells producing water, oil, gas or geothermal energy, or in access wells to hydrocarbon storage, it is critical to evaluate the permeability of the formation as a function of depth, to improve the reservoir model, and also to identify the zones where additional investigation or special completions are especially useful.

A new technique is proposed, consisting of scanning the open hole (uncased section of the wellbore) with an interface between two fluids with a large viscosity contrast. The injection rate into the formation depends on interface location and well pressure history. An inverse problem should be solved: estimate permeability as a function of depth from the evolution of flow rates with time. The wells are usually equipped with a central tube. The scanning is done by injecting a liquid in the central tube at constant wellhead pressure. Injection and withdrawal rates are measured at the wellhead; the difference between these two rates is the formation injection rate.

To validate and improve this technique, we used a laboratory model mimicking a multi-layer formation, already available at LMS. We also made use of in-situ tests performed on an ultra-low permeable cap rock above an underground gas storage reservoir. In these tests, a viscous fluid contained in the open hole was displaced by a less-viscous fluid (a method called *opening* WTLog). The more permeable layers were correctly identified (Manivannan et al. 2017), but a quantitative estimation was challenging due to transient phenomena in the vicinity of the wellbore (near-wellbore zone). In addition, the investigation radius was small.

These challenges are addressed by proposing a slightly modified test procedure and a new interpretation workflow. Laboratory tests with a modified test setup showed the advantages of the *closing* method in which the well is filled with a less-viscous fluid at the start of the test. We also added a stabilization period before the injection of viscous fluid to minimize the transient effects; this period is also used to estimate the average permeability of the open hole and the effect of near-wellbore damage (skin), allowing us to constrain the inverse problem.

Then the test proper is performed (*closing* WTLog). The injection profile of the less-viscous fluid is computed from the wellhead flow rate history. A permeability profile is estimated from the injection profile. The permeability estimation considers a monophasic flow in each layer and the same skin value for all the formation layers. Major uncertainties in the permeability estimates are caused by formation pressures and heterogeneities in skin values; these uncertainties are estimated using an analytical formula. We have verified on the laboratory setup that the estimated permeability profiles are well correlated to the permeabilities measured before the tests.

An attempt was made to perform a WTLog in a 1750-m long wellbore opening in a salt formation. The first phase was successful and the average permeability was correctly assessed. However, this permeability was so small ($4 \ 10^{-21}$ m^2 or 4 nD) that the gauges and the flow meters were not accurate enough to allow a clear distinction between the permeabilities of the various parts of the open hole.

Résumé

Dans les puits de production d'eau, de pétrole, de gaz et de chaleur géothermique, ou dans les puits d'accès à un stockage d'hydrocarbures, il est précieux de connaître la perméabilité de la formation ou de sa couverture en fonction de la profondeur, soit pour améliorer le modèle de réservoir, soit pour choisir les zones dans lesquelles procéder à des opérations spéciales.

On propose une technique qui consiste à balayer la hauteur du découvert par une interface entre deux liquides de viscosités très contrastées. Le débit total qui pénètre la formation à chaque instant est ainsi une fonction de la position de l'interface et de l'historique des pressions dans le puits. On doit alors résoudre un problème inverse : rechercher la perméabilité fonction de la profondeur à partir de l'historique des débits dans le temps. Dans la pratique, le puits est équipé d'un tube central. Le balayage est effectué par injection d'un liquide à pression d'entrée constante dans le tube central et soutirage d'un autre liquide par l'espace annulaire. On mesure les débits d'injection et de soutirage dont la différence est le débit qui entre dans la formation. Le tube central peut être constitué par les tiges carrées utilisées pendant le forage, et les autres équipements nécessaires à l'essai, débitmètres, capteurs de pression, liquides, sont le plus souvent déjà disponibles sur le chantier de forage. Aucun outil n'est descendu dans le puits. L'essai est donc rapide et peu coûteux en comparaison de toutes les techniques qui visent au même objectif.

Pour valider et améliorer cette technique, on a d'abord utilisé une maquette simulant un découvert multi-couches disponible au LMS. On a exploité aussi des essais en place réalisés dans la couverture peu perméable d'un stockage souterrain de gaz. Dans ces essais, un liquide visqueux placé dans le découvert était déplacé par un liquide moins visqueux (méthode dite « opening »). Les couches plus perméables étaient correctement identifiées (Manivannan et al. 2017), mais une estimation quantitative était un défi en raison des phénomènes transitoires qui affectent le voisinage immédiat des puits. De plus, le rayon investigué dans le massif était petit.

La thèse a relevé ces défis en proposant un essai légèrement différent et une nouvelle technique d'interprétation. Les essais avec une maquette modifiée ont montré la supériorité d'une méthode « closing » dans laquelle le puits est d'abord rempli du liquide le moins visqueux. On ménage une période de stabilisation avant l'injection du liquide visqueux pour réduire les effets transitoires ; elle permet aussi d'estimer la perméabilité moyenne et l'influence de la zone endommagée à la paroi (le « skin ») et d'utiliser de solutions analytiques pour estimer le profil de perméabilité. Puis on conduit l'essai proprement dit. L'historique des débits mesurés en tête de puits constitue le profil d'injection au moyen des équations de conservation de la masse des deux liquides. On estime le profil de perméabilité du profil d'injection et une solution analytique qui suppose un écoulement monophasique dans chaque couche et le même skin pour toute la formation. Les incertitudes principales portent sur les pressions de formation et les variations possibles du skin. Elles sont estimées au moyen d'un calcul analytique.

Une séquence de quatre essais à pressions et débits différents a été réalisée sur la maquette. On faisait circuler la boue de forage avant les essais pour créer un « mudcake » (et donc un skin) comme dans un forage réel. Les profils de perméabilité estimés présentent une bonne concordance avec les perméabilités mesurées avant les essais. L'hypothèse d'un skin uniforme a été ainsi confortée et on a vérifié la répétabilité de la technique à l'échelle laboratoire.

On a réalisé un essai sur un sondage de 1750 m de long atteignant une couche de sel dont on a correctement estimé la perméabilité moyenne pendant la période de stabilisation. Toutefois celle-ci était si faible (4 10-21 m2) que l'utilisation de deux fluides n'a pas permis de faire de différence qu'entre les parties cuvelée découverte du puits.

Contents

Part I

Main Text

Chapter 1

Introduction

Sedimentary basins are made of layers formed over millions of years and stacked on top of each other. These formation layers are characterized by physical properties that vary with depth. A wellbore passes through several such formation layers. Measuring these subsurface properties and their heterogeneities along the well, a procedure called logging, is crucial to understand the production capacity of a petroleum well. They are equally important in water production wells, geothermal wells and underground storage wells. The first well log, invented by the Schlumberger brothers in the 1920s, measured the electrical resistance at different wellbore depths using an electrical probe. Current logging techniques can estimate a long list of formation properties such as porosity, permeability, lithology, saturation levels of fluids, geomechanical properties, etc. (Fig. 1.1).

One of the most desired logs, probably also the most elusive, is a continuous permeability log. Permeability is the ease with which a fluid of given viscosity can flow through the porous media. It is analogous to conductivity in heat conduction problems. Permeability is an important indicator of expected production rates in petroleum wells and hence, estimating permeability heterogeneities along the wellbore is critical for designing well completion, selecting the zones in which stimulation treatments are performed and modeling the flow in the reservoir.

1.1 Fluid flow in porous media

1.1.1 Darcy's law and diffusivity equation

Darcy's law for a 1D monophasic flow is given in Eq. 1.1. The gravity term in Eq. 1.1 disappears for flows at a constant elevation. The forerunner to this equation was first derived empirically by Henri Darcy in 1856 from his experiments at Dijon, France. A rigorous derivation of Darcy's law from the Navier-Stokes equation can be obtained using homogenization principles (Sánchez-Palencia, 1980).

$$\vec{u} = -\frac{k}{\mu}\vec{\nabla}(p - \rho g z) \tag{1.1}$$

where, k/μ is the mobility of the fluid, p is the pore pressure in the fluid and $\vec{u}$ is the flux discharged per unit cross-sectional area (dimensions are LT^{-1}). Permeability k is the single-phase permeability, i.e. when the porous medium is 100% saturated with a single flowing fluid; μ is the

	Permeability	Porosity	Saturation	Lithology	Geomechanical properties
Electrical resistivity	influenced				
Laterolog	influenced		direct	influenced	
Induction			direct	influenced	
Microlaterolog	influenced		direct	influenced	
Spontaneous potential	influenced			influenced	
Electromagnetic propagation		direct	direct	influenced	
Nuclear					
Gamma ray density		direct			
Neutron porosity		direct			
Natural radiactivity				direct	
Induced gamma ray spectroscopy	influenced			direct	
Nuclear Magnetic Resonance (NMR)	direct	direct			influenced
Acoustic	direct	direct		direct	direct
Dipmeter and imaging		influenced			direct
Formation testing and sampling					
Rock sampling	direct	direct		direct	direct
Fluids sampling					
Fluids pressure testing	direct				
Seismic				influenced	

 Measurement provides direct information about reservoir property
 Measurement is influenced by reservoir property
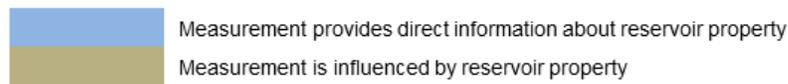
Figure 1.1: Some common logging techniques that estimate geological properties in the wellbore. Recreated from Andersen (2011).

viscosity of the flowing fluid. When the porous media contains more than one fluid, the permeability of each fluid is smaller than the single-phase permeability. In such cases, permeabilities are obtained by multiplying k with a dimensionless relative permeability term. The relative permeability is a function of fluid saturation; it is also fluid and formation dependent. Additional discussion on relative permeability can be found in chapter 3. Throughout the thesis, k is the single-phase permeability and the flow is monophasic unless specified otherwise.

Darcy's law is a momentum balance equation for the flowing fluid obtained rigorously through homogenization of Navier-Stokes equation by Sánchez-Palencia (1980). In addition, the fluid should also satisfy the continuity equation (mass conservation) and the state equation. When the following assumptions are made, the resulting equation takes the mathematical form of a diffusion equation with one unknown p (pore pressure in the fluid).

1. The pore volumes are saturated with only one fluid, which is also the flowing fluid.

2. The temperature of the reservoir fluid and the rock matrix are constant at all times. The reservoir fluid and the pore volume are slightly compressible and their compressibilities c_f and c_p, respectively, are constant due to small pore pressure changes in such problems. Hence,

the iso-thermal state equations for the fluid and the pore volume are $\frac{1}{\rho}\frac{\partial \rho}{\partial p} = c_f$ and $\frac{1}{\phi}\frac{\partial \phi}{\partial p}$, respectively. The stress changes in the rock matrix due to a change in pore volume is ignored. The total compressibility c_t is $c_p + c_f$.

3. Gravity effects are negligible.

4. Darcy's law is applicable, i.e. $\vec{u} = -\frac{k}{\mu}\vec{\nabla}p$.

5. The reservoir is homogeneous and isotropic.

Mass conservation demands that the difference in mass flux entering and leaving the pore volume should be equal to the mass accumulation in the pore volume (Eq. 1.2). Using Darcy's law and the state equation, the divergence term can be expressed as a function of fluid pressure (Eq. 1.3). For small fluid velocities and slightly compressible liquids the higher order term $c_f \left(\vec{\nabla}p\right)^2$ in Eq. 1.3 can be neglected. This term, however, becomes significant for gas flows. Similarly, the right-hand side of Eq. 1.2 can be expressed as a function of pressure p and total compressibility c_t (Eq. 1.4). The resulting equation in Eq. 1.5 is a diffusion equation that allows the computation of transient pressure evolution and in turn transient flow rates. $K\,(= k/\mu\phi c_t)$ is the hydraulic diffusivity of the fluid flowing in the porous media.

$$- div\left(\rho\vec{u}\right) = \frac{\partial\left(\rho\phi\right)}{\partial t} \tag{1.2}$$

$$- div\left(\rho\vec{u}\right) = \frac{k}{\mu}\rho\left[\frac{1}{\rho}\vec{\nabla}p.\vec{\nabla}\rho + \nabla^2 p\right] = \frac{k}{\mu}\rho\left[c_f\left(\vec{\nabla}p\right)^2 + \nabla^2 p\right] \tag{1.3}$$

$$\frac{\partial\rho\phi}{\partial t} = \rho\phi\left[\frac{1}{\rho}\frac{\partial\rho}{\partial p} + \frac{1}{\phi}\frac{\partial\phi}{\partial p}\right]\frac{\partial p}{\partial t} = \rho\phi c_t\frac{\partial p}{\partial t} \tag{1.4}$$

$$K\nabla^2 p = \frac{\partial p}{\partial t} \tag{1.5}$$

1.1.2 Formation damage

In the previous section, rock formation was considered homogeneous. However, the formation properties in the near-wellbore region are modified by the invasion of mud filtrate and solid mud components during drilling, completion and work-over operations. *Muds* are complex mixtures of solid particles like clay, polymers and surfactants contained in a continuous fluid phase (*filtrate*) which can be water, base oil, or other synthetic fluids. During the widely practiced *over-balance* drilling, the wellbore pressure at a given depth (*sandface pressure*) is larger than the reservoir pressure at the same depth. The drilling fluid invades the *near-wellbore zone*, carrying with it the solid mud components that form the internal *mudcake* and creating a *damaged zone* with reduced permeability. Also, there is a deposition of these solid mud components at the sandface which creates an external mudcake (Fig. 1.2). The mudcakes are typically a few centimeters thick with highly reduced permeabilities (Fig. 2). A secondary reduction in permeability, typically smaller than that of drilling fluid invasion, occurs due to the redistribution of mechanical stresses and deformations in the near-wellbore zone when a cavity (the wellbore) is created in a continuous rock matrix.
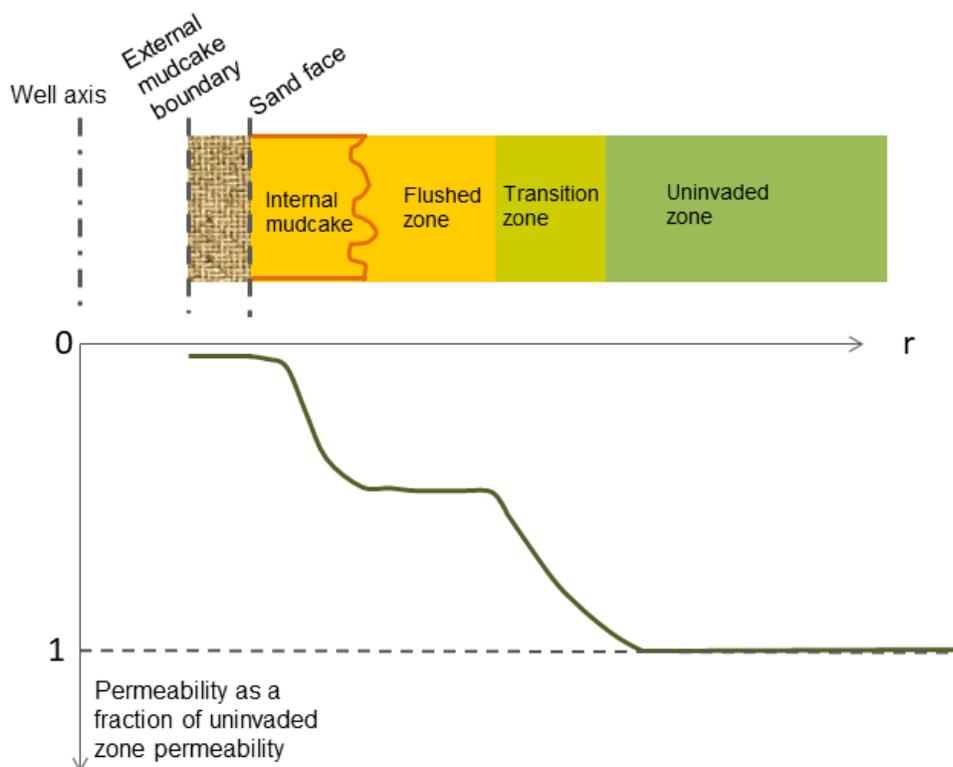
Figure 1.2: A schematic of formation damage. With elements from Mikhailov et al. (2015)

The mudcakes also play a positive role by reducing the injection rates of mud filtrate, hence limiting the radius of the invaded ('damaged') zone to less than 1-m in most cases. The invaded zone outside the internal mudcake comprises of two zones: a flushed zone predominantly saturated with the mud filtrate (and some residual formation fluid), and a transition zone with decreasing saturation levels of the mud filtrate. When the mud filtrate is different from the initial formation fluid, the relative permeability to the flow of formation fluid in the invaded zone is reduced (Mikhailov et al., 2015).

However, permeability in the damaged zone is partially recovered during/before production. During clean-up procedure, the sandface pressure is reduced to some critical value and the produced hydrocarbon lifts off the external mudcake. Also, some of the trapped solid particles (internal mudcake) and the mud filtrate flow back into the wellbore, improving the permeability in the damaged zone. In addition, well completion procedures include techniques like perforations that connect the wellbore directly to the *uninvaded zone*, bypassing partially or completely the damaged zone.

1.2 Existing permeability logging techniques

There are three major ways to evaluate permeability heterogeneities in a wellbore: rock (core) sampling, formation testing (pressure transient testing) and continuous logging. Rock sampling provides permeability values at discrete depths; formation testing estimates the average permeability of a section isolated by two packers from in-situ pressure and flow rate measurements; continuous logging techniques use electrical, acoustic, or magnetic signals to estimate permeability, often through em-

pirical correlations. It is a regular industry practice to combine permeability estimations from these multiple sources to derive a permeability log.

1.2.1 Rock (core) sampling

Rock (core) samples are extracted at different depths and tested in the laboratory for permeability, porosity, geomechanical properties, among others. Permeability anisotropy and relative permeability can also be obtained from these tests. However, the permeability estimated from the rock samples can be different from the formation permeability if the laboratory conditions are different from the in-situ conditions. It is difficult to re-establish formation conditions (stresses in particular) and native formation fluids should be used to have an accurate permeability estimation (Cantini et al., 2013). Also, the core samples are quite small, typically a few centimeters thick, and their permeabilities could be different from the formation permeabilities due to heterogeneities like fractures. Finally, collecting samples and performing laboratory tests are expensive, and it could take a few months before the test results are available. In spite of these shortcomings, rock sampling remains the gold standard against which other continuous logs are compared and correlated.

1.2.2 Formation pressure testing

These are flow-based techniques that provide reliable in-situ estimates of average permeability and near-wellbore damage. The general practice consists of isolating a section of the formation using downhole tools, drawing fluids from this section at a known, constant, rate, and finally, effecting a shut-in period during which the sandface flow rate is zero. The pressure evolution during the drawdown and the shut-in periods are interpreted to obtain the average permeability of the tested section. The different approaches listed below differ mainly in their radius of investigations, test duration and tools used; the interpretation techniques are very similar. The radius of investigation is proportional to the square root of test duration and hydraulic diffusivity of the investigated zone, $r_{inv} \propto \sqrt{Kt}$ (discussed in detail in chapter 3).

Wireline Formation Testers (WFT): The initial formation tester tool that was introduced in 1955 could collect only one fluid sample and measure one formation pressure in a single run. The improved version of 1975, called repeat formation tester, could measure formation pressures at multiple depths, hence providing the initial formation pressure as a discrete function of depth. In the late 90s, techniques to test reservoir permeability with probes attached to the formation tester tool were introduced (Proett et al., 2003).

A common criticism of this technique is that only small test durations are possible with these tools (several minutes to a few hours), and hence, the radius of investigation is quite small. The permeability estimated can, at times, be that of the region invaded by the drilling mud filtrate (Cantini et al., 2013). This permeability could be an order of magnitude smaller than the permeability of the uninvaded zone, depending on the rock type and fluid saturation levels.

Mini-Drill Stem Tests (mini-DST) or Interval Pressure Transient Tests (IPTT) are much longer and the radius of investigation is beyond the invaded zone (10-m to 40-m), thus allowing the estimation of the permeability of the uninvaded zone (Cantini et al., 2013).

Well Tests date back to the 1950s (Gringarten, 2008). The entire formation is tested simultaneously for a few hours to several days. The other pressure transient methods discussed above are inspired from the well tests. In addition to permeability and near-wellbore damage, reservoir boundaries and other radial heterogeneities can be estimated from these tests. The evolution of well test interpretation workflows and current research topics are discussed by Gringarten (2008). The permeability measured during well tests is the average permeability of the entire formation.

One limitation of the pressure testing techniques like wireline formation testing or mini-DST is that they do not provide continuous logs. Also, they can be quite expensive — 0.5 to 1 million USD for a mini-DST test in the North sea (Cantini et al., 2013).

1.2.3   Continuous logs

The search for a continuous permeability logging technique that can work in all formations has been long, and to some extent unfulfilled. The initial suggestion was to link the formation properties derived from conventional logs, like porosity, to permeability, motivated by the laboratory tests that often show a positive correlation between permeability and porosity. Such methods may provide a rough estimate of single-phase permeability, but petroleum reservoirs contain more than one fluid and the relative permeabilities are smaller (Delhomme, 2007). Timur (1968), based on his tests on 155 sandstone samples from different US oil fields, proposed $k\,(\text{mD}) = 0.136 \times \phi^{4.4}/s_{wc}^2$, where s_{wc} is the irreducible water saturation defined in section 3.3.1 (connate water saturation). This empirical relationship, once widely used in the petroleum industry, is acceptable for clean mature sandstones but yields poor estimates of permeability elsewhere since the effect of clay type and morphology on permeability is not taken into account (Delhomme, 2007). Acoustic logging and NMR logging developed in the 80s and the 90s provide more accurate permeability logs, with the latter being the widely adopted technique at present.

1.2.3.1   Acoustic logging (Stoneley waves):

Stoneley waves are low-frequency boundary waves that typically propogate along a solid-solid interface. During acoustic logging, a downhole tool generates Stoneley waves that propagate up and down the borehole. The tool consists of a transmitter, and a series of receivers, to increase the vertical resolution. While the waves conserve most of their energy in the borehole, some energy is lost in front of the permeable zones as the wave pushes the borehole fluid into the formation. The resulting decrease in the wave velocity can be related to the ratio of formation permeability and fluid velocity. In the absence of a mudcake, the permeability can be estimated from this wave velocity.

1.2.3.2   Nuclear Magnetic Resonance (NMR) log

The physical principle of nuclear magnetic resonance is the response of atomic nuclei to an externally applied magnetic field. In most elements, the measured signals are weak, but in hydrogen, which is present in abundant quantities in formation water and hydrocarbons, the magnetic moments are relatively strong. The protons spinning in the atoms of the formation fluid are initially aligned to Earth's magnetic field. An NMR tool creates a strong magnetic field perpendicular to Earth's

magnetic field and the fluid nuclei slowly align themselves parallel to this field, like a bar magnet. As soon as the magnetic field is turned off, the spin relaxation begins and the protons start to wobble, just like a child's spinning top precessing in Earth's gravitational field with its axis describing a cone (Delhomme, 2007). The two main NMR relaxation mechanisms are bulk fluid relaxation due to collisions between neighboring protons and grain surface relaxation caused by collisions between protons and grain surface. Bulk fluid relaxation can often be neglected except when there are very large pores containing large volumes of water.

The characteristic time for the nuclei to revert back to their initial state is called lateral relaxation time T_2. A receiver records the magnetic response of the spinning protons as a function of time, from which T_2 is estimated. In sandstones, the relaxation time T_2 depends on the frequency of collisions between the protons and the grain surface which in turn depends on the surface to volume ratio. This gives information on the pore size and pore throat diameter. Empirical relations that relate NMR T_2 data to permeability were obtained from laboratory tests in which brine permeability and NMR response were measured on hundreds of samples. The two widely used models are Schlumberger Doll Research (SDR) model and Timur-Coates model. The SDR model, for example, uses NMR-derived porosity and the logarithmic mean of T_2: $k_{NMR} = C(\phi_{NMR})^4(T_{2,log})^2$. The coefficient C is formation dependent ($C = 4$ for sandstones and 0.1 for carbonates).

While NMR-derived permeabilities are useful in characterizing sandstones and chalk, they are less accurate in carbonates (Delhomme, 2007). Also, SDR and Timur-Coates models are not directly applicable in tight reservoirs and research is underway to identify new interpretation workflows (Di and Jensen, 2016; Wei et al., 2015). Even in the best case scenarios, NMR-derived permeability can show a good correlation to core permeabilities at wellbore scale but not without significant local deviations (see the figure in Allen et al., 2000, page 6).

1.2.3.3   Other logs that are influenced by permeability

Resistivity logs measure the electrical resistance of the formation fluid to the flow of electric current. Formation water is mostly saline which makes it a good conductor of electricity, reducing the electrical resistance. Hydrocarbons are poor conductors and increase the electrical resistance. Formation water saturation as a function of depth can be derived from this log. Also, the invasion of the drilling fluid filtrate is larger in the more permeable layers and its resistivity could be different from that of formation fluids. Hence, permeability exerts an indirect influence on the resistivity measurements in the near-wellbore region.

Spontaneous potential logs measure the electric potential generated by the exchange of ions between the formation fluid and the drilling mud filtrate in the near-wellbore region (Varhug, 2016). The reference line is set by the impermeable shales in which there is no filtrate invasion. If the formation fluid is more saline (water-bearing layers) than the mud filtrate, the spontaneous potential deflection is negative. In the hydrocarbon-bearing layers, the deflection is positive (since hydrocarbons are typically less saline than the mud filtrate).

Electromagnetic propagation tools consist of transmitters that emit electromagnetic waves at a frequency of few kHz and receivers that measure wave attenuation and phase-shift of the reflected waves (Allen et al., 1989). Phase shift depends on formation electrical resistivity at a shallow
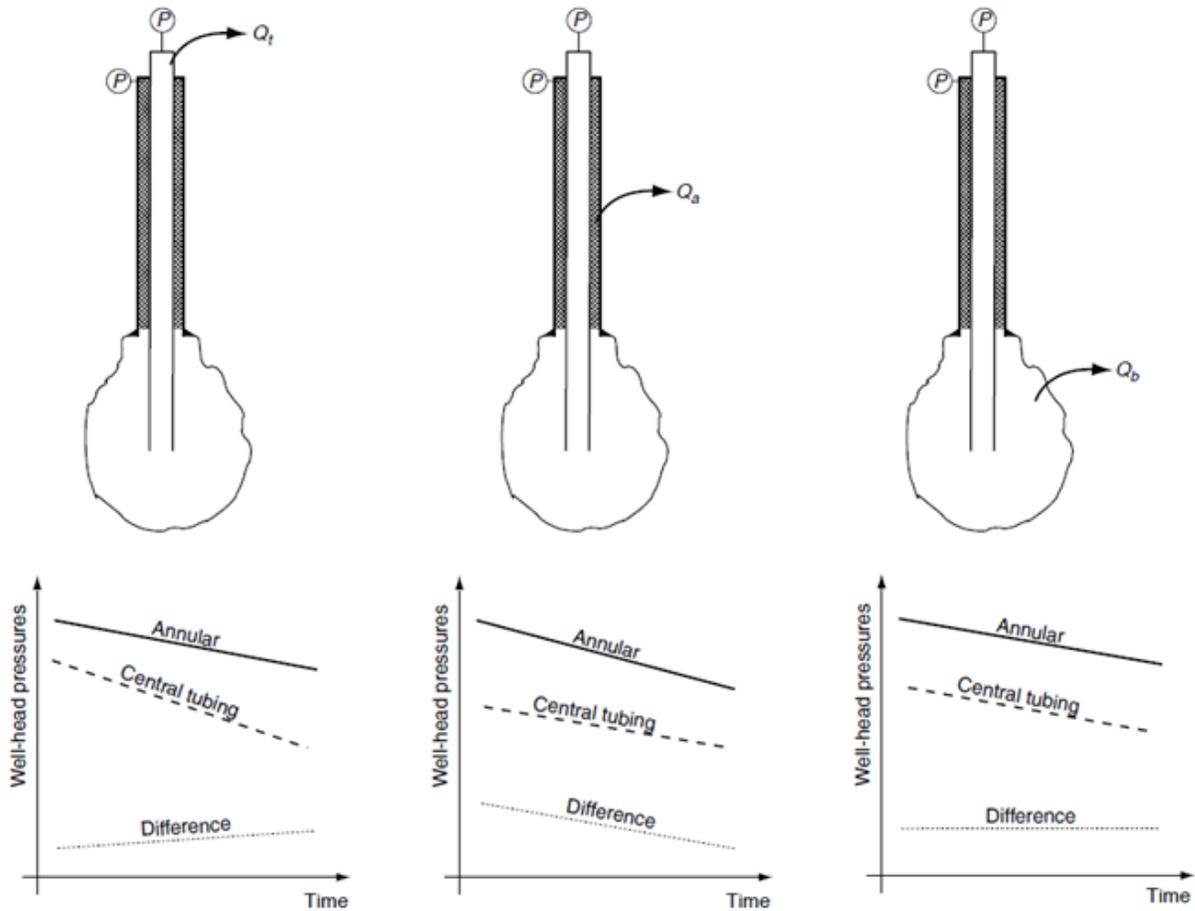
Figure 1.3: Different leak types and their influence on well pressure during an MIT. Reprinted with permission from Berest et al. (2001).

investigation radius and attenuation depends on formation resistivity at a deeper investigation radius. The difference in resistivities can be attributed to the invasion by the drilling fluid filtrate which can indicate the presence of a permeable zone.

Gamma-ray spectroscopy records the spectrum of gamma rays emitted by the formation after bombardment by high-energy neutrons. Formation mineralogy can be obtained from these measurements. Changes in mineralogy are usually accompanied by changes in size, shape and morphology of rock grains. These changes affect the pore system and in turn the permeability (Delhomme, 2007).

1.3 The proposed injection log

We have developed a novel technique to obtain a continuous sandface injection log without downhole tools. Under certain conditions, a continuous permeability log can be derived from this injection log.

The proposed technique derives its inspiration from the Mechanical Integrity Tests (MIT) performed in underground salt caverns used for hydrocarbon storage. During these tests, the well is equipped with a central tube. The annulus is filled with two immiscible fluids with different densities

(usually brine and a hydrocarbon or nitrogen) and the wellhead pressure is increased to maximum operational pressure (Fig. 1.3). A downhole logging tool tracks the interface location between the two fluids. Any interface displacement after thermal equilibrium is reached can be attributed to the loss of one of the two fluids in the annulus. Berest et al. (2001) proposed using the 'wellhead pressure differential', i.e. tubing wellhead pressure minus annulus wellhead pressure, measured by accurate pressure sensors to track the interface location, eliminating the need for a downhole logging tool.

1.3.1 Injection log before thesis - early results and shortcomings

In petroleum wells, such an interface can be placed at different depths in the open hole. The discrete procedure can be generalized to a continuous procedure, in which the fluid interface in the open hole is continuously displaced by fluid circulation at the wellhead and the evolution of pressures and flow rates at the wellhead are recorded. The test data could be interpreted to obtain wellbore heterogeneities like permeability, formation pressures, etc. (US patent: Jacques et al., 2013).

The following test procedure was developed and tested before the beginning of the thesis.

- Two liquids with a large viscosity contrast were used. This makes the formation injection rate of the viscous liquid negligible compared to that of the less-viscous liquid. During in-situ tests, the liquids were separated by a viscous gel to avoid mixing between the two liquids. During laboratory tests, the density difference between the two liquids was large enough to guarantee a stable interface.

- The liquids were continuously circulated during the test and the circulation rates at tubing and annulus wellheads were measured by wellhead flow meters. The difference between the two rates can be attributed to liquid accumulation in the wellbore or injection into the formation. The tests were performed at constant wellhead pressures and liquid accumulation in the wellbore was very small.

- At the beginning of the test, the wellbore was filled with a viscous liquid (usually drilling mud). Wellhead pressure was increased. The less-viscous liquid was injected in the tubing and the drilling mud was withdrawn from the annulus. As the less-viscous liquid displaced the viscous liquid in the open hole, an increase in the 'differential flow rate', tubing wellhead injection rate minus annulus wellhead withdrawal rate, was observed due to an increase in the formation injection rate.

In 2012, a laboratory model was designed by Benoît Brouard, and built by Vincent de Greef and Pierre Valli at Ecole Polytechnique, France, to test this technique. Several hollow, cylindrical rock samples were stacked on top of each other to mimic a multilayered formation. Test data from one such laboratory test was interpreted at the beginning of the thesis and the results were compared to benchmark permeabilities (Fig. 1.5); the interpretation workflow is discussed in the Annex. The laboratory tests correctly identified the more permeable samples but their permeabilities were underestimated. This underestimation was even larger for the permeable layers at the top of the
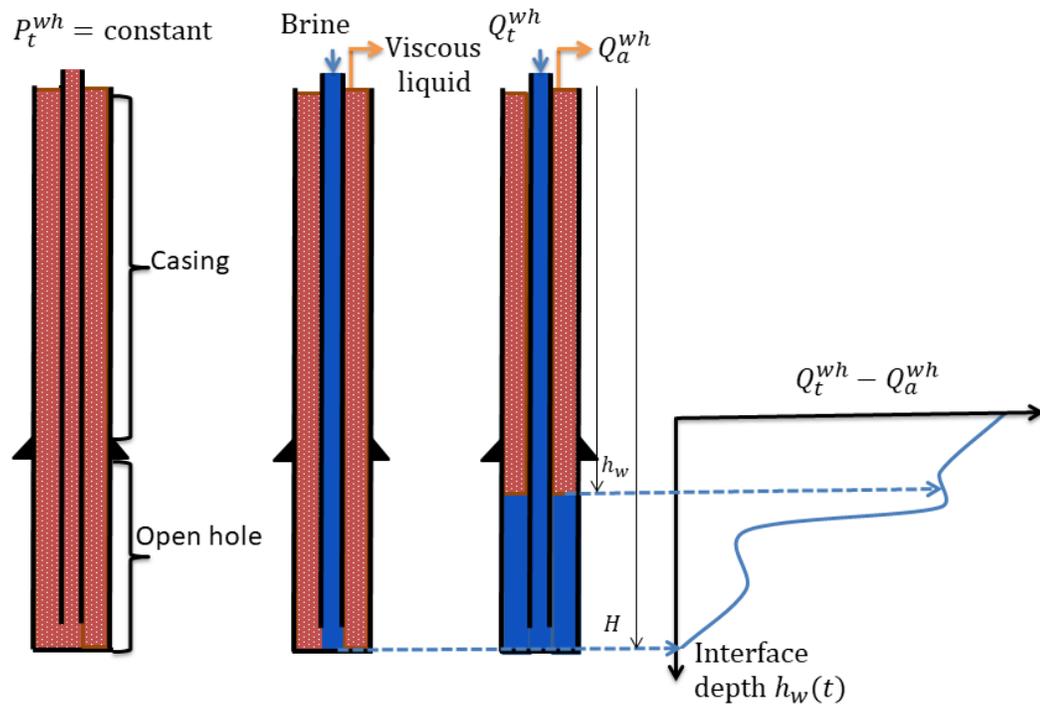
Figure 1.4: Logging procedure developed before the thesis (Manivannan et al., 2017)
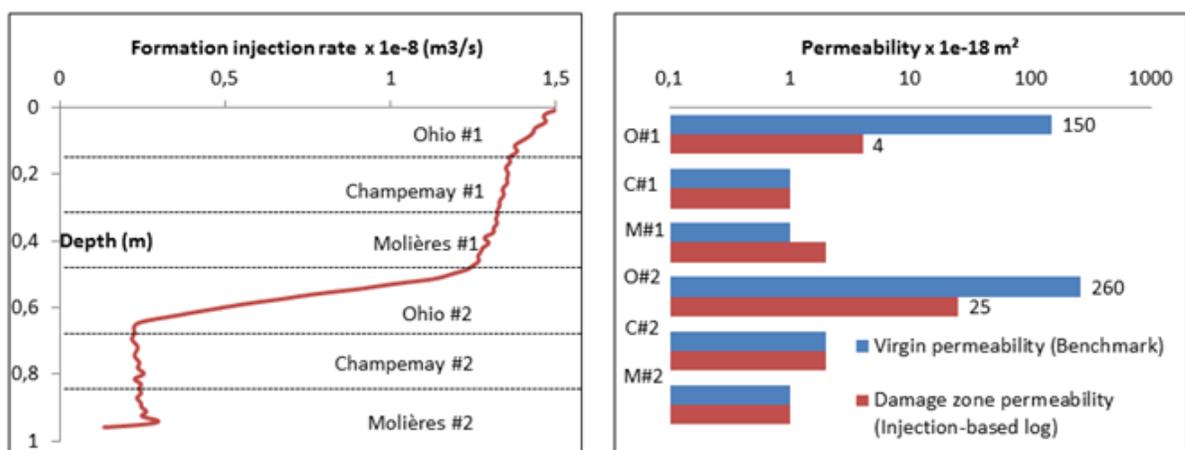
Figure 1.5: Total formation injection rate and permeability logs from an opening WTLog test. Skin $S=0$ is used to derive the permeability log in red.

stack which undergo additional damage during the test since they are exposed to the viscous liquid for a longer duration.

In 2015, an in-situ test was performed in a tight overburden formation in France (permeabilities less than 1 μD) by Antoine Jacques, Benoît Brouard, Vincent de Greef and Pierre Bérest. An NMR log was also run in the same formation and the results were interpreted by IFPEN and Total. Permeabilities derived from the two methods are compared in the Annex. Once again, there was a good qualitative agreement in identifying the more permeable layers. But, a quantitative comparison of the two logs shows large differences (Manivannan et al., 2017). This could be explained by the following shortcomings of the previous technique.

- Transient effects like viscous fingering or permeability changes in the near-wellbore region can occur during the test. These transient phenomena occurring in the layers already exposed to the less-viscous liquid could be misinterpreted as heterogeneity of the formation layer in contact with the liquid interface in the annulus.

- Formation damage, typically quantified by skin value S (defined in chapter 3) could not be estimated. An assumption had to be made on the average skin value of the open hole to derive the permeability logs.

- The formation permeability at depth z is interpreted from the rate data recorded immediately after the interface has reached this depth. It is evident that the flow has not been given enough time to develop beyond the near-wellbore damage zone. The estimated permeability corresponds to the permeability in the damaged zone.

1.3.2 Improvements made to the test procedure during the thesis

The thesis was begun with the objective of addressing these shortcomings. It was soon identified that changes to both test procedure and interpretation workflow were required. The test design should allow for the use of a simple and robust interpretation workflow to estimate the permeability profile in the uninvaded zone.

The first improvement to the test procedure was made by beginning the logging test with the open hole filled with the less-viscous liquid (*phase 1*). The viscous liquid was subsequently injected into the tubing to cover the open hole. This eliminates transient effects like viscous fingering or permeability changes in the near-wellbore zone during the test, because the test now begins with a well-established flow. This also helps in choosing appropriate wellhead pressures at the beginning of the test since the maximum formation injection rate is known from phase 1.

Another critical addition to the test procedure was a slightly longer phase 1 during which the well is completely filled with the less-viscous liquid which is injected into the formation under constant pressure (same pressure as the subsequent logging phase). The average skin value of the open hole (global skin) is interpreted from the transient decay of formation injection rate. This average skin value is used to derive a permeability log during phase 2 (the logging phase). Also, the duration of this phase can be designed to ensure that the investigation radius is beyond the damaged near-wellbore zone.

In addition, the interpretation workflow is vastly simplified, partly aided by the improvements to the test procedure: a monophasic flow model can be used for interpretation; transient decay during phase 2 is negligible; the skin estimate from phase 1 constrains the inverse problem. The new interpretation procedure is robust, computationally less-intensive and provides error estimates. Laboratory tests were performed with this new procedure after making small modifications to the existing test setup. Permeability profiles estimated from these tests show good quantitative agreement with the benchmark permeabilities of the test samples.

1.4 Organization of the thesis

Chapter 2 discusses the new test procedure and the interpretation workflow developed during the thesis. A wellbore circulation model computes the formation injection rates from wellhead flow rates. Data from phase 1 is interpreted using a derivative-based approach. Data from phase 2 is interpreted to first obtain an injection log, i.e. formation injection rate vs well depth. A permeability log is derived by assuming a monophasic flow in the formation and same skin value (formation damage) for all formation layers. The sensitivity of the permeability log to non-uniform skin is discussed using analytical solutions.

Chapter 3 discusses some basic reservoir flow models: homogeneous reservoir with skin and radial composite model. An interpretation workflow is presented to obtain the total permeability-thickness of the open hole, kh, and global skin. The interpretation workflow is similar to the derivative approach extensively used in the petroleum industry for pressure transient analysis. A two-phase flow model is also discussed in this chapter. The mobilities of the zones containing the original formation fluid and the injected fluid can be obtained with the same derivative approach.

Chapter 4 presents laboratory test results in which injection logs are obtained using the test procedure and the interpretation workflow discussed in chapter 2. A wide range of permeabilities (40 μD - 4 D) were tested. Good correlations were obtained between the estimated permeability logs and benchmark permeabilities. The results prove the repeatability of the test and validate the interpretation workflow at laboratory scale. Also, a few tests were performed with the test procedure developed before the thesis. An interesting transient phenomenon that could be attributed to viscous fingering was observed.

The Annex contains three standalone chapters. The first chapter in the Annex presents an in-situ test performed in a salt formation in France to test a variant of the WTLog technique developed during the thesis. The average permeability of the open hole was interpreted as 4 nD and the formation injection rates were less than 2 L/Day. The heterogeneities in the open hole could not be measured since the test equipment were not designed to handle such extremely low permeabilities and injection rates. The second chapter is a shortened version of an SPE conference article (Manivannan et al., 2017) that discusses laboratory and in-situ tests performed before the start of the thesis (with the old test procedure) but interpreted during the thesis. The last chapter discusses analytical solutions to the unsteady-state flow problem using Bessel-Fourier series. The solution is a truncated series and is computationally faster since it doesn't require numerical inversions or integrals evaluation. The downside is that only homogeneous reservoirs can be modeled.

Chapter 2

Test Procedure and Inversion Workflow

The shortcomings of the earlier test procedure were discussed in the previous chapter and some changes were proposed to overcome them. With the addition of phase 1, the transient decay of formation injection rate can be used to interpret global skin $\bar{S}$ and permeability-thickness kh (discussed in detail in chapter 3). The estimated kh is not used in the derivation of the permeability log and can be used for validation. The global skin $\bar{S}$ is used to derive the permeability log with the assumption that skin value is the same in each layer. Although this assumption is far from ideal, error analysis discussed in this chapter and laboratory test results interpreted in chapter 4 show that the corresponding error in the permeability estimate is quite small compared to the permeability variations in the open hole.

In the earlier method, the permeability estimate of a layer depended on the estimates of other layers since the transient decay of formation injection rate was significant during the test. With the new test procedure, the transient decay during the logging phase (phase 2) is negligible and the permeability of each layer is estimated independently of the permeability of other layers. Hence, there is no accumulation of error. Also, permeability logs could be derived for a section of the open hole even if parts of the flow rate data measured during phase 2 contain large noises and are not interpretable. The interpretation workflow is developed by recognizing that in-situ test data could be noisy and the interpretation workflow should be simple and robust enough to handle such non-ideal scenarios.

As before, the proposed interpretation workflow uses only surface measurements from wellhead flow meters and pressure sensors. A simple wellbore circulation model is used to derive a continuous injection log. A continuous permeability log can be derived from the injection log by considering: a monophasic flow, known formation pressures and uniform skin (formation damage). The sensitivity of the estimated permeability log to these input formation parameters are given by analytical equations. The proposed interpretation workflow is applicable to oil or water reservoirs. Gas reservoirs are out of the scope of the thesis.

2.1 Test equipment

- Wellhead pressure sensors. [These measure the tubing and the annulus wellhead pressures, to be referred hereafter by P_t^{wh} and P_a^{wh} , respectively.]

- Wellhead flow meters. [These are very accurate Coriolis flow meters which measure the liquid injection rate in the central tube, Q_t^{wh}, and the withdrawal rate at the annulus, Q_a^{wh}. They also measure the liquid densities at the wellhead, ρ_t^{wh} and ρ_a^{wh}.]

- Pressure regulator. [This maintains the liquid in the annulus (or, in some cases, the tubing) wellhead at a constant pressure.]

- Temperature sensors. [These measure the liquid temperatures at wellhead.]

- A less viscous liquid (e.g., brine or base oil) and a viscous liquid (e.g., water-based or oil-based drilling muds). Brine and water-based muds are used to test water bearing reservoirs and overburden formations. Base oil and oil-based muds are used to test oil reservoirs. The two circulating liquids have a large viscosity contrast. Also, the two circulating liquids are engineered to have the same density to avoid any change in the wellbore pressure due to a change in the weight of the liquid columns. A thin layer of viscous gel is placed between the circulating liquids to avoid any mixing between the two liquids.

- A pump to inject liquids in the well.

- A surface data-acquisition system with real-time monitoring.

2.2 Test procedure

During **phase 1,** the wellbore is completely filled with the less-viscous liquid which is circulated by injection through tubing wellhead and withdrawal from annulus wellhead (Fig. 2.1). The injection rate at the tubing wellhead, Q_t^{wh}, is maintained constant by a choke. Annulus wellhead pressure P_a^{wh} is increased so that the sandface pressures in the open hole are larger than the reservoir pressures; P_a^{wh} is maintained constant by the pressure regulator. In the absence of frictional losses and temperature changes in the wellbore, the two wellhead pressures would be the same. Total formation injection rate is computed from wellhead flow rates. The duration of this phase is long enough to ensure that non-dimensional time t_D is larger than 200 ($t_D = Kt/r_w^2$). This is required for the use of reciprocal-rate derivative approach (discussed in chapter 3) to interpret the total kh of the open hole and global skin $\bar{S}$. A large t_D also ensures that the transient decay of formation injection rate is very small during phase 2.

    Phase 2 begins with the injection of the viscous liquid in the central tube (Fig. 2.1). The annulus wellhead pressure P_a^{wh} and the injection rate at tubing wellhead Q_t^{wh} are not changed. As the viscous liquid rises up in the annulus, it displaces the less-viscous liquid in the open hole and the total formation injection rate decreases progressively. The test ends when the interface reaches the casing shoe and the viscous liquid fills the open hole. At the end of the test, the less-viscous liquid
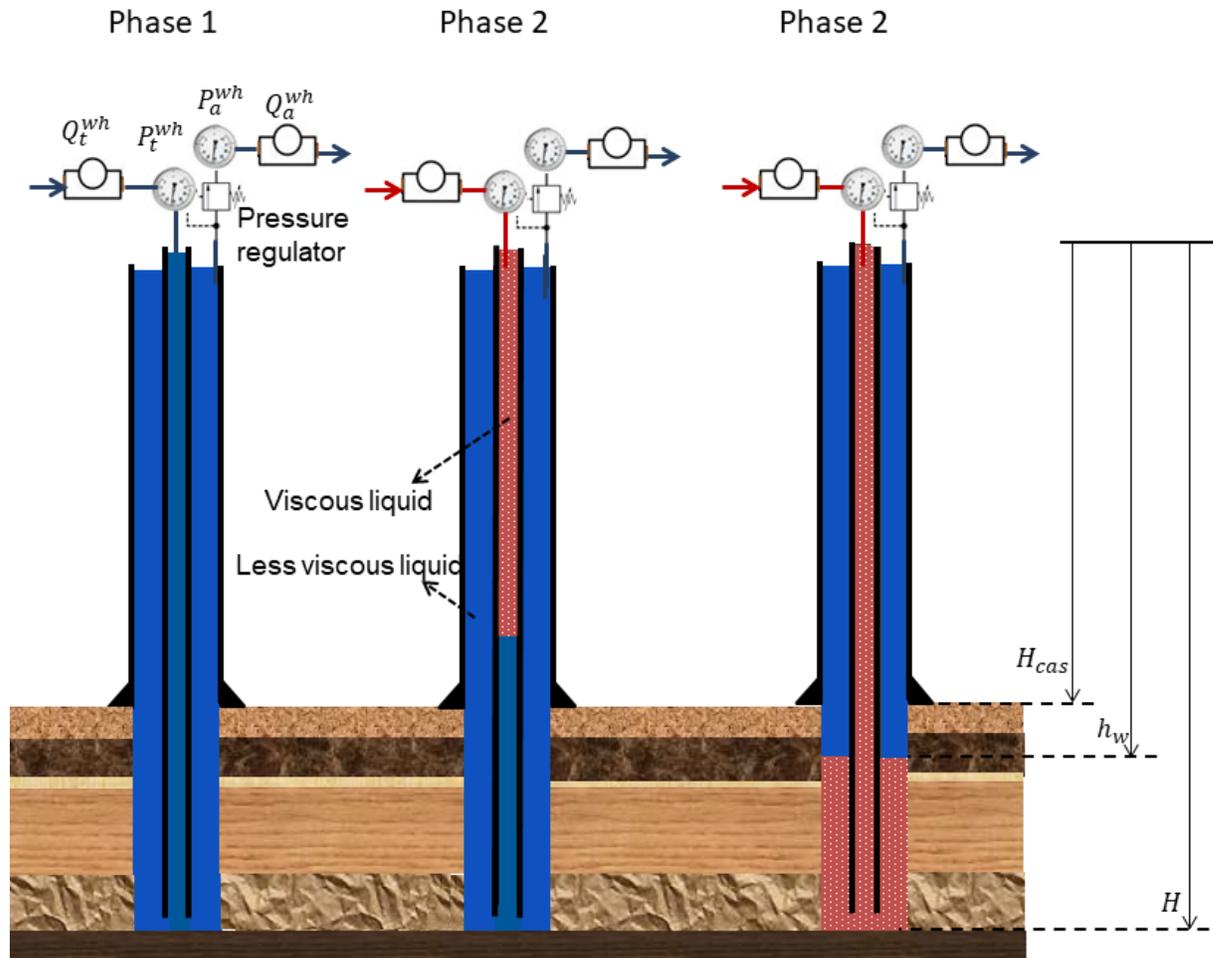
Figure 2.1: Schematic of the new WTLog test proposed

contained in the cased part of the annulus is flushed out of the well and the wellhead pressures are restored to their initial values.

2.3   Interpretation workflow

A wellbore circulation model is discussed below to estimate formation injection rates from wellhead flow rates. The frictional losses are too small to induce any density changes and mass accumulation in the wellbore. When thermal effects are neglected, the total formation injection rate equals $Q_t^{wh} - Q_a^{wh}$. Thermal effects, however, may not be negligible for deep high-temperature wells, and the circulation model takes this into account.

Data from phase 1 is interpreted for total kh of the open hole and global skin $\bar{S}$ using reciprocal-rate derivative analysis (discussed in detail in chapter 3), inspired from the pressure derivative analysis introduced by Bourdet et al. (1983). Interpretation of phase 2 comprises of two parts: deriving an injection log, i.e. sandface injection rate vs well depth, and estimating a permeability log, k vs depth, from the injection log. The derivation of the injection log takes advantage of the fact that the transient decay of formation injection rates is negligible when the interface is in the open hole, thanks to a rather long phase 1. This transient decay between $t_D = 0$ and 200 is 42%; between $t_D = 200$ and 300, it is less than 5% (Fig 3.4 in chapter 3). The transient decay is further smaller in the presence of skin ($< 2\%$ when skin $\bar{S} = 10$). The injection log provides the formation injection rate of less-viscous liquid per unit thickness, $q_{\mu-}^{wf}(z, \tau(z))$, as a function of wellbore depth z; $\tau(z)$ is the time (computed) at which the interface in the open hole reaches depth z. With the knowledge of the formation injection rate at a single time instant for any depth z, only one unknown reservoir parameter can be estimated. The interpretation workflow estimates a permeability log, $k(z)$.

2.3.1   Wellbore circulation model

Coupled 'reservoir + wellbore' simulator models compute the evolution of wellbore pressure, temperature and sandface injection rate. Several such models are discussed in the literature. Kabir et al. (1996a) proposed a model in which the fluid flows in the wellbore and the reservoir are coupled and solved simultaneously. The wellbore flow is modeled using mass, momentum, and energy balance equations; and state equation for gas. The momentum balance equation considers inertial effects due to fluid accelerations in the wellbore and frictional losses are modeled by a drag-like term proportional to the square of fluid velocity. The energy balance takes into account radial heat exchange between the wellbore and the rock formation. These equations are solved numerically using a finite difference scheme. The flow in the reservoir is given by an analytical solution of the diffusion equation derived from Darcy's law.

Izgec et al. (2007) improved the model of Kabir et al. (1996a) by modeling wellbore heat transfer in both radial and vertical directions using a semi-analytical solution developed by Hasan et al. (2005). This eliminated the need for energy equations in matrix operations, delivering significant reductions in the computational time. All these models consider oil/gas production through a single conduit, i.e. there is no central tubing.

Coupled numerical models are required when the pressures and the flow rates in the wellbore
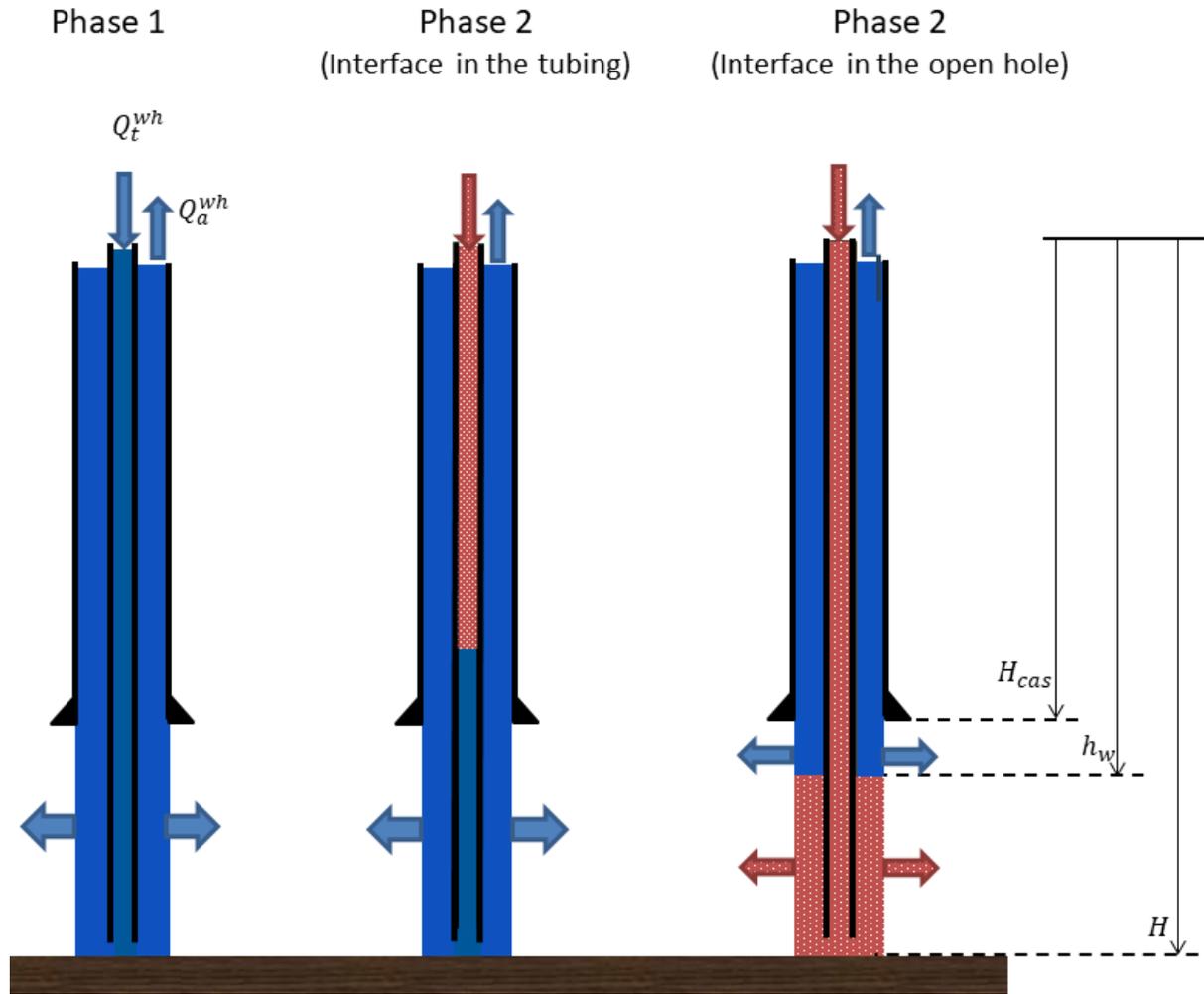
Figure 2.2: Mass exchanges during a WTLog test

undergo large changes and the wellbore fluid is very compressible. Such changes occur when there are drastic changes in wellhead production rates, for example a producing wellhead is shut-in or vice-versa. During WTLog tests, the injection rate into the tubing wellhead, Q_t^{wh}, and the annulus wellhead pressure, P_a^{wh}, are constant. Also, the density of the two fluids circulated in the well are the same. The flow rate in the cased part of the annulus may vary slightly to reflect the changes in the total injection rate into the formation and this may alter a bit the frictional losses in the wellbore. However, these effects are too small to modify the liquid densities in the wellbore. The only changes to the liquid densities result from thermal effects due to heat transfer between the two wellbore spaces (tubing and annulus) and the surrounding rock formation.

Kabir et al. (1996b) have developed an analytical model to compute the temperature evolution in the tubing and the annulus when circulation rate is constant. The model is based on thermal energy balance between the rock formation and a single fluid circulating in the wellbore. Heat transfer is limited to the radial direction with steady-state heat transfer in the wellbore and transient heat transfer in the rock formation. This thermal model, combined with the state equations of the liquids, can be employed to estimate the change in fluid densities in the wellbore.

Finally, mass conservation for the wellbore liquids can be expressed as: mass accumulation in the wellbore = injection at the tubing wellhead – withdrawal from the annulus wellhead – injection into the formation (Eqs. 2.2 to 2.6). It is assumed that the formation injection rate of the viscous liquid is negligible compared to that of the less-viscous liquid. The liquid densities in the wellbore ρ_t and ρ_a depend on depth because the pressure and the temperature in the wellbore increase with depth. The subscripts $'t'$ and $'a'$ denote central tube and annulus, respectively. They also depend on time t when the thermal effects are not negligible. The liquid densities at the wellhead, ρ_t^{wh} and ρ_a^{wh}, are measured by the surface flow meters and could slightly vary with time. The cross-sections, S_t and S_a, are known functions of depth. The injection rate per unit thickness of the less-viscous liquid, i.e. the Darcy flux in Eq. 1.1 multiplied by the perimeter of the open hole, is $q_{\mu-}^{wf}$. The integrals in Eqs. 2.2 to 2.6 (mass accumulation) are computed both in the central tube and the annulus.

Some simplifications are made to Eqs. 2.1 to 2.5 in the following pages. The mass accumulation due to the change in wellbore liquid density is absorbed into wellhead flow rates to give $Q_t^*(t)$ and $Q_a^*(t)$. When temperature changes in the wellbore are negligible, $Q_t^* = Q_t^{wh}$ and $Q_a^* = Q_a^{wh}$. When the temperatures changes are significant, as in high-temperature wells, Q_t^* and Q_a^* are computed from the wellhead flow rates Q_t^{wh} and Q_a^{wh}, heat transfer model of Kabir et al. (1996b), and state equations. Early in the thesis, we had developed a heat transfer model for a wellbore with two different circulating fluids and uniform fluid velocities in the tubing and the annulus; only radial heat transfer was considered; the wellbore was discretized along the well depth and heat transfer at each depth was computed using a semi-analytical solution (Manivannan et al., 2015). This model was used to study the apparent leak rates induced by thermal evolution during the interpretation of tightness tests in salt caverns.

Open holes in vertical wells could be a few hundred meters long which is quite small compared to the well depth (typically a few km). The liquid density in the open hole is more or less uniform and can be replaced by an average density $\bar{\rho}_{oh}$. This average density can be estimated from the temperature and pressure distribution in the open hole and state equations. This also applies to long horizontal open holes in which pressure and temperature are almost uniform.

Phase 1 (only less-viscous fluid in the well):

$$\frac{d}{dt}\left[\int_0^H \rho_t(z,t)S_t(z)dz + \int_0^H \rho_a(z,t)S_a(z)dz\right] = \rho_t^{wh}(t)Q_t^{wh}(t) - \rho_a^{wh}(t)Q_a^{wh}(t)$$

$$- \int_{H_{cas}}^H \rho_a(z,t)q_{\mu-}^{wf}(z,t)dz \quad (2.1)$$

Phase 2 (interface in the tubing):

Viscous liquid:

$$\frac{d}{dt}\left[\int_0^{h_w(t)} \rho_t(z,t)S_{tub}(z)dz\right] = \rho_t^{wh}(t)Q_t^{wh}(t) \quad (2.2)$$

Less-viscous liquid:

$$\frac{d}{dt}\left[\int_{h_w(t)}^{H}\rho_t(z,t)S_t(z)dz + \int_0^{H}\rho_a(z,t)S_a(z)dz\right] = -\rho_a^{wh}(t)Q_a^{wh}(t) - \int_{H_{cas}}^{H}\rho_a(z,t)q_{\mu-}^{wf}(z,t)dz \quad (2.3)$$

Phase 2 (interface in the open hole):

Viscous liquid:

$$\frac{d}{dt}\left[\int_0^{H}\rho_t(z,t)S_t(z)dz + \int_{h_w(t)}^{H}\rho_a(z,t)S_a(z)dz\right] = \rho_t^{wh}(t)Q_t^{wh}(t) \quad (2.4)$$

Less-viscous liquid:

$$\frac{d}{dt}\left[\int_0^{h_w(t)}\rho_a(z,t)S_a(z)dz\right] = -\rho_a^{wh}(t)Q_a^{wh}(t) - \int_{H_{cas}}^{h_w(t)}\rho_a(z,t)q_{\mu-}^{wf}(z,t)dz \quad (2.5)$$

Leibniz integral rule (Eq. 2.6) is applied to split the Left-Hand Side (L.H.S.) of Eqs. 2.2 to 2.5 into two terms: mass accumulation due to density changes and mass changes resulting from interface displacement. For example, upon application of Leibniz rule Eq. 2.2 expands into Eq. 2.7. To simplify the equations, we introduce effective circulation rates Q_t^* and Q_a^* that absorb the storage term into wellhead rates. In Eq. 2.7, the effective circulation rate is $Q_t^*(t) = Q_t^{wh} - (1/\rho_t^{wh})\int_0^{h_w(t)}S_t(z)\frac{\partial}{\partial t}\rho_t(z,t)dz$. These effective circulation rates are computed from wellhead flow rates, heat transfer model discussed earlier and state equations.

$$\frac{d}{dt}\int_{a(t)}^{b(t)}f(z,t)dz = f(b,t)\frac{d}{dt}b(t) - f(a,t)\frac{d}{dt}a(t) + \int_{a(t)}^{b(t)}\frac{\partial}{\partial t}f(z,t)dz \quad (2.6)$$

$$\int_0^{h_w(t)}S_t(z)\frac{\partial}{\partial t}\rho_t(z,t)dz + \rho_t(h_w,t)S_t(h_w)\dot{h}_w(t) = \rho_t^{wh}(t)Q_t^{wh}(t) \quad (2.7)$$

In Eqs. 2.8 to 2.12, Eqs. 2.1 to 2.5 are re-written using effective circulation rates given in Table 2.1. Eq. 2.8 is used to compute the total formation injection rate vs time which will be interpreted for total kh and global skin $\bar{S}$. Interface velocities during phase 2 are computed using Eqs. 2.9 and 2.11. Interface location in the wellbore is obtained by integration of interface velocities. The total formation injection rate during phase 2 is computed using Eqs. 2.10 and 2.12.

Phase 1 (only less-viscous fluid in the well):

$$\bar{\rho}_{oh}(t)\int_{H_{cas}}^{H}q_{\mu-}^{wf}(z,t)dz = \rho_t^{wh}(t)Q_t^*(t) - \rho_a^{wh}(t)Q_a^*(t) \quad (2.8)$$

Phase 2 (interface in the tubing):

Viscous liquid:

$$\rho_t(h_w)S_t(h_w)\dot{h}_w(t) = \rho_t^{wh}(t)Q_t^*(t) \quad (2.9)$$

	$Q_t^*(t)$	$Q_a^*(t)$
Phase 1	$Q_t^{wh}(t)$	$Q_a^{wh}(t) - \frac{1}{\rho_t^{wh}(t)}\int_0^H S_t \frac{\partial \rho_t}{\partial t} dz - \frac{1}{\rho_a^{wh}(t)}\int_0^H S_a \frac{\partial \rho_a}{\partial t} dz$
Phase 2 (interface in the tubing)	$Q_t^{wh}(t) - \frac{1}{\rho_t^{wh}(t)}\int_0^{h_w} S_t \frac{\partial \rho_t}{\partial t} dz$	$Q_a^{wh}(t) - \frac{1}{\rho_a^{wh}(t)}\int_{h_w}^H S_t \frac{\partial \rho_t}{\partial t} dz - \frac{1}{\rho_a^{wh}(t)}\int_0^H S_a \frac{\partial \rho_a}{\partial t} dz$
Phase 2 (interface in the open hole)	$Q_{tub}^{wh}(t) - \frac{1}{\rho_t^{wh}(t)}\int_0^H S_t \frac{\partial \rho_t}{\partial t} dz$ $\quad - \frac{1}{\rho_t^{wh}(t)}\int_{h_w}^H S_a \frac{\partial \rho_a}{\partial t} dz$	$Q_a^{wh}(t) - \frac{1}{\rho_a^{wh}(t)}\int_0^{h_w} S_a \frac{\partial \rho_a}{\partial t} dz$

Table 2.1: Effective circulation rates $Q^*(t)$ are expressed as a function of wellhead rates

Less-viscous liquid:

$$- \rho_t(h_w)S_t(h_w)\dot{h}_w(t) = -\rho_a^{wh}(t)Q_a^*(t) - \bar{\rho}_{oh}(t)\int_{H_{cas}}^{H} q_{\mu-}^{wf}(z,t)dz \tag{2.10}$$

Phase 2 (interface in the open hole):

Viscous liquid:

$$- \bar{\rho}_{oh}(t)S_a(h_w)\dot{h}_w(t) = \rho_t^{wh}(t)Q_t^*(t) \tag{2.11}$$

Less-viscous liquid:

$$\bar{\rho}_{oh}(t)S_a(h_w)\dot{h}_w(t) = -\rho_a^{wh}(t)Q_a^*(t) - \bar{\rho}_{oh}(t)\int_{H_{cas}}^{h_w} q_{\mu-}^{wf}(z,t)dz \tag{2.12}$$

2.3.1.1   A note on sandface pressure

Ehlig-Economides and Ramey Jr. (1981) proposed the simplified momentum equation in Eq. 2.13 to compute the sandface pressure during constant pressure tests; f is the friction factor (dimensionless), v is the liquid velocity in the wellbore and d is the diameter of the flowing section. For a downward pointing z axis, the friction term is negative in the tubing and positive in the annulus (due to opposite flow directions).

$$\frac{dp}{dz} = \rho g \pm \rho \frac{2fv^2}{d} \tag{2.13}$$

The change in sandface pressure during the test is negligible due to the following reasons. The liquid velocity in the central tubing is constant due to the constant injection rate at the tubing wellhead. The formation injection rate in the open hole varies during the test and this changes the liquid velocity in the cased part of the annulus. However, the circulation rate Q_t^{wh} is typically much

larger than the formation injection rate and hence, the velocity changes in the annulus are negligible. The friction loss between the annulus wellhead and the sandface can be considered constant. Except in the case of very deep high-temperature wells, the density changes in the wellbore with respect to time can be neglected in the estimation of the sandface pressures.

2.3.2 Deriving an injection log

An injection log is derived using Eqs. 2.11 and 2.12. The interface velocity, when the interface is in the annulus, given by Eq. 2.11 is re-written in Eq. 2.14. The total formation injection rate is given in Eq. 2.15. An injection log, i.e. $q_{\mu-}^{wf}(h_w, t)$ vs h_w, is derived using Eq. 2.16. The second term on the Right-Hand Side (R.H.S.) of Eq. 2.16 is the error due to the transient decay of the injection rate. This error is considered to be negligible since the long duration of phase 1 has ensured that the transient decay during phase 2 is quite small (between $t_D = 200$ and 300, the transient decay is less than 5%).

$$\dot{h}_w(t) = \frac{\rho_t^{wh}(t)Q_t^*(t)}{\bar{\rho}_{oh}(t)S_a(h_w)} \tag{2.14}$$

$$\int_{H_{cas}}^{h_w} q_{\mu-}^{wf}(z, t)dz = \frac{\rho_t^{wh}(t)Q_t^*(t) - \rho_a^{wh}(t)Q_a^*(t)}{\bar{\rho}_{oh}(t)} \tag{2.15}$$

$$q_{\mu-}^{wf}(h_w, t) = \frac{d}{dh_w(t)}\int_{H_{cas}}^{h_w} q_{\mu-}^{wf}(z, t)dz - O\left(\frac{\int_{H_{cas}}^{h_w} \frac{\partial}{\partial t}q_{\mu-}^{wf}(z, t)dz}{\dot{h}_w(t)}\right) \tag{2.16}$$

2.3.3 Deriving permeability log

A radial flow model in a homogeneous reservoir is used to derive a permeability log from the injection log. The injection rate at large times $\left(kt/(\mu\phi c_t r_w^2) > 200\right)$ is given by Uraiet and Raghavan (1980) (Eq. 2.17). Derivation of Eq. 2.17 is discussed in chapter 3. The near-wellbore damage is quantified by a non-dimensional skin term S. The difference between the sandface pressure and the initial reservoir pressure, $P_a(z) - P_{res}(z)$, is constant throughout the test and will be denoted by pressure head $\triangle P(z)$. If the sandface pressure during the test is not constant, permeability interpretation can be done using the convolution model discussed in chapter 3.

$$q(\tau) = 2\pi\frac{k}{\mu}[P_a - P_{res}]\frac{2}{ln(\frac{k\tau}{\mu\phi c_t r_w^2}) + 2S + 0.81} \tag{2.17}$$

Almost all the parameters in Eq. 2.17 vary with depth. The viscosity of the injected liquid $\mu(z)$ depends on the temperature in the open hole. Reservoir pressure $P_{res}(z)$ and porosity $\phi(z)$ estimated by other logs are used as inputs. Total compressibility $c_t(z)$ can be computed from fluid saturation logs and fluid properties. Sandface pressure P_a and the time at which the interface $h_w(t)$ reaches depth z, $\tau = h_w^{-1}(z)$, are computed from the test data. The only unknowns in Eq. 2.17 are permeability $k(z)$ and skin $S(z)$. The skin value is assumed to be the same for all formation layers and equal to the global skin $\overline{S}$ (estimated from the interpretation of phase 1). This leads to Eq.

2.18 in which $\widehat{k}(z)$ is an implicit function of $q(z,\tau)$, the sandface injection rate at depth z at time τ after the pressure head is imposed (input from the injection log).

$$q(z,\tau) = 2\pi \frac{\widehat{k}(z)}{\mu(z)} \triangle P(z) \frac{2}{ln\left(\frac{\widehat{k}(z)\tau(z)}{\mu(z)[\phi c_t](z)r_w^2}\right) + 2\bar{S} + 0.81} \tag{2.18}$$

To derive the permeability log, the total kh estimated from phase 1 has not been used. This offers the advantage of comparing $\int_H^{H_{cas}} \widehat{k}(z)dz$ from the permeability log and the total kh from phase 1 to validate the interpretation.

2.3.4 Error analysis

The assumption of uniform skin is not strictly valid and there could be some local variations in the skin value. Also, there could be uncertainties in formation pressure, P_{res}, and storativity, ϕc_t. In the subsequent pages, analytical equations are developed using Eq. 2.18 to quantify the error in the permeability estimates due to local skin variations and uncertainties in other input data.

2.3.4.1 Sensitivity to skin

When the actual local skin is $\bar{S} + \delta S$, an error δk is made in the permeability estimate. In Eq. 2.19, the flow rate solution from Eq. 2.18 is used to express skin $\bar{S}$ as a function of permeability estimate $\widehat{k}$ and measured injection rate which is a constant. Similarly the skin $\bar{S} + \delta S$ can be expressed using $\widehat{k} + \delta k$. These two equations and a bit of algebra yield Eq. 2.20, which quantifies the error in the permeability estimate due to local skin variations.

$$2\bar{S} = \frac{4\pi\triangle P}{q\mu}\widehat{k} - ln(\frac{\widehat{k}\tau}{\mu\phi c_t r_w^2}) - 0.81 \tag{2.19}$$

$$\frac{\delta k}{\widehat{k}} - \frac{ln(1 + \frac{\delta k}{\widehat{k}})}{ln(\frac{\widehat{k}\tau}{\mu\phi c_t r_w^2}) + 2\bar{S} + 0.81} = \frac{\delta S/\bar{S}}{1 + \frac{1}{2\bar{S}}\left(ln(\frac{\widehat{k}\tau}{\mu\phi c_t r_w^2}) + 0.81\right)} \tag{2.20}$$

Fig. 2.3 shows the computed error estimates for three different global skin vales $\bar{S} = 5,\ 20\ \text{and}\ 50$ and $\widehat{k}\tau/(\mu\phi c_t r_w^2) = 200$. The relationship between $\delta k/\widehat{k}$ and $\delta S/\bar{S}$ is linear. This is expected since the second term on the Left-Hand Side (L.H.S.) of Eq.2.21 is negligible compared to the first $\left(\text{since } [ln(\widehat{k}\tau/\mu\phi c_t r_w^2) + 2\bar{S} + 0.81] \gg 1\right)$. The slopes of the error curves are less than 1 and this can be inferred from the denominator on the R.H.S. The slopes increase with the global skin value $\bar{S}$, because, for small global skins, the influence of $ln(\widehat{k}\tau/\mu\phi c_t r_w^2)$ on flow rate is relatively larger.

2.3.4.2 Sensitivity to reservoir pressure

P_{res} is the initial formation pressure estimate which is an input used to estimate the permeability $\widehat{k}$. When the actual formation pressure is $P_{res} + \delta P_{res}$, the corresponding error in the permeability estimate is represented as δk. As in the previous case, the flow rate in Eq. 2.17 is used to express the pressure head as a function of estimated permeability in Eq. 2.21. A similar equation can be written for $P_{res} + \delta P_{res}$ and $\widehat{k} + \delta\widehat{k}$ and solving the two yields Eq. 2.22. The numerator on the L.H.S.
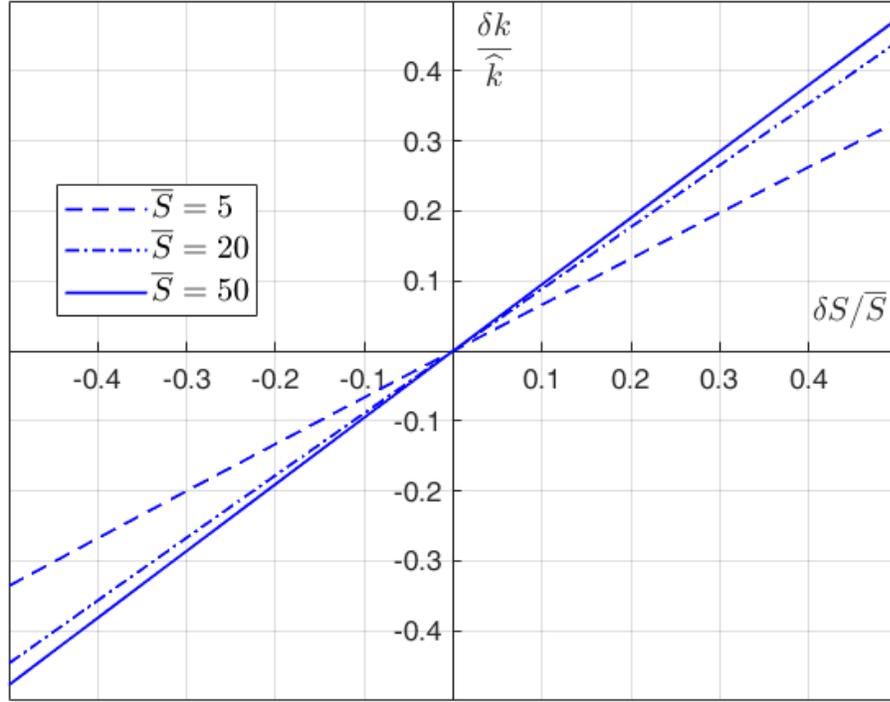
Figure 2.3: Relative error in permeability estimates $(\delta k/\widehat{k})$ due to local skin variations $(\delta S/\bar{S})$ computed using Eq. 2.20 and $\widehat{k}\tau/(\mu\phi c_t r_w^2) = 200$.

of Eq. 2.22 is the same as the L.H.S. of Eq. 2.20 from the skin sensitivity analysis. As discussed before, the second term in the numerator is negligible compared to the first. Hence, the simplified expression in Eq. 2.23 is sufficient to estimate the error due to uncertainties in formation pressure.

Fig. 2.4 shows the relative error in the permeability estimate due to uncertainties in the formation pressure. The solid curve is computed using Eq. 2.23. To compute the dotted curve Eq. 2.22, $\bar{S} = 5$ and $\widehat{k}\tau/(\mu\phi c_t r_w^2) = 200$ are used. As expected, the two curves are very similar. When the actual formation pressure is smaller than the input formation pressure (negative x-axis), the relative error in the permeability estimate is quite small. But, when the actual formation pressure is larger than the input formation pressure (positive x-axis), the relative error increases exponentially and goes to infinity when the actual formation pressure equals sandface pressure. To avoid this, the test design should ensure that the sandface pressures are larger than the maximum possible formation pressure (after taking into account the uncertainties). The objective should be to minimize $|max(\delta P_{res})|/(P_a - P_{res})$; $|max(\delta P_{res})|/(P_a - P_{res}) < 0.2$ could be acceptable.

$$\frac{q\mu}{4\pi\widehat{k}}\left[ln(\frac{\widehat{k}\tau}{\mu\phi c_t r_w^2}) + 2\bar{S} + 0.81\right] = P_a - P_{res} \tag{2.21}$$

$$\frac{\left[\frac{\delta k}{\widehat{k}} - \frac{ln(1+\frac{\delta k}{\widehat{k}})}{ln(\frac{\widehat{k}\tau}{\mu\phi c_t r_w^2})+2\bar{S}+0.81}\right]}{1 + \frac{\delta k}{\widehat{k}}} = \frac{\triangle P_{res}}{P_a - P_{res}} \tag{2.22}$$
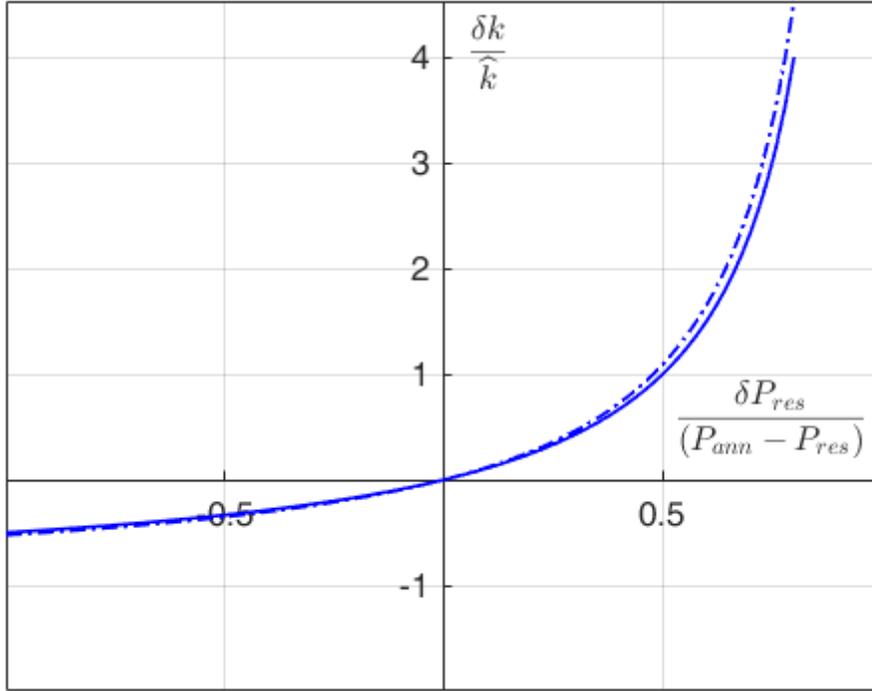
Figure 2.4: Relative error in permeability estimate to uncertainties in formation pressure. Dotted curve is computed using Eq. 2.22 and the solid curve using Eq. 2.23.

$$\frac{\delta k}{\widehat{k}} = \frac{\triangle P_{res}/(P_a - P_{res})}{1 - \triangle P_{res}/(P_a - P_{res})} \tag{2.23}$$

If formation pressures are unknown two WTLog tests could be performed at different wellhead pressures and derive both permeability log and initial reservoir pressure log through combined interpretation of the two tests. Further work is needed in developing an interpretation workflow for this scenario.

2.3.4.3 Sensitivity to storativity

Using the same technique as before, the relative error in the permeability estimate due to an error in the storativity value $\delta(\phi c_t)$ is given in Eq. 2.24. Permeability estimate is less sensitive to variations in storativity because the logarithm attenuates the effect of storativity on permeability. This is confirmed by Fig. 2.5 The relative error in permeability estimate is an order of magnitude less than the corresponding error in the storativity estimate. To generate Fig. 2.5, $\bar{S} = 5$ and $\widehat{k}\tau/(\mu \phi c_t r_w^2) = 100$ were used; the relative error in the permeability estimate even smaller when these quantities are larger.

$$\frac{\delta k}{\widehat{k}} - \frac{ln(1 + \frac{\delta k}{\widehat{k}})}{ln(\frac{\widehat{k}\tau}{\mu \phi c_t r_w^2}) + 2\bar{S} + 0.81} = -\frac{ln(1 + \frac{\delta(\phi c_t)}{\phi c_t})}{ln(\frac{\widehat{k}\tau}{\mu \phi c_t r_w^2}) + 2\bar{S} + 0.81} \tag{2.24}$$
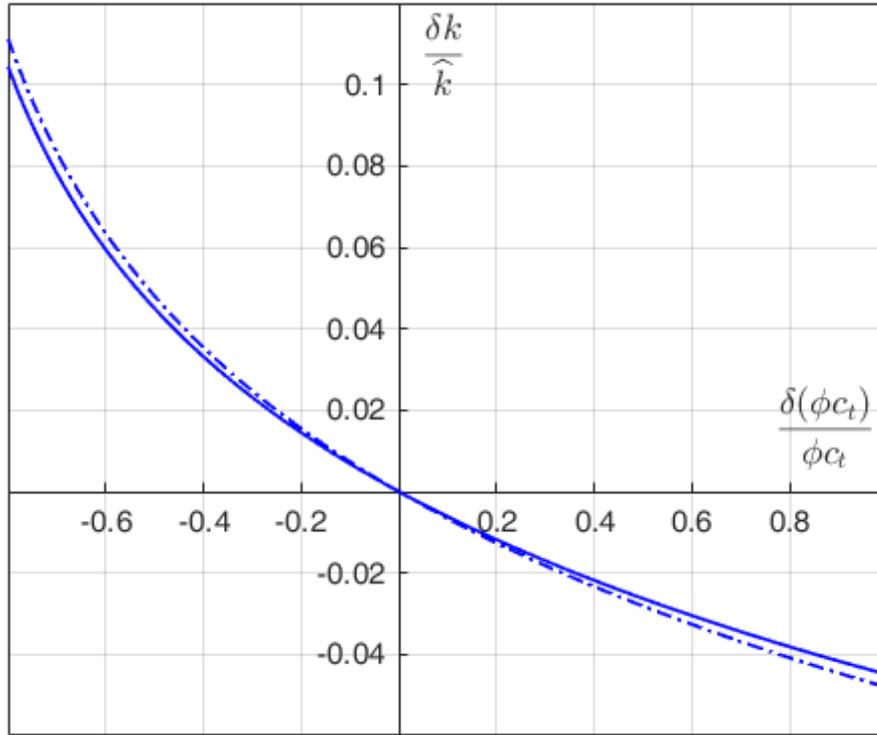
Figure 2.5: Relative error in permeability estimate due to error in storativity value. Dotted line is computed using Eq. 2.24, $\bar{S} = 5$ and $\widehat{k}\tau/(\mu\phi c_t r_w^2) = 100$. The solid line is computed by neglecting the higher order term (second term in the L.H.S.).

2.3.5 Investigation radius

The injection rates are a response to all the heterogeneities between the wellbore radius and the farthest radius in the reservoir that has experienced the pressure changes predicted by the diffusion equation. The heterogeneity in the near-wellbore region is taken into account by the skin term $\bar{S}$. Hence, the permeability estimated $\widehat{k}$ is the 'effective permeability' of the interval between the near-wellbore zone captured by skin term $\bar{S}$ and the farthest radius of pressure change; this radius is greater than $2\sqrt{Kt}$ (derivation discussed in chapter 3). For $Kt/r_w^2 = 200$ and $r_w = 0.1$ m, the farthest radius of investigation is greater than 2.8 m. This translates into a test duration of $\tau = 33$ minutes when $k = 10^{-16}$ m^2 (0.1 mD), $\mu = 10^{-3}$ Pa.s (1 cP) and $\phi c_t = 10^{-4}$ MPa^{-1}.

2.3.6 Vertical resolution

The vertical resolution of the permeability log depends on the ability of the wellhead flow meters to detect a change in total formation injection rate as the interface traverses the open hole. Hence, the vertical resolution is higher for the permeable layers with large injection rates and smaller for the less permeable layers. In the laboratory tests, vertical resolutions of about 2 cm ($1/50^{th}$ of the open hole length) have been obtained using very accurate Coriolis flow meters.

2.4 Summary

A new test procedure is proposed in this chapter without compromising on the simplicity of the old procedure. The proposed procedure makes the interpretation workflow more robust and simple. As before, all measurements are made at the surface; drilling string serves as the central tube to circulate the fluids; pressure regulation can be done using Managed Pressure Drilling (MPD) systems are available by default in most newly drilled wells; drilling fluids and drilling fluid filtrate are used as the viscous and the less-viscous fluids, respectively. The test uses equipment that are readily available at the drilling site; this, combined with the absence of downhole tools make this procedure cost-effective.

During phase 1, the wellbore is filled completely with the less-viscous liquid which is circulated in the wellbore. The wellhead pressure in the annulus and the injection rate into the tubing are maintained constant. Phase 2 begins with the injection of a viscous liquid in the tubing which rises up in the annulus, after reaching the bottom of the well. The wellhead pressure in the annulus and the pumping rate at the tubing wellhead remain unchanged during the entire test (phase 1 and phase 2). The test ends when the interface reaches the casing shoe.

Because the test is performed under constant wellhead pressure and the circulating liquids have same densities, the wellbore pressure is constant; a simple mass balance equation estimates the total formation injection rate and the interface location. The fomation injection rate from phase 1 (no interface) is interpreted for total kh and global skin $\overline{S}$ through reciprocal-rate derivative analysis. The formation injection rate and the interface location from phase 2 is used to first compute an injection log. A permeability log is derived from this injection log using a large-time asymptotic solution. Skin is considered to be uniform in all layers and equal to the global skin value $\overline{S}$ (estimated at the previous step); initial formation pressure and storativity are other inputs used. This use of analytical solution to derive a permeability log enables an error analysis that can quantify the error in the permeability log due to non-uniform skin and uncertainities in other input data.

Chapter 3

Constant Pressure Well Tests

Constant rate well tests provide an accurate estimation of the average values of near-wellbore damage (from data at early times), formation permeability (at middle times) and reservoir boundaries (at late times). During these tests, the well is produced at a constant wellhead production rate for several hours, followed by an equally long shut-in period during which the production rate is zero (Fig. 3.1). Pressure data from the shut-in period are preferred for interpretation due to the better quality of the input signal – maintaining zero sandface flow rate is easier than maintaing a constant sandface flow rate (or constant sandface pressure). An exhaustive account of the evolution of well test interpretation workflows is given in Gringarten (2008).
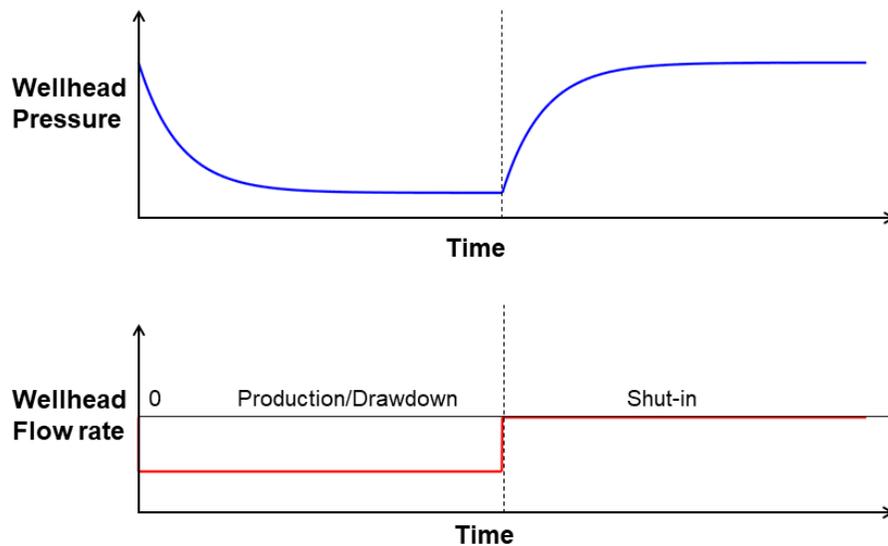
Figure 3.1: Wellhead flow rate (input) and wellhead pressure (output) during constant rate well tests

Constant pressure well tests have taken a back seat all along due to difficulties in creating an input signal of similar quality. Also, the pressure sensors available in the market have always been more accurate than the flow meters, yielding better output data. Hence, very few articles have been written on the interpretation of constant pressure well tests. Fetkovich (1980) was the first to propose an interpretation workflow based on type-curve analysis of non-dimensional flow rate vs time (q_D vs

t). Uraiet and Raghavan (1980) suggested computing kh from the slope of $1/q_D$ vs t, at middle times. They made use of the similarity between 'reciprocal flow rate' ($1/q_D$ vs t) in constant pressure tests and pressure ($p_D$vs t) in constant rate tests, an observation first made by Jacob and Lohman (1952). Subsequent authors (Turki et al., 1989; Zhang and Grader, 1994) proposed the use of rate derivative ($dq_D/dlnt$) to interpret kh, inspired by the pressure derivative approach introduced by Bourdet et al. (1983) for the interpretation of constant rate tests. To the best of our knowledge, Nashawi and Malallah (2006) are the only authors to have studied reciprocal-rate derivative, $d(1/q_D)/dlnt$. They proposed a constant pressure well test to interpret infinite-conductivity hydraulic fractures that intercept oil wells. These fractures are usually hidden by the wellbore storage effects when interpreting constant rate tests.

Recent innovations in Managed Pressure Drilling (MPD) have created automated systems that can maintain constant wellhead pressures (Chustz et al., 2007; Kamps and Dow, 2017). Also, the accuracy of flow meters has drastically improved over the years. These innovations encourage a re-look at constant pressure well tests

In this chapter, we try to impress upon the reader that the diagnostic plots and interpretation workflows of pressure derivative analysis are easily adaptable to reciprocal-rate derivative analysis. Homogeneous reservoir and radial composite reservoir models are discussed for a well producing at a constant sandface pressure. The corresponding reciprocal-rate derivative plots are similar to the pressure derivative plots for constant rate tests. An interpretation workflow is discussed for the case when the sandface pressures are step-wise constant and the initial reservoir pressure is known. During WTLog tests, when there is no interface in the open hole (phase 1), total kh and global skin $\bar{S}$ are estimated using this workflow.

A two-phase flow model is discussed to simulate the injection of a fluid different from the initial formation fluid. This case is outside the scope of the current WTLog technique and the studies are mainly of academic interest. The 'reciprocal-rate derivative' shows, yet again, remarkable similarities to the pressure derivative from constant rate injection tests.

Advantages of constant pressure tests

Constant pressure tests offer certain advantages over constant rate tests, in some cases. One of them is the absence of wellbore storage effect during constant pressure tests and this has been noted by several authors. Here is a brief explanation of the wellbore storage effect. The volume of the hydrocarbon column between the wellhead and the well bottom is V; the density of the fluid in the well is ρ. The mass balance in the well is given by Eq. 3.1, where Q^{wh} and Q^{wf} are the flow rates at wellhead and formation depth, respectively. For simplicity, the fluid density in the well is considered to be uniform. The derivative on the Left-Hand Side (L.H.S.) of Eq. 3.1 can be developed as $\rho\beta V\dot{P}$, where β is the sum of the compressibility of the well and the compressibility of the fluid in the well. This yields $\beta V\dot{P} = Q^{wh} - Q^{wf}$. Due to the accumulation/reduction of fluid mass in the well, called wellbore storage, the sandface flow rate approaches asymptotically the wellhead flow rate when the rate of pressure change is negligible (Fig. 3.2).

$$\frac{d}{dt}(\rho V) = \rho(Q^{wh} - Q^{wf}) \tag{3.1}$$

Wellbore storage effect often masks the signature of near-wellbore heterogeneities on the pressure derivative plot. Also, longer test duration may be required compared to the case without wellbore storage effect. A widely adopted solution to minimize wellbore storage effect is to use downhole shut-in tools, when possible, which reduces the 'effective' fluid volume V.
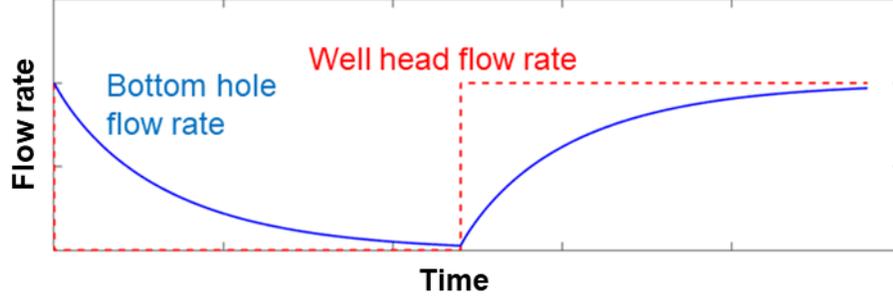
Figure 3.2: Evolution of wellhead (Q^{wh}) and sandface (Q^{wf}) flow rates during constant rate well tests

3.1 Flow Models

The most commonly used flow model is the radial, monophasic flow of a slightly compressible fluid in a homogeneous reservoir. The change in reservoir pressure, $p(r_D, t_D)$, is governed by Eq. 3.2. Non-dimensional time t_D ($= Kt/r_w^2$) is a function of mobility k/μ, storativity ϕc_t ($K = k/\mu\phi c_t$) and well radius r_w; r_D ($= r/r_w$) is the non-dimensional radius.

$$\left[\frac{\partial^2}{\partial r_D^2} + \frac{1}{r_D} \frac{\partial}{\partial r_D} \right] p(r_D, t_D) = \frac{\partial p}{\partial t_D}(r_D, t_D) \tag{3.2}$$

The initial pressure in the reservoir, P_{ini}, is uniform (Eq. 3.3) and the sandface pressure, P_w, is constant (Eq. 3.4); $\triangle P$ ($= P_w - P_{ini}$) is the applied pressure head. The reservoir is assumed to be infinitely large in the radial direction; as a consequence $p(r_D, 0) = 0$ in a diffusive problem, we also have $p(\infty, t_D) = 0$. Depending on the presence of near-wellbore damage, and how it is modeled, three different flow models are possible. Eqs. 3.2 to 3.4 are common for all the three models.

$$p(r_D, 0) = 0 \tag{3.3}$$

$$p(1, t_D) = \triangle P \tag{3.4}$$

3.1.1 No near-wellbore damage

We begin by considering a reservoir with radially uniform permeability and storativity. In this case, there are multiple techniques to solve Eqs. 3.2 to 3.4. A couple of them are discussed below and the rest is discussed in the Annex.

Solution using Green's function

Smith (1937) solved the problem of heat flow in an infinite solid, internally bounded by a cylinder at a constant temperature, using Green's functions. Jacob and Lohman (1952) adapted this solution to the flow problem (Eq. 3.5). J_0 and Y_0 are zero-order Bessel functions of the first and the second kind, respectively, and $q(t_D)$ is the sandface flow rate per unit thickness. The integral should be evaluated numerically. For simplicity, flow rates are expressed in this chapter in their non-dimensional form, $q_D(t_D) = q\mu/2\pi k \triangle P$.

$$q_D(t_D) = \frac{4t_D}{\pi} \int_0^\infty x e^{-t_D x^2} \{\frac{\pi}{2} + tan^{-1}[Y_0(x)/J_0(x)]\} dx \tag{3.5}$$

Solution through Laplace transformation

Eq. 3.6 is the Laplace transformation of Eq. 3.2 using the initial condition in Eq. 3.3 and Laplace transformation variable s. Eq. 3.6 is a Bessel differential equation whose fundamental solution is the modified Bessel function of the second kind, $K_0(r_D\sqrt{s})$. The other modified Bessel function $I_0(r_D\sqrt{s})$ is not admissible for infinite reservoirs since it is not bounded when $r_D \to \infty$. Using the constant pressure boundary condition in Eq. 3.7, the full solution is derived in Eq. 3.8, using which, the sandface flow rate is given in Eq. 3.9. The solution described here was first given by Van Everdingen and Hurst (1949). Inverse Laplace transformation of Eq. 3.9 should be performed numerically and Stehfest (1970) algorithm is widely used for this task. Stehfest's algorithm works well for inverse Laplace transformation of signals that exponentially decay in the time domain.

$$\left[\frac{\partial^2}{\partial r_D^2} + \frac{1}{r_D}\frac{\partial}{\partial r_D}\right] \bar{p}(r_D, s) = s\bar{p}(r_D, s) \tag{3.6}$$

$$\bar{p}(1, \sqrt{s}) = \frac{1}{s}\triangle P \tag{3.7}$$

$$\bar{p}(r_D, s) = \frac{\triangle P}{sK_0(\sqrt{s})}K_0(r_D\sqrt{s}) \tag{3.8}$$

$$\bar{q}_D(s) = -\frac{1}{\triangle P}\frac{\partial \bar{p}(r_D, s)}{\partial r_D}(1, s) = \frac{K_1(\sqrt{s})}{s\sqrt{s}K_0(\sqrt{s})} \tag{3.9}$$

3.1.2 With near-wellbore damage

3.1.2.1 Skin definition

The damaged zone (skin zone) can be modeled as a hollow cylinder at borehole wall, of inner radius 1 and outer radius $r_{D,s}$, whose permeability k_s is different from the reservoir permeability k. After early times, when $\sqrt{t_D}$ is larger than the thickness of the damaged zone ($r_{D,s} - 1$), the assumption of steady-state pressure in the damaged zone, i.e. $\partial p_s/\partial t_D = 0$, is valid. The solution to the steady-state flow problem is derived in chapter 4 while discussing the flow rates in laboratory test samples. The final solution is given in Eq. 3.10; $p_s(r_D)$ is the pressure in the damaged zone and $p(r_{D,s}^+, t_D)$

is the pressure at the inner radius of the undamaged zone. Additional details on the governing equation and the solution for steady-state pressure problem are available in chapter 4.

$$p_s(r_D) = \triangle P + \frac{p(r_{D,s}^+, t_D) - \triangle P}{ln(r_{D,s})} ln(r_D), \ \ 1 \leq r_D \leq r_{D,s} \tag{3.10}$$

The steady-state assumption results in a uniform flow rate in the damaged zone. Eq. 3.11 is the continuity equation for the flow rates at the damaged zone boundary $r_{D,s}$. Combining Eqs. 3.10 and 3.11, the constant pressure applied at the sandface boundary is transferred to an equivalent boundary condition at the inner boundary of the undamaged zone, $r_{D,s}^+$, and expressed using the pressure in the undamaged zone, p (Eq. 3.12).

$$-\frac{k_s}{\mu} \frac{\partial p_s}{\partial r_D}(r_{D,s}^-, t_D) = -\frac{k}{\mu} \frac{\partial p}{\partial r_D}(r_{D,s}^+, t_D) \tag{3.11}$$

$$p(r_{D,s}^+, t_D) - \left[\frac{k}{k_s} ln(r_{D,s})\right] r_{D,s} \frac{\partial p}{\partial r_D}(r_{D,s}^+, t_D) = \triangle P \tag{3.12}$$

Solving Eq. 3.12 requires the knowledge of two additional parameters, $r_{D,s}$ and k_s. Further simplifications can be made to reduce the number of additional parameters to one (Hawkins Jr., 1956; Van Everdingen, 1953). This is done by transferring the boundary condition at $r_{D,s}$ (Eq. 3.12) to an equivalent boundary condition at the well radius ($r_D = 1$) that would allow replacing the damaged zone with the undamaged zone. The influence of damaged zone is already captured in the boundary condition in Eq. 3.12.

It will be shown later in this chapter that, during constant pressure tests, the flow rate in the reservoir is almost uniform except in a small 'investigation zone'. After early times, this zone is beyond r_{Ds} and $r_{Ds}[\partial p/\partial r_D](r_{D,s}^+, t_D) = [\partial p/\partial r_D](1, t_D)$. As a generalization, Eq. 3.13 is valid in this zone of uniform flow rate. This also allows us to write $p(r_{D,s}^+, t_D) = p(1, t_D) + [\partial p/\partial r_D](1, t_D) ln(r_{D,s})$. Using these relations, the equivalent boundary condition at the well radius is given in Eq. 3.14. The skin term S (Eq. 3.15), which quantifies the damage caused to the reservoir, was first introduced by Hawkins Jr. (1956) for constant rate tests and is now widely used in the petroleum industry. Ehlig-Economides and Ramey Jr. (1981) have used Eq. 3.14 to solve the very same problem discussed here.

$$p(r_D, t_D) - p(1, t_D) = \int_1^{r_D} \frac{1}{r_D} \frac{\partial p}{\partial r_D}(1, t_D) \, dr_D \tag{3.13}$$

$$p(1, t_D) - S \frac{\partial p}{\partial r_D}(1, t_D) = \triangle P \tag{3.14}$$

$$S = \left(\frac{k}{k_s} - 1\right) ln(r_{D,s}) \tag{3.15}$$

3.1.2.2 Solution through Laplace transformation

Eq. 3.16 is the Laplace transformation of the inner boundary condition given in Eq. 3.14. The fundamental solution is the same as before. The solutions in Eqs. 3.17 and 3.18 reduce to the earlier

homogeneous model when $S = 0$.

$$\bar{p}(1, s) - S\frac{\partial \bar{p}}{\partial r_D}(1, S) = \frac{\triangle P}{s} \tag{3.16}$$

$$\bar{p}(r_D, s) = \frac{\triangle P}{s[K_0(\sqrt{s}) + SK_1(\sqrt{s})]}K_0(r_D\sqrt{s}) \tag{3.17}$$

$$\bar{q}_D(s) = \frac{K_1(\sqrt{s})}{s\sqrt{s}[K_0(\sqrt{s}) + SK_1(\sqrt{s})]} \tag{3.18}$$

3.1.3 Radial composite model

A more accurate model of the early time behavior would include the transient effects in the damaged zone. Let $M = (k/\mu)/(k/\mu)_s$ be the ratio of the mobilities and $\eta = K/K_s$ be the ratio of the hydraulic diffusivities in the two zones. Eq. 3.19 is the diffusion equation in the damaged zone. Eq. 3.20 is the constant pressure boundary condition at the inner boundary of the damaged zone. Eqs. 3.21 and 3.22 are the pressure continuity and the flux continuity equations, respectively, at the outer boundary of the damaged zone.

$$\left[\frac{\partial^2}{\partial r_D^2} + \frac{1}{r_D}\frac{\partial}{\partial r_D}\right]p_s = \eta\frac{\partial p_s}{\partial t_D} \tag{3.19}$$

$$p_s(1, t_D) = \triangle P \tag{3.20}$$

$$p_s(r_{D,s}^-, t_D) = p(r_{D,s}^+, t_D) \tag{3.21}$$

$$\frac{\partial p_s}{\partial r_D}(r_{D,s}^-, t_D) = M\frac{\partial p}{\partial r_D}(r_{D,s}^+, t_D) \tag{3.22}$$

Laplace transformations of Eqs. 3.19 to 3.22 are obtained as before. The linear partial derivative equation (3.19) admits both $I_0(r_D\sqrt{\eta s})$ and $K_0(r_D\sqrt{\eta s})$ as fundamental solutions since the outer radius is finite. The general solutions for the damaged zone pressure and the reservoir pressure are given in Eqs. 3.23 and 3.24, respectively. The coefficients C_i are estimated by solving the linear system in Eq. 3.25 which results from Laplace transformation of the boundary conditions given by Eqs. 3.20 to 3.22.

$$\bar{p}_s(r_D, s) = \triangle P[C_1 I_0(r_D\sqrt{\eta s}) + C_2 K_0(r_D\sqrt{\eta s})] \tag{3.23}$$

$$\bar{p}(r_D, s) = \triangle P C_3 K_0(r_D\sqrt{s}) \tag{3.24}$$

$$
\begin{bmatrix} I_0(\sqrt{\eta s}) & K_0(\sqrt{\eta s}) & 0 \\ I_0(r_{D,s}\sqrt{\eta s}) & K_0(r_{D,s}\sqrt{\eta s}) & -K_0(r_{D,s}\sqrt{s}) \\ \sqrt{\eta s}I_1(r_{D,s}\sqrt{\eta s}) & -\sqrt{\eta s}K_1(r_{D,s}\sqrt{\eta s}) & M\sqrt{s}K_1(r_{D,s}\sqrt{s}) \end{bmatrix} \begin{Bmatrix} C_1 \\ C_2 \\ C_3 \end{Bmatrix} = \begin{Bmatrix} \frac{1}{s} \\ 0 \\ 0 \end{Bmatrix} \tag{3.25}
$$

$$
\bar{q}_D(s) = \frac{\sqrt{\eta s}}{M}[-C_1 I_1(\sqrt{\eta s}) + C_2 K_1(\sqrt{\eta s})] \tag{3.26}
$$
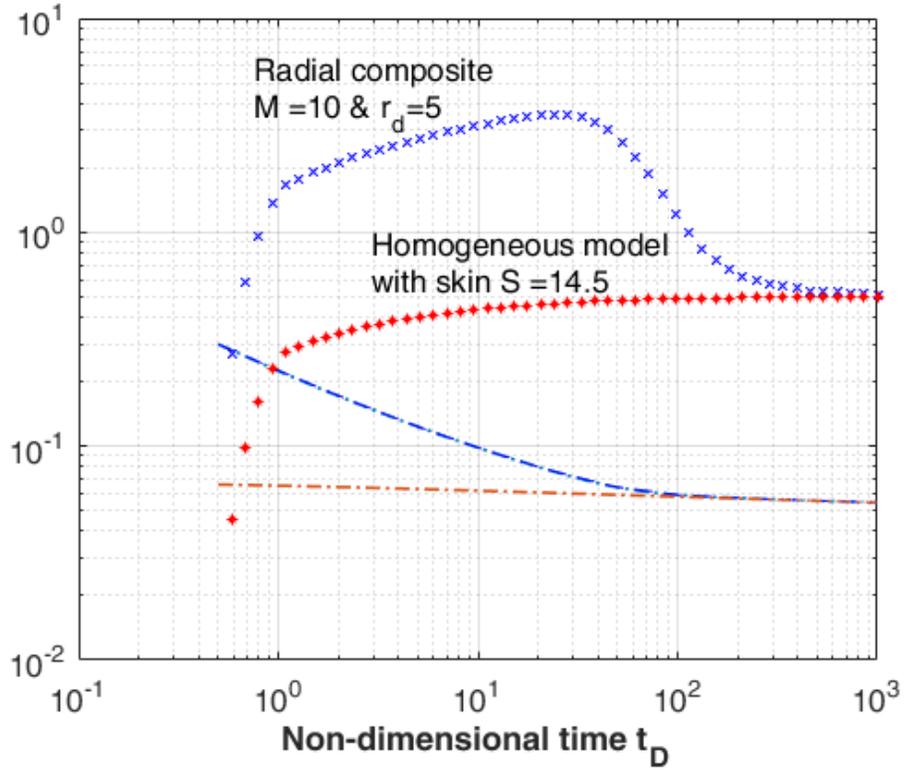
Figure 3.3: Non-dimensional flow rates q_D (dashed lines) and reciprocal-rate derivatives $d(1/q_D)/dlnt_D$ (scattered markers) for steady-state skin (red) and radial composite (blue) models $[S = (M-1)ln(r_{D,s})]$. The derivatives are similar to the pressure derivatives in constant rate tests.

3.1.4 Asymptotic solutions

The solutions discussed above contain integrals that should be computed numerically. Asymptotic solutions to some of these problems, valid at very small or large times, can be found in the literature. We will discuss here only the large-time solutions valid when $t_D > 200$; the small-time solutions are discussed in the Annex. Jacob and Lohman (1952) numerically estimated the integral in Smith's

solution (Eq. 3.5) and compared it to $2/[ln(t_D) + 0.8109]$, the reciprocal of the sandface pressure solution to the constant rate problem. Observing a striking similarity between the two, they gave Eq. 3.27 as the large-time asymptotic solution for a homogeneous reservoir without skin.

$$q_{D,Jacob} = \frac{2}{ln(t_D) + 0.8109} \tag{3.27}$$

Carslaw and Jaeger (1946) used Mellin's inversion formula and obtained an inverse Laplace transformation for the same problem that is valid at large times (Eq. 3.28); $\gamma \simeq 0.57722$ is Euler's constant. This series, when simplified (Eq. 3.29), is similar to Jacob's solution in Eq. 3.27. Carslaw's work provides the theoretical background for the solution by Jacob and Lohman (1952), which was based on observation. In Fig. 3.4 (top), the asymptotic solution is compared to the exact solution discussed earlier. The % difference between the two solutions is given by the red curve and the right y-axis. The difference is 5% at $t_D = 200$ and 2% at $t_D = 5000$. This is consistent with the error estimations of Jacob and Lohman (1952).

$$q_{D,Carslaw} = 2\left\{\frac{1}{ln(4t_D) - 2\gamma} - \frac{\gamma}{[ln(4t_D) - 2\gamma]^2} - \cdots\right\} \tag{3.28}$$

$$q_{D,Carslaw} = \frac{2}{ln(t_D) + 0.8091} \tag{3.29}$$

Uraiet and Raghavan (1980) used a finite difference model to compute flow rate vs time for different combinations of k/k_s and $r_{D,s}$. They observed a close agreement between the flow rates with same $[(k/k_s) - 1]ln(r_{D,s})$ which motivated them to quantify the near-wellbore damage using skin S, as Van Everdingen (1953) did for the constant rate problem. The earlier subsection on skin definition provides the theoretical basis for the work of Uraiet and Raghavan (1980). They added the skin S to the solution by Jacob and Lohman (1952) (Eq. 3.27), leading to Eq. 3.30. In Fig. 3.4 (bottom), the asymptotic solution is compared to the exact solution when skin equals 10. The % error, in this case, is much smaller compared to the case with no skin. The reason could be that the skin term exponentially increases the effective time $(t_D e^{2S})$ in Eq. 3.30.

$$q_D = \frac{2}{ln(t_D) + 2S + 0.81} \quad \text{(or)}$$

$$q = \frac{2\pi k(P_w - P_{ini})}{\mu} \frac{2}{ln(Kt/r_w^2) + 2S + 0.81} \tag{3.30}$$

3.2 Interpretation workflow

Mobility k/μ, reservoir pressure P_{ini} and skin S control the production rate (Eq. 3.30). The main objective of a well test is to estimate these quantities. Here, we will adapt the pressure derivative analysis of Bourdet et al. (1983) to constant pressure tests — reciprocal-rate derivative analysis. The effect of the pressure history of the well on sandface flow rates can be taken into account through a convolution. The unknown reservoir parameters can be estimated using the superposition principle
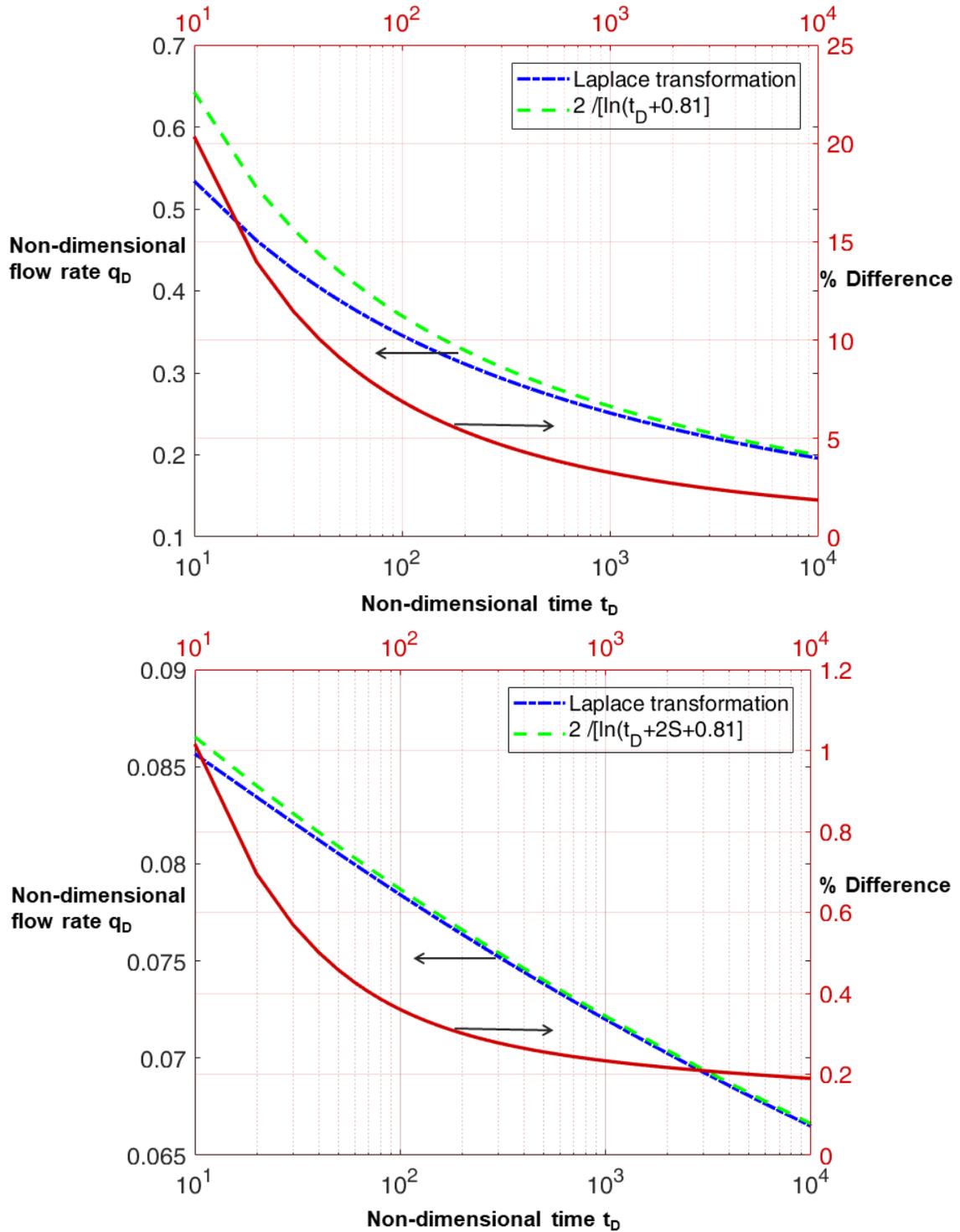
Figure 3.4: Asymptotic solution vs exact solution when there is no skin (upper plot) and when skin is $S = 10$ (lower plot). Red curve is the % difference between the two solutions.
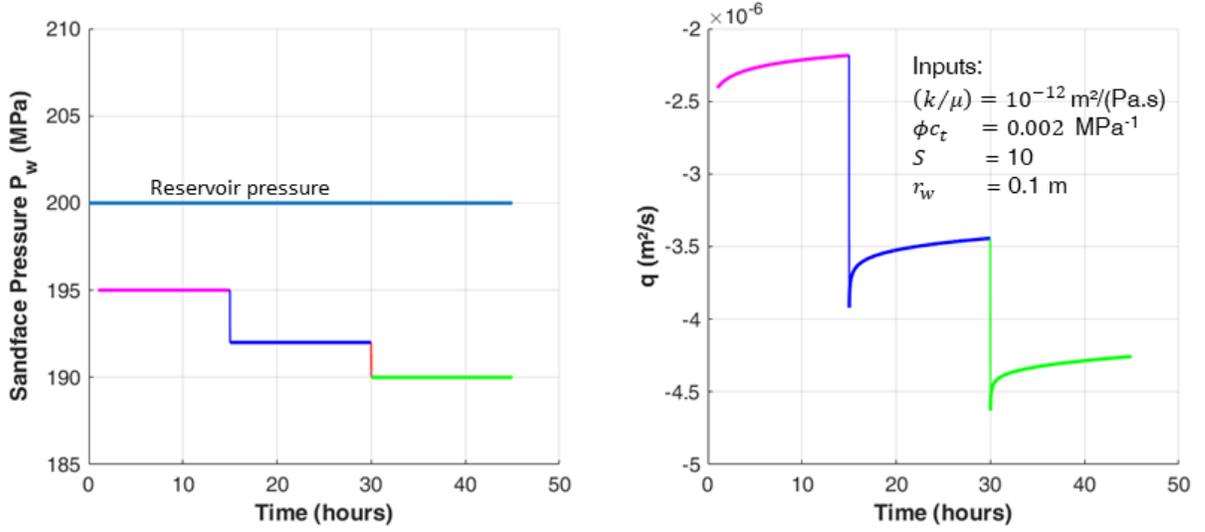
Figure 3.5: Flow rate for multi-step pressure is simulated using the convolution equation (Eq. 3.32) and the flow model with steady-state skin (Eq. 3.18)

when the sandface pressures are step-wise constant. An interpretation workflow is presented below for a producing well; it is equally applicable to an injection well when the injected fluid is the same as the formation fluid.

3.2.1 Convolution

The flow rate q_{conv} vs time for any pressure history can be obtained through a convolution (Eq. 3.31). If the pressures are step-wise constant (as in Fig. 3.5), Eq. 3.31 can be simplified into a summation (Eq. 3.32). Using q_D from the homogeneous reservoir model with steady-state skin (Eq. 3.18), the flow rates are simulated for the input pressure history in Fig. 3.5.

$$\frac{q_{conv}(t)}{2\pi\frac{k}{\mu}} = \int_0^t \frac{\partial[P_w(\tau) - P_{ini}]}{\partial\tau} q_D(t - \tau)d\tau \tag{3.31}$$

$$\frac{q_{conv}(t)}{2\pi\frac{k}{\mu}} = \sum_{i=1}^N (P_{w,i} - P_{w,i-1})q_D(t - t_{i-1}) \tag{3.32}$$

In Fig. 3.6, flow rate per unit pressure difference and reciprocal rate derivative are plotted against $t - t_{i-1}$. The reciprocal-rate derivative curves for different flow periods have different stabilization values and interpreting them without taking into account the pressure history would result in an incorrect estimation of mobility. Theoretically, two interpretation workflows are possible, each with its own advantages and limitations.

3.2.1.1 Deconvolution

In deconvolution algorithms, measured flow rates and pressure are used to identify the function q_D, mobility k/μ, and reservoir pressure P_{ini} by solving a minimization problem. The radial heterogeneities in the reservoir and reservoir boundaries can also be identified from the shape function q_D.
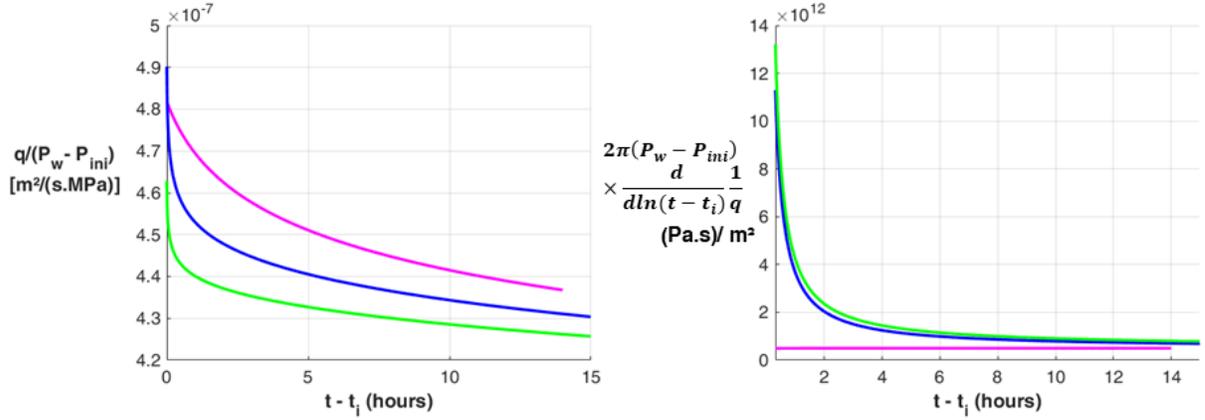
Figure 3.6: Flow rate and reciprocal-rate derivative for each flow period. The quantities are non-dimensionalized using pressure head for effective comparison.

However, deconvolution algorithms are very sensitive to measurement errors in pressures and flow rates (Von Schroeter et al., 2004; Gringarten, 2010; Cumming et al., 2013).

3.2.1.2 Superposition

In this method, an assumption is made on the type of the reservoir (homogeneous, radial composite, etc.); q_D is an input, along with measured flow rates and pressures; mobility k/μ and skin S are interpreted outputs. In the workflow discussed below, q_D from the reservoir model with steady-state skin zone is used. Also, the initial reservoir pressure P_{ini} is considered as an input; this assumption can be relaxed when multiple flow periods are interpreted simultaneously.

3.2.2 Interpreting kh and skin

Let us assume that the initial reservoir pressure P_{ini} is known. The only unknowns are mobility k/μ and skin S. Only the last flow period in Fig. 3.5 (green curve, $t > 30$ h) will be used for the interpretation since it is possible that the flow rates during earlier periods were measured with less accurate flow meters. An initial estimation of mobility is obtained using Eq. 3.33. The jump in the flow rate during a sudden pressure change is used to estimate the skin (Eq. 3.34). The estimated quantities carry a hat symbol on their top.

$$\widehat{\left(\frac{k}{\mu}\right)}_{ini} = \frac{1}{2} \times \frac{1}{2\pi(P_w - P_{ini})d(1/q)/dlnt} \tag{3.33}$$

$$\hat{S} = \frac{2\pi\widehat{\left(\frac{k}{\mu}\right)}_{ini}(P_{w,N} - P_{w,N-1})}{q(t_{N-1}^+) - q(t_{N-1}^-)} \tag{3.34}$$

Fig. 3.7 compares the original data to the simulation using initial estimates. Clearly, there is room for improvement. To have a better match of the derivatives, a second mobility estimate is done using Eq. 3.35. The skin is re-estimated with the new mobility value, using Eq. 3.34.
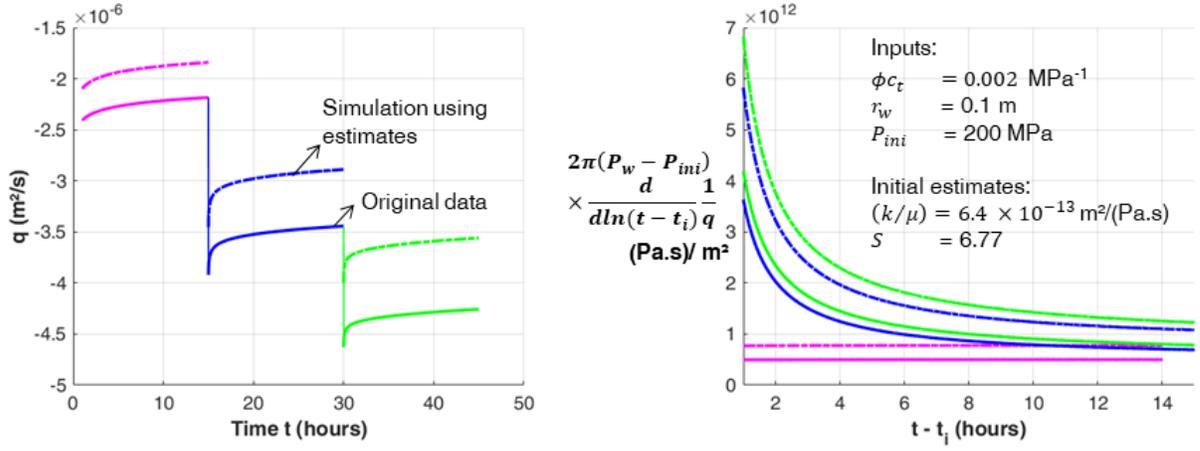
Figure 3.7: Interpretation of mobility and skin - Initial estimation
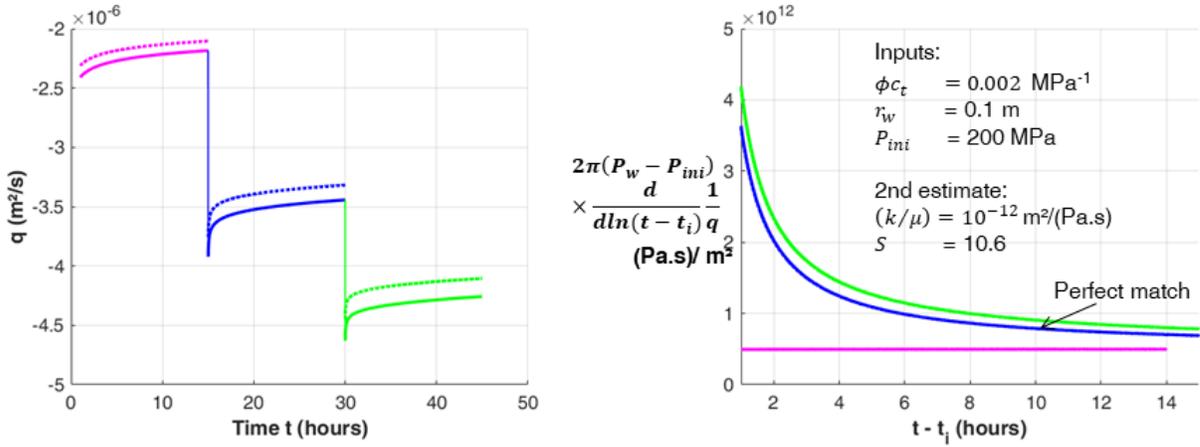
Figure 3.8: Interpretation of mobility and skin - 2nd estimation

$$\left(\widehat{\frac{k}{\mu}}\right)_{2nd} = \left(\widehat{\frac{k}{\mu}}\right)_{ini} \times \frac{[d(1/q)/dlnt]_{simulated}}{[d(1/q)/dlnt]_{Original\ data}} \tag{3.35}$$

The new estimations are shown in Fig. 3.8 and a perfect match is obtained in the derivative plot. There is a slight offset in the flow rate plot and the skin value is fine-tuned to have a better match (Fig. 3.9). The final permeability and skin estimations are a perfect match to the input values used to generate the original data.

3.2.3   Radius of investigation

The radius of investigation is a quantity that is independent of sandface pressures or flow rates and much larger than the radius of the zone impregnated by the injection fluid, $\sqrt{\int_0^t [q(\tau)/\pi\phi]d\tau}$.

Any change in the sandface boundary condition results in a pressure diffusion in the reservoir. The reservoir volume that has experienced this pressure diffusion is a concentric cylinder to the wellbore. The outer radius of this cylinder is proportional to $\sqrt{Kt}$ (Eq. 3.36, when appropriate value for C_r is chosen). For the derivative approach discussed above, the radius of investigation is
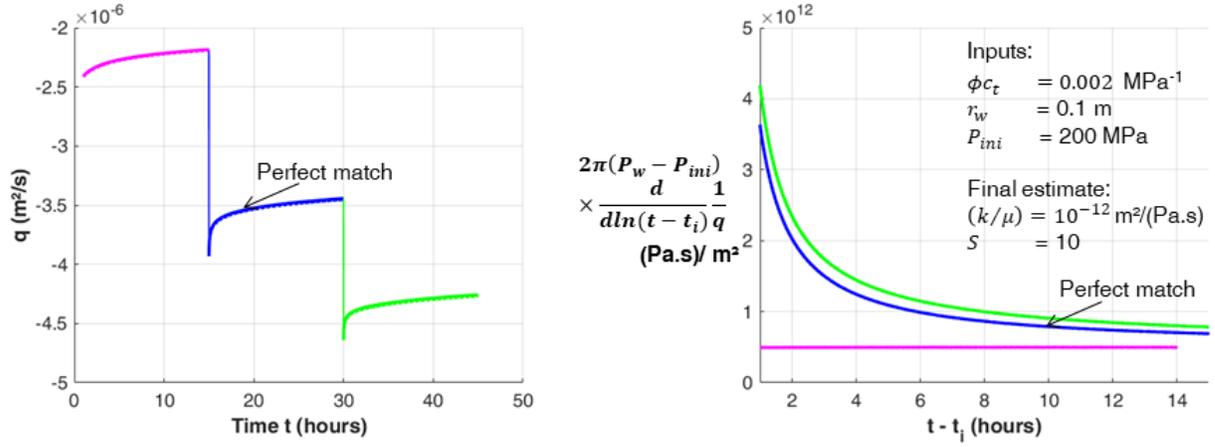
Figure 3.9: Interpretation of mobility and skin - Final estimation
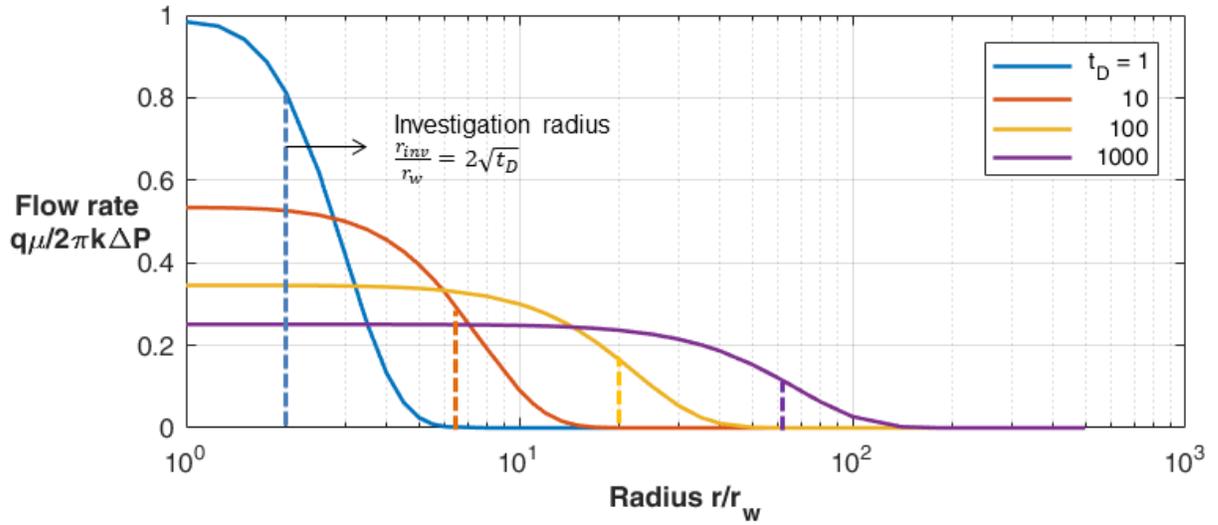
Figure 3.10: Flow rate in the reservoir during a constant pressure test and the evolution of investigation radius

within this cylinder, although the exact value is debatable. This is shown in Eq. 3.36, in which, different values for C_r have been proposed by several authors (Kuchuk, 2009). Among these, the most commonly occurring value is $C_r = 2$ which corresponds to the radius at which the rate of pressure change is maximum (Eq. 3.40).

$$r_{inv} = C_r\sqrt{Kt} \tag{3.36}$$

For constant rate tests, pressure evolution at radius r is given by Theis (1935) line source solution (Eq. 3.37), where q is the constant sandface flow rate per unit thickness. Theis (1935) considered $r_w \to 0$, an assumption that is valid to estimate the sandface pressure evolution when $4Kt/r_w^2 > 25$. However, $r_w \to 0$ is not valid when the sandface pressure is constant and a solution for sandface flow rate is sought because $q \to \infty$ when $r_w \to 0$. This prohibits simple solutions like Eq. 3.37 for constant sandface pressure. Hence, we study the radius of investigation for the constant rate case.

An equivalence is made to the constant pressure case in Fig. 3.10.

$$p(r,t) = \frac{q\mu}{4\pi k} \int_{\frac{r^2}{4Kt}}^{\infty} \frac{e^{-u}}{u} du \tag{3.37}$$

$$\frac{\partial}{\partial t}p(r,t) = \frac{q\mu}{4\pi k} \frac{e^{-\frac{r^2}{4Kt}}}{t} \tag{3.38}$$

$$\frac{\partial^2}{\partial t^2}p(r,t) = \frac{q\mu}{4\pi k} \frac{e^{-\frac{r^2}{4Kt}}}{t^2} \left[\frac{r^2}{4Kt} - 1\right] \tag{3.39}$$

$$\frac{\partial^2}{\partial t^2}p(r,t) = 0 \implies r_{inv} = 2\sqrt{Kt} \tag{3.40}$$

Differentiating Eq. 3.39 once again with respect to time and substituting $r_{inv} = 2\sqrt{Kt}$ will show that it is indeed a maximum. Eq. 3.41 is the dimensionless form of Eq. 3.40.

$$\frac{r_{inv}}{r_w} = 2\sqrt{t_D} \tag{3.41}$$

Fig. 3.10 shows the flow rate in the reservoir and the investigation radius, at different times t_D, during a constant pressure test. Fig. 3.10 also validates the hypothesis used in skin definition — after early times, the flow rate in the near-wellbore zone is uniform.

3.3 Injection testing with two-phase flow

During conventional well tests in exploratory or appraisal wells, hydrocarbon are withdrawn from the well and are often flared due to lack of infrastructure. Apart from the usual CO_2 and methane emissions, flaring can also release sulphur dioxide and other volatile organic compounds into the atmosphere. New environmental regulations demand reducing these emissions and several authors have proposed replacing conventional well tests with injection tests (Verga et al., 2011; Beretta et al., 2007; Levitan, 2003) to avoid any emission.

However, due to the presence of multiple fluids in the reservoir with changing saturation levels, modeling and interpreting injection tests is challenging. The relative permeabilities of the reservoir fluids are a function of their respective saturation levels and the monophasic flow models are no longer valid. The surface tension between the fluids create a capillary pressure, which is again a function of saturation. Finally, fluid viscosities vary with temperature and injecting a cold fluid into a warm reservoir would further increase the complexity of the problem.

Several authors have discussed flow models and interpretation workflows for constant rate injection tests with more than one fluid flowing in the reservoir. Buckley and Leverett (1941), while estimating the saturation profile, decoupled the saturation evolution from the pressure evolution by neglecting the fluid compressibilities. They proposed a self-similar solution in which the saturation distribution in the reservoir depends only on the relative mobilities and the volume of injected fluid. Several authors have used Buckley-Leverett saturation profile in combination with pressure diffusion equation to model injection/fall-off tests. Abbaszadeh and Kamal (1989) proposed a solution

that approximated the Buckley-Leverett saturation profile using step functions. Bratvold and Horne (1990) developed a model that used the exact Buckley-Leverett saturation profile and also included convective heat transfer effects due to cold fluid injection into a warm reservoir. Their solution is valid for a single constant rate injection period. Levitan (2003) extended this solution to handle multi-rate injections (step-wise constant) since convolution is not valid in this non-linear problem. In all these analytical models, temperature and saturation were decoupled and computed independently of pressure, an assumption that may not be valid for gas-bearing reservoirs. Verga et al. (2011) proposed a numerical model for heterogeneous reservoirs, in which, pressure and saturation are strongly coupled and temperature, viscosity and density are weakly coupled. The model also takes into account the forces due to gravity and the capillary effects which are neglected in the analytical models.

Constant pressure injection tests are seldom discussed in the literature. Also, there are no analytical solutions for this case and commercial software use numerical finite difference models to simulate constant pressure injection. In the subsequent pages, we will discuss a weakly coupled numerical model for constant pressure injection with assumptions similar to Levitan (2003). The model provides useful insights on estimating formation fluid mobility and injected fluid mobility through reciprocal-rate derivative analysis.

3.3.1 Relative permeability

The relative permeability of the fluids increase with their respective saturation levels (Fig. 3.11). At water saturation s_{wc} (connate water saturation) water becomes immobile and at oil saturation s_{or} (residual oil saturation) oil becomes immobile. $k_{ro}(s_{wc})$ and $k_{rw}(s_{or})$ are the relative permeabilities of oil and water when the other fluid is immobile.

$$k_{rw}(s_w) = k_{rw}(s_{or}) \left[\frac{s_w - s_{wc}}{1 - s_{or} - s_{wc}} \right]^{e_w} \tag{3.42}$$

$$k_{ro}(s_w) = k_{ro}(s_{wc}) \left[\frac{1 - s_w - s_{or}}{1 - s_{or} - s_{wc}} \right]^{e_0} \tag{3.43}$$

3.3.2 Governing equations for two-phase flow

Filtration velocities for the flow of two immiscible fluids can be given by Darcy's law using relative permeabilities (Eqs. 3.44 and 3.45). The pressure in the two fluids differ by the capillary pressure (Eq. 3.46). Eqs. 3.47 and 3.48 ensure mass conservation pore volumes. State equations express fluid densities as functions of fluid pressures in Eqs. 3.49 and 3.50. This yields 7 equations and as many unknowns: $\vec{u_w}$, $\vec{u_o}$, p_o, p_w, ρ_o, ρ_w and s_w. However, the system is non-linear and should be decoupled using Buckley-Leverett's solution.

$$\vec{u}_w = -\frac{k k_{rw}(s_w)}{\mu_w} \left(\vec{\nabla} p_w - \rho_w \vec{g} \right) \tag{3.44}$$

$$\vec{u}_o = -\frac{k k_{ro}(s_w)}{\mu_o} \left(\vec{\nabla} p_o - \rho_o \vec{g} \right) \tag{3.45}$$
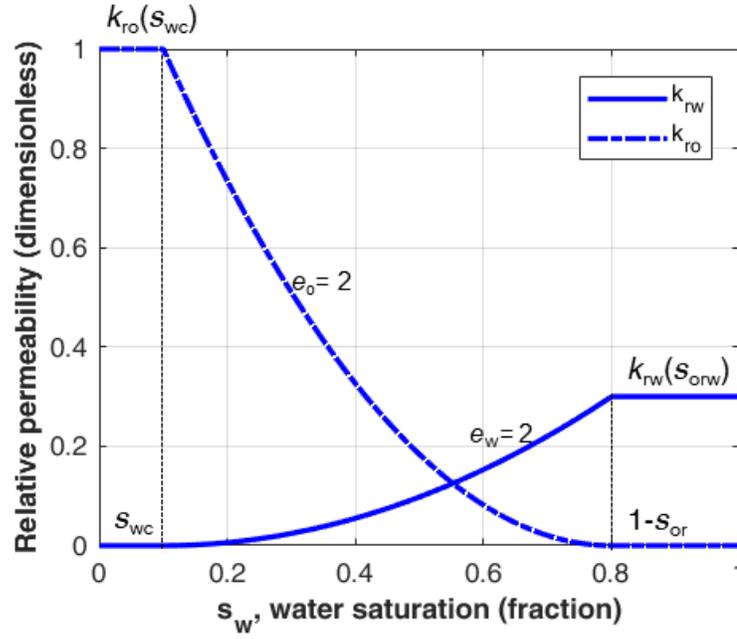
Figure 3.11: Typical relative permeability curves for oil and water (Levitan, 2003). The exponents e_w and e_o equal 2.

$$p_o - p_w = p_c(s_w) \tag{3.46}$$

$$\vec{\nabla}.\rho_w \vec{u}_w + \frac{\partial}{\partial t} \phi \rho_w s_w = 0 \tag{3.47}$$

$$\vec{\nabla}.\rho_o \vec{u}_o + \frac{\partial}{\partial t} \phi \rho_o (1 - s_w) = 0 \tag{3.48}$$

$$\rho_w = \rho_w(p_w) \tag{3.49}$$

$$\rho_o = \rho_o(p_o) \tag{3.50}$$

3.3.3 Buckley-Leverett solution for saturation profiles

Neglecting gravity effects and considering a radial flow, Darcy's law can be reduced to Eqs. 3.51 and 3.52, where r, θ, and z are cylindrical coordinates.

$$u_w = -\frac{k k_{rw}(s_w)}{\mu_w} \frac{\partial}{\partial r} p_w(r, t) \tag{3.51}$$

$$u_o = -\frac{k k_{ro}(s_w)}{\mu_o} \frac{\partial}{\partial r} p_o(r, t) \tag{3.52}$$

A new variable f_w is defined as the fraction of the injected fluid at any point in the flowing
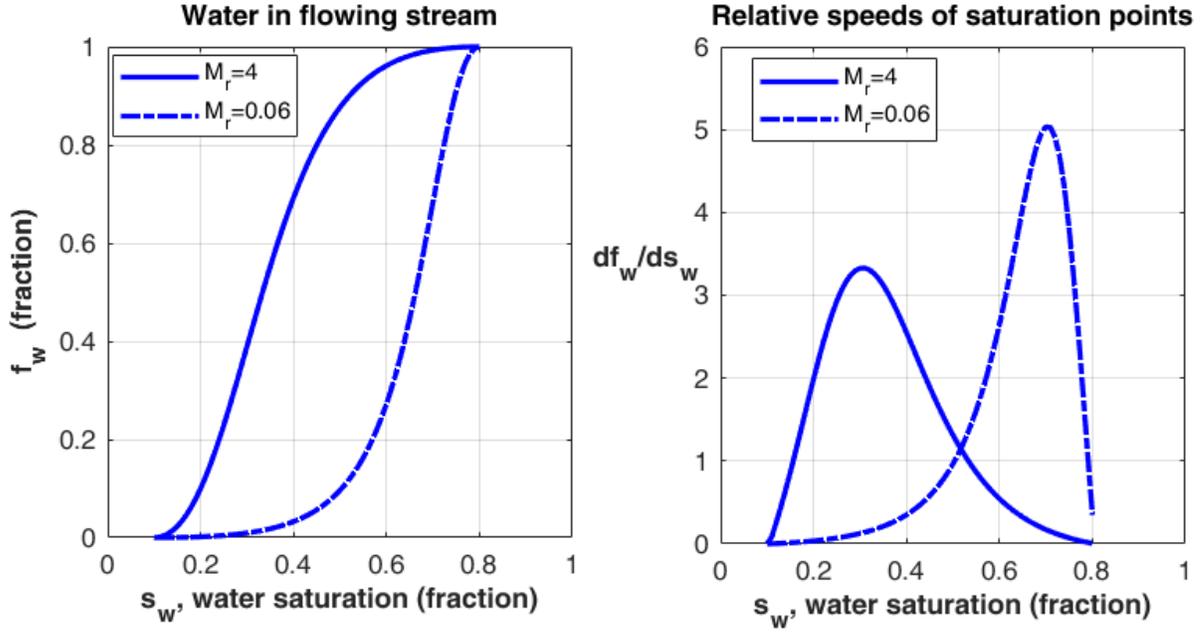
Figure 3.12: Fraction of the injected fluid in the flowing stream, f_w, and $f'_w(s_w)$ are computed using the relative permeability curves from Fig. 3.11.

stream (Eq. 3.53).

$$f_w = \frac{u_w}{u_w + u_o} \tag{3.53}$$

Substituting $u_w = f_w(u_w + u_o)$ in Eq. 3.51 and $u_o = (1 - f_w)(u_w + u_o)$ in Eq. 3.52 and subtracting the two equations yields Eq. 3.54. Upon neglecting capillary pressure changes with saturation, i.e. $\partial p_c / \partial s_w = 0$, Eq. 3.54 simplifies into Eq. 3.55 which is same as Eq. 3 of Buckley and Leverett (1941); f_w depends only on saturation s_w through the relative permeability curves (Fig. 3.12).

$$f_w(s_w) = \frac{\frac{\mu_o}{k_{ro}(s_w)}}{\frac{\mu_w}{k_{rw}(s_w)} + \frac{\mu_o}{k_{ro}(s_w)}} + \frac{k}{(u_w + u_0)} \frac{1}{\frac{\mu_w}{k_{rw}(s_w)} + \frac{\mu_o}{k_{ro}(s_w)}} \frac{ds_w}{dr} \frac{dp_c}{ds_w} \tag{3.54}$$

$$f_w(s_w) = \frac{1}{\frac{k_{ro}(s_w)/\mu_o}{k_{rw}(s_w)/\mu_w} + 1} \tag{3.55}$$

Neglecting compressibility effects, mass conservation laws in Eqs. 3.47 and 3.48 can be added (and subtracted) to give Eq. 3.56 (and Eq. 3.57). Using $u_w - u_o = (u_w + u_o)(2f_w - 1)$ and Eq. 3.56, Eq. 3.57 can be simplified as Eq. 3.58.

$$\frac{1}{r} \frac{\partial}{\partial r} [r(u_o + u_w)] = 0 \tag{3.56}$$

$$\frac{1}{r} \frac{\partial}{\partial r} [r(u_w - u_o)] + 2\phi \frac{\partial s_w}{\partial t} = 0 \tag{3.57}$$

$$\frac{\partial s_w}{\partial t} + \left[\frac{u_w + u_o}{\phi} \frac{df_w}{ds_w} \right] \frac{\partial s_w}{\partial r} = 0 \tag{3.58}$$
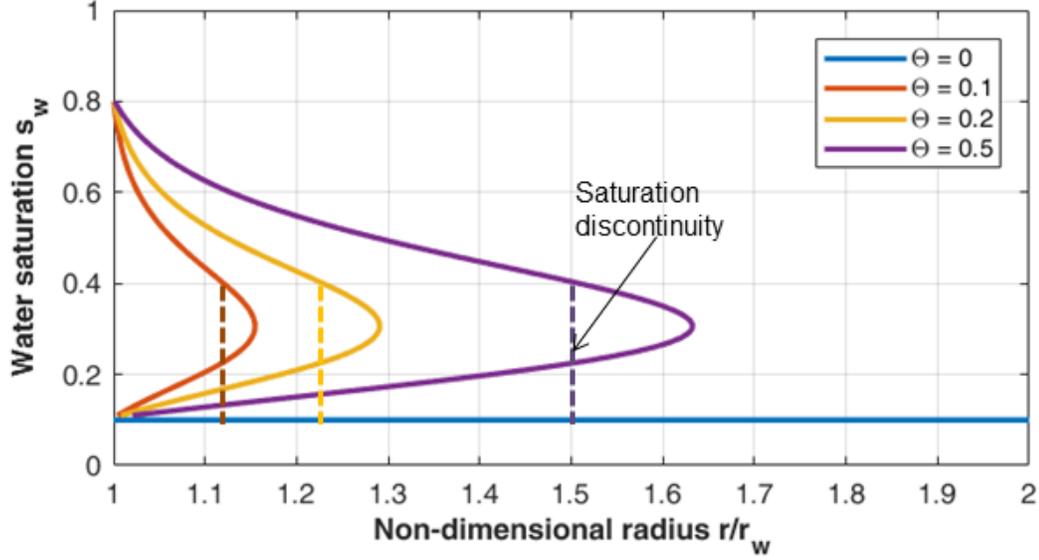
Figure 3.13: Buckley-Leverett saturation profile for ($M_r = 4$).

Eq. 3.58 is a 1st order partial derivative equation; it shows that a constant-saturation point s_w moves forward with a velocity $\frac{dr}{dt}|_{s_w} = \frac{[u_w + u_o](r,t)}{\phi} f'_w(s_w)$. Eq. 3.56 shows that $r(u_o + u_w)$ is uniform in the reservoir, a result of neglecting fluid compressibilities. Because the injected fluid is water, the flux rate of oil at the sandface is zero, i.e. $u_o(r_w, t) = 0$; this yields Eq. 3.59.

$$[u_w + u_o](r,t) = \frac{r_w}{r} u_w(r_w, t) = \frac{q(t)}{2\pi r} \tag{3.59}$$

$$\Rightarrow \frac{dr}{dt}|_{s_w} = \frac{q(t)}{2\pi\phi} f'_w(s_w) \tag{3.60}$$

Integrating Eq. 3.60 from time 0 to t yields the radial location of a saturation point at any time t (Eq. 3.61) when its initial location $r_D(s_w, 0)$ is known; $r_D = r/r_w$.

$$r_D(s_w, t) = \sqrt{r_D^2(s_w, 0) + f'_w(s_w) \frac{\int_0^t q(\tau)d\tau}{\pi r_w^2 \phi}} \tag{3.61}$$

Fig. 3.13 shows the evolution of the saturation profile with non-dimensional time variable $\Theta(t) = [\int_0^t q(\tau)d\tau]/\pi r_w^2 \phi$. Saturation points with larger $f'_w(s_w)$ travel faster, as suggested by Eq. 3.60. However, certain radial locations have multiple saturation values which is physically impossible and is a consequence of neglecting the effect of $\partial p_c/\partial s_w$. Buckley and Leverett (1941) rightly noted that a part of the curve is physically incorrect and the real saturation distribution curve has a discontinuity. They also showed that the radial location of the discontinuity can be obtained by applying mass conservation to the two saturation profiles.

$$\int_{s_w^{ini}}^{s_{wf}} \pi \left[r_{D,f}^2 - r_D^2(s_w) \right] ds_w = 0 \tag{3.62}$$

Several authors (Verga et al., 2011; Bratvold and Horne, 1990) have compared the Buckley-
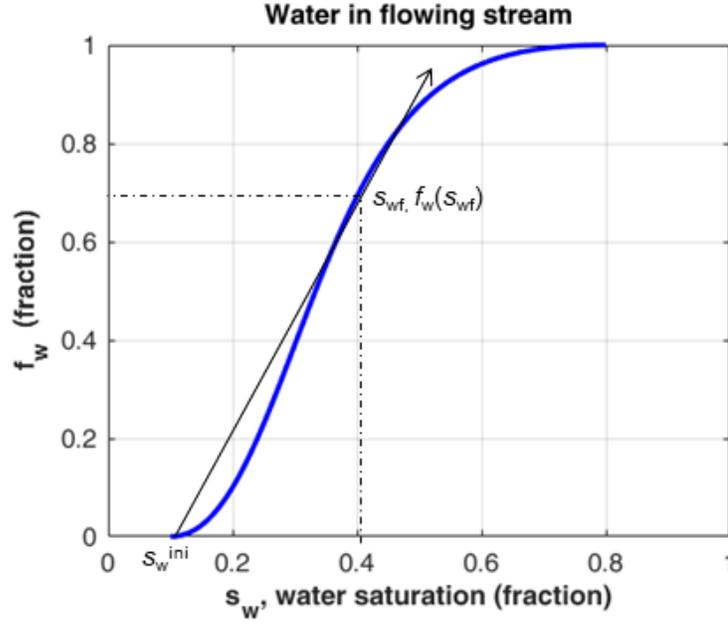
Figure 3.14: Welge tangent method ($M_r = 4$). The line connecting $f_w(s_w^{ini})$ and $f_w(s_{wf})$ is a tangent to the curve at $(s_{wf}, f_w(s_{wf}))$

Leverett saturation profile to numerical models and found very good agreements. Their numerical models showed a slightly smoothed saturation discontinuity due to strong capillary pressure effects at the discontinuity, also predicted by Buckley and Leverett (1941).

Welge tangent method

When the initial saturation profile in the formation is uniform, computing the mass conservation integral in Eq. 3.62 is not required and the front r_f can be estimated by a simple technique proposed by Welge (1952). The mass balance relation in Eq. 3.62 can be simplified into Eq. 3.63 by substituting $r_D(s_w)$ from Eq. 3.61. Also, the radius of the front $r_{D,f}$ and saturation at the front s_{wf} must be compatible with the Buckley-Leverett saturation profile (Eq. 3.64).

$$r_{D,f}^2(t) = 1 + \Theta(t)\frac{f_w(s_{wf}) - f_w(s_w^{ini})}{s_{wf} - s_w^{ini}} \tag{3.63}$$

$$r_{D,f}^2(t) = 1 + \Theta(t)f_w'(s_{wf}) \tag{3.64}$$

From Eqs. 3.63 and 3.64, it is evident that the line connecting initial fractional flow $f_w(s_w^{ini})$ and fractional flow at saturation front $f_w(s_{wf})$ should be a tangent to the curve f_w at saturation front s_{wf} (Eq. 3.65). Only one such point exists (Fig. 3.14) and the saturation value at the front, s_{wf}, remains constant at all times.

$$f_w'(s_{wf}) = \frac{f_w(s_{wf}) - f_w(s_w^{ini})}{s_{wf} - s_w^{ini}} \tag{3.65}$$

3.3.4 Reduced governing equation for two-phase flow

It is a general practice to replace the diffusivity equations for the two flowing fluids (Eqs. 3.47 and 3.48) with a single diffusivity equation. This involves making the following assumptions.

- The capillary pressure is constant, $\partial p_c / \partial s_w = 0$

- The fluids are slightly compressible and their state equation is given by Eq. 3.66, in which, ρ_i and c_i are the density and compressibility of fluid i, respectively

- Higher order terms in the diffusivity equation, $c_i (\nabla P)^2$, are neglected due to small compressibilities and flow velocities

- Gravity effects are neglected and the flow is radial

$$\frac{\partial \rho_i}{\partial t} = \rho_i^0 c_i \frac{\partial P}{\partial t} \tag{3.66}$$

Combining Eqs. 3.44 to 3.50 and 3.66, yields the combined governing equation in Eq. 3.67.

$$\frac{1}{r}\frac{\partial}{\partial r}\left[r\lambda(s_w)\frac{\partial p}{\partial r}\right] - \phi c_t(s_w)\frac{\partial p}{\partial t} = 0 \tag{3.67}$$

Eq. 3.67 is similar to the diffusivity equation for monophasic flow (discussed in the introduction), expect that the mobility λ $(= k\,[(k_{rw}/\mu_w) + (k_{ro}/\mu_o)])$ and the total compressibility c_t $(= s_w c_w + [1 - s_w]c_o + c_p)$ are dependent on saturation s_w. The variables are non-dimensionalized using $\lambda(s_w^{ini})$ and $c_t(s_w^{ini})$, the mobility and the total compressibility of the formation fluid at initial saturation levels:

Time, $\quad t_D = \lambda(s_w^{ini})t/\phi c_t(s_w^{ini})r_w^2$

Mobility, $\quad \lambda_D = \lambda(s_w)/\lambda(s_w^{ini})$

Compressibility, $\ c_D = c_t(s_w)/c_t(s_w^{ini})$

Flow-rate, $q_D = q/2\pi\lambda(s_w^{ini})\triangle P$

Pressure, $\quad p_D = (p - P_{ini})/\triangle P.$

The non-dimensionalized governing equation is given in Eq. 3.68 and sandface flow rate is given in Eq. 3.69. When the initial saturation profile is uniform, the saturation profile between the sandface and Buckley-Leverett front is given by Eq. 3.70.

$$\frac{1}{r_D}\frac{\partial}{\partial r_D}\left[r_D\lambda_D(s_w)\frac{\partial p_D}{\partial r_D}\right] - c_D(s_w)\frac{\partial p_D}{\partial t_D} = 0 \tag{3.68}$$

$$q_D = -\lambda_D r_D \frac{\partial p_D}{\partial r_D} \tag{3.69}$$

$$r_D(s_w, t_D) = \sqrt{2c_t(s_w^{ini})\triangle P}\sqrt{f_w'(s_w)\int_0^{t_D} q_D d\tau} \tag{3.70}$$

Relative permeability		Fluid/rock properties		Initial/Boundary condition	
$k_{rw}(s_{or})$	0.3	μ_w	10^{-3} Pa.s (1 cP)	s_w^{ini}	0.1
$k_{ro}(s_{wc})$	1	μ_o	$2\ 10^{-4}$ Pa.s (0.2 cP)	$\triangle P$	1 MPa
s_{or}	0.2	c_w	$1.95\ 10^{-4}$ MPa^{-1}		
s_{wc}	0.1	c_o	$1.4\ 10^{-3}$ MPa^{-1}		
e_o	2	c_p	$4.35\ 10^{-4}$ MPa^{-1}		
e_w	2				

Table 3.1: Formation properties used for finite element simulation

Analytical solutions exist for this problem when the sandface is exposed to a constant injection rate. During constant pressure injection, the sandface flow rate varies with time and the variable transformations of Bratvold and Horne (1990) or Levitan (2003) are not applicable. Also, their solution technique involves moving the inner boundary to $r = 0$, which is not feasible for the constant pressure case. Hence, the equations are solved numerically using a finite element scheme discussed at the end of this chapter.

3.3.5 Results and Discussion

A finite element simulation was performed using the formation properties given in Table 3.1. One dimensional mesh elements were used with increased element density in the near-wellbore region, to capture accurately the movement of saturation discontinuity. Commercial software packages typically use finite difference schemes which consider uniform saturation in each element. This creates a large saturation jump when the saturation front moves from one element to the other, leading to numerical oscillations which are typically addressed through pseudo relative permeability curves. Pseudo relative permeability curves are obtained by modifying the relative permeability curves from laboratory tests to avoid the numerical oscillations of the finite different difference model while closely capturing the expected flow behavior. The finite element scheme discussed here results in a linear variation in saturation between two nodes. The mobility matrix and the compressibility matrix are updated at each time instant, to reflect the movement of the saturation front even within an element. This reduces the numerical errors and eliminates the need for pseudo relative permeability curves. Non-uniform time steps, resembling a geometric series, were used for faster computation. The computational time was less than 10 minutes on a personal computer.

At large times, the results compare well against that of the commercial software (Figs. 3.15 and 3.16). At early times, the results from the commercial software contain some numerical errors.
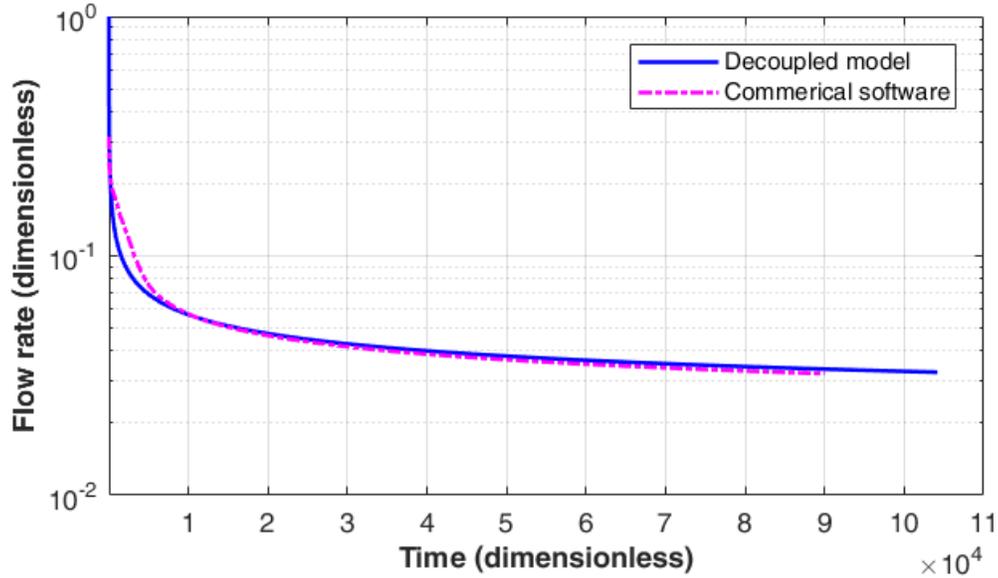
Figure 3.15: Comparing flow rates from the finite element model to a commercial software using a coupled finite difference model
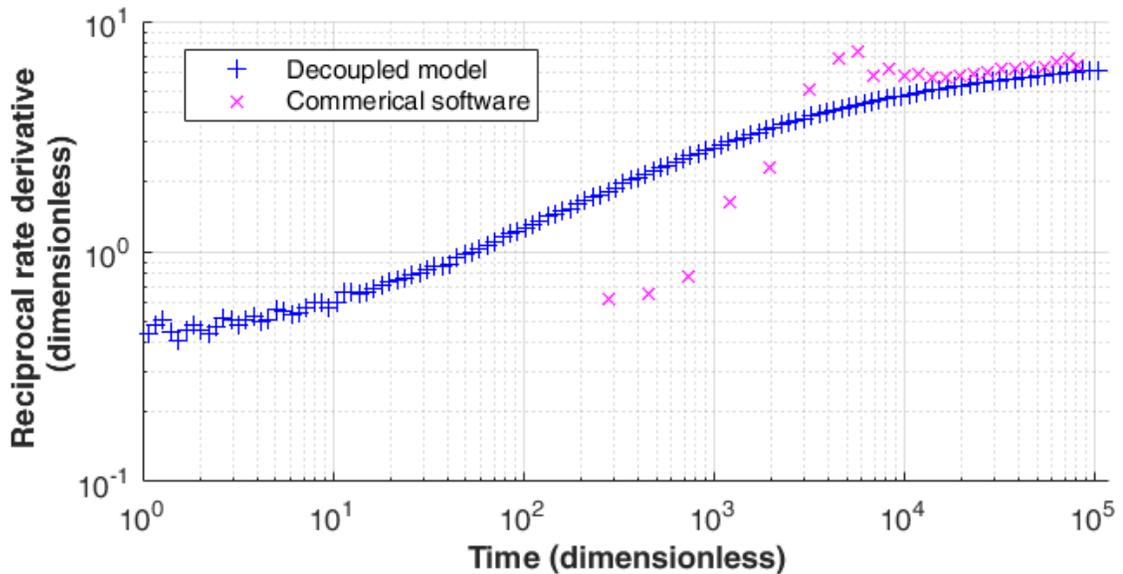
Figure 3.16: Decoupled finite element model yields a better prediction of early time derivative. The early time stabilization (0.5) gives the formation fluid mobility; the late time stabilization gives the injected fluid mobility.
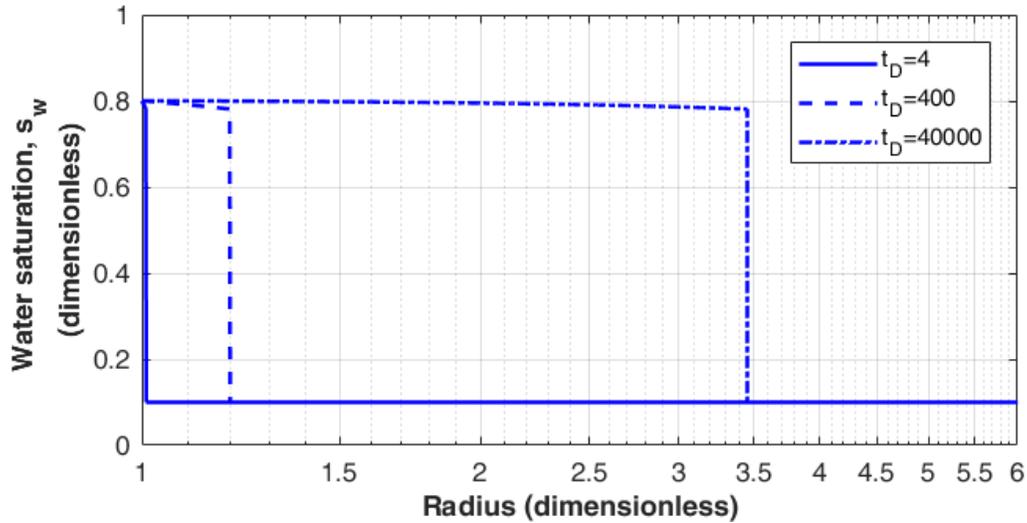
Figure 3.17: Evolution of water saturation in the reservoir. The 'two bank profile' is due to the large mobility contrast.

However, the works of Bratvold and Horne (1990) and Levitan (2003) provide an alternative source to validate the early time data. Their analytical solutions showed that the pressure derivative (non-dimensionalized using the initial reservoir fluid properties), at very early times, shows a stabilization at 0.5 and the same is observed in the reciprocal-rate derivative in Fig. 3.16. While this early time derivative could be masked by wellbore storage effects during constant rate tests, it provides a small window to obtain the initial reservoir fluid mobility during constant pressure injection tests. This time window is quite small (< 1s) when $k = 1$ mD. However, when $k = 1\,\mu$D the early stabilization period could last for about 10 to 20 minutes. The stabilization at large times yields the mobility of the injected fluid.
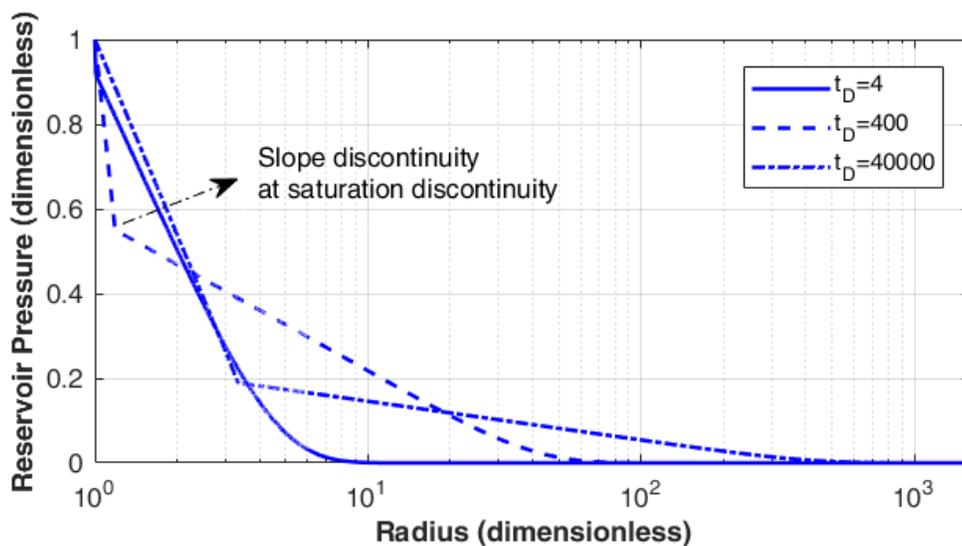
Figure 3.18: Pressure evolution in the reservoir. The two slopes are representative of the mobilities of the two zones.
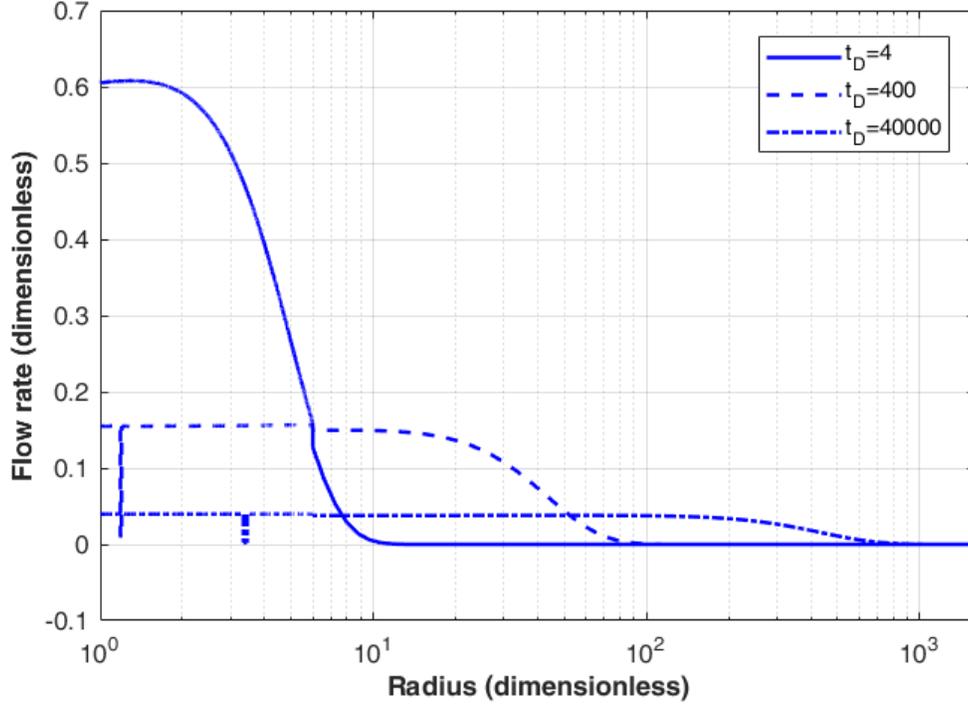
Figure 3.19: Flow rate evolution in the reservoir.

Fig. 3.17 shows that the saturation profiles are similar to that of a two bank model. This is expected since the maximum mobility of the injected fluid is 15 times smaller than that of the reservoir fluid, i.e. $M_r = 0.06$. The pressure distribution in the reservoir (Fig. 3.18) is similar to that of a radial composite reservoir, except that the boundary between the two zones is continuously moving. As in a radial composite reservoir, the pressure is continuous at the interface, whereas, velocity continuity requires $\partial p_D / \partial r_D$ at the interface to be discontinuous to account for the jump in mobility. Fig. 3.19 shows the flow rates in the reservoir at different times. The sharp spikes in the dotted curves are numerical and should be ignored. The flow rate profiles in Fig. 3.19 are similar to that of the monophasic flow problem in Fig. 3.10.

3.3.6   Finite Element Model (FEM)

The weak formulation of the governing equation in Eq. 3.68 is given by Eq. 3.71. In the weak formulation, the diffusivity equation is not satisfied at every point in the volume but the sum of the weighted residuals is zero in each volume element.

$$\int_v p^* \frac{1}{r_D} \frac{\partial}{\partial r_D} \left[r_D \lambda_D \frac{\partial \widetilde{p}_D}{\partial r_D} \right] dv - \int_v p^* c_D \frac{\partial \widetilde{p}_D}{\partial t_D} dv = 0 \qquad \forall p^*(r_D = 1) = 0 \tag{3.71}$$

$\widetilde{p}_D$ is an approximate solution for the pore pressure expressed using a combination of linear shape functions φ_n given in Eq. 3.72; $\widetilde{p}_{D,n}$ is the pressure at node $r_{D,n}$. The weight function p^* is constructed using the same set of shape functions and arbitrarily chosen nodal values p^*_m for $\forall m > 1$;

for $m = 1$, $p_1^* = 0$ inorder to satisfy the constant pressure boundary condition at the sandface (inner radius).

$$\varphi_n(r_D) = \begin{cases} \dfrac{r_D - r_{D,n-1}}{r_{D,n} - r_{D,n-1}} & r_{D,n-1} \leq r_D \leq r_{D,n} \\[2em] \dfrac{r_{D,n+1} - r_D}{r_{D,n+1} - r_{D,n}} & r_{D,n} \leq r_D \leq r_{D,n+1} \\[2em] 0 & Otherwise \end{cases} \tag{3.72}$$

$$\widetilde{p}_D = \sum_{n=1}^{N} \widetilde{p}_{D,n} \varphi_n(r_D)$$

$$\tag{3.73}$$

$$p^* = \sum_{m=1}^{N} p_m^* \varphi_m(r_D)$$

Combining Eqs. 3.71, 3.72 and 3.73, and integrating by parts yields Eq. 3.74. The volume elements are concentric disks and the sum of the weighted residuals should go to zero in each of these disks. Since Eq. 3.74 must be satisfied for all real values of p_m^*, the term in the set brackets in Eq. 3.74 must go to zero. This yields the Eq. 3.75 with mobility matrix $\Lambda_{mn} = \int_1^{r_{De}} r_D \lambda_D \frac{\partial \varphi_m(r)}{\partial r_D} \frac{\partial \varphi_n(r)}{\partial r_D} dr_D$ and compressibility matrix $C_{mn} = \int_1^{r_{De}} r_D c_D \varphi_m(r) \varphi_n(r) dr_D$.

Time discretization of Eq. 3.75 yields Eq. 3.76 which is then solved using a MATLAB program.

$$-\int_1^{r_{De}} \left[\frac{\partial p^*}{\partial r_D} \right] r_D \lambda_D \frac{\partial p_D}{\partial r_D} 2\pi dr_D - \int_1^{r_{De}} \left[p^* c_D \frac{\partial p_D}{\partial t_D} \right] 2\pi r_D dr_D = 0$$

$$\sum_{m=1}^{N} p_m^* \left\{ \sum_{n=1}^{N} \left[\int_1^{r_{De}} r_D \lambda_D \frac{\partial \varphi_m(r)}{\partial r_D} \frac{\partial \varphi_n(r)}{\partial r_D} dr_D \right] \widetilde{p}_{D,n} + \sum_{n=1}^{N} \left[\int_1^{r_{De}} r_D c_D \varphi_m(r) \varphi_n(r) dr_D \right] \frac{\partial \widetilde{p}_{D,n}}{\partial t_D} \right\} = 0$$

$$\tag{3.74}$$

$$[\![\Lambda]\!]_{N \times N} \{\widetilde{p}_{D,n}\}_{N \times 1} + [\![C]\!]_{N \times N} \frac{\partial}{\partial t_D} \{\widetilde{p}_{D,n}\}_{N \times 1} = 0 \tag{3.75}$$

$$[\![\Lambda]\!]^{i+1} \{\widetilde{p}_{D,n}\}^{i+1} + [\![C]\!]^{i+1} \frac{\{\widetilde{p}_{D,n}\}^{i+1} - \{\widetilde{p}_{D,n}\}^i}{t_D^{i+1} - t_D^i} = 0 \tag{3.76}$$

3.4 Summary

Flow models for reservoirs produced/injected at constant pressure is discussed in this chapter. When the flow is radial and momophasic, analytical solutions are obtained in the Laplace domain; inversion is done numerically through Stehfest's algorithm. During drilling, the invasion of solid components

in the drilling fluid often reduces the permeability in the near-wellbore zone; this is captured in the flow model using a non-dimensional skin term S. Also, a large-time asymptotic solution is discussed for this case.

The typical unknowns in a monophasic flow model are permeability k and skin S; these are usually obtained through well tests performed under constant flow rate. Here, we have discussed an interpretation workflow for constant pressure well tests—reciprocal rate derivative analysis—that is similar to the pressure derivative analysis widely used to interpret constant rate well tests. The interpretation workflow can handle multiple constant pressure flow periods.

When the injected fluid is different from the reservoir fluid, only a two-phase flow model can capture the complexity of the reservoir flow. When the sandface injection rate is constant, Buckley-Leverett saturation profile yields a constant velocity for the saturation front and analytical solutions for the sandface pressure evolution have been obtained in the literature. For constant pressure injection, the front velocity is not constant and numerical solutions are needed; we have developed a finite element scheme to model this problem. The reciprocal-rate derivative during constant pressure tests, obtained using the finite element model, resembles the pressure derivative plots obtained in the literature for the constant rate tests.

Chapter 4

Laboratory Tests

A laboratory model was built at Ecole Polytechnique in 2012 (long before the thesis began) to refine and perfect the WTLog method. It consists of a stack of 6 (or less) hollow rock cylinders; liquids are circulated in a central hole (Fig. 4.1). The test procedure of that time involved displacing the viscous liquid in the central hole by a less-viscous liquid and measuring the increase in total formation injection rate (later on, this procedure was called: "opening WTLog"). Several tests were performed by Benoît Brouard with this test procedure. Results from one such test are interpreted in the Annex. The interpreted permeabilities provide some qualitative information on the permeability heterogeneities in the central hole but a comparison with benchmark permeabilities do not produce a very good agreement. It will be shown in the latter half of the chapter that the near-wellbore flow during opening WTLog is biphasic and, at times, there could be instabilities like viscous fingering. Hence, interpretation using monophasic flow models provides permeability estimates that are less accurate. Using a 2 phase flow model to interpret the test data brings in more unknowns and additional uncertainties. Also, it is not possible to estimate the skin value during opening WTLog tests.

These limitations of opening WTLog were identified early in the thesis. In response, a new test procedure was proposed in which the test begins with the less-viscous liquid in the central hole. The viscous liquid then displaces the less-viscous liquid, decreasing the total formation injection rate (closing WTLog). Also, a phase-1 was added before the logging phase during which the less-viscous liquid is injected into the formation for a long duration, at the same pressure head as the logging phase (phase-2). In this new test procedure, the flow in the samples (and rock formations) can be modeled using monophasic flow models. The average skin value can be obtained from phase 1 using reciprocal-rate derivative analysis. Several laboratory tests were performed with this new procedure and the estimated permeability logs, i.e. permeability vs depth, compare very well to the benchmark permeability logs. The test setup that was built in 2012 by Vincent de Greef and Pierre Valli was used during these tests with the addition of some connections and valves to allow circulation of liquids in both directions in the central hole.

Test results are discussed in this chapter in their order of importance rather than in a chronological order; a more exhaustive list of laboratory tests can be found at the end of the chapter, in Table 4.2. During laboratory tests, steady-state is reached in the test samples quite rapidly and

the global skin cannot be interpreted using reciprocal-rate derivative analysis which is based on the transient response of the well. Hence, only non-dimensional permeability logs can be derived. The first half of the chapter discusses closing WTLog tests and derives some important inferences: the injection logs, i.e. formation injection rate of less-viscous liquid vs depth, derived from a series of tests performed on the same set of samples at different circulation rates and pressure heads are very similar; the permeability logs derived from these injection logs display a high correlation to benchmark permeabilities. The latter half of the chapter discusses opening WTLog tests that show two-phase flow and possibly viscous fingering.

4.1 Test setup
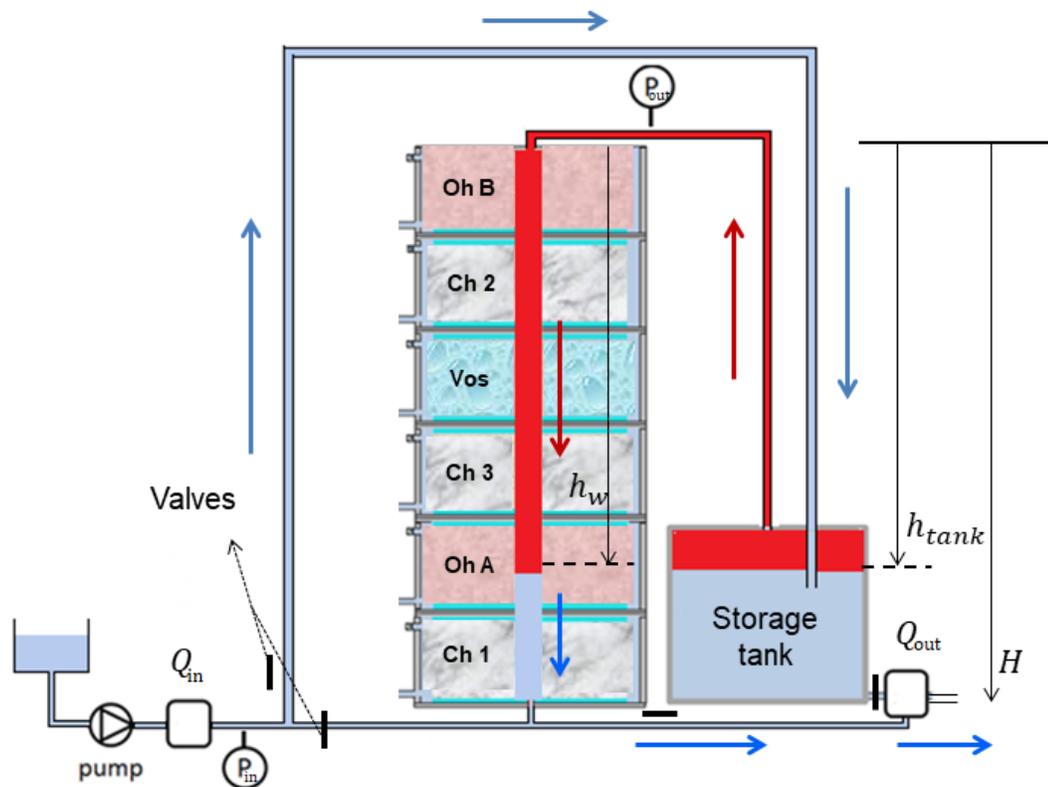
Figure 4.1: Schematic of the test setup. The arrows show the flow directions during closing WTLog.

Cylindrical rock samples of inner radius 1 cm, outer radius 8 cm and height 15 cm are enclosed inside transparent Plexiglas compartments of slightly larger height and radius. To prevent any flow between the central hole and the outer surface of the samples from bypassing the porous media, the two flat surfaces of the sample are coated with Silicone and Silastic. The inner surfaces of the samples are exposed to the pressure of the liquid circulating in the central hole. The outer surfaces are exposed to atmospheric pressure. The outflow from each sample is collected in a small tube attached to the Plexiglas (Fig. 4.2). The outflow rate (Q_R^i) through the cylindrical outer surface of each sample is measured by an outflow meter (a Coriolis flow meter). It is possible to close this outflow and impose a no-flow boundary condition at the outer surface but this was not done for the
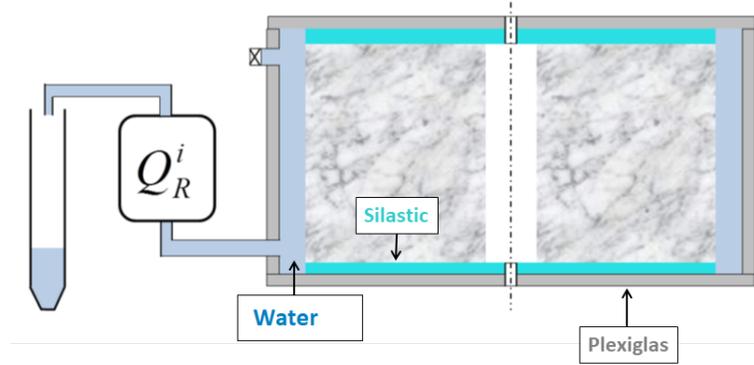
Figure 4.2: Schematic of a test sample enclosed in Plexiglass and coated with Silastic. Q_R^i is the outflow rate measured by the outflow meter.

tests discussed in this chapter. However, the outflow meter is bypassed during some tests for reasons discussed in section 4.4.3 ('Other closing WTLog tests').

Six such samples are stacked on top of one another, hydraulically connected only through the central hole. This creates a multi-layered commingled system. Before stacking, the samples are saturated with tap water in a vacuum chamber. During saturation, CO_2 is first injected into the samples to displace any ambient air, followed by depressurization and water injection until the samples are saturated with water. This ensures that any gas potentially trapped in the pore volume of the samples is mainly CO_2, which is highly soluble in water. The absence of a gaseous phase in the pore volume ensures that the total compressibilities of the samples are not modified drastically. This is supported by the initial tests which showed that steady-state is reached in the samples in less than 3 minutes. (Pierre Valli and Vincent de Greef contributed immensely to the preparation of the test samples.)

Two Coriolis flow meters measure the liquid injection rate (Q_{in}) and withdrawal rate (Q_{out}) in and out of the system, respectively (Fig. 4.1). The accuracy of the flow meters is $\pm 0.2\%$ and their resolution is 0.1 mL/h. An electronic pressure regulation system controls the inflow Q_{in} to maintain a constant inlet pressure P_{in}. Pressure regulation works better when the liquid body contained between the inlet and the outlet is more compressible because a larger volume change is needed to effect a significant pressure change. For this reason, a storage tank is set in the circuit to increase the compressibility of the system by increasing the liquid volume contained in the system. Pressures are regulated up to an accuracy of 0.1 KPa (10^{-3} bar).

The setup is designed to withstand a maximum pressure of 0.8 MPa (8 bars). Data can be monitored in real time (Fig. 4.3). A system of four valves enables the circulation of liquids in both directions, allowing the system to return quickly to the initial configuration at the end of each test. Samples from different geological formations (Ohio, Champenay, Clasach, Vosges, etc.) with permeabilities ranging between 10 μD and 3 D were tested.
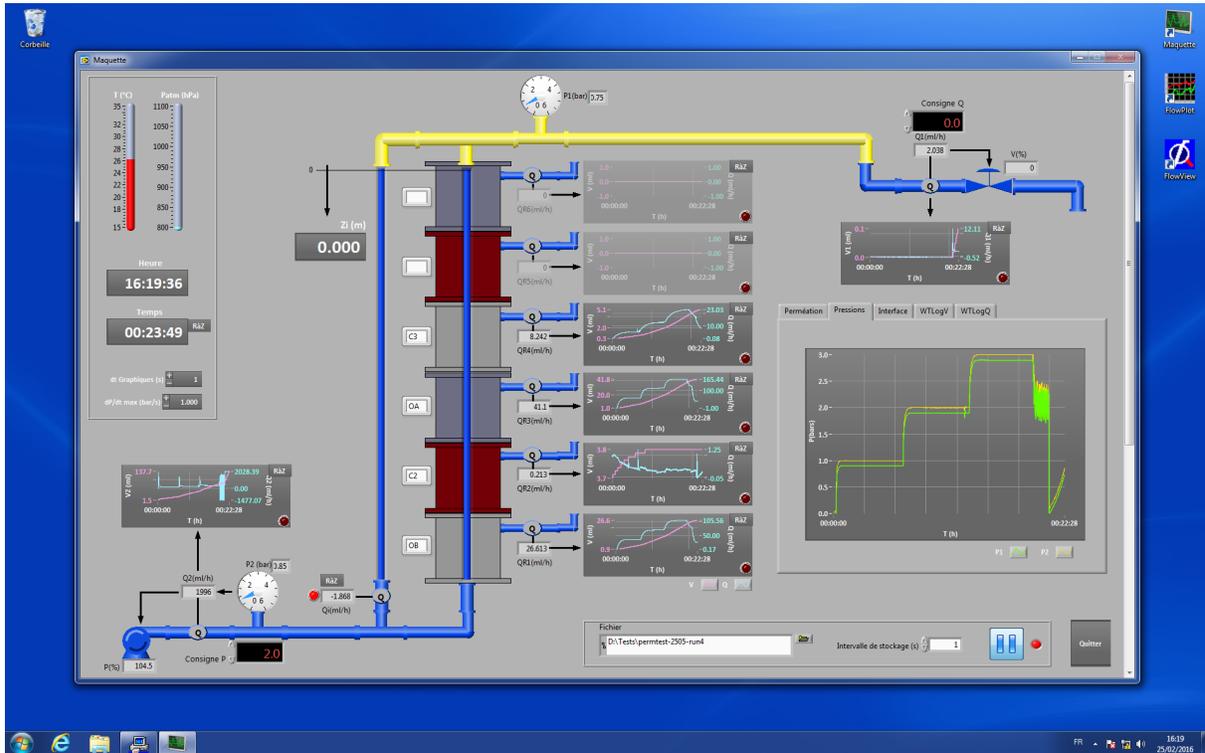
Figure 4.3: User interface for real time monitoring and control. In red are inputs P_2 (bottom left) and Q_1 (top right); the other quantities are measured outputs.

4.2 Steady state flow rates

In the previous chapter on constant pressure well tests, solutions to unsteady state flow problems in an infinite reservoir with a near-wellbore skin were discussed. An analytical solution that is valid at large times was presented. In the laboratory tests, the dimensions of the samples are quite small and steady-state is reached within several seconds to a few minutes. Using the expression for investigation radius developed in the previous chapter ($r_{inv} = 2\sqrt{Kt}$), it can be deduced that the investigation radius reaches the outer boundary ($r_e = 8$ cm) of Ohio B sample ($K = 2\ 10^{-5}$ m^2/s) in 80 seconds.

When steady-state is reached, the pressure in the sample, $p = p(r)$, is governed by Eq. 4.1, where r_w and r_e are the inner and the outer radii, respectively. The derivation of the inner boundary condition in the presence of a near-wellbore damage is discussed in the previous chapter (Eq. 3.14 in chapter 3). The damage is quantified by a non-dimensional skin term S. $\triangle P$ is the pressure head, i.e. the pressure in the central hole relative to the atmospheric pressure which applies at the external radius.

$$\nabla^2 p(r) = 0$$

$$p(r_w) - Sr_w \frac{\partial p}{\partial r}(r_w) = \triangle P \tag{4.1}$$

$$p(r_e) = 0$$

The pressure distribution in the sample is given by Eq. 4.2 and the flow rate per unit thickness is given by Eq. 4.3.

$$\triangle p(r) = \frac{\triangle P}{S + ln(r_e/r_w)} ln(r_e/r) \tag{4.2}$$

$$q = -\frac{k}{\mu} 2\pi r \frac{\partial \triangle p}{\partial r} = \frac{2\pi k \triangle P}{\mu} \frac{1}{\left[S + ln(\frac{r_e}{r_w})\right]} \tag{4.3}$$

4.3 Benchmark sample permeabilities

Benchmark permeabilities were estimated at Ecole Polytechnique through brine injection in the cylindrical rock samples that were later used to test the logging technique. To estimate benchmark permeabilities, four samples (Ohio A, Ohio B, Champenay 2 and Champenay 3) were placed in the test setup, leaving empty the two slots at the top. Step changes were made to the pressure in the central hole and the corresponding outflow rates through each of the samples (Q_R^i) were measured. The permeabilities of Ohio A, Ohio B and Champenay 3 were estimated from the slope of the pressure head vs steady-state flow rates (Fig. 4.4). The outflow through Champenay 2 was less than 1 mL/h and hence, the sample was initially considered impermeable. Later, it was found that the outflow meter of Champenay 2 sample was out of order.

Estimating the virgin permeability of the samples was slightly more involved due to a couple of reasons. For relatively more permeable samples ($k > 10^{-14}$ m^2 or 10 mD), the outflow rates through the samples were quite high and beyond the range of the outflow meters. Also, there were flow-induced pressure losses in these outflow meters. As the outflow meters were exposed to the ambient atmospheric pressure at one end, this pressure loss led to a pressure increase at the other end (at the outer surface of the sample). This pressure increase reduced the effective pressure head in the samples.

$$P_{loss}^i = 0.01 \, \text{MPa} + 7.96 \, 10^{-4} \, \frac{\text{MPa}}{\text{mL/h}} \times (Q_R^i - 12 \, \text{mL/h}) \tag{4.4}$$

The vendor has provided a linear relationship between the outflow rates and the pressure loss in the outflow meters (Eq. 4.4) which allowed computing the effective pressure head and estimating the correct permeability. This explains why no two lines in Fig. 4.4 have the same abscissa in spite of experiencing the same pressures at their inner radii. For example, when Clasach hard was exposed
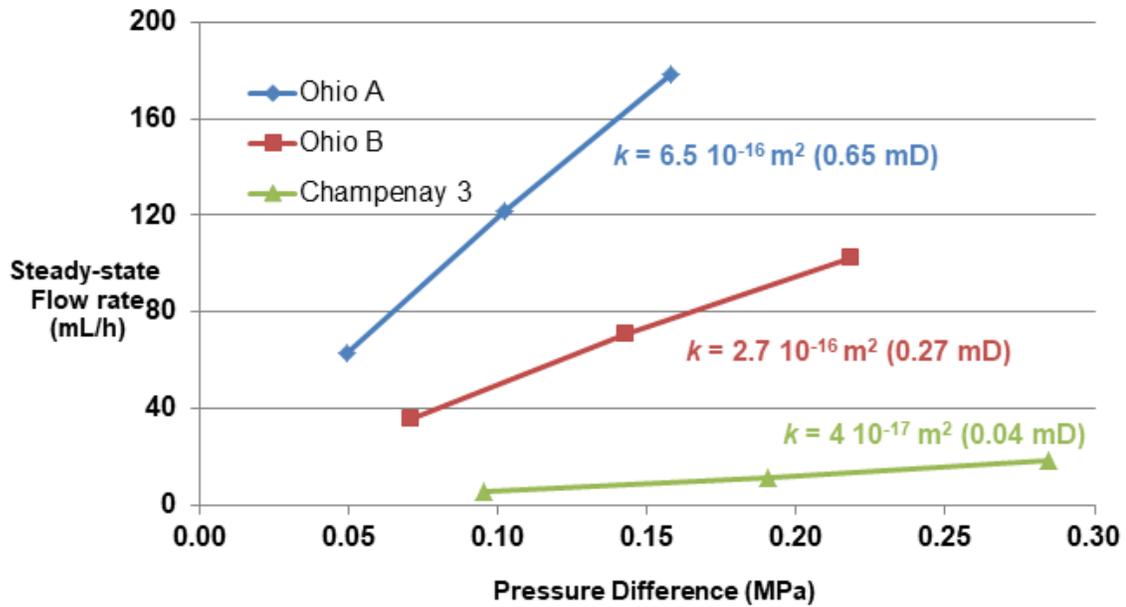
Figure 4.4: Permeabilities estimated at LMS from the slope of pressure vs steady-state flow rate curves.

to 0.2 MPa (2 bars) at the inner radius, the outflow rate was 158 mL/h. The corresponding pressure increase at the outer radius, estimated using Eq. 4.4, is 0.126 MPa (1.26 bars). This translates into an effective pressure head of 0.2-0.126= 0.074 MPa (0.74 bar) and the sample permeability is estimated to be 1.31 10^{-15} m^2 or 1.31 mD (using Eq. 4.3 and $S = 0$).

To avoid pressure changes at the outer radius during WTLog tests, the outflow meters were bypassed (disconnected) during these tests except in some early tests performed with four samples.

Benchmark permeabilities were also estimated by TOTAL using core plugs of diameter 2 to 3 inches (5 to 7.5 cm) through gas injection. Either step decay method — increasing pressure at one end and observing subsequent fall-off — or steady-state method was used, depending on the sample permeability. Because gases do not adhere to the pore surfaces as liquids do, the slippage of the gases results in an over-estimation of permeability (Klinkenberg effect). Klinkenberg correction was applied to the estimated gas permeabilities to obtain an equivalent brine permeability. Fig. 4.5 compares the permeabilities estimated at Ecole Polytechnique to the estimates by TOTAL. There is a good agreement for Champenay 3. For Ohio and Clasach hard samples, the permeabilities estimated at Ecole Polytechnique are smaller. Such variations in permeability are expected due to several reasons:

- TOTAL's estimations were made from plugs with smaller dimensions than the cylindrical samples tested at Ecole Polytechnique. Formation heterogeneities like fissures can cause variations in permeabilities measured at different scales.

- The plugs used by TOTAL and the samples used at Ecole Polytechnique come from different blocks.

- Clay swelling could have occurred when the samples were saturated with water, reducing their
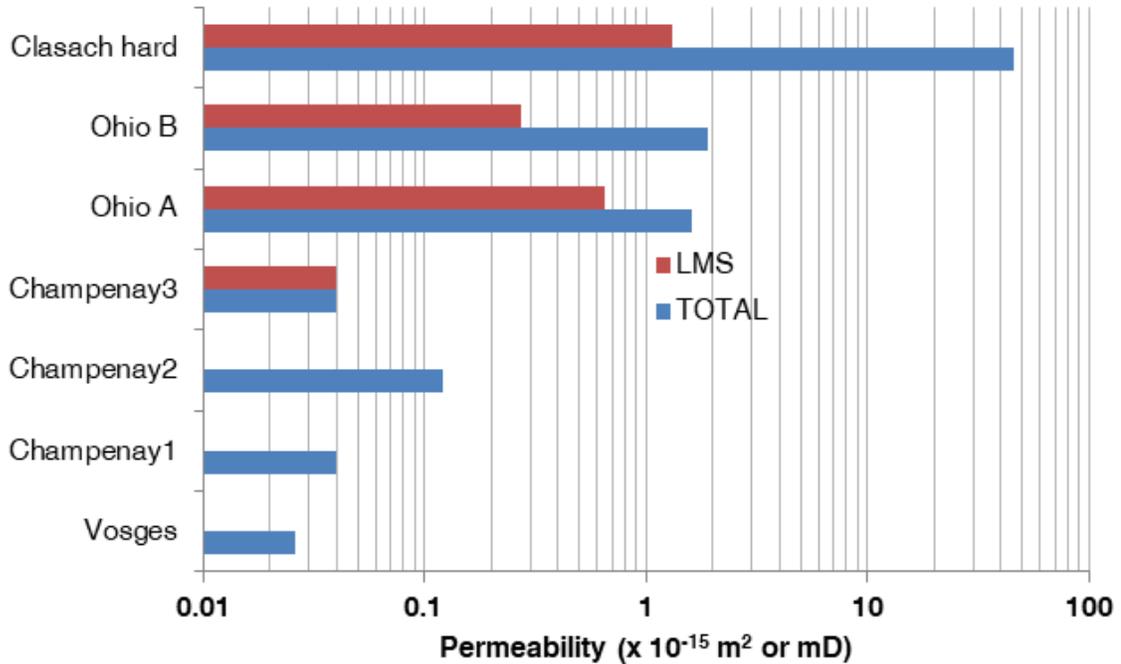
Figure 4.5: Benchmark permeabilities of the test samples measured at TOTAL and at Ecole Polytechnique

permeability.

For Ohio and Clasach hard samples, permeabilities estimated at Ecole Polytechnique are used as benchmark permeabilities for comparing WTLog results. For Champenay 3, the two estimates are the same. For other Champenay and Vosges samples, permeabilities estimated at TOTAL are used as benchmark permeabilities.

4.4   Closing WTLog

At the beginning of a closing WTLog test, the central hole is filled with tap water and the viscous liquid is stored in the storage tank. The inflow pressure P_{in} is increased, which increases the pressure in the central hole. The injection rates in the samples reach a steady state within a few minutes. A valve is opened at $t = t_{beg}$ and the tap water is withdrawn from the bottom of the central hole at a rate Q_{out}; the viscous liquid in the storage tank enters the central hole displacing the less-viscous liquid. The withdrawal rate Q_{out} is controlled by a choke and is maintained constant at a pre-specified value. Similarly, the inflow pressure P_{in} is maintained constant by an electronic pressure regulation system which controls the injection rate Q_{in} to maintain a constant pressure P_{in}. Pressure P_{out} is not regulated; its value is slightly smaller than P_{in} (by less than 0.01 MPa) due to the hydrostatic pressure difference and frictional losses. As in the phase 2 of in-situ closing WTLog, the total injection rate into the samples decreases as the viscous liquid displaces the less-viscous liquid in the open hole.
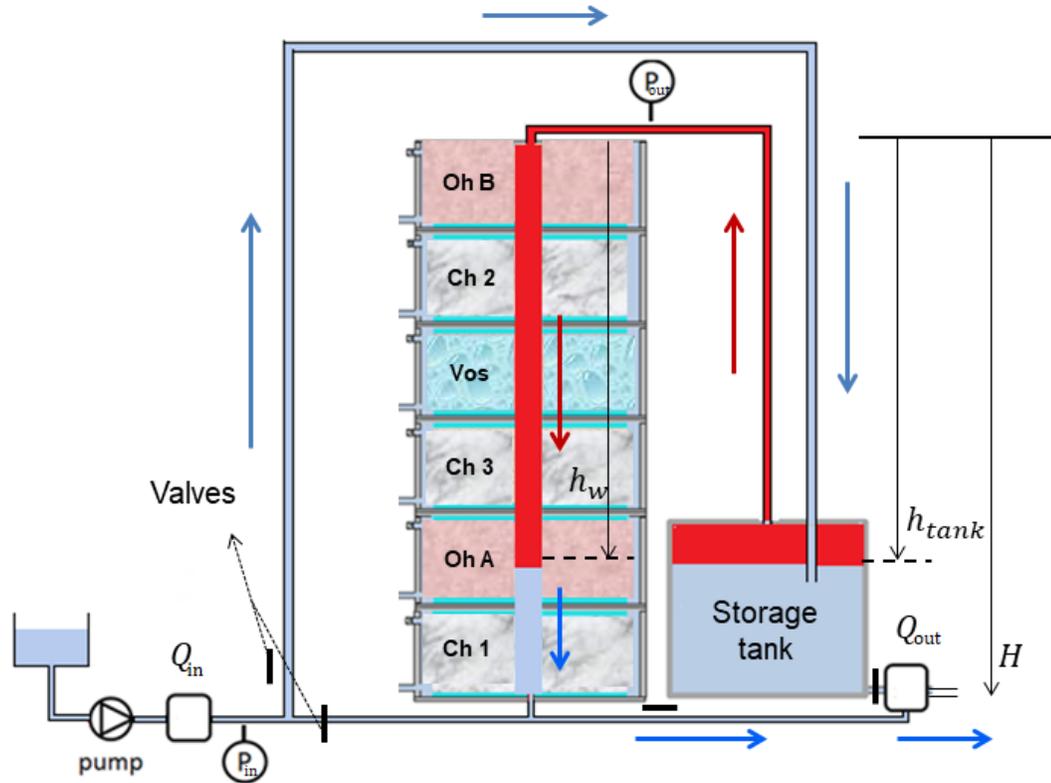
Fig. 4.1 (repeated) Schematic of the test setup. The arrows show the flow directions during closing WTLog.

When the interface reaches the bottom of the open hole at $t = t_{end}$, the valves that were open are closed and vice versa. This changes the direction of circulation without changing either P_{in} or Q_{out}. The total sample injection rate increases as the sample inner surfaces are again exposed to the less-viscous liquid — opening WTLog. When the interface arrives back at the top of the test setup ($t = t_{end}^{open}$), P_{in} is lowered to the atmospheric pressure, outflow Q_{out} is reduced to zero and the test ends. The results from closing WTLog are interpreted here. Opening WTLog is discussed separately in the latter part of the chapter.

4.4.1   Interpretation workflow for laboratory tests

An initial criticism of the WTLog technique was that the near-wellbore permeability is reduced due to fluid and mud component invasion during drilling and the permeabilities could be underestimated if this is not taken into account. We introduced a phase 1 (for in-situ tests) which allows for the estimation of average open-hole skin $\bar{S}$. Using $\bar{S}$, the effect of near-wellbore damage is isolated and the permeability of the undamaged zone is estimated. However, the interpretation assumes that the skin value is uniform for all layers; the error caused by this assumption should be studied. In chapter 2, in the section on error analysis, we studied this assumption through analytical expressions. In the next subsection, we study the same through laboratory tests.

Before the actual WTLog test, a viscous mud (similar to drilling fluid) was circulated in the central hole to create a near-wellbore damage similar to the in-situ tests. A closing WTLog test was

performed and a permeability log was derived using the interpretation workflow discussed below. The results compare very well to the benchmark permeability values. To go further, multiple tests were performed on the same set of samples and there was additional near-wellbore damage created during each of these tests. Permeability logs derived from these test data were very similar to the benchmark permeabilities.

The interpretation workflow for laboratory tests closely follows that of the in-situ tests discussed in chapter 2. Due to the small sample radius (8 cm), steady state is reached in the permeable samples in less than a minute and this hinders the interpretation global skin $\bar{S}$ through reciprocal-rate derivative analysis, which is based on transient flow. However, the phase 2 of closing WTLog can be used to derive an injection log as in the case of in-situ tests. Only a non-dimensional permeability log can be derived from the injection log since the global skin value is not known.

4.4.1.1 Circulation model

Heat-transfer and compressibility effects are negligible during laboratory tests. Laboratory temperature is maintained constant during the tests; pressure variations in the central hole and the storage tank are very small (<0.01 MPa or 0.1 bar) and hence, the liquid densities are almost constant. The circulation model is given by the conservation of mass as in the in-situ case (or conservation of volume, since the densities are constant). In Fig. 4.1, there are two interfaces between the viscous liquid (red) and the less-viscous liquid (blue) and this results in three control volumes. The interface velocities in the storage tank and the central hole are $\dot{h}_{tk}$ and $\dot{h}_w$, respectively, and their cross-sectional areas are S_{tk} and S_w, respectively. The mass balance for the three control volumes is given by Eqs. 4.5 to 4.7, which basically say that the injected liquid volume that has not seeped into the samples is used to move the interface between the circulating liquids. During in-situ tests, mud viscosity ensures that the viscous fluid loss into the formation, $q_{\mu+}^{wf}$, is negligible. However, laboratory tests were performed with vegetable oils and the viscous fluid loss was not negligible during these tests.

$$Less - viscous\ fluid\ in\ the\ tank: \quad -\dot{h}_{tk}S_{tk} = Q_{in}(t) \tag{4.5}$$

$$Viscous\ fluid: \quad \dot{h}_w S_w + \int_0^{h_w} q_{\mu+}^{wf}(z)dz = -\dot{h}_{tk}S_{tk} \tag{4.6}$$

$$Less - viscous\ fluid\ in\ the\ central\ hole: \quad \dot{h}_w S_w - \int_{h_w}^{H} q_{\mu-}^{wf}(z)dz = Q_{out}(t) \tag{4.7}$$

where, $q_{\mu+}^{wf}(z)$ and $q_{\mu-}^{wf}(z)$ are the injection rates per unit thickness in the samples for the viscous and the less-viscous liquids, respectively. The injection rates are not a function of time since steady state is reached in the samples. Combining Eqs. 4.5 to 4.7, the total sample injection rate is given by Eq. 4.8 and the interface velocity in the central hole is given by Eq. 4.9.

$$\int_0^{h_w(t)} q_{\mu+}^{wf}(z)dz + \int_{h_w(t)}^H q_{\mu-}^{wf}(z)dz = Q_{in}(t) - Q_{out}(t) \tag{4.8}$$

$$\dot{h}_w(t) = \frac{Q_{out}(t) + \int_{h_w(t)}^H q_{\mu-}^{wf}(z)dz}{S_w} \tag{4.9}$$

4.4.1.2 Deriving an injection log

Table 4.1 shows that the injection rate of the viscous liquid at the end of closing WTLog ($t = t_{end}$) could be as high as 40% of that of the less-viscous liquid. When the viscous liquid injection can be modeled as a monophasic flow, the ratio of the injection rates (under constant pressure head) of the viscous and the less-viscous liquids will be equal to their viscosity ratios [$q_{\mu+}^{wf}(z) = (\mu_-/\mu_+)q_{\mu-}^{wf}(z)$]. However, in reality, the viscous liquid injection into the samples is a two-phase flow and the ratio of the injection rates are higher (but always less than 1). The ratio of injection rates is denoted by Ω (Eq. 4.10). An assumption is made here: Ω is the same for all samples; this is valid when the relative permeability curve is the same for all samples. Eq. 4.11 is used to estimate Ω.

$$q_{\mu+}^{wf}(z) = \Omega q_{\mu-}^{wf}(z) \tag{4.10}$$

$$\Omega = \frac{[Q_{in} - Q_{out}](t_{end})}{[Q_{in} - Q_{out}](t_{beg})} \tag{4.11}$$

The equations that are used to derive an injection log, i.e. $q_{\mu-}^{wf}(h_w)$ vs h_w, are obtained by solving Eqs. 4.8 to 4.10. Eq. 4.12 computes the interface velocity in the central hole. Eq. 4.13 gives the total injection rate of the less-viscous liquid into the samples. Using the interface location computed from Eq. 4.12, Eq. 4.14 provides the injection rate per unit thickness into the samples.

$$\dot{h}_w = \frac{[Q_{in} - \Omega Q_{out}](t) - [Q_{in} - Q_{out}](t_{end})}{(1 - \Omega) S_w} \tag{4.12}$$

$$\int_{h_w}^H q_{\mu-}^{wf}(z)dz = \frac{[Q_{in} - Q_{out}](t) - [Q_{in} - Q_{out}](t_{end})}{1 - \Omega} \tag{4.13}$$

$$q_{\mu-}^{wf}(h_w) = -\frac{d}{dh_w}\left[\frac{[Q_{in} - Q_{out}](t) - [Q_{in} - Q_{out}](t_{end})}{1 - \Omega}\right] \tag{4.14}$$

4.4.1.3 Deriving a permeability log

Pressure differences in the water column are quite small when compared to the pressure applied in the central hole. This allows us to consider the pressure head $\triangle P$ to be the same for all stacked samples when the outflow meters are disconnected (i.e. the head losses through the outflow metres are zero), which is the case for the test with 6 samples discussed below. The pressure head $\triangle P$ equals the inflow pressure P_{in}. Also, r_e/r_w is uniform and equals 8. The viscosity of tap water, μ_-, is a known value ($= 10^{-3}$ Pa.s or 1 cP). The two unknowns in Eq. 4.3, i.e. $q_{\mu-} = (2\pi k \triangle P/\mu)/[S + ln(r_e/r_w)]$,

are permeability k and skin S. As in the in-situ case, uniform skin is considered for all samples to derive a permeability log.

As the reciprocal-rate derivative analysis is not available for laboratory tests (due to the absence of transient flow), the global skin value is not known. However, the conditions listed in the previous paragraph and the flow rate from Eq. 4.3 allow us to derive a non-dimensional permeability log using Eq. 4.14.

$$\frac{k}{\langle k \rangle_{avg}} = \frac{q_{\mu-}^{wf}(z)}{\left[\int_0^H q_{\mu-}^{wf}(z)dz/H \right]} = \frac{q_{\mu-}^{wf}(z)}{[Q_{in} - Q_{out}](t_{beg})/H} \tag{4.15}$$

It is evident from Eq. 4.15 that the non-dimensional permeability log is the same as the non-dimensional injection log. Although Eq. 4.15 allows the estimation of a continuous permeability log, the benchmark permeabilities are average permeabilities of the samples. Hence, the permeability log estimated using Eq. 4.15 is averaged at the sample scale for effective comparison against benchmark permeabilities.

4.4.1.4   Comparing different logs

Pearson's linear correlation in Eq. 4.16 is used to quantitatively compare the logs with each other and with benchmark permeabilities (in Figs. 4.8, 4.9, 4.11 and 4.13). Pearson's method consists of comparing two sequences x_i and y_i, $i \in [1, n]$, whose means are $\bar{x}$ and $\bar{y}$, respectively. The correlation coefficient, $-1 \leq r \leq 1$, is computed by dividing the covariance between the two sequences by their standard deviations. This normalizes the correlation coefficient. A maximum correlation of $r = 1$ is obtained when the variations from the mean for the two sequences are the same; $r = 0$ indicates a complete lack of correlation between the two sequences. For the correlations computed in section 4.4.2, $n = 6$ is used for comparisons at samples scale (6 samples of 16.67 cm each) and $n = 50$ is used for comparisons at a finer scale of 2 cm (the 100 cm central hole is divided into 50 equal sections).

$$r = \frac{\sum_{i=1}^{n}(x_i - \bar{x})(y_i - \bar{y})}{\sqrt{\sum_{i=1}^{n}(x_i - \bar{x})^2}\sqrt{\sum_{i=1}^{n}(y_i - \bar{y})^2}} \tag{4.16}$$

4.4.2   A test that validates the interpretation workflow

Six samples were stacked up in the order shown in Fig. 4.1; Oh, Ch and Vos denote Ohio, Champenay and Vosges samples, respectively. The permeabilities of the Ohio samples were larger than the rest by an order of magnitude. Before the test, a water-based viscous mud was circulated in the central hole under a small pressure head to create some near-wellbore damage (mudcake) similar to the damage observed in the in-situ open holes. As a result, total injection rate in the samples reduced by about 5 times when compared to the injection rates in virgin samples. Tap water ($\mu_- = 10^{-3}$ Pa.s or 1 cP) and canola oil ($\mu_+ = 5 \ 10^{-2}$ Pa.s or 50 cP) were used as the less-viscous and viscous liquids, respectively.

Four tests were performed on the same set of samples at different pressure heads $\triangle P$ and circulation rates Q_{out}. Test inputs and selected outputs are listed in Table 4.1, in the same sequence
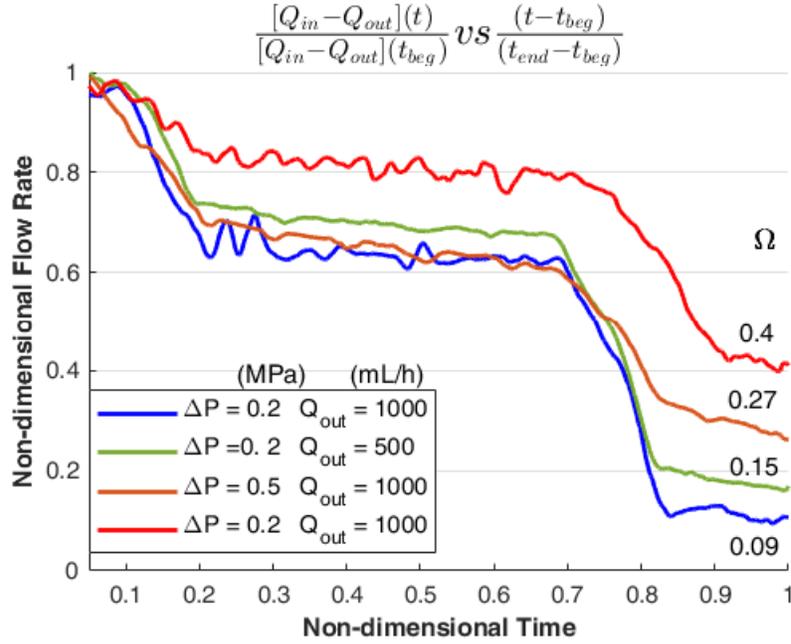
Figure 4.6: Total sample injection rate $[Q_{in} - Q_{out}]$ vs time measured during the tests. Non-dimensionalization enables comparison of tests performed at different pressure heads and circulation rates.

in which the tests were performed. The observed test duration in Table 4.1 is given by visual observation of the interface entering and exiting the central hole; the injection rates at corresponding times are also given in Table 4.1 as $[Q_{in} - Q_{out}](t_{beg})$ and $[Q_{in} - Q_{out}](t_{end})$.

The following observations can be made from Table 4.1. The total injection rate of the viscous oil per unit pressure head, $[Q_{in} - Q_{out}](t_{end})/\triangle P$, increases slightly with the number of tests because the increasing saturation in viscous oil in the near-wellbore region increases its relative permeability. There is an abnormally large viscous liquid loss for the test performed at $\triangle P = 0.5$ MPa (5 bars). The total injection rate of the less-viscous liquid per unit pressure head, $[Q_{in} - Q_{out}](t_{beg})/\triangle P$, suffers a reduction due to the invasion of the viscous oil during the previous tests. As a result, the ratio between the two quantities, Ω, increases.

Fig. 4.6 shows the total sample injection rate, i.e. the combined injection rate of the viscous and the less-viscous liquids into the samples or $Q_{in} - Q_{out}$. Flow rates and time are non-dimensionalized using values from Table 4.1.

4.4.2.1 Noise reduction in test data

In Fig. 4.6, $Q_{in} - Q_{out}$ is shown after filtering some high-frequency noises in the measured flow rate data. It takes about 3 minutes for the interface to pass through a sample of thickness 16.6 cm (when $Q_{out} = 1000$ mL/h). But, flow rates are measured every second and can contain high-frequency signals that are not sample responses. A cut-off frequency is chosen depending on the desired vertical resolution for injection/permeability log. In our analysis, we have chosen a vertical resolution of 2 cm which translates into a cut-off frequency of about 0.04 Hz (cut-off frequency = desired vertical resolution / interface velocity). A low-pass filter (inbuilt in MATLAB) performs fast

Test Inputs			Observed outputs			
S.no.	$\triangle P$ MPa (bar)	Q_{out} (mL/h)	Test duration $t_{end} - t_{beg}$ (min)	$[Q_{in} - Q_{out}](t_{beg})$ (mL/h)	$[Q_{in} - Q_{out}](t_{end})$ (mL/h)	$\Omega = \frac{[Q_{in}-Q_{out}](t_{end})}{[Q_{in}-Q_{out}](t_{beg})}$ (Dimension-less)
1	0.2 (2)	1000	18.2	120	11	0.09
2	0.2 (2)	500	34.4	86	13	0.15
3	0.5 (5)	1000	17.7	190	51	0.27
4	0.2 (2)	1000	19.0	35	14	0.4

S.no.	Pressure $\triangle P$ MPa (bar)	$\frac{[Q_{in}-Q_{out}](t_{beg})}{\triangle P}$ (mL/h/bar)	$\frac{[Q_{in}-Q_{out}](t_{end})}{\triangle P}$ (mL/h/bar)
1	0.2 (2)	60	5.5
2	0.2 (2)	43	6.5
3	0.5 (5)	38	10.2
4	0.2 (2)	17.5	7

Table 4.1: Inputs for laboratory tests and selected observed outputs. $[Q_{in} - Q_{out}](t_{beg})/\triangle P$ decreases due to formation damage by the viscous oil invasion. Ω increases with decreasing $[Q_{in} - Q_{out}](t_{beg})/\triangle P$.
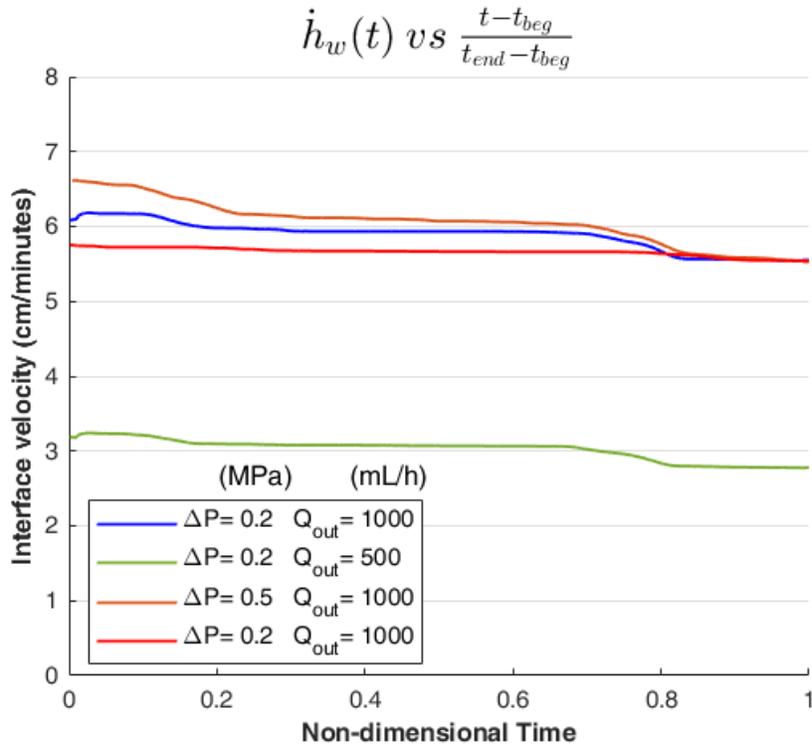
Figure 4.7: Interface velocity in the central hole vs time.

Fourier transform analysis of the input data, dampens the signals with frequencies higher than the cut-off frequency, and recreates a filtered output data. Yet, small, low-frequency fluctuations can be seen in Fig. 4.6, due to the pressure regulation system. The oscillations are more visible when the sample injection rates are small (red curve).

The small oscillations pose the risk of interpreting negative injection rates at some layers and must be dealt with before deriving an injection log. For the analysis discussed in this chapter, the total injection rates in Fig. 4.6 are converted into monotonically decreasing functions by replacing the oscillations with straight lines connecting their minima. The small magnitude and time period of the oscillations support this approach.

4.4.2.2 Injection logs

Interface velocities are computed using Eq. 4.12 (shown in Fig. 4.7) and, upon integration with respect to time, they yield the interface location in the central hole $h_w(t)$. The interface location is used to compute the sample injection rate per unit thickness, $q_{\mu-}^{wf}(h_w)$ using Eq. 4.14. Fig. 4.8 (top) shows the derived injection logs for different tests. The injection rates through Ohio samples are larger than the injection rates through other less permeable samples. Ohio A appears to be two-layered, as suggested by all four injection logs.

The scatter plot in Fig. 4.8 (bottom) shows the Pearson's correlation between the injection logs. Each injection log is compared to the three other logs and the correlation values are placed on a vertical scale with corresponding marker colors. The logs are compared at a vertical resolution of 2 cm, i.e. $1/50^{th}$ of the height of the central hole. Correlation between two injection logs A and B is

$$\frac{q_{\mu-}^{wf}(h_w)}{[Q_{in}-Q_{out}](t_{beg})/H} \; vs \; h_w$$
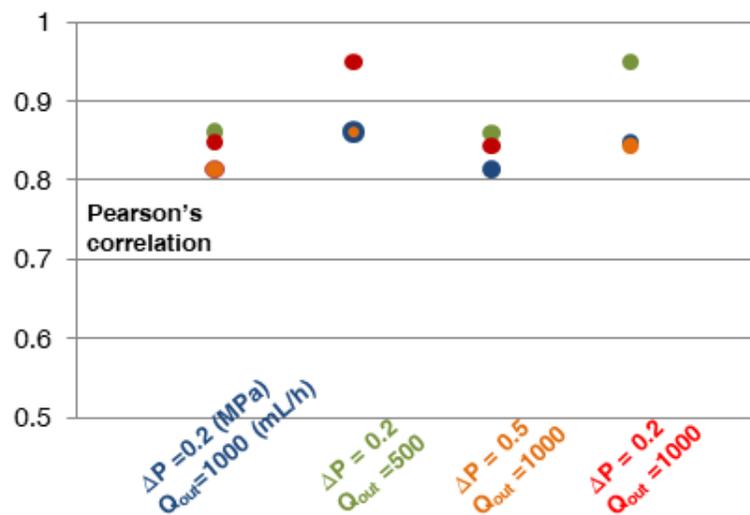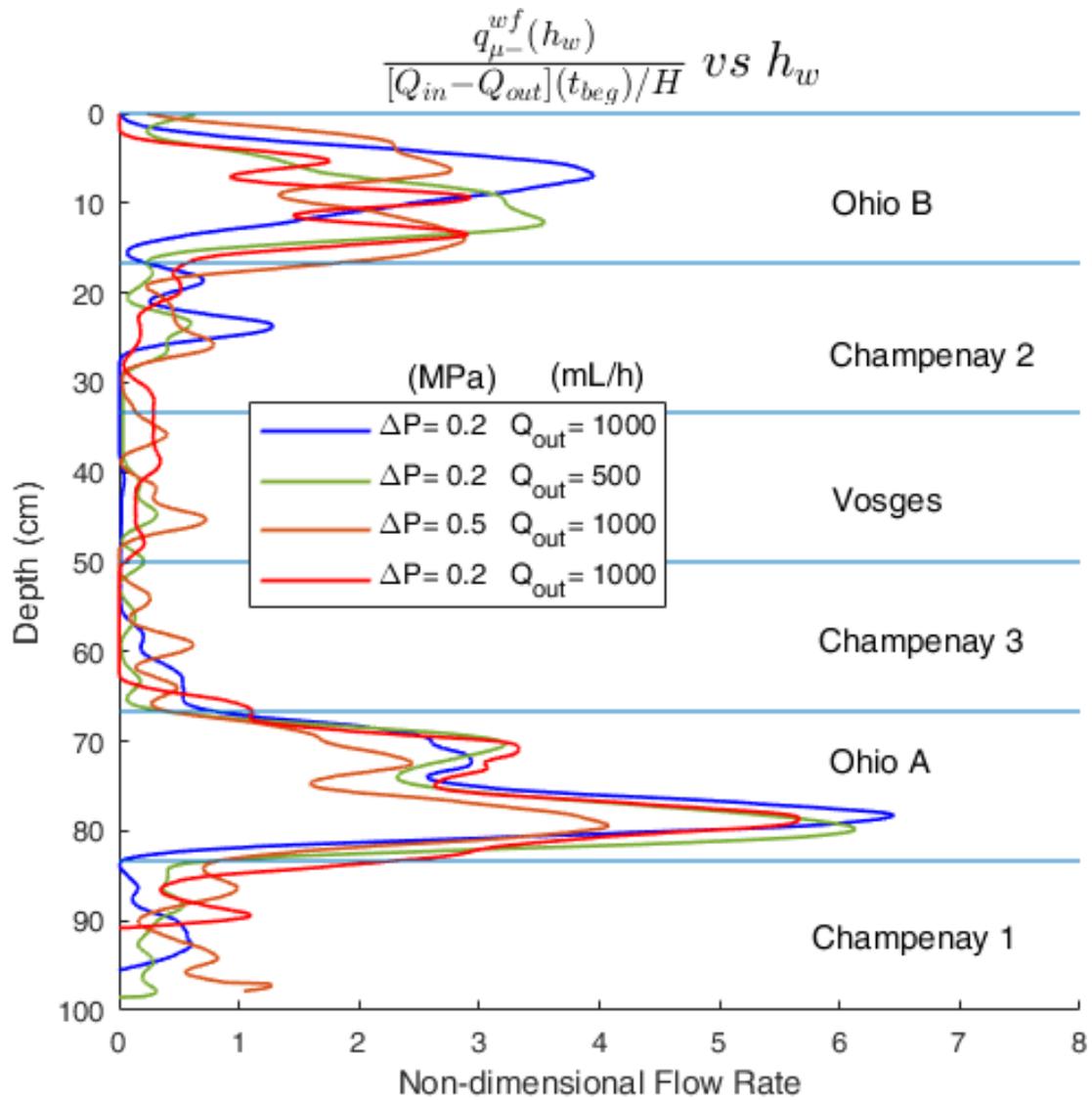
Figure 4.8: Injection logs derived from the test data (top) — sample injection rate per unit thickness vs depth. Pearson's correlation between the injection logs (bottom) are computed using Eq. 4.16.

repeated twice in the plot, once above A and again above B (note that the topmost red and green dots have the same correlation value). Most correlation values lie between 0.8 and 0.9, showing a strong correlation between the successive injection logs.

The skin increase due to the viscous liquid loss into the samples increased the Ω value for the latter tests, but the injection logs derived are more or less consistent. Pearson's correlation between the first test (during which $\Omega = 0.09$ is negligible) and the last test (during which $\Omega = 0.4$) is 0.85. This shows that Eq. 4.10 is an acceptable approximation to describe the viscous liquid loss in the samples.

4.4.2.3 Permeability logs
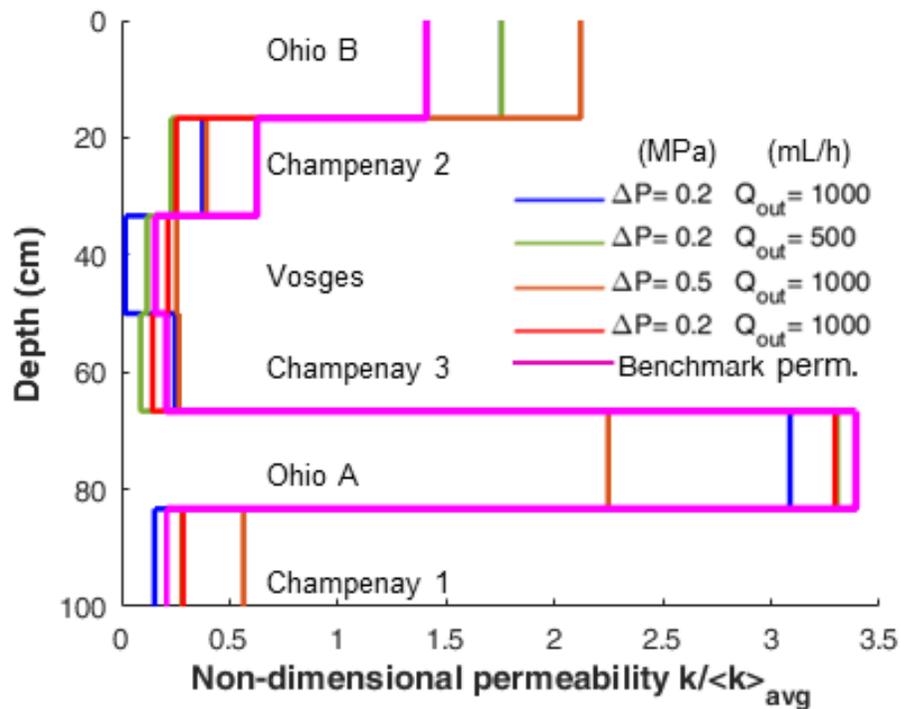
Pearson's correlation between the estimated permeability logs and benchmark permeability log			
$\triangle P = 0.2$ MPa	$\triangle P = 0.2$ MPa	$\triangle P = 0.5$ MPa	$\triangle P = 0.2$ MPa
$Q_1 = 1000$ mL/h	$Q_1 = 500$ mL/h	$Q_1 = 1000$ mL/h	$Q_1 = 1000$ mL/h
0.98	0.99	0.94	0.98

Figure 4.9: Non-dimensional permeability logs, derived by averaging the injection logs at sample scale (Eq. 4.15), are compared to benchmark permeability logs.

As stated earlier, the following assumption is used to derive a permeability log from the injection log: uniform skin value for all samples. But the change in the average skin value between two tests is taken into account. The non-dimensional permeability is estimated using Eq. 4.15. Due to the uniform pressure head $\triangle P$ and the absence of transient flow, the non-dimensional permeability logs are the same as the injection logs in Fig. 4.8 (see Eq. 4.15). For effective comparison with benchmark permeabilities, the permeability logs are averaged at the sample scale and compared to the benchmark permeability log in Fig. 4.9. The Pearson's correlation between the four estimated permeability logs and the benchmark permeability log is shown in the table enclosed in Fig. 4.9. The correlations are quite high (> 0.94). The correlations, in this case, are higher than in the case of injection logs because the injection logs are compared at a very fine scale of 2 cm and the correlation increases when the logs are compared at larger scales. The key result is that the uniform skin assumption is supported by these high correlation values.

In chapter 2, we discussed that there could be local variations in the skin value compared to the 'global average skin' interpreted from the reciprocal-rate derivative analysis. We also estimated the sensitivity of the permeability log to the local variations in skin value and this showed that when the skin variations are $\pm 50\%$ and global skin $\bar{S} = 5$, the error in permeability estimations are $\mp 32\%$ with a near-linear relationship between the two quantities. Similar variations can be seen between the benchmark permeabilities and the estimated permeabilities in Fig. 4.9. Ohio B permeability is slightly overestimated whereas Ohio A permeability is underestimated. However, the large permeability variations between the samples and the ability of the logging technique to capture these variations results in high correlations with the benchmark permeabilities, in spite of the errors caused by a non-uniform skin. Similarly, in the permeability logs derived from Nuclear Magnetic Resonance (NMR) or acoustic logs, the local deviations in permeabilities are often masked by the presence of different orders of magnitude. In NMR logs, deviations of 500% or 1000% between NMR-derived permeabilities and core permeabilities are not uncommon (see the figure in page 6, Allen et al., 2000). Permeability logs in Fig. 4.9 are relatively more accurate. Also, the proposed interpretation workflow can provide uncertainty estimates for the permeability log when the expected local skin variations are known.

4.4.3 Other closing WTLog tests

The early WTLog tests were performed with four samples. The outflow meters were connected during these tests which induced a pressure buildup at the outer surface of the samples. Hence, the effective pressure heads $\triangle P_i$ were not uniform for all samples. Fig. 4.10 (left) shows the measured injection rate for a test with a different set of Ohio samples from the same batch. This was the first ever closing WTLog test, performed in March 2016. As before, colza oil ($\mu_+ = 5 - 6\,10^{-2}$ Pa.s or $50 - 60$ cP) was used as the viscous liquid and tap water ($\mu = 10^{-3}$ Pa.s or 1 cP) was used as the less-viscous liquid. Unlike the earlier test, there was no mud circulation before this test but the samples had been exposed to the viscous oil, for a short duration, and this halved the total water injection rate in the samples compared to the injection rates in the virgin samples. The equivalent global skin is approximately $\bar{S} = 2$ (estimated using Eq. 4.3). An injection log is derived from the test data (Fig. 4.10 right) using the same procedure used for the test with 6 samples.
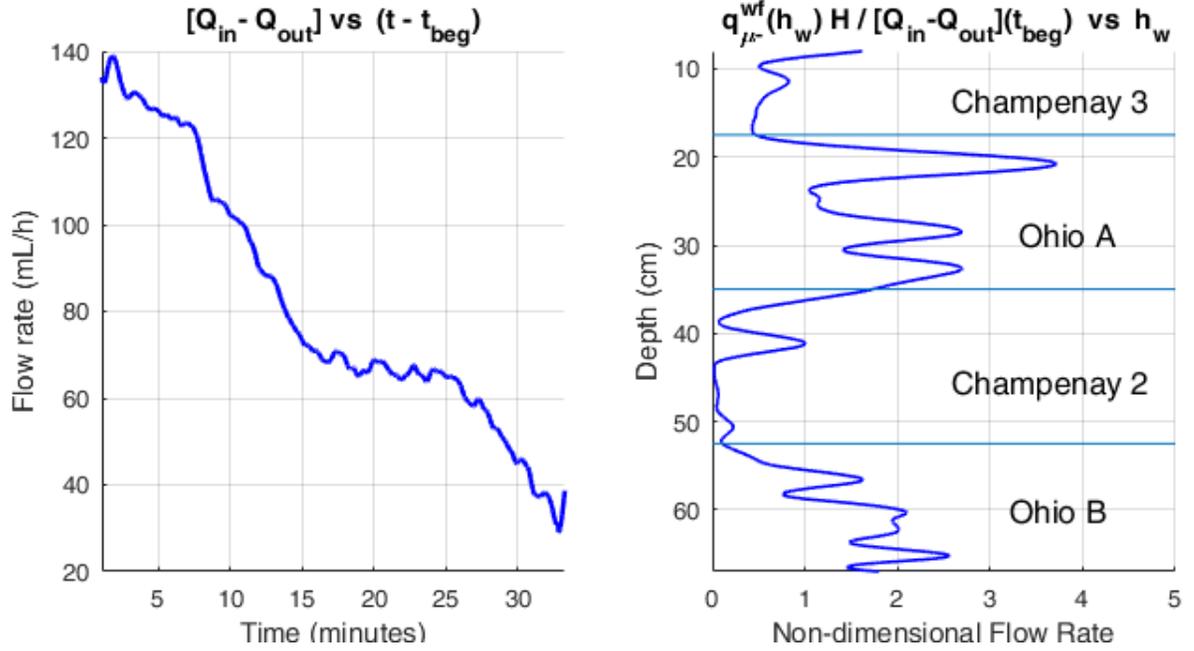
Figure 4.10: An early test (March 2016) with Ohio samples. On the left are the measured test data; on the right is the derived injection log.

A new set of equations are required to derive a permeability log from the injection log because of the head losses in the outflow meters. The total injection rate in each sample, Q^i, is estimated from the injection log in Fig. 4.10 (right). Using Q^i, the pressure loss in the outflow meters are computed from Eq. 4.4 and the effective pressure head in the sample are calculated, $\triangle P^i = \triangle P - P^i_{loss}$. Eq. 4.17 is the ratio between the average permeability of a sample and the combined average of all samples. Substituting Eq. 4.3 in Eq. 4.17 shows that the sample permeabilities can be expressed in terms of sample flow rates and effective pressure heads (Eq. 4.18).

$$\frac{\langle k \rangle^i_{samp}}{\langle k \rangle_{avg}} = \frac{\left[\int_{i \times h_{samp}}^{(i+1) \times h_{samp}} k(z)dz \right] / h_{samp}}{\left[\int_0^H k(z)dz \right] / H} \tag{4.17}$$

$$\frac{\langle k \rangle^i_{samp}}{\langle k \rangle_{avg}} = \frac{Q^i / \triangle P^i}{\sum Q^j / \triangle P^j} \times \frac{H}{h_{samp}} \tag{4.18}$$

Fig. 4.11 compares the estimated permeability log to the benchmark permeability log. Ohio A is the most permeable sample and its dimensionless permeability is slightly underestimated (by about 30%), probably due to local skin variations. The permeabilities of the other layers (less permeable than Ohio A) are slightly over-estimated, probably due to the same reason. In spite of these local variations, the permeability heterogeneities in the central hole are captured well and this results in a high Pearson's correlation of 0.98.

A few months later (May 2016), a closing WTLog test was performed with a Clasach sample ($k = 1.31\,10^{-15} \mathrm{m}^2\, or\, 1.31$ mD) in place of one of the Champenay samples. The samples were rearranged in the order shown in Fig. 4.12 (right). As in the previous test, the outflow meters were connected, and colza oil was used as the viscous liquid. However, the viscous liquid loss, in this
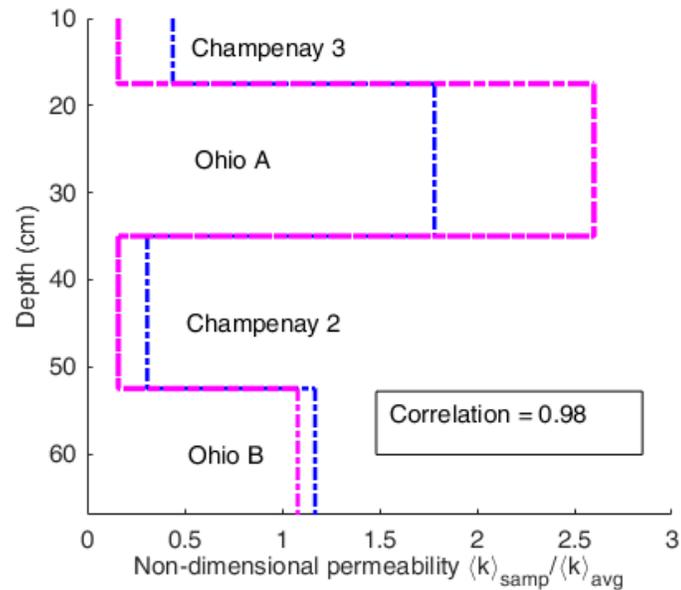
Figure 4.11: Permeability log estimated using Eq. 4.18 (blue) is compared to benchmark permeability log (pink)
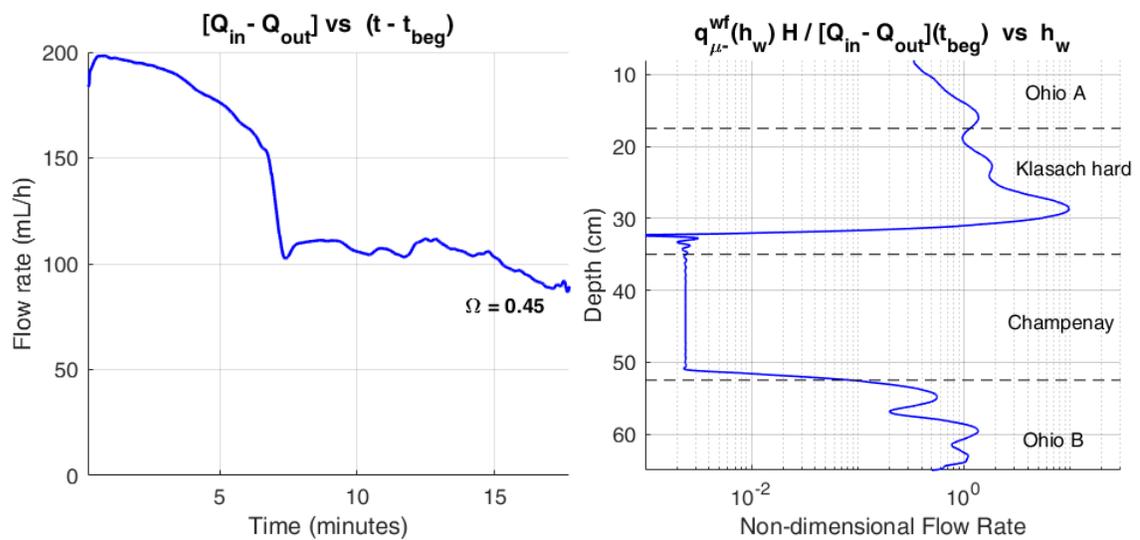
Figure 4.12: A test with permeabilities differing by 3 orders of magnitude. Test data is on the left and the derived injection log is on the right.
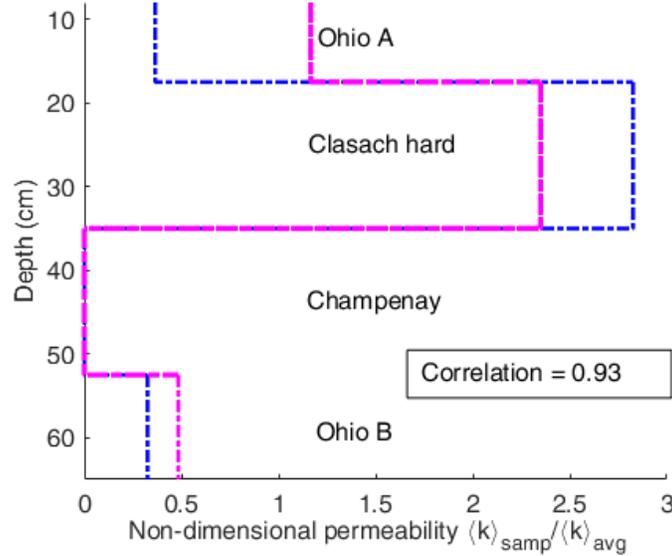
Figure 4.13: A test with permeabilities differing by 3 orders of magnitude. Permeability log estimated using Eq. 4.18 (blue) is compared to benchmark permeability log (pink)

case, was significantly higher due to the large permeability of the Clasach sample; in Fig. 4.12 (left), the formation injection rate of the viscous liquid at the end of the test is almost half that of the less-viscous liquid at the beginning of the test. The injection log derived from the test data (Fig. 4.12 right) is quite sensitive to Eq. 4.10 in the interpretation workflow: $q_{\mu+}^{wf}(z) = \Omega q_{\mu-}^{wf}(z)$.

The estimated and benchmark permeability logs are compared in Fig. 4.13. Clasach permeability is slightly over-estimated but the permeability of other less permeable layers are under-estimated. This is expected since Clasach sample was fresh (without any near-wellbore damage) whereas the other samples had been exposed to the viscous liquid during earlier tests. The key result here is that the presence of three different orders of permeability has been correctly captured.

4.5 Opening WTLog

4.5.1 Flow behavior is bi-phasic during opening WTLogs

After each closing WTLog test shown in Fig. 4.6, the interface was moved back to its initial position under constant inflow pressure P_{in} and withdrawal rate Q_{out}. The measurement of flow rates continued. This is the same as the opening WTLog test procedure developed before the thesis. At the beginning of opening WTLog, all the samples were exposed to the viscous liquid and $Q_{in} - Q_{out}$ (at $t = t_{end}$) is the rate of loss of the viscous liquid into the samples. As the less-viscous liquid displaces the viscous liquid in the central hole, $Q_{in} - Q_{out}$ increases.

Fig. 4.14 shows the total sample injection rate vs time during the opening WTLog tests that were performed immediately after each of the closing WTLog tests shown in Fig. 4.6. The sample injection rate at the beginning of the closing WTLog test, $[Q_{in} - Q_{out}](t_{beg})$, is used to non-dimensionalize the flow rates. At the end of the opening WTLog, when all the samples were exposed to the less-viscous

$$\frac{[Q_{in}-Q_{out}]}{[Q_{in}-Q_{out}](t_{beg})} \ vs \ \frac{(t-t_{beg})}{(t_{end}-t_{beg})}$$
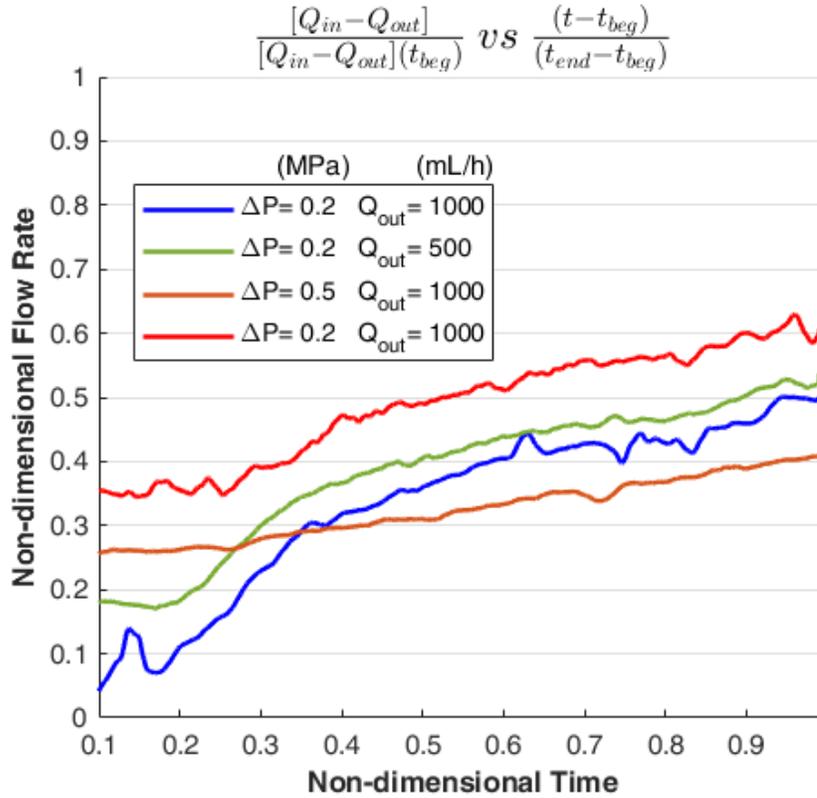
Figure 4.14: Total injection rate through the samples vs time — Opening WTLog.

liquid, $Q_{in} - Q_{out}$ had not recovered back to its initial value, due to the damage caused during the test by the viscous liquid loss. This reduction in $Q_{in} - Q_{out}$ was the largest for the test with $\Delta P = 0.5$ MPa (5 bars) during which the largest viscous liquid loss happened.

During closing WTLog (Fig. 4.6), there were large reductions in $Q_{in} - Q_{out}$ when the interface passed through the permeable layers and it stayed almost constant at other times. However, during opening WTLog, $Q_{in} - Q_{out}$ continues to increase throughout the test even when the interface is in the less permeable layers (Fig. 4.14). The following hypothesis can be made to explain this phenomenon.

The invasion of viscous liquid during the test creates a near-wellbore zone predominantly saturated with viscous liquid and containing some residual brine. When the sample is exposed to brine, the relative permeability of brine in the near wellbore zone is very small initially and slowly increases as the viscous liquid is swept away by the brine. This process could be longer than the test duration itself.

Outflow meters were disconnected during the tests in Fig. 4.14 to avoid any pressure loss at the outer radius. However, the outflow rates from an earlier opening WTLog test, performed with a different set of Ohio samples, support the above hypothesis. During this test, the outflow rates through the samples continued to increase for several minutes after the interface had passed through the samples (Fig. 4.15). This was not the case with the initial virgin permeability tests, during which steady-state was reached in the outflow meters in less than 3 minutes (Fig. 4.16). Only a 2 phase flow model can capture the complexity of an opening WTLog but this will add additional

unknowns like relative permeability curves and capillary pressures to the inversion problem. As we have already seen, only one reservoir parameter can be interpreted from the injection log which makes it impossible to solve this inversion problem.
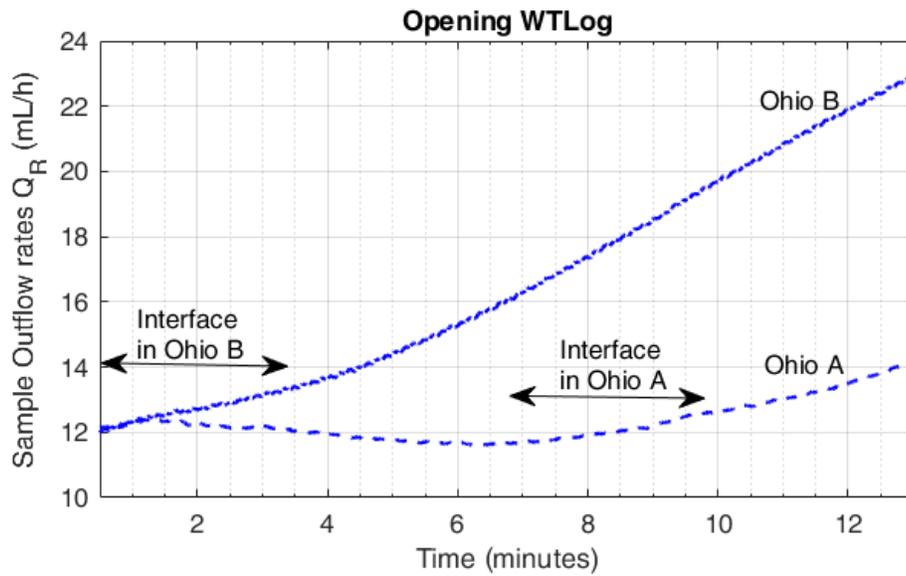
Figure 4.15: Evolution of outflow rates during an opening WTLog test
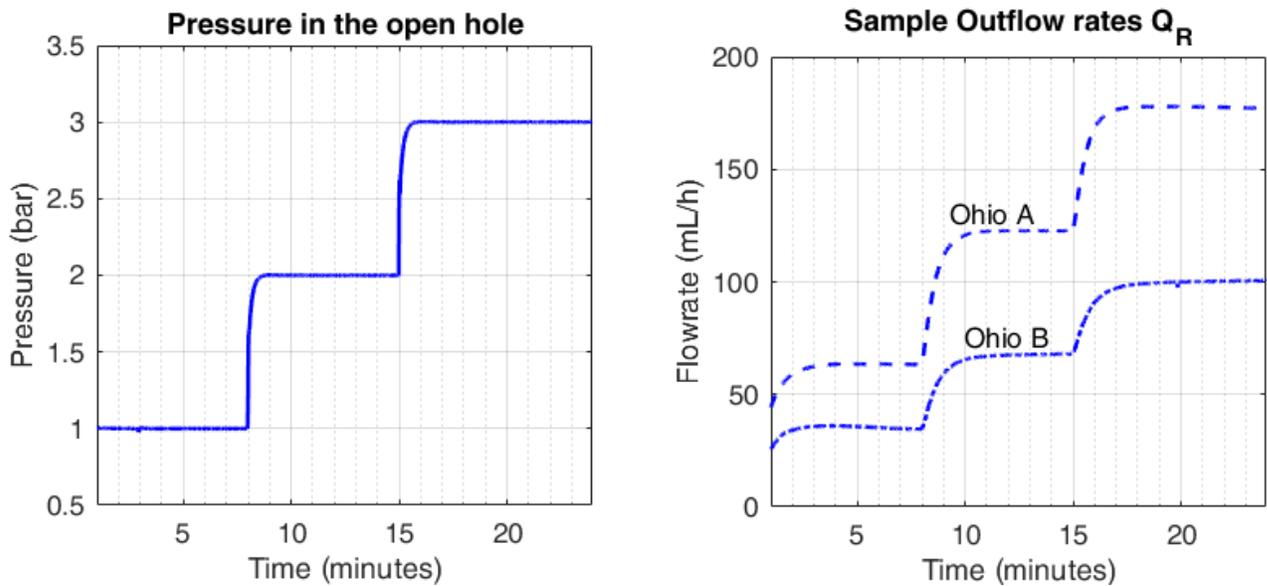
Figure 4.16: Evolution of outflow rates during virgin permeability test

4.5.2   Viscous fingering

An opening WTLog test performed with a water-based polymer solution as the viscous liquid produced some interesting results (Test 1 in Fig. 4.17). A second test was performed under the same conditions to verify that the results were not a one-off event, and they were not. Fig. 4.17 shows the total sample injection rate as a function of interface depth during the two tests. In Ohio B and
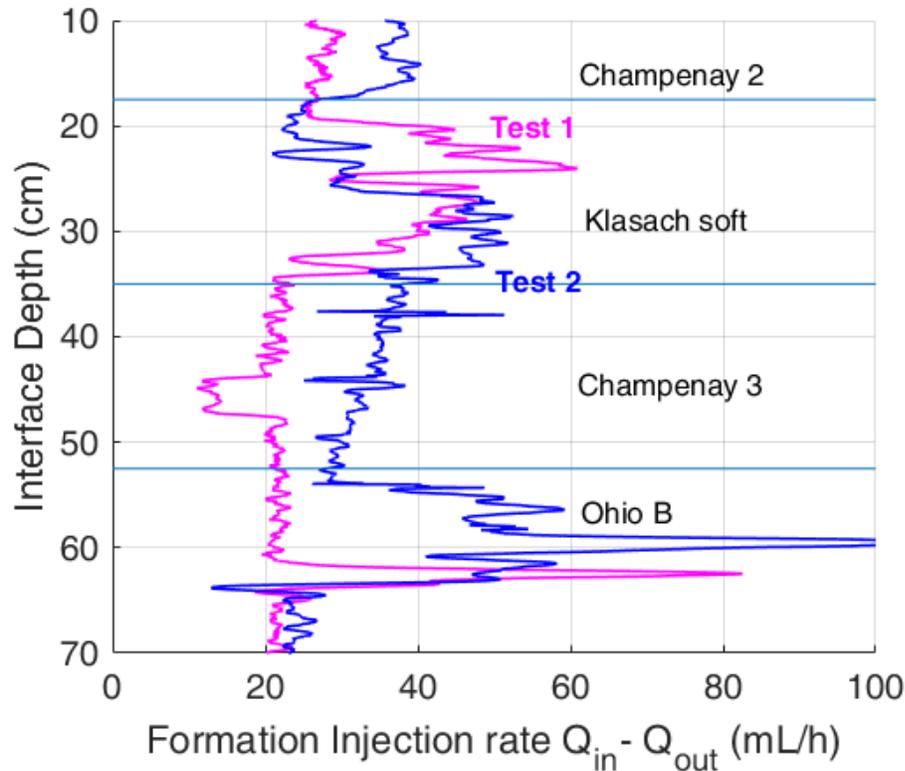
Figure 4.17: Measured total injection rate $(Q_2 - Q_1)$ during two opening WTLog tests with a water based polymer solution. $\triangle P = 0.1$ MPa (1 bar); $Q_1 = 400$ mL/h

Clasach soft layers, there is a sharp increase in $Q_{in} - Q_{out}$ and a subsequent reduction to the initial value, shaped like a 'shark-tooth'. The magnitudes of these shark-teeth are larger in Ohio B than in the more permeable Clasach, which is counter-intuitive. Also, the shark-teeth in tests 1 and 2 do not coincide perfectly in spite of the pressure and the interface velocity being the same for the two tests. This could be due to the difference in the invasion radius of the viscous liquid between the two tests. Neither the monophasic model nor the two-phasic model can explain this phenomenon.

Our hypothesis is that the shark-teeth could be due to Saffman-Taylor instabilities. When the injected fluid mobility $(k/\mu)_1$ is larger than the displaced fluid mobility $(k/\mu)_2$, Saffman-Taylor instabilities — called 'viscous-fingering' in the oil industry — can occur. To the best of our knowledge, all experiments on this subject have been performed under constant rate injection in artificially manufactured samples or Hele-Shaw cells. In the next few paragraphs, we briefly discuss the nature of this instability and future numerical studies that can be performed to verify our hypothesis.

Saffman and Taylor (1958) and Chuoke et al. (1959) were the first to explain this phenomenon using linear stability analysis of one-dimensional fluid displacement. Saffman and Taylor (1958) also presented experimental results performed with Hele-Shaw cells and constant rate injection, which became the standard experimental setup to study this phenomenon. A detailed review of the experimental and theoretical works on viscous fingering can be found in Homsy (1987). In the same article, the following simple argument is made to explain this instability.

Darcy's law for one-dimensional flow with negligible gravity is given by Eq. 4.19. The fluid

pressures in the invading and the displaced fluids are p_1 and p_2, respectively. Considering a sharp fluid interface in the porous media which results in a sharp mobility change, the pressure acting on the displaced fluid $(p_2 - p_1)$ when the interface is displaced by δx is given by Eq. 4.20. If $(k/\mu)_1 > (k/\mu)_2$, a small interface displacement will induce additional pressure on the displaced fluid, amplifying the displacement and resulting in an instability.

$$\frac{dp_i}{dx} = -\frac{U}{(k/\mu)_i} \tag{4.19}$$

$$p_2 - p_1 = -\frac{U}{(\frac{k}{\mu})_2 - (\frac{k}{\mu})_1} \tag{4.20}$$

The propagation of viscous fingers depends on whether the two fluids are immiscible, miscible, or miscible & non-Newtonian (Homsy, 1987). This might explain the presence of shark-teeth in tests performed with polymer solution (miscible in water & non-Newtonian) as the viscous fluid and the absence of shark-teeth when canola (immiscible with injected water) was used.

Several authors have studied the difference in the propagation of viscous fingers in homogeneous and heterogeneous porous media. Araktingi and Orr Jr (1993) developed a particle tracking model to simulate viscous fingering in heterogeneous porous media (for miscible, Newtonian fluids). Brock and Orr Jr (1991) performed laboratory tests in heterogeneous porous media manufactured using compressed glass beads of different diameters. Miscible, Newtonian fluids were used in these tests and the flow patterns were compared to the simulations from the particle tracking model. The following conclusions were drawn from their study:
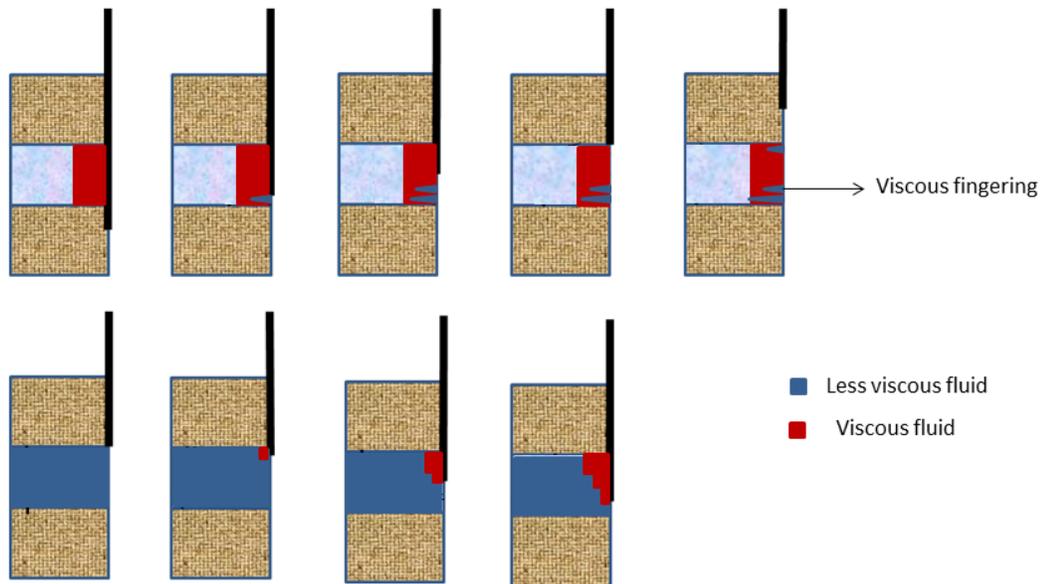
Figure 4.18: Opening WTLog vs Closing WTLog

- In homogeneous porous media, the viscous fingers propagate by splitting and shielding. As the viscous fingers overtake the ones nearby, they prevent these neighbors from growing further. Hence, the number of viscous fingers decrease as the flow progresses.

- In heterogeneous porous media, the flow propagation occurs mainly through viscous fingers in the high permeability zone.

The experiments of Brock and Orr Jr (1991) were performed under constant rate injection during which the entire sample was exposed to injection at the same time. This is slightly different from the boundary conditions during an opening WTLog test. The particle tracking model could be a good starting point to simulate opening WTLog tests in heterogeneous samples and verify the existence of shark-teeth.

Closing WTLog tests do not exhibit viscous fingers. In closing WTLog, we start with a well-established flow of the less-viscous liquid. When the samples are exposed to the viscous liquid, the mobility ratios are unfavorable for viscous fingering (Fig. 4.18). This is confirmed by Fig. 4.19 which shows $Q_{in} - Q_{out}$ from a closing WTLog test with the same set of samples and liquids as the opening WTLog tests in Fig. 4.17 which exhibited shark-teeth. Also, the viscous liquid loss in Fig. 4.19 is quite small compared to the viscous liquid loss when colza oil is used (Fig. 4.12, left) in spite of Clasach soft being several times more permeable than Clasach hard. This supports one of the hypotheses made in chapter 2 — the viscous liquid loss is negligible during in-situ tests with viscous muds.
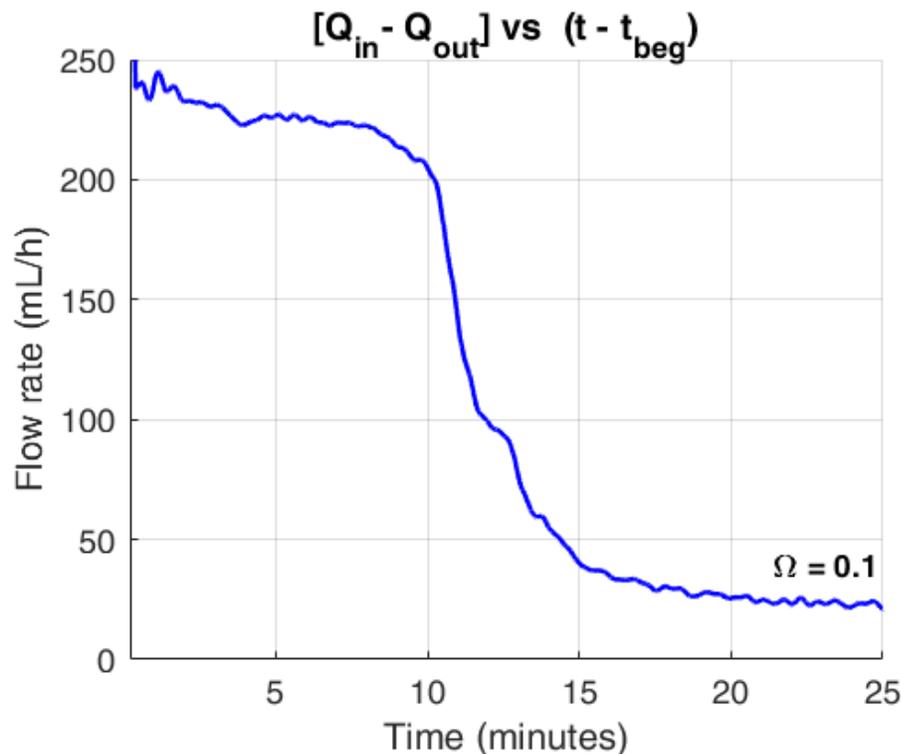
Figure 4.19: Measured injection rate from a closing WTLog test performed with Clasach soft ($k > 1$ D) and water-based viscous mud. No shark-teeth can be seen.

4.6   A chronological summary of laboratory tests

Date	Most permeable sample	Test type	Viscous liquid	Comments
02/03/16	Ohio A & B	Benchmark permeability	None	Results in Fig. 4.4. k (Ohio A) = 0.65 10^{-15} m^2 or 0.65 mD k (Ohio B) = 0.27 10^{-15} m^2 or 0.27 mD
17/03/16	Ohio A & B	Closing (1st ever)	Colza oil ($\mu_+ \sim 5.5$ 10^{-2} Pa.s)	Figs. 4.10 and 4.11.
17/03/16	Ohio A & B	Opening	Colza oil	$Q_{in} - Q_{out}$ continued to increase even when the interface was in the less-permeable samples. Outflow rates in the samples also continued to increase (Fig. 4.15).
29/03/16	Clasach hard	Benchmark permeability	None	k (Clasach hard) = 1.31 10^{-15} m^2 or 1.31 mD It was also observed that the outflow rates in Ohio samples had reduced substantially due to the damage caused during the previous tests
30/03/16	Clasach hard	Closing	Colza oil	Results in Figs. 4.12 and 4.13. A large viscous liquid loss at the end of the test.
30/03/16	Clasach hard	2 opening tests	Colza oil	Flow behavior was similar to the opening tests on 17/03 with Ohio samples. A large viscous liquid loss at the beginning of the test and a small increase in $Q_{in} - Q_{out}$ during the test

28/04/16, 29/04/16, 12/05/16	Clasach hard	3 opening tests	Castor oil ($\mu_+ = 0.65$ Pa.s)	Castor oil is 10 times more viscous than colza oil and it was hoped that this would limit the viscous liquid loss at the beginning of opening WTLog and create monophasic flow conditions for the less-viscous liquid. But this was not the case and the results were similar to the previous tests.
17/05/16- 19/05/16	Clasach soft ($k \sim 10^{-12}$ m^2 or 1 D)	Both opening and closing	Castor oil	Attempts were made to add a transparent glass tube parallel and connected to the central hole. The idea was to have a visually observable replication of the interface in the central hole. However, the interface locations in the two spaces were quite different, probably due to the difference in frictional losses.
30/05/16	Clasach soft	Closing	Water-based viscous mud (Non-newtonian liquid)	Results in Fig. 4.19. The viscous liquid loss was at its lowest in spite of very large permeabilities. This is a promising result for minimizing viscous liquid loss during in-situ tests.
31/05/16	Clasach soft	2 opening tests	Water-based viscous mud	Fig. 4.17. 'Shark-teeth' were seen during both tests.
01/06/16	Clasach soft	Both opening and closing	Water-based viscous mud	Tests were not successful. The interface between the less-viscous liquid (tap-water) and the viscous mud was no longer distinct. The two liquids had mixed due to their prolonged contact.

Table. 4.2. The first batch of laboratory tests from March 2016 to June 2016

After these first batch of tests, it was evident that opening WTLog cannot be accurately in-

terpreted using a monophasic flow model. However, closing WTLog tests yielded very promising results with flow behavior similar to a monophasic flow. An interpretation workflow was developed for the closing WTLog tests during the second year of the thesis. For reasons described earlier, it was not possible to avoid the uniform skin assumption and a second batch of tests was planned in November 2017 to test this assumption. The test results are discussed in section 4.2.2 (Figs. 4.6 to 4.9). A very good agreement between the estimated and the benchmark permeability logs can be seen in Fig. 4.9.

4.7 Summary

The experimental setup discussed in this chapter is a multilayered commingled system without formation cross-flow that can house upto six samples. It was built long before the thesis and several openeing WTLog tests were performed (discussed in chapter 7 in the Annex). Additional opening WTLog tests were performed during the thesis and it was observed that the flow beavior during these tests is not monophasic and their interpretation is challenging. Also, instabilities similar to viscous-fingering were observed when the drilling mud was used as the viscous liquid.

Several closing WTLog results are discussed in this chapter; it is evident that the flow behavior during these tests is monophasic and a simple interpretation work flow estimates an accurate permeability log. A sequence of 4 closing WTLog tests were performed on the same set of samples; drilling mud was circulated in the central hole before these tests to create a mud cake similar to that of the in-situ case; also there were viscous fluid losses in to the samples during these tests. The near-wellbore skin during these tests had two components: a constant skin due to mudcake and an additional skin which increased with each test due to the viscous fluid loss. A continuous injection log and a permeability log are derived. Permeability logs are averaged at the sample scale and compare to the benchmark permeability log; correlations are greater than 0.94. This shows that the effect of local skin variations on the permeability estimate is negligible in an open hole containing several orders of permeability.

During the closing WTLog tests discussed above, $\triangle P$ was same in all samples. Closing WTLog tests during which $\triangle P$ is different in each sample were also performed during the thesis. The permeability logs derived from these tests again showed very high correlation to the benchmark permeability logs.

Chapter 5

Conclusion

Permeabilities derived from Nuclear Magnetic Resonance (NMR) or acoustic logs are not as accurate as the flow-based pressure transient methods. Nevertheless, they are widely adopted because they offer the only means to derive a continuous permeability log. These permeability logs typically show significant variations from the core (or formation tester) permeability at the same depth; acceptable correlations can be obtained when the permeability logs for the entire open hole are compared. Also, the interpretation workflows often rely on empirical relations that are formation dependent.

The injection-based logging technique developed during this thesis is not formation dependent. It is also cost-effective: all measurements are made at the surface; the equipment used during the test are typically available at the well site at the end of drilling. The closing method proposed during the thesis eliminates some of the challenges that existed with the opening method: the flow duing closing method is monophasic; skin can be estimated from the transient decay of formation injection rate; investigation radius is beyond the damaged near-wellbore zone. The test consits of two phases: phase 1 during which the well is filled only with a less-viscous liquid; phase 2 during which a viscous liquid is injected into the tubing which eventually rises up in the annulus. Wellhead pressure in the annulus and the injection rate into the tubing are maintained constant during the test.

Phase 1 is designed to be slightly long ($Kt/r_w^2 > 200$) which offers several advantages: total kh (permeability-thickness) of the open hole and global skin $\langle S \rangle$ can be estimated through reciprocal-rate derivative analysis; the investigation zone moves beyond the near-wellbore damaged zone; analytical expressions can be used to interpret data from phase 2; also, transient decay during phse 2 becomes negligible. Interpretation of phase 2 begins with the derivation of a continuous injection log using a wellbore circulation model, which is basically a mass balance equation for the two liquids in the wellbore. A continuous permeability log is derived from the injection log using a large-time asymptotic solution, considering an uniform skin and known formation pressures. Analytical expressions in chapter 2 quantify the uncertainties in the permeability estimates due to local skin variations or uncertainties in the formation pressure data. They show that the local skin variations can induce proportional errors in the permeability estimates but these errors are negligible in an open hole containing several orders of permeability.

This is confirmed by the laboratory test results discussed in chapter 4. Multiple tests were performed on the same set of samples at different pressure heads, circulation rates and increasing skin

89

values. Estimated permeability logs were averaged at the sample scale and compared to benchmark permeability logs. Although there were small local variations in permeabilities, the correlations between the estimated and benchmark logs were greater than 0.94 (on a scale of 0 to 1). Also, these local variations are smaller than what is generally observed in NMR log estimates. Earlier in the chapter, injection logs were compared at a fine scale of 2 cm ($1/50^{th}$ of the central hole) and the correlations were found to be greater than 0.8.

In chapter 3, it is shown that the reciprocal-rate derivative plot is very similar to the pressure derivative plot and can be used to identify radial heterogeneities. Using reciprocal-rate derivative analysis, total kh and skin are estimated when the sandface pressures are step-wise constant. A two-phase constant pressure injection model (numerical) has also been discussed. The reciprocal-rate derivative plot for two-phase flow shows two stabilizations: an early-time stabilization (derivative curve parallel to the x-axis) corresponding to the formation fluid mobility and a late-time stabilization representative of the injected fluid mobility. Similar results have been obtained by other authors for the pressure derivative plot during constant rate injection.

Part II

Annexes

Chapter 6

In-situ test in a salt formation

During the course of 2017 and 2018, we were actively looking for newly drilled wells to test the closing WTLog method. Initially, we thought of performing one such test in the geothermal wells that were being drilled at the Saclay plateau, but the information on their drilling reached us a little late; the drilling plan was already established and it was not possible to include in it, the closing WTLog test.

Another opportunity presented itself at the end of 2017, when Jean Barottin from Inovyn, to whom we are very grateful, informed us that a borehole, drilled into a salt formation and equipped with a central tube, could be available for a few months at the Marboz site in the Ain department of France. It was expected that the formation would be very low permeable ($k \approx 10^{-21}$ to 10^{-20} m^2) with extremely small variations in formation injection rates a permeability test; these conditions were not conducive for a closing WTLog test with a continuous displacement of the interface between the liquids in the wellbore. Hence, we planned a 'discrete' WTLog test, during which the interface between the viscous (diesel) and the less-viscous (brine) liquids – instead of scanning the open hole continuously – would be placed at three different depths in the open hole, with the hope of estimating the permeability contrasts between these zones. This testing methodology could also provide a new tool to evaluate permeability contrasts in salt formations which are known to contain fairly large, more permeable sub-layers (salt layer in Jintang, China, for example).

The method was tested between February and May 2018. The permeability difference between the entire wellbore (which also includes the leaks through cemented casing and casing shoe) and the open hole was estimated successfully; the average permeability of the open hole was extremely small ($k \approx 4\ 10^{-21}$ m^2); as feared, it was not possible to evaluate the permeability contrasts in the open hole. Nevertheless, the test result was useful for Inovyn, the operator of the wellbore, in showing that the well permeability and in turn the leak rates are extremely small.

The rest of the chapter is a reproduction of an article published in the proceedings of the SMRI fall meeting 2018 at Belfast, Ireland. This article, titled "In-situ permeability test in a salt formation at Marboz, France" was co-authored by J. Barottin, P. Bérest, B. Brouard, V. De Greef and A. Jacques.

6.1 Introduction

INOVYN operates a brine field at Marboz in the département of Ain, France. In the same Bresse salt formation, about 10 km (6 miles) from this brine field, twenty gas-storage caverns are operated by the utility company Storengy. The salt formation includes two thick layers separated by a "sterile" intermediate layer whose insoluble content is high. At Étrez, the lower salt layer (having top and bottom with depths of 1340-m (4396 ft) and 1970-m (6463 ft) deep, typically) contains fewer impurities (Curial, 1986) and is considered generally to be less permeable than the upper layer.

In 2017, a borehole (AT032) was drilled at Marboz. It remained available for testing for a couple of months before solution mining began. It was decided to perform a multi-step test to assess the permeability of the salt formation. Brouard et al. (2001) had reviewed a dozen of Mechanical Integrity Tests performed at Étrez. During these tests, a packer was set a few meters above the casing shoe (to isolate any leak through the casing), and water was injected into the tubing twice a day to maintain a constant testing gradient. The average permeability of the "lower salt layer + casing shoe" estimated from these tests was in the $4.6 - 19 \times 10^{-21}\,\mathrm{m}^2$ range.
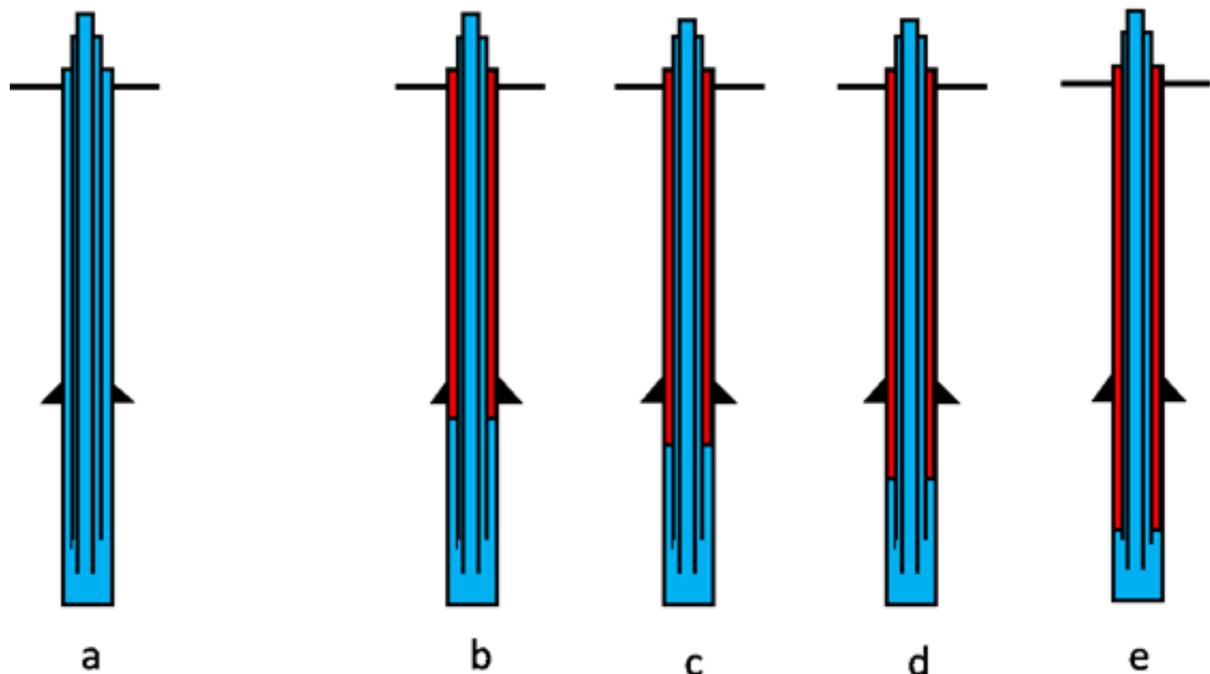
Figure 6.1: Brine permeability test (a) and "MIT" test (b), an attempt to test formation permeability as a function of depth (b, c, d)

The test at Marboz was two-fold (see Fig. 6.1). During the first phase (Fig. 6.1a), the wellbore was filled with brine, and wellhead pressure was increased to 1.8 MPa (18 bars) and 3.7 MPa (37 bars), successively. After each pressure increase, wellhead pressure evolution was measured over 19 days and 28 days, respectively. The average permeability of the well was estimated from these pressure evolution; it includes brine seepage through the open-hole walls, and leaks through the casing shoe and the steel casing.

The second phase was an attempt to measure the permeability of the open hole as a function of depth: diesel was injected in the annular space to develop a brine-diesel interface at various depths. (Rock salt is considered to be almost impermeable to diesel, due to capillary pressure and the low relative permeability of brine-saturated salt.) At the beginning of the second phase, the interface was lowered a few meters below the casing shoe (Fig. 6.1b), and wellhead pressure was maintained constant through brine injection into the central string. Permeability of the open hole alone was estimated from the wellhead injection rates. Then, the interface was lowered to three greater depths (Figs. 6.1c, 1d, 1e), and injection rates were measured in an attempt to differentiate between the permeabilities of various parts of the open hole. However, this permeability was so small that the designed method was not accurate enough to differentiate the permeability variations (if any) in the open hole. This method, whose objective is to assess permeability as a function of depth in a borehole, is called "discrete WTLog" (Manivannan et al., 2017).

6.2 Well geometry

The well is 1698-m (5571 ft) deep and 1747-m (5732 ft) long, with a deviated section in the lower part of the cemented well (Fig. 6.2). The diameter of the last cemented casing is $11^{3/4}$". The open hole has a vertical section 352 m (1155 ft) long and runs entirely through the lower salt layer. Two strings, with diameters $5^{1/2}$" and $8^{5/8}$", respectively, were run in the wellbore, creating three different spaces in the upper part of the well: a central string, an intermediate annulus, and an external annulus. The casing shoe is set at 1346 m (4416 ft) true vertical depth (TVD). Lengths — i.e., measured depth (MD) — and internal volumes of these three spaces are given in Table. 6.1.

The overall volume of the open hole, as measured by caliper log, is 51.72 m^3, (1826 ft^3) which is 2.2 m^3 (78 ft^3) larger than the volume computed using nominal cross-sectional areas. It is highly likely that the cross-section of the open hole is not uniform. The computed volume of the liquid contained in the $8^{5/8}$" x $11^{3/4}$" external annulus, above the casing shoe, is 29.42 m^3 (1039 ft^3).

6.3 Rock and liquid properties

The temperature measured at 1698 m (TVD) is 65 °C. The overburden pressure gradient is approximately $\gamma_R = 0.022$ MPa/m (0.22 bar/m). Fig. 6.3 shows the density and the viscosity of the liquids used in the test as a function of temperature. The hydro-static pressure gradient of the brine column, computed using the brine density at 20 °C, is $\gamma_b = 0.0166$ MPa/m (0.116 bar/m).
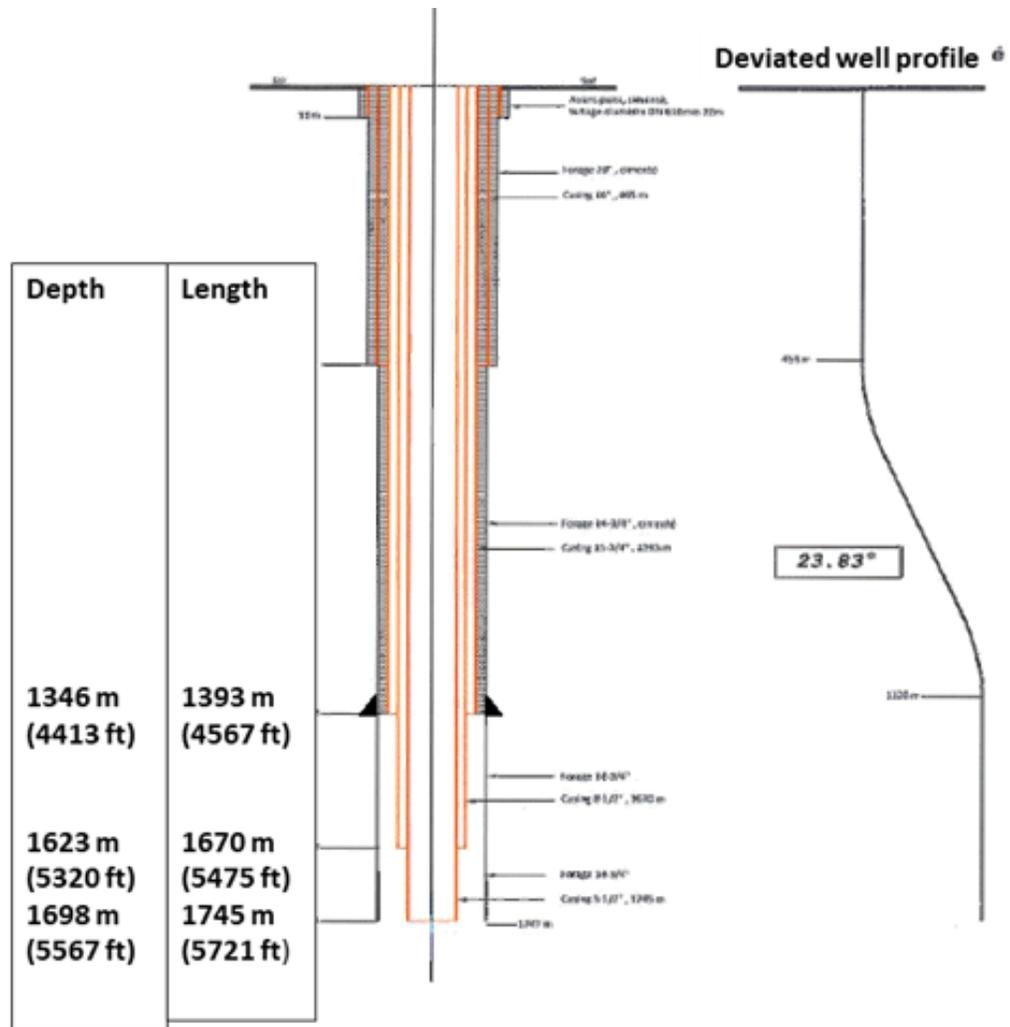
Figure 6.2: Schematic of the well.
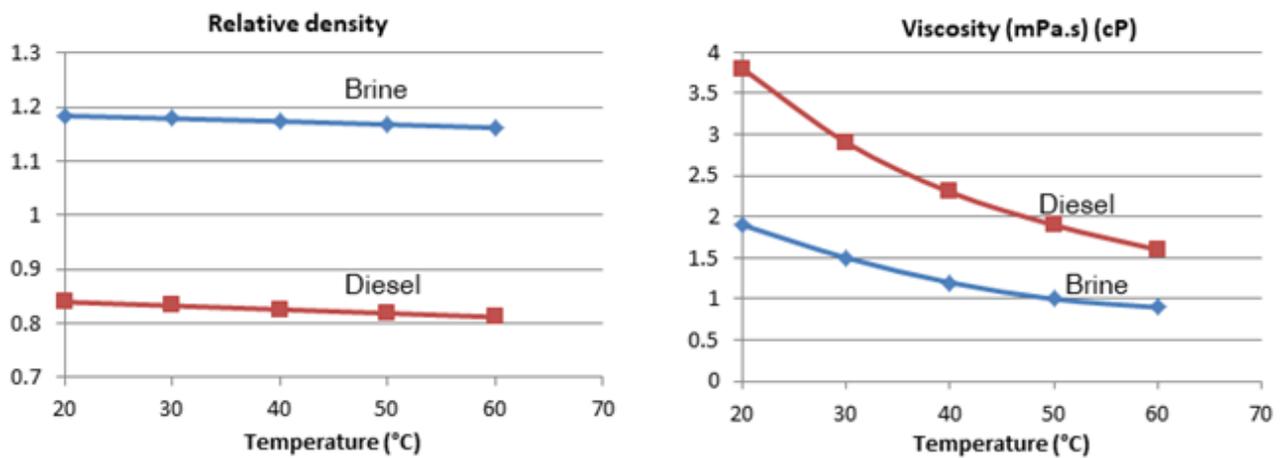
Figure 6.3: Relative density and viscosity of the brine and the diesel used during the test.

	Length m (MD)	External diameter (mm)	Internal diameter (mm)	Cross-sectional area (L/m)
$5^{1/2}$"	1745	139.70	121.30	11.56
$8^{5/8}$"	1670	219.08	201.28	16.49 ($5^{1/2}$" x $8^{5/8}$")
$11^{3/4}$"	1393	298.45	273.65	21.12 ($8^{5/8}$" x $11^{3/4}$")
Open hole	1747-1393	374.65		72.55* ($8^{5/8}$" x $14^{3/4}$") 94.91* ($5^{1/2}$" x $14^{3/4}$")

Table 6.1: AT032 cross-sections (*nominal value — the as-measured value is slightly larger).

6.4 Test procedure and equipment
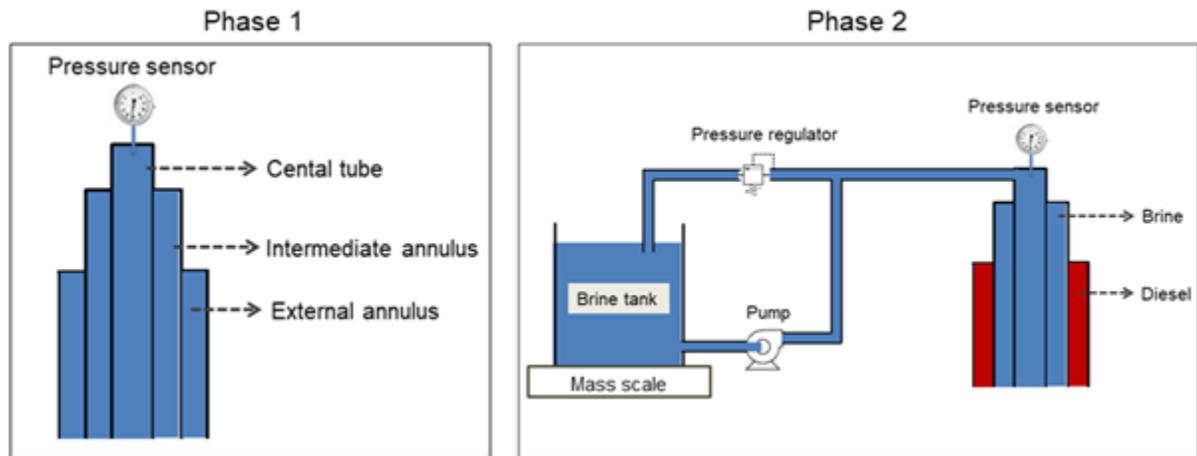
Figure 6.4: Wellhead schematic design: (left) during Phase 1, when the well is shut-in; and (right) during phase 2, pressure regulation system injects brine into the tubing to maintain constant wellhead pressure.

6.4.1 Phase 1

On February 14, 2018, the wellhead-tubing pressure was increased from 0 to 1.8 MPa (0 to 18 bars) by injecting brine in the central tubing. By dividing the injected brine volume, δV, by the wellhead pressure change, δP, well compressibility was estimated to be $\delta V/\delta P = \beta V = $ (38 L/MPa) 3.8 L/bar. The well was kept closed, and the pressure evolution was recorded by a pressure sensor at the central tubing wellhead over 19 days, from February 14 to March 5 (Fig. 6.4, left). The well

Date	Wellhead pressure	Duration (days)	Comments
February 14, 2018	1.8 MPa (18 bars)	19	First pressure step of Phase 1
March 5, 2018	0 MPa	7	Work-over
March 12, 2018	3.7 MPa (37 bars)	28	Second pressure step of Phase 1

Table 6.2: Test schedule during Phase 1 (effecting a change in wellhead pressure).

was depressurized for a work-over that lasted one week. On March 12, the well was re-pressurized to 3.7 MPa (37 bar) , and evolution of the tubing wellhead pressure was measured for 28 days (until April 10).

6.4.2 Phase 2

On April 11-12, 30 m^3 (190 bbls) of diesel were injected (over 2 days) in the external annulus, and a similar volume of brine was removed from the central tubing. This placed the brine-diesel interface just below the casing shoe. At the end of this injection, wellhead pressure was 3.9 MPa (39 bars) at 3 pm on April 12. A pressure regulation system was added to maintain constant pressure at the tubing wellhead. A schematic of the pressure regulation system is shown in Fig. 6.4 (right). When the wellhead pressure is less than the desired value, the choke in the pressure regulator remains closed. When the pressure is higher, the choke opens, brine is withdrawn from the tubing, and the prescribed pressure is re-established. A scale measures the mass of the brine contained in the storage tank with an accuracy of 0.05 kg. As before, the tubing wellhead pressure was measured by a pressure sensor. Note that after the April 11-12 injection, the pressure drop was so swift that it could not be accommodated fully by the regulation system, whose maximum injection rate is 14 L/day (3.5 gallon/day). It took nearly 6 days for the pressure to be reestablished at about 4.3 MPa (43 bars).

After April 30, the brine-diesel interface was lowered to greater depths through additional diesel injections, and the test was repeated. These tests were shorter than the earlier ones, lasting 4-10 days each (Table 6.3); their objective was to estimate possible heterogeneities in the permeability of the open hole.

Fig. 6.5 shows the tubing wellhead pressure recorded daily at 18h00 (6 pm) during the entire test. The wellhead brine-injection rate (in the tubing) during Phase 2 is shown in Fig. 6.6. The brine injection rates are computed by dividing the daily change in the mass of the tank brine by brine density (1184 kg/m3).

Date	Diesel volume injected (m^3)	Interface location	Test duration (days)
April 11-12	30	Just below the casing shoe	17
April 20	6.7	$1/3^{rd}$ of the tested length	9
May 9	6.77	$2/3^{rd}$ of the tested length	5
May 14	6.7	Bottom of the $8^{5/8}$" tube	4

Table 6.3: Test schedule during Phase 2 (diesel injections). [The tested length from 1393 m (4567 ft) to 1670 m (5470 ft).]
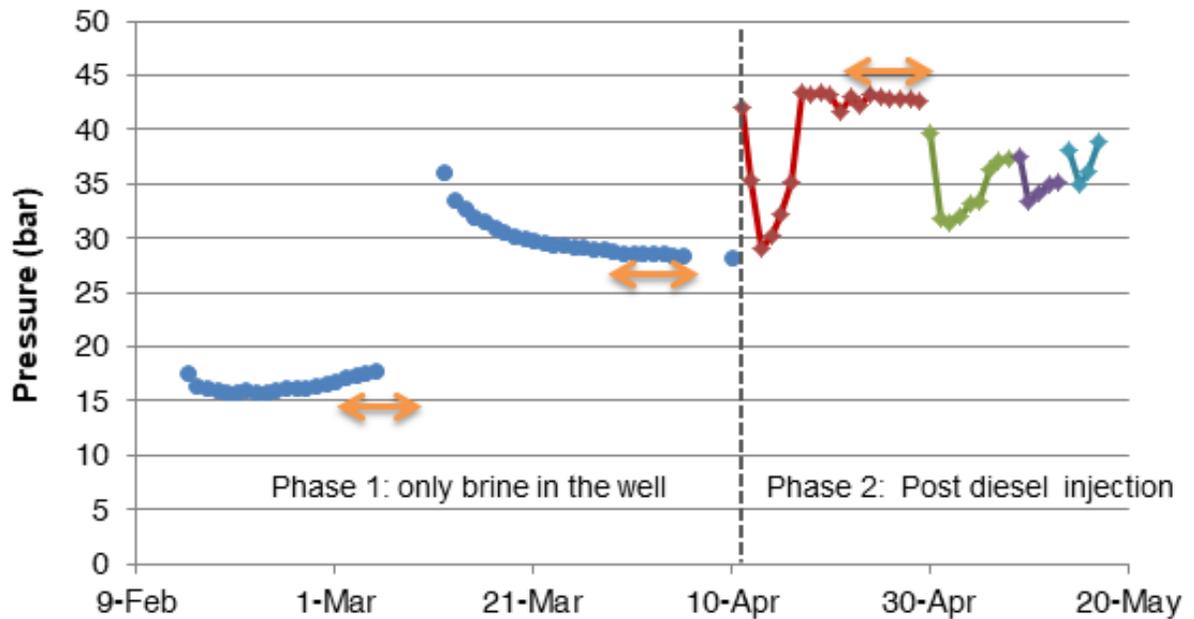
Figure 6.5: Tubing wellhead pressure (measured daily at 6 pm) during the duration of the entire test.
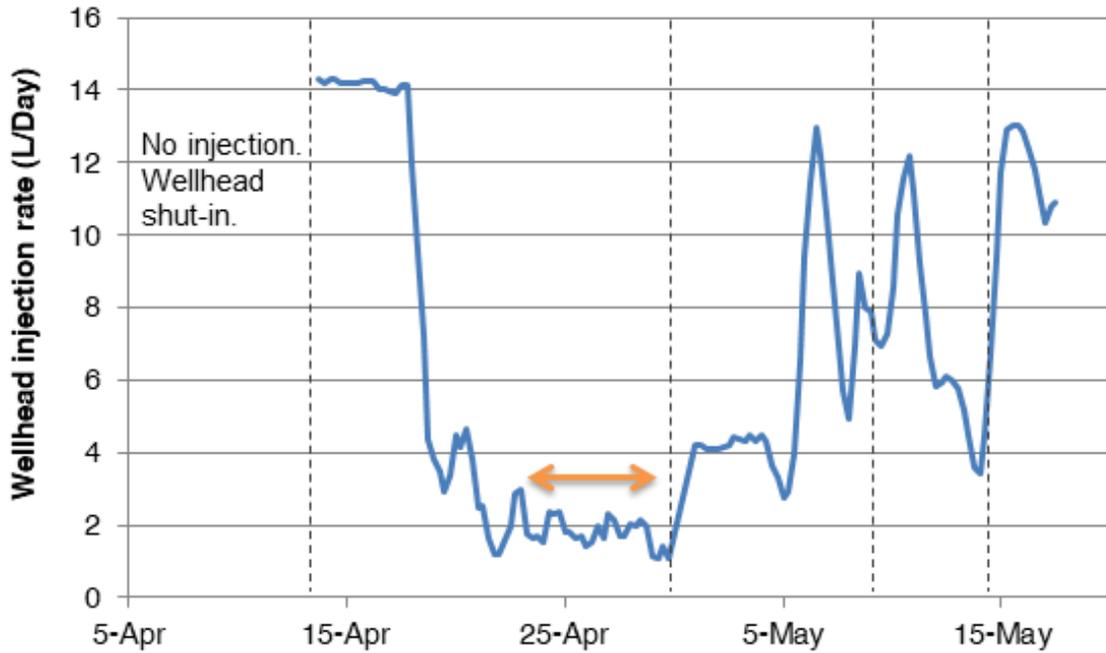
Figure 6.6: Wellhead brine-injection rate during Phase 2.

6.5   Physical phenomena

After a swift liquid injection (or withdrawal), pressure evolution in a shut-in wellbore is governed by several effects, including temperature changes, additional salt dissolution, creep closure and brine permeation through the cavern walls.

Thermal effects and additional dissolution are early time effects; they are effective mostly during a short period (1 - 4 days) after a thermal or chemical disequilibrium is created. Creep closure and brine permeation are much slower processes.

5.1. Thermal effects occur when the wellbore liquid temperature is different from the geothermal temperature of the rock mass. Liquids warming or cooling in the wellbore leads to changes in liquid volumes and densities, resulting in pressure changes in a shut-in well (Skaug et al., 2011; Lampe and Ratigan, 2014; Manivannan et al., 2015).

Consider first the effects of daily (night/day) temperature changes at ground level. In the upper part of the wellbore, at shallow depths (typically, less than a dozen meters), liquid temperature is the sum of average temperature and daily fluctuations, $T(r, t) = T_{av}(z) + \theta(z, t)$. These fluctuations can be integrated with respect to depth along the wellbore. (For simplicity, no string is taken into account):

$$I(t) = \int_0^H \theta(z, t) \, dz$$

where H is the borehole depth (From a practical perspective, daily fluctuations are exceedingly small when $z > 10$ m, see Brouard et al. (2013).)

These temperature changes lead to a liquid volume change by $\alpha S I(t)$, where S is the wellbore cross-sectional area ($S = 60$ L/m is typical.); $I(t)$ as defined above; α is the liquid thermal expansion
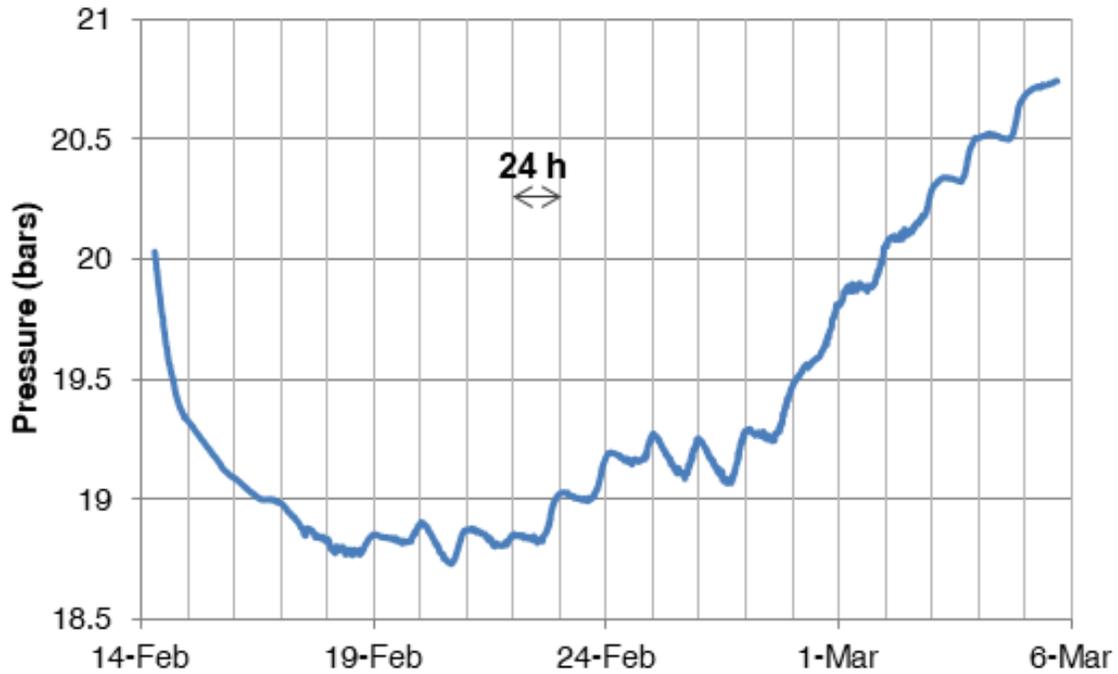
Figure 6.7: Tubing wellhead pressure during Phase 1. The small fluctuations in wellhead pressure (with a time period of 24 hours) is due to daily fluctuations in ambient temperature.

coefficient (For brine, $\alpha = 4.4\ 10^{-4}/°$C; for diesel, $\alpha = 10^{-3}/°$C are typical.), and to a cavern pressure change by $\alpha SI(t)/\beta V$, where βV is the compressibility of the wellbore. (At Marboz, $\beta V = 38$ L/MPa (3.8 L/bar) when the wellbore is filled with brine.) In addition, as the liquid density in the wellbore changes, the difference between wellbore average pressure and wellhead pressure increases by $\rho g \alpha I(t)$. The overall wellhead pressure change is

$$(S/\beta V + \rho g)\, \alpha I(t)$$

The value $S/\beta V = 1.5\ 10^6$ Pa/m is much larger than $\rho g = 1.2\ 10^4$ Pa/m (The opposite is true in a full-size cavern.), and the pressure change is $S\alpha/\beta V = 660$ Pa/°C-m. The maximum possible value of $I(t)$ must be computed (or measured) on a case-by-case basis. During the initial days of Phase 1, the daily fluctuations in ambient temperature were quite small due to the winter weather. Assuming that the temperature fluctuations in the wellbore are uniform ($\simeq 3$ °C) and limited to 10 m below the wellhead, the amplitude of $I(t)$ can be given as 30 °C-m. This translates into daily pressure fluctuations of 0.02 MPa (0.2 bars), not far from the magnitude of the fluctuations observed in Fig. 6.7. During Phase 2, the wellbore contains diesel oil, which has a relatively large thermal expansion coefficient; also, $I(t)$ can be as large as several dozens of °C-m due to larger temperatures fluctuations in the spring.

Consider, now, the effects of cold diesel injection during Phase 2. On April 11-12, 30 m^3 of cold diesel were injected in the external annulus; the brine contained in the central string (20 m^3) was withdrawn together with 10 m^3 of hot brine (65 °C) contained in the lower part of the borehole. As a result, the central string was filled with hot brine. Straightforward computations proved that, as

a whole, wellbore liquids cooled after injection was completed, leading to a large pressure drop from April 11 to 13 (Fig. 6.5). Such an effect did not exist during Phase 1, as no brine was withdrawn from the central tubing.

5.2. Additional dissolution/re-crystallization of salt occurs because the concentration of brine at saturation is an increasing function of pressure (and temperature). When brine pressure increases, additional dissolution takes place, leaving more space for brine and reducing the magnitude of the original pressure change. This process ends after the brine is saturated in the new pressure conditions (Bérest et al., 2007).

When these two transient effects vanish, long-term creep closure and permeation can be observed.

5.3. Long-term creep closure of the open hole occurs due to the visco-plastic behavior of salt. Wellbore pressure in the open hole typically is smaller than the overburden pressure, leading to creep closure and a gradual reduction in the open-hole volume. When the wellhead is closed, the reduction in the open-hole volume manifests itself as pressure increase. The long-term creep closure rate decreases when wellhead pressure increases.

5.4. Permeation of the wellbore fluid into the salt/rock formation. Pore pressure in the salt formation is difficult to assess. In the Bresse salt formation, Durup (1994) proved that it was close to halmostatic pressure ($P_h = \gamma_b z$) and that permeation obeys Darcy law. When the well is filled with brine with pressure higher than halmostatic, brine permeation occurs, liquid mass in the wellbore decreases, and brine pressure drops.

These two last phenomena have opposite effects: (1) creep closure rate decreases when brine pressure increases and vanishes when brine pressure is geostatic ($P_\infty = \gamma_R z$); and (2) permeation rate vanishes when brine pressure is halmostatic ($P_h = \gamma_b z$) and increases when brine pressure increases. In principle, brine pressure remains constant when the creep-closure rate exactly equals the permeation rate.

6.6 Results

In the figure below (Fig. 6.5, repeated here for convenience), after the wellbore pressure was increased to 1.8 MPa (18 bars) on February 14, a transient pressure decrease was observed. After 3 - 4 days, wellhead pressure stabilized, then increased, suggesting that when wellhead pressure is 1.8 MPa (18 bars) or less, the brine-permeation rate is smaller than the creep-closure rate. After 19 days (since the beginning of the test), the well was kept open for one week. On March 12, the wellhead pressure was increased to 3.7 MPa (37 bars). The transient pressure decrease was steeper than when the initial pressure increase was 1.8 MPa (18 bars); the pressure kept decreasing, suggesting that, when wellhead pressure is larger than 3.7 MPa (37 bars), the permeation rate is faster than creep closure rate. The wellhead pressure at the end of Phase 1 was (2.83 MPa) 28.3 bars. It is likely that an equilibrium wellhead pressure should be reached, somewhere between (2 MPa) 20 bars and 2.83 MPa 28.3 bars, such that permeation equals creep rate and the wellhead pressure remains constant. However, the test duration is too short to draw definite conclusions.
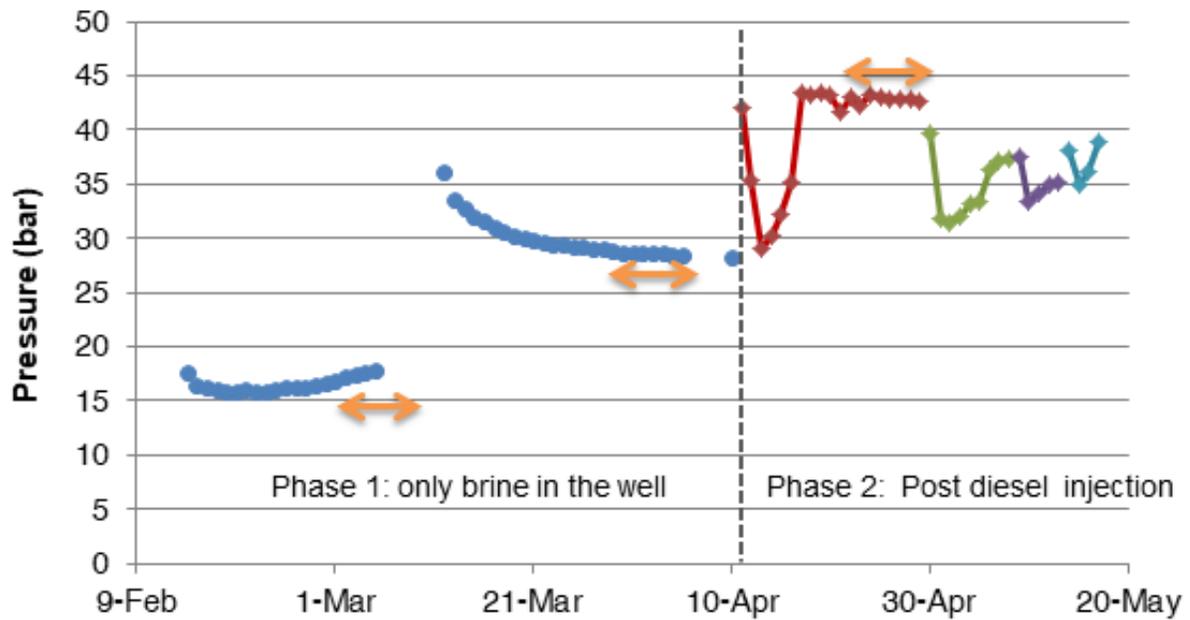
During the initial days of Phase 2, the pump injection rate was at its maximum power (14 L/day, or 4 gallons /day); however, it was not able to restore the initial pressure, as thermal effects were too large. It is only after 5 - 6 days, after these effects vanish, that the regulation system was able to increase the wellhead pressure to 4.3 MPa or 43 bars (Figs. 6.5 and 6.7). The additional salt-dissolution effects persist for another 3 - 4 days. After April 24, the injection rate at wellhead approximately equaled the permeation rate minus the creep-closure rate; it is about 1.8 L/day (half a gallon per day). When the interface was lowered further on April 30, the cycle repeated. However, this time, the pump does not seem to be injecting at its maximum power. Some salt crystallization was observed in the pump at the end of the test. Data after April 30 are not interpretable, as there was no pressure stabilization. (Test duration was too short, due to operational constraints; in addition, open-hole permeability was so small that differentiating the permeabilities of the different parts of the open hole was impossible).

6.7 Interpretation

When pressure changes are small, the short time transients, such as additional dissolution and temperature changes, become negligible after a few days. This is the case during the periods marked on Fig. 6.5 by orange double-headed arrows, which will be used, below, for quantitative interpretation.

6.7.1 Creep closure in the open hole

Creep closure raises a difficult problem. To describe steady-state creep, a Norton Hoff creep law $(d\varepsilon/dt = A^*(T)\sigma^n)$ often is accepted; simple calculations prove that, for a cylindrical hole, the resulting steady-state creep closure rate can be written as

$$dV/dt = C^{ss}_{creep}(T, n)\, \Delta P^n \qquad (6.1)$$

where ΔP is the gap between geostatic pressure and borehole pressure, and $C^{ss}_{creep}(T,n) = \sqrt{3}\,(\sqrt{3}/n)^n/2$. However, numerical computations prove that, in a wellbore, transient creep is much longer (many years) than in the case of a test on a cylindrical sample (several months), because of slow stress redistribution (Manivannan and Bérest, 2018). To allow simple computations, it is accepted that Eq. 6.1 still holds and that exponent n is identical to the exponent that describes the results of tests performed on salt samples. The steady-state creep coefficient, C^{ss}_{creep}, is replaced by a pseudo steady-state coefficient C_{creep}, which remains constant during the relatively brief test duration.

In Eq. 6.1, both ΔP and T are functions of depth. The creep rates in salt vary with temperature. However, from casing shoe to open-hole bottom, the difference between uppermost (at hole bottom) and lowermost (at casing shoe) temperatures is less than 5 °C; hence, a uniform creep coefficient, C_{creep}, is used for the open hole. Influence of the pressure gap, ΔP, is more significant, and the rate of volume change due to creep closure is integrated along the open hole — see Eq. 6.2. The exponent n is 3.1 for Étrez salt (Brouard and Bérest, 1998):

$$\dot{V} = -C_{creep} S_{ann} \int_{H_{cas}}^{H} \left[-P^{wh}_{tub} + (\gamma_R - \gamma_b)\, z \right]^n dz \qquad (6.2)$$

6.7.2 Permeation in the wellbore

The characteristic time for transient permeation in salt can be a few weeks to few months. Hence, transient flow evolution and the pressure history of the wellbore must be taken into account (Eq. 6.3). The relevant parameters are: open-hole height, $h = 352$ m (1154 ft); porosity of the lower salt formation, $\phi = 0.01$ (Durup, 1994); open-hole radius, r_w ; and the total compressibility taken to be $c_t = 6$ x 10^{-4} MPa^{-1} (6 x 10^{-5} bar^{-1}). The possible near-wellbore damage created in the salt layers during drilling is neglected. The non-dimensional flow rate, Q_D, for constant wellbore pressure is computed from the Laplace transformation of unsteady-state Darcy's equation (Van Everdingen and Hurst, 1949), resulting in

$$Q_{perm.} = \frac{2\pi k h}{\mu} \int_0^t \dot{P}^{wh}_{tub}(\tau) q_D \left(\frac{k[t-\tau]}{\mu \phi c_t r_w^2} \right) d\tau \qquad (6.3)$$

Note that this solution holds for an infinitely long cylinder. For such a geometry, no steady-state regime can be reached even after an infinite period of time. The actual open hole is an elongated cylinder [diameter $14^{3/4"}$, length 352 m (or 1154 ft); it is not infinite. However, the difference between the two geometries is not relevant except when very long periods of time are considered.

6.7.3 Mass conservation in wellbore

It can be inferred from Fig. 6.3 that the variations of brine density resulting from temperature distribution in the well is less than 2%. Hence, brine density in the well is assumed to be uniform. The mass balance for liquids in the well is given by Eq. 6.4. It is assumed that salt is impermeable to diesel. The total well compressibility, (βV), has a value of 38 L/MPa (3.8 L/bar) during Phase 1. The injection rate at the wellhead, Q^{wh}_{tub}, was zero during this phase. Between April 22 and April

29, (Phase 2), the average pressure change at the wellhead, $\dot{P}_{tub}^{wh}$, was almost zero:

$$(\beta V)_w \dot{P}_{tub}^{wh} = Q_{tub}^{wh} + C_{creep} \int_{H_{cas}}^{H} S_{ann}[-P^{wh} + (\gamma_R - \gamma_b)z]^n dz + \frac{2\pi k h}{\mu} \int_0^t \dot{P}_{tub}^{wh}(\tau) q_D \left(\frac{k[t-\tau]}{\mu \phi c_t r_w^2}\right) d\tau \tag{6.4}$$

6.7.4 Solving the minimization problem

Using the simplifications made above, only two unknown quantities appear in Eq. 6.4, C_{creep} (/MPa^n/yr) and k/μ (m^2/Pa.s), which are relative to the creep rate and the formation mobility, respectively. Their values can be estimated by minimizing the error R^2, which quantifies the average variation between the simulated data and the test data (Eq. 6.5):

$$min_{C_{creep}, k/\mu} \left\{ R^2 = \sum \left[P_{tub,test}^{wh} - P_{tub,simul}^{wh}(C_{creep}, \frac{k}{\mu}) \right]^2 \right\} \tag{6.5}$$

$$C_{creep} \in [0.5, 50] \times 10^{-6} \,/\mathrm{MPa}^n/\mathrm{yr}$$

$$k/\mu = [0.1, 100] \times 10^{-21} \, m^2/\mathrm{Pa.s}$$

Data from Phase 1 are sufficient to estimate the creep coefficient and the average mobility of the wellbore (including open hole, casing shoe and steel casing). Data from Phase 2 enable the estimation of salt permeability by isolating the leak through the casing shoe and cementing. The simulations are performed using Eq. 6.4 for the time periods highlighted by the double-headed arrows in Fig. 6.5. The pressure history from the test is used to start the simulation, and the simulated pressures are used for the subsequent time-steps. Eq. 6.4 is nonlinear, and a 4th-order Runge-Kutta scheme is used to solve it. The steady-state creep coefficient for the Étrez lower layer is $A^* = 3$ x 10^{-6} /MPa^n/yr (Brouard and Bérest, 1998); the pseudo steady-state creep coefficient at early times, C_{creep}, is expected to be slightly larger than A^*. The permeability of the lower salt layer is $k = 4.6\,10^{-21}$m^2 to $19\,10^{-21}$ m^2 (Brouard et al., 2001). The solution space in Eq. 6.5 is chosen to investigate one order of magnitude on either side of Étrez values. Brine viscosity at 60 °C is $\mu = 9\,10^{-4}$ Pa.s (Fig. 6.3).

The solution space is reduced after an initial iteration and the error for the reduced solution space is evaluated in Fig. 6.8. R^2 is the 'distance' between the test data and the simulated data for different combinations of mobility and creep coefficients. The error is minimum along one of the diagonals and maximum along the other. The two boundary points highlighted in Fig. 6.8 do not provide a good match against the test data. However, there are interior points with smaller error values (Fig. 6.9). The solution space is reduced further to the neighborhood of these points and discretized on a finer scale. Fig. 6.10 shows the best solution which corresponds to a permeability of $k = 6\,10^{-21}$ m^2 (6 nD).
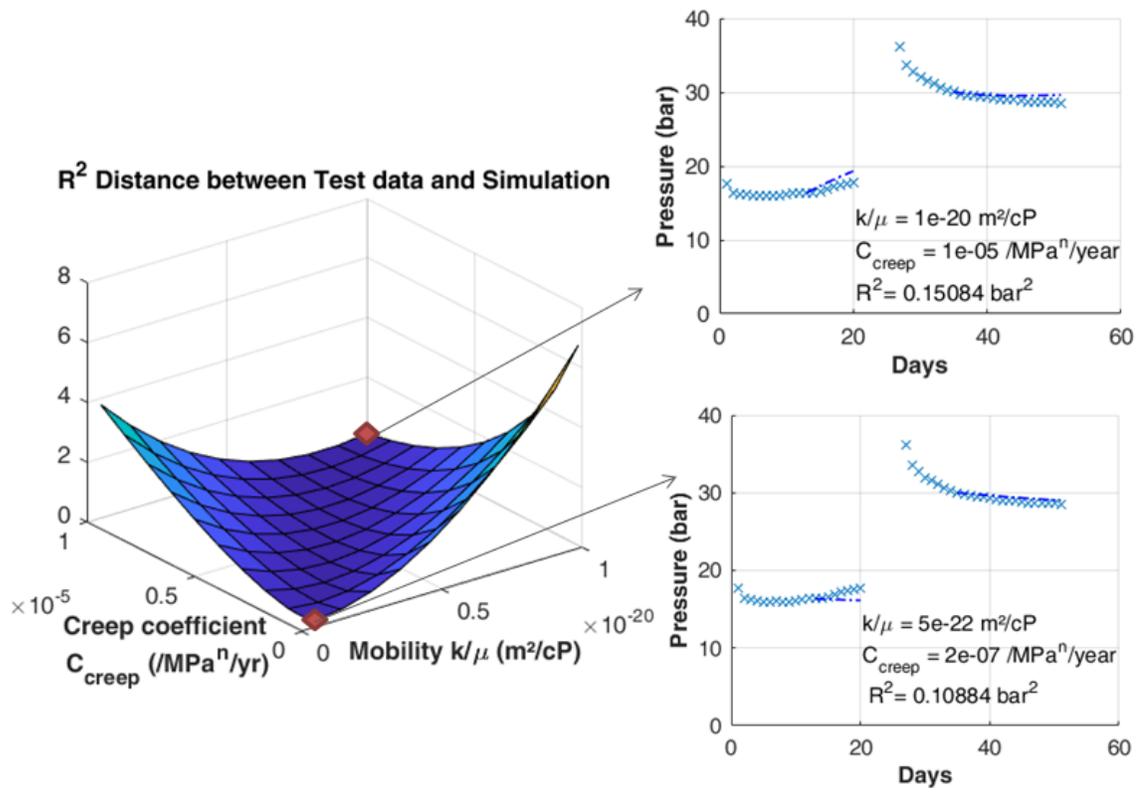
Figure 6.8: Error R^2 at boundary points. [Comparison of Test data ('x') and simulation (dotted lines) does not show a good match.]
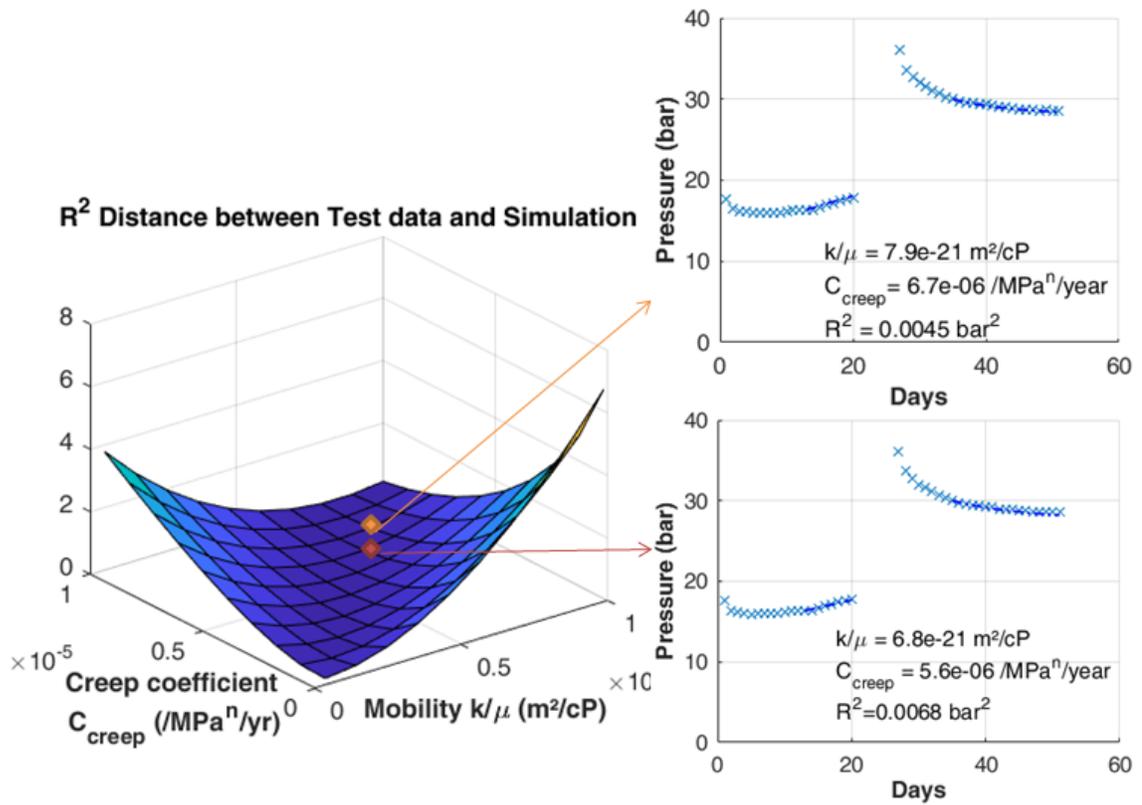
Figure 6.9: Error R^2 at interior points are much lower than that at boundary points. [Comparison of test data ('x') and simulation (dotted lines) shows reasonable agreement.]
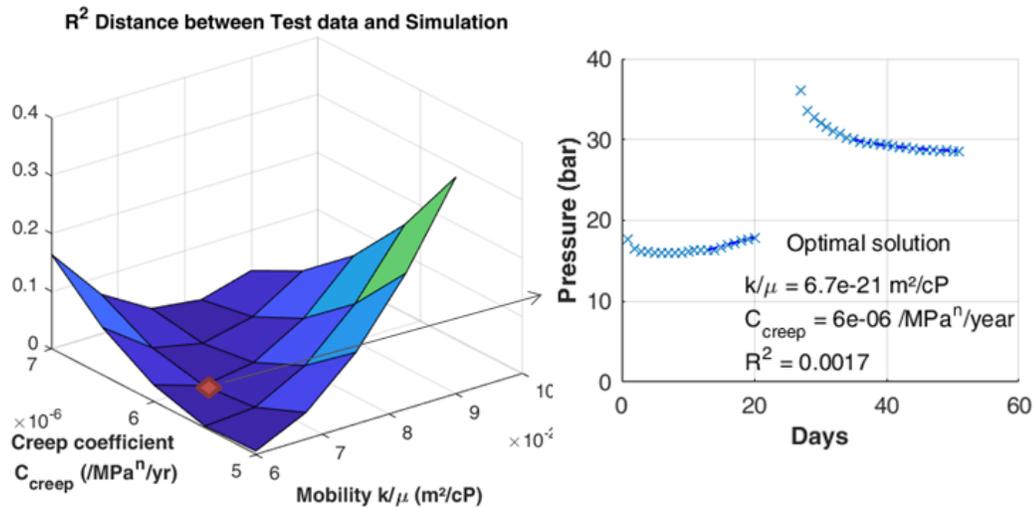
Figure 6.10: Error R^2 reduces further upon finer discretization. (There is very good agreement between the Test data ('x') and simulation (dotted lines) —— the optimal solution. Error R^2 here is the least among all crossplots.
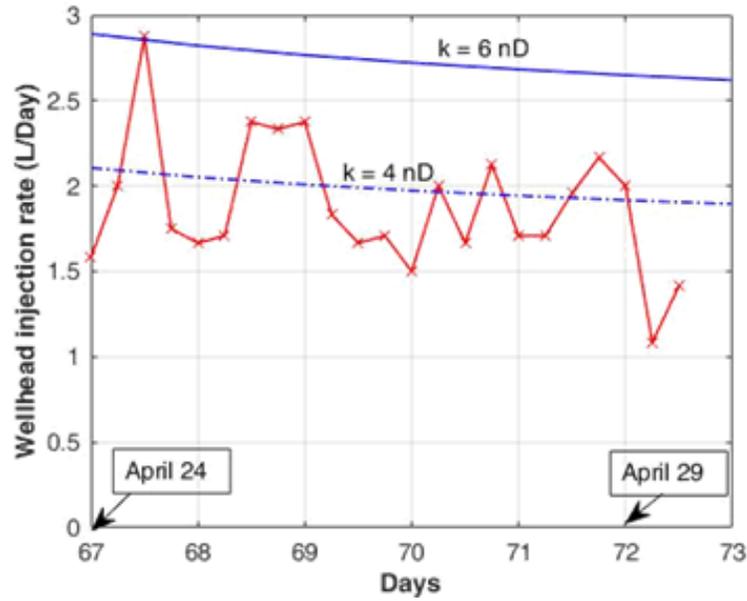
Figure 6.11: Average open-hole permeability estimated from Phase 2 data (red curve) compared to wellbore average permeability (blue curve).

Quantity	AT032 Marboz	Étrez
Creep coefficient	$C_{creep} = 6\,10^{-6}/\text{MPa}^n/\text{yr}$	$A^* = 3\,10^{-6}/\text{MPa}^n/\text{yr}$
Salt permeability	$k_{salt} = 4\,10^{-21}\text{m}^2$	$k_{salt+cas-shoe} = 4.6 - 19\,10^{-21}\text{m}^2$
Well permeability	$k_{well} = 6\,10^{-21}\text{m}^2$	

Table 6.4: Comparison of test results with those of the lower salt layer at Étrez.

Small leaks through the casing shoe and cementing are common. At the beginning of Phase 2, the casing shoe was covered with diesel, whose leak rate is negligible when compared to that of brine. This allowed the salt formation to be tested in isolation and the salt permeability estimated (Fig. 6.11). The creep coefficient from the earlier estimation is used. The average permeability of the open hole is estimated to be $k = 4\,10^{-21}$ m^2, slightly less than the average permeability of the wellbore. The estimated salt permeability is slightly less than the estimations by Brouard et al. (2001) [shown on Table 6.3]. This is expected because the estimations by Brouard et al. (2001) also include the seepage through casing shoe. (During the tests described by Brouard et al. (2001) , the steel casing seepage was isolated by a packer assembly.) In addition, the creep coefficient compares well against the estimates for the lower salt layer at Étrez (Table 6.3). (A^* is the steady-state creep coefficient, whereas C_{creep} is a pseudo steady-state coefficient).

6.8   Conclusion

The coefficients describing average well permeability, open-hole permeability and closure rate of AT032, a borehole drilled at Marboz, France, were estimated. The assessed creep coefficient and permeabilities are in good agreement with those measured at Étrez in the same salt formation at a 6-mile distance from Marboz. This well is found to be quite tight, with leak rates less than 1 L/day (2 bbls/year).

A new method (*discrete WTLog*) had been designed to measure salt permeability as a function of depth. However, the resolution of this method was not good enough to provide useful results, as average salt permeability ($4\,10^{-21}$ m^2, or 4 nD) is too small. Longer testing periods and more accurate pressure sensors might provide better results.

Chapter 7

Opening WTLog: in-situ and laboratory tests

This chapter discusses the interpretation of some early opening WTLog tests. The tests were performed before the beginning of the thesis by Antoine Jacques, Benoît Brouard and Vincent de Greef. Interpretation of the test results was done during the thesis. The interpretation workflow discussed in this chapter shows clearly the limitations posed by a large transient decay of formation injection rates during the test and the non-availability of skin estimation. The test results show good qualitative agreements at certain locations but a quantitative comparison of the results leaves much to be desired.

The rest of the chapter is partly reproduced from a conference paper: SPE Europec featured at 79th EAGE Conference and Exhibition at Paris, France, in 2017. This article, titled "A Novel Injectivity and Permeability Log for Tight Reservoirs" was co-authored by A. Jacques, B. Brouard, P. Bérest, J.-L. Boutaud de la Combe, V. Jaffrezic, and M. Fleury.

7.1   Test procedure

At the beginning of the test, the well is filled completely with a viscous liquid. A less viscous liquid, injected into the well through a tubing string, displaces the viscous liquid in the string and, later, in the annular space (Fig. 7.1). The well is then subjected to a pressure increase that is maintained constant by a pressure regulator for the entire test duration. Wellhead pressure sensors measure the pressure at both wellheads while accurate flow meters measure the flow rates into the tubing string, $Q_t^{wh}(t)$, and out of the annulus, $Q_a^{wh}(t)$. Their difference, $Q_t^{wh}(t) - Q_a^{wh}(t)$, gives the total injection rate into the formation, $Q_{\mu-}^{wf}(t)$. The combined effect of high viscosity and low permeability ensures that the injection rate of the viscous liquid into the formation is negligible.

When the interface rises up in the annulus, the total injection rate into the formation increases, as more and more formation layers are now being exposed to the less-viscous liquid. Larger the permeability of the formation layer, larger is the injection rate increase when the liquid interface in the annulus passes through it. At the same time, there is a transient decay of the injection rates in the layers already exposed to the less-viscous liquid and this decreases the total formation injection
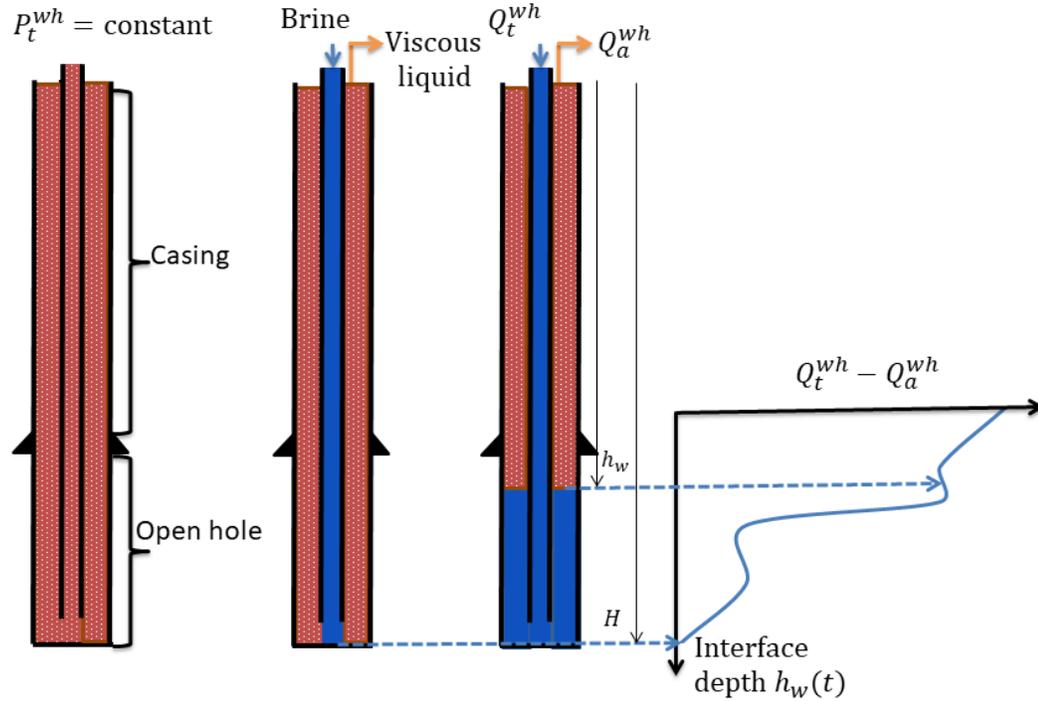
Figure 7.1: The test procedure for opening WTLog

rate. The competition between these two effects sometimes leads to a reduction in the total injection rate even as the thickness of the formation exposed to the less-viscous liquid increases. This could create small teeth-like structures in the $Q_{\mu-}^{wf}(t)$ vs depth plot (Fig. 7.2). A similar behavior was observed during an in-situ test in a very permeable ($k > 10^{-12}$ m^2 or 1 D) aquifer.
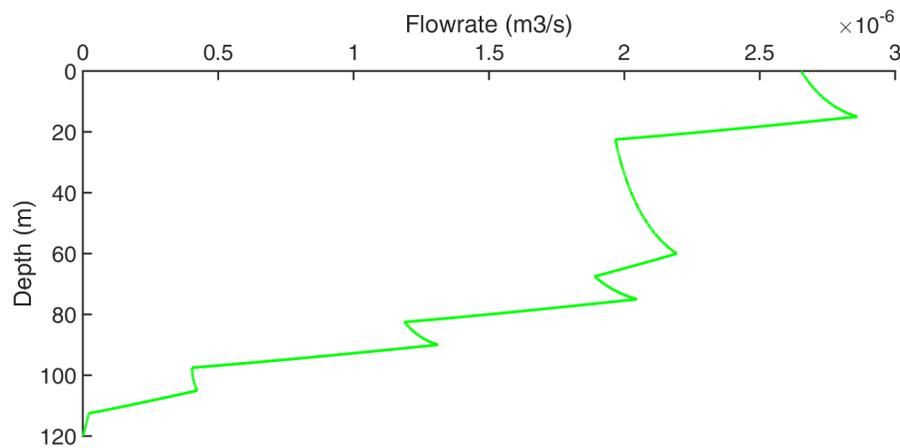
Figure 7.2: $Q_{\mu-}^{wf}(t)$ vs depth, simulated using the permeability profile shown in Fig. 7.3.

7.2   Interpretation workflow

7.2.1   Interface depth

Interface velocity, which remains more or less constant during the test, can be computed from the annulus withdrawal rate of the viscous liquid using Eq. 7.1. The annulus cross-sectional area, $S_a(h)$, could vary with depth. In Eq. 7.1, $\dot{h}_w(t)$ is negative because the interface moves upward and the z-axis points downward. For simplicity, liquid densities, which are dependent on pressure and temperature, are assumed to be constant. Interface depth $h_w(t)$ is equal to the well depth H at time $t = 0$ and $h_w(t) < H$ for all $t > 0$.

$$\dot{h}_w(t) = -\frac{Q_a^{wh}(t)}{S_a(h)}$$

(7.1)

$$h_w(t) = H + \int_0^t \dot{h}_w(\tau)d\tau$$

The computation of interface depth can be easily cross-checked using the following methods:

The volume of the central tube and the lined part of the annular space are usually known. When the cumulative volume of the liquid injected into the central tube equals the volume of the tube, the interface is at the bottom of the well. Also, when the cumulative volume of the viscous liquid withdrawn from the annulus equals the sum of the volumes of open-hole annulus and tubing, the time at which the interface reaches the casing shoe can be obtained.

Another approach to track the interface location is to use the pressure difference between the central tube and the annulus as measured by the surface pressure sensors. When the specific gravities of the two liquids are different, this pressure difference changes as the interface moves up in the annulus. However, this effect could sometimes be hidden by frictional losses which need to be minimized.

7.2.2   Inversion to derive a permeability log

The total formation injection rate, $Q_{\mu-}^{wf}(t) = Q_t^{wh}(t) - Q_a^{wh}(t)$, is related to the injection rate per unit thickness $q_{\mu-}^{wf}$ by Eq. 7.2; $\tau(z)$ is the time at which the interface reaches depth z.

$$Q_{\mu-}^{wf}(t) = \int_{h_w(t)}^{H} q_{\mu-}^{wf}[z, t - \tau(z)]dz \tag{7.2}$$

When $Q_{\mu-}^{wf}$ is continuous and, at least, a piece-wise smooth function in $h_w(t)$, the derivative of $Q_{\mu-}^{wf}$ with respect to h_w can be expressed using Leibniz rule (Eq. 7.3). Since $h_w = h_w(t)$ is a monotonic function on t, we can write $t = f^{-1}(h_w)$ and $dt/dh_w = 1/\dot{h}_w$. Using the chain rule for differentiation, Eq. 7.3 can be re-written as in Eq. 7.4.

$$\frac{dQ_{\mu-}^{wf}}{dh_w}(h_w, t) = -q_{\mu-}^{wf}(h_w, t - \tau(h_w)) + \int_{h_w(t)}^{H} \frac{\partial q_{\mu-}^{wf}}{\partial h_w}[z, t - \tau(z)]dz \tag{7.3}$$

$$\frac{dQ_{\mu-}^{wf}}{dh_w}(h_w, t) = -q_{\mu-}^{wf}(h_w, t - \tau(h_w)) + \int_{h_w(t)}^{H} \frac{1}{\dot{h}_w(t)} \frac{\partial q_{\mu-}^{wf}}{\partial t}[z, t - \tau(z)]dz \qquad (7.4)$$

$$\left[\!\left[\frac{dQ_{\mu-}^{wf}}{dh_w}(h_w, t)\right]\!\right]_{h_w^+(t)}^{h_w^-(t)} = -\left[\!\left[q_{\mu-}^{wf}(h_w, t - \tau(h_w))\right]\!\right]_{h_w^+(t)}^{h_w^-(t)} + \int_{h_w^-(t)}^{h_w^+(t)} \frac{1}{\dot{h}_w(t)} \frac{\partial q_{\mu-}^{wf}}{\partial t}[z, t - \tau(z)]dz \qquad (7.5)$$

The jump in $dQ_{\mu-}^{wf}/dh_w$ at depth h_w is given in Eq. 7.5 where, $h_w^-(t) = h(t) - \epsilon$ and $h_w^+(t) = h(t) + \epsilon$. It is evident from Eq. 7.1 that the interface velocity $\dot{h}_w(t)$ is a non-zero quantity. The transient decay of the formation injection rate $\partial q_{\mu-}^{wf}/\partial t$ is also a finite quantity. Hence, when $\epsilon \to 0$, $h_w^+ \to h_w^-$ and

$$lim_{h_w^+ \to h_w^-} \int_{h_w^-(t)}^{h_w^+(t)} \frac{1}{\dot{h}_w(t)} \frac{\partial q_{\mu-}^{wf}}{\partial t}[z, t - \tau(z)]dz \ll \left[\!\left[q_{\mu-}^{wf}(h_w, t - \tau(h_w))\right]\!\right]_{h_w^+(t)}^{h_w^-(t)} \qquad (7.6)$$

Using Eq. 7.6, the integral in Eq. 7.5 can be neglected yielding Eq. 7.7.

$$\left[\!\left[\frac{dQ_{\mu-}^{wf}}{dh_w}(h_w, t)\right]\!\right]_{h_w^+(t)}^{h_w^-(t)} = -\left[\!\left[q_{\mu-}^{wf}(h_w, t - \tau(h_w))\right]\!\right]_{h_w^+(t)}^{h_w^-(t)} \qquad (7.7)$$

The large time asymptotic solutions for $q_{\mu-}^{wf}$ are not valid because $t - \tau(h_w(t)) \to 0$. In the next chapter, titled 'solutions using Bessel-Fourier series', the exact solution to the monophasic flow problem with constant pressure inner boundary and a near-wellbore skin is discussed. The solution is given in Eq. 7.8. When, $[t - \tau] \to 0$, $exp(-\alpha_i^2[t_D - \tau_D]) \to 1$. Combining Eqs. 7.7 and 7.8 yields Eq. 7.9, in which, $f(S) = 1/[S + ln(r_{De})] - \sum_{i=1}^{\infty} C_{Di}\alpha_i Z_0'(\alpha_i)$. For $S \gg 1$, $f(S) \approx 1/S$.

$$q_{\mu-}^{wf}(t_D) = \frac{2\pi k \triangle P}{\mu}\left[\frac{1}{S + ln(r_{De})} - \sum_{i=1}^{\infty} C_{Di}\alpha_i Z_0'(\alpha_i)exp(-\alpha_i^2 t_D)\right] \qquad (7.8)$$

$$\left[\!\left[\frac{dQ_{\mu-}^{wf}}{dh_w}(h_w, t)\right]\!\right]_{h_w^+(t)}^{h_w^-(t)} = \frac{2\pi}{\mu}\left[\!\left[k(z)\triangle P(z)f(S(z))\right]\!\right]_{h_w^+(t)}^{h_w^-(t)} \qquad (7.9)$$

When the pressure head at sandface $\triangle P(z)$ and skin $S(z)$ are known, permeability $k(z)$ can be derived. The skin value is not known and an assumption has to be made on its value to derive the permeability log. Fig. 7.3 shows the validation of the interpretation workflow using synthetic data. The horizontal bars in Fig. 7.3 are the input permeabilities and the simulated flow rates are shown in Fig. 7.2. The flow rates are interpreted using Eq. 7.9 and the interpreted permeability log is shown by a continuous green line in Fig. 7.3. Skin S and pressure difference $\triangle P$ are considered to be uniform and known values during the interpretation. The perfect agreement between the input and interpreted permeability shows that in the presence of sharp permeability contrasts Eq. 7.9 is sufficient to provide an accurate interpretation.

Eq. 7.9 was derived with the assumption that there is a sharp jump in the permeability of the formation layers. When there is no sharp permeability contrast between the two layers, or when the
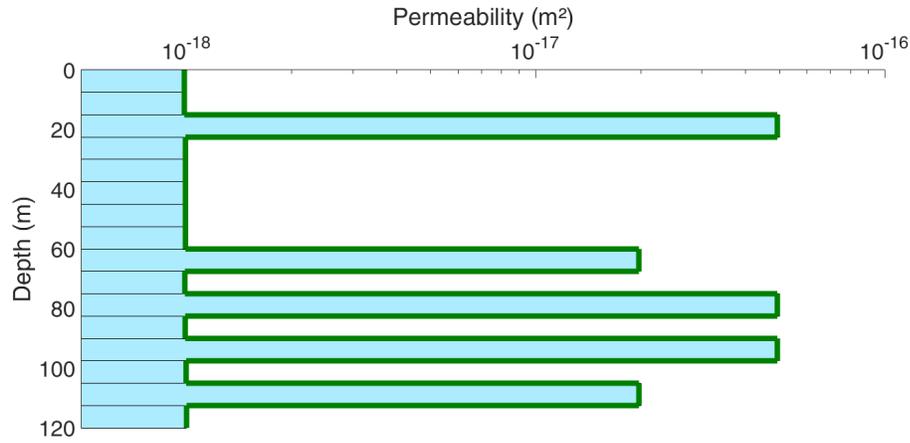
Figure 7.3: Validation of interpretation workflow (Eq. 7.9) for a multilayered formation using synthetic data. Horizontal bars are the input permeabilities and the green line is the interpreted permeability log

interface is traversing through a thick layer of homogeneous properties, the integral in Eq. 7.5 can no longer be neglected. An approximate estimation of the integral can be obtained assuming that, when $h_w^+ > z > h_w^-$, the formation parameters are constant and equal to their values at $z = h_w^+$. This approximation is valid because there is no sharp contrast in formation properties. If there is a sharp contrast, the integral becomes insignificant compared to the other terms and Eq. 7.9 can be used.

When $Q_{\mu-}^{wf}$ is not smooth

Total formation injection rate, $Q_{\mu-}^{wf}$, estimated from wellhead flow rates during in-situ tests are often not smooth enough to use Eq. 7.9 with the jump condition. In such cases, an alternate approach based on cumulative injected volume, which is a lot smoother, is better suited for interpretation. This approach divides the open hole into several sections of uniform permeability. The permeability of a layer is estimated from the additional liquid volume injected into the formation when the interface passes through the layer, after taking into the account the transient decay of the injection rates in other layers. This interpretation workflow was developed by Pierre Bérest and Benoît Brouard before the start of the thesis.

7.3 In-situ test in a tight overburden formation

An in-situ test was performed in an overburden formation with permeabilities mostly smaller than 1 μD and at some locations more permeable layers reaching about 100 μD. Porosity was in the 8% to 15% range. In the new well drilled, full $5^{1/4}$" diameter, preserved cores were available to perform various petrophysical and mineralogical tests. In addition to standard wireline logs, an NMR log was run to study the possibility of deriving a permeability from this log. Permeability and NMR data were systematically acquired on core plugs by IFPEN, France. A reasonably good correlation was established between the log average of the T_2 distribution and the measured water permeability of
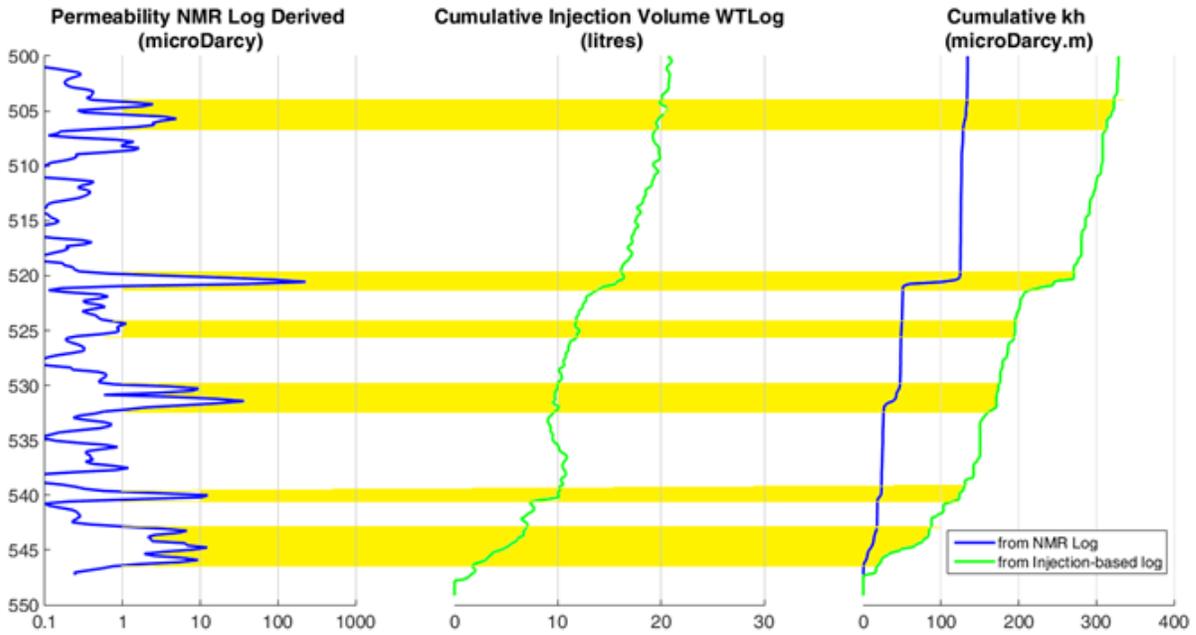
Figure 7.4: Comparison of in-situ test results from NMR log and opening WTLog.

the plugs, without including porosity. Using the in-situ NMR log and the results from core samples, a petrophysical log was built by TOTAL. We are thankful to Dr. Marc Fleury, IFPEN, for his valuable insights on the similarities between the NMR log and the cumulative injection volume from WTLog.

The NMR derived permeability log and cumulative injected volume from opening WTLog test are compared in Fig. 7.4 (first 2 left tracks) for a 50-m interval which contains most of the permeable layers. The pressure regulation during the test was less than perfect and this led to large oscillations in the flow rates measured at the wellhead. The injected volume data is comparatively much smoother and hence used to interpret permeability. A good qualitative agreement can be observed between these two tracks: a variation in permeability corresponds to a variation in the injected volume. The two logs are better compared by (i) calculating a cumulative NMR permeability log (units of μD.m) to mimic the injected volume log and (ii) interpreting the cumulative volume as a permeability-thickness kh (same units) log using the workflow described earlier. The interpretation of opening WTLog log was done by Benoît Brouard using the volume-based approach. Similar trends are observed on both tracks of cumulative kh. An absolute comparison of cumulative kh is not meaningful here since the derivation NMR permeability log uses correlations performed at core scale and the derivation of opening WTLog permeability has used an assumption of zero skin. However, it is evident that the opening WTLog gives an appropriate qualitative response.

7.4 Laboratory test

The laboratory test setup and the test procedure are already described in the main text. Only the results from a test performed by Benoît Brouard is present here. The interpretation of this test was done during the thesis using the interpretation workflow with jump condition (also developed during
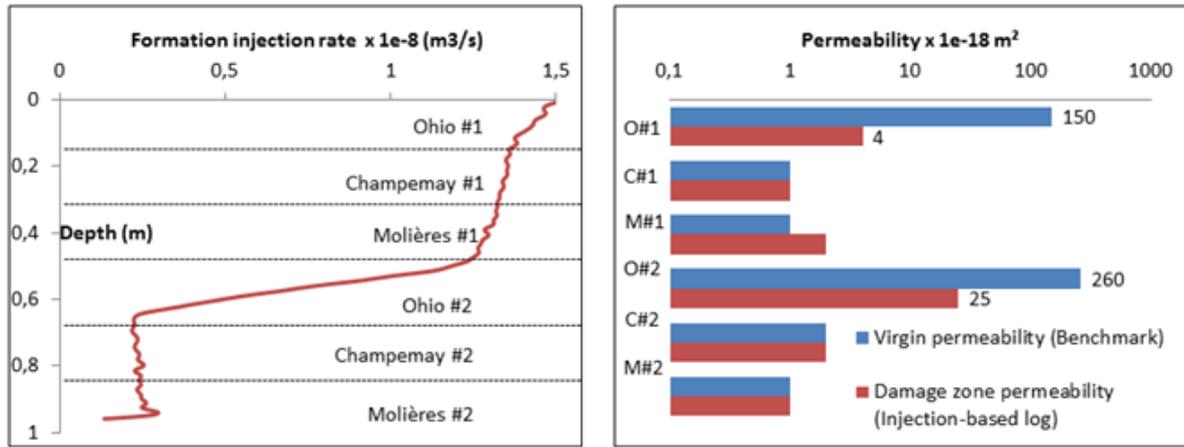
Figure 7.5: Total formation injection rate and permeability logs from an opening WTLog test. Skin $S= 0$ is used to derive the permeability log in red.

the thesis).

The formation injection rate $(Q_{in} - Q_{out})$ vs interface depth curve from the laboratory test is shown in Fig. 7.5 (left). The Ohio samples are much more permeable than the others. However, during the course of the test, there was a loss of viscous liquid into the samples, which created a 'damaged zone' around the inner radius and reduced the injection rates. The average sample permeability in the vicinity of the inner radius (damaged zone) is interpreted using Eq. 7.9 and $S = 0$, and shown in Fig. 7.5 (right). In Fig. 7.5, there clearly exists a positive correlation between virgin permeability (benchmark) and permeability in the damaged zone. Also, Ohio #1 is at the top of the experimental set-up and is exposed to the viscous liquid for a relatively longer duration than Ohio #2. Hence, Ohio #1 suffers the maximum reduction in permeability in the near-well zone. Fig. 7.5 (right) also suggests that the less permeable samples have not experienced significant damage due to the filtration of the viscous liquid.

In conclusion, laboratory and in-situ tests show that the opening WTLog allows for the interpretation of near-well permeability and the results are qualitative. The closing WTLog developed during the thesis provides better quantitative estimates of formation permeability and is also easier to interpret.

Chapter 8

Solutions using Bessel-Fourier series

In chapter 2, the unsteady-state flow problem was solved using Laplace transformation. The inverse Laplace transformation is done numerically through Stehfest (1970) algorithm. There exists an alternative solution technique using Bessel-Fourier series to obtain analytical solutions that do not require any numerical inversion or computing integrals. In the subsequent pages, Bessel-Fourier solutions are discussed for a homogeneous reservoir (with skin) and compared to the Laplace transformation solutions. The earlier assumption of an infinite reservoir is relaxed and different reservoir boundary conditions are discussed. Computations using Bessel-Fourier solutions were found to be faster than those using Laplace transformation solutions.

In the latter half of the section, the pressure loss in outflow meters is modeled as an outer skin. The initial objective was to use this model for reciprocal-rate derivative analysis of laboratory tests. But this analysis was later abandoned since the steady-state is reached in the samples rather quickly.

8.1 Solutions to diffusivity equation: from heat conduction to fluid flow

The governing equation for the monophasic flow of a slightly compressible fluid in porous media (Eq. 8.1) is same as the heat equation. Just as the heat equation is derived from Fourier's law of thermal conduction and law of conservation of energy, the unsteady state flow equation in porous media is derived from Darcy's law and mass conservation in the pore volume.

$$\nabla^2 p = \frac{1}{K}\frac{\partial p}{\partial t} \tag{8.1}$$

where p is the fluid pressure and K is the hydraulic diffusivity of the fluid in the porous media. Making use of the striking similarity between the heat equation and the flow equation, ground water hydrologists and petroleum engineers adopted the solutions of widely studied heat conduction problems. There are four main solution techniques that appear in the literature of heat transfer problems: line source method, Bessel-Fourier series, Green's functions and Laplace transformation.

The history of transient heat transfer solutions begins with Lord Kelvin, after whom SI unit of temperature is named, in the later half of 19th century. He introduced a point-source solution to estimate the age of the earth from temperature gradients measured in underground mines. Kelvin's

solution for temperature gradient at the surface of a semi-infinite body, initially at a uniform temperature and bound by an infinite plane (earth's surface) kept at zero temperature, is given by Eq. 8.2.

$$\frac{dT}{dx}(0,t) = \frac{T_0}{\sqrt{\pi \kappa t}} \tag{8.2}$$

where T_0 is the initial temperature of the semi-molten earth and κ is the thermal diffusivity constant (m^2/s). Carslaw (1921) extended this point-source to an 'instantaneous line-source' of strength F_{source} which is the quantity of heat added or removed instantaneously divided by specific heat capacity per unit volume of the solid (Eq. 8.3). Theis (1935), in his work on ground water hydrology, extended Carslaw's instantaneous line source method to a vertical, lasting line source at the center of a cylindrical well (Eq. 8.4).

$$T(x,y,t) = \frac{F_{source}}{4\pi\kappa t}exp(-\frac{x^2+y^2}{4\kappa t}) \tag{8.3}$$

$$P(r,t) = \frac{Q}{4\pi kh/\mu} \int_{\frac{r^2}{4Kt}}^{\infty} \frac{exp(-u)}{u}du \tag{8.4}$$

where, Q is the flow rate; k and h are the permeability and the thickness of the formation, respectively. μ is the viscosity of the fluid in the formation.

Muskat (1934) and Hurst (1934), in their independent works, used Bessel-Fourier series to solve the unsteady flow problem in a homogeneous porous media, internally and externally bounded by cylindrical surfaces, with constant pressure or constant flux boundary condition at the inner radius. The technique was first introduced by Carslaw (1921) in heat conduction problems. Muskat (1934) and Hurst (1934) adopted this technique and applied it to boundary conditions relevant to the petroleum industry.

Nicholson (1921) was the first to use Green's functions to solve heat conduction problems but his solution was too complex for practical use. Smith (1937) later combined the Green's functions with contour integral techniques of Carslaw (1921) and obtained a solution that simplifies numerical computations. Both Nicholson (1921) and Smith (1937) studied the problem of heat transfer in an infinite solid bounded internally by a cylinder at constant temperature. This was of particular interest due to its direct practical applications in underground electric cables and cooling of underground mines.

Until 1946, the solutions to the heat equation (or flow equation) in cylindrical coordinates were either infinite series (Bessel-Fourier solution) or integrals that had to be computed numerically (Line source method and Green's functions). Carslaw and Jaeger (1946) were the first to apply Laplace transformation techniques to the heat transfer problems. They also computed small and large-time asymptotic solutions for constant flux and constant temperature boundary conditions. The asymptotic solutions of Carslaw and Jaeger (1946) are given in Eqs. 8.5 to 8.8. When the heat flux per unit area, F, at the inner boundary of the cylinder is constant, the asymptotic solutions valid for very small and large values of $\kappa t/r^2$ are given by Eqs. 8.5 and 8.6, respectively.

$$T(r,t) = \frac{2F}{K_{th}}\sqrt{\frac{\kappa r_w t}{r}} + O(\frac{\kappa t}{r^2}) \tag{8.5}$$

$$T(r,t) = \frac{F}{2K_{th}}[ln(\kappa t/r^2) + 0.8091] + O(\frac{r^2}{\kappa t}) \tag{8.6}$$

where, K_{th} is the thermal conductivity of the solid. When the temperature at the inner boundary, of radius r_w, is held constant, asymptotic solutions for small and large values of $\kappa t/r^2$ are given by Eqs. 8.7 and 8.8, respectively. The similarity between Eq. 8.2 (Kelvin's solution) and Eq. 8.7 is expected, because at small times, the curvature of the surface is less important and the assumption of a planar or a cylindrical (or spherical) surface gives similar result.

$$F(r_w,t) = \frac{\Delta T_0 K_{th}}{\sqrt{\pi \kappa t}} + O(\frac{\kappa t}{r_w^2}) \tag{8.7}$$

$$F(r_w,t) = \frac{2\Delta T_0 K_{th}}{r_w}\frac{1}{[ln(\kappa t/r_w^2) + 0.2319]} + O(\frac{r_w^2}{\kappa t}) \tag{8.8}$$

Van Everdingen and Hurst (1949) introduced to the petroleum industry the Laplace transformation technique of Carslaw and Jaeger (1946) and the large-time asymptotic solution for constant rate case (Eq. 8.9) . For the constant pressure case, Jacob and Lohman (1952) compared the large-time asymptotic solution of Carslaw (Eq. 8.8) to the integral solutions of Smith (1937) and found that the error associated with using the asymptotic solution is less than 5% when $t_D = Kt/r_w^2 > 200$.

$$\Delta p_{D(Q)} = \frac{1}{2}[ln(t_D) + 0.81] \tag{8.9}$$

$$Q_{D(P)} = \frac{2}{ln(t_D) + 0.81} \tag{8.10}$$

where $\Delta p_{D(Q)} = 2\pi kh\Delta p_w/Q\mu$ is the dimensionless pressure when the flow rate at r_w is constant and $Q_{D(P)} = Q\mu/2\pi kh\triangle p_w$ is the dimensionless flow rate when the pressure in the well is constant.

Of the four solution techniques discussed here, Laplace transformation technique is the one that is widely used in petroleum industry. Solutions using Bessel-Fourier series can be computationally faster than Laplace transformation (Fig. 7.3), but are not available for all heterogeneous models. Solutions using Green's functions are more computationally intensive and 'line-source method' is not applicable to constant pressure problems. Hence, Bessel-Fourier series and Laplace transformation technique are used to discuss the flow problems in the following sections.

8.2 Radial monophasic flow in a homogeneous reservoir

Let us consider the simple case of a radial monophasic flow in a homogeneous, cylindrical reservoir. The governing equation and the initial condition are given in Eqs. 8.11 and 8.12. The boundary conditions at the inner and the outer boundary are given in Eqs. 8.13 and 8.14, respectively.

$$\frac{\partial^2}{\partial r_D^2}\Delta p(r_D, t_D) + \frac{1}{r_D}\frac{\partial}{\partial r_D}\Delta p(r_D, t_D) = \frac{\partial}{\partial t_D}\Delta p(r_D, t_D) \tag{8.11}$$

$$\Delta p(r_D, 0) = 0 \tag{8.12}$$

$$\Delta p(1, t_D) = P_w - P_{ini} \ (or) \ -\frac{kh}{\mu}\frac{\partial \Delta p}{\partial r_D}(1, t_D) = Q \tag{8.13}$$

$$\Delta p(r_{De}, t_D) = 0 \ (or) \ \frac{\partial \Delta p}{\partial r_D}(r_{De}, t_D) = 0 \tag{8.14}$$

where, $r_D = r/r_w$ is the dimensionless radius, r_{De} ($=r_e/r_w$) is the dimensionless outer radius and $t_D = Kt/r_w^2$ is the dimensionless time.

8.2.1   Bessel-Fourier solution

The general solution to Eq. 8.11 can be expressed using Bessel-Fourier series through separation of variables when the boundary conditions are homogeneous. However, the boundary conditions are seldom homogeneous (see Eq. 8.13) and hence it is necessary to express Δp as sum of steady-state and transient pressures, i.e $\Delta p(r_D, t_D) = \Delta p^{ss}(r_D) + \Delta p^{tr}(r_D, t_D)$, to obtain homogeneous boundary conditions for the transient problem. The general expression for steady state pressure distribution in cylindrical coordinates is given in Eq. 8.15.

$$\Delta p^{ss}(r_D) = A + Bln(r_D) \tag{8.15}$$

Using separation of variables, the transient pressure can be expressed as a product of two functions $\Pi(r_D)$ and $\xi(t_D)$. Using $\Delta p^{tr}(r_D, t_D) = \Pi(r_D)\xi(t_D)$, Eq. 8.13 can be rewritten as in Eq. 8.16.

$$\frac{1}{\Pi(r_D)}\left[\frac{\partial^2}{\partial r_D^2}\Pi(r_D) + \frac{1}{r_D}\frac{\partial}{\partial r_D}\Pi(r_D)\right] = \frac{1}{\xi(t_D)}\frac{\partial \xi(t_D)}{\partial t_D} = -\alpha_i^2 \tag{8.16}$$

$\frac{\partial^2}{\partial(\alpha_i r_D)^2}\Pi(\alpha_i r_D) + \frac{1}{\alpha_i r_D}\frac{\partial}{\partial(\alpha_i r_D)}\Pi(\alpha_i r_D) + \Pi(\alpha_i r_D) = 0$ is Bessel's differential equation of order zero, which is satisfied by any linear combination of zero order Bessel functions of first (J_0) and second (Y_0) kind. The coefficients of this linear combination, henceforth denoted by $Z_0(\alpha_i r_D)$, depend on the boundary conditions (see Fig. 8.1). Also, it is evident from Eq. 8.14 that $\xi(t_D)$ is an exponential function of the form $exp(-\alpha_i^2 t_D)$. The transient pressure evolution, Δp^{tr}, is given in Eq. 8.17 and total pressure evolution is given in Eq. 8.18.

$$\Delta p^{tr}(r_D, t_D) = \sum_{i=1}^{\infty} C_i Z_0(\alpha_i r_D)exp(-\alpha_i^2 t_D) \tag{8.17}$$

$$\Delta p(r_D, t_D) = A + Bln(r_D) + \sum_{i=1}^{\infty} C_i Z_0(\alpha_i r_D)exp(-\alpha_i^2 t_D) \tag{8.18}$$

When the sandface flow rate Q is constant, the non-dimensional sandface pressure $\Delta p_{D(Q)}$ is

given by Eq. 8.19. When the sandface pressure P_w is constant, the non-dimensional sandface flow rate $Q_{D(P)} = Q\mu/2\pi kh(P_w - P_{ini})$ is given by Eq. 8.20.

$$\Delta p_{D(Q)}(1, t_D) = A_D + \sum_{i=1}^{\infty} C_{Di} Z_0(\alpha_i) exp(-\alpha_i^2 t_D) \tag{8.19}$$

$$Q_{D(P)}(1, t_D) = -B_D - \sum_{i=1}^{\infty} C_{Di} \alpha_i Z_0'(\alpha_i) exp(-\alpha_i^2 t_D) \tag{8.20}$$

where, A_D, B_D and C_{Di} are the dimensionless forms of coefficients A, B and C_i, respectively. The initial condition given in Eq. 8.12 and re-written in Eq. 8.21 is used to compute the coefficients C_{Di}. Because $\int_1^{r_{De}} r_D Z_0(\alpha_i r_D) Z_0(\alpha_j r_D) dr_D = 0$ when $\alpha_i \neq \alpha_j$, the coefficients C_{Di} can be computed in the same fashion as the coefficients in a Fourier series. Muskat (1934) and Hurst (1934) have discussed in detail the computation of the coefficients C_i and we will directly present the final result here (Eq. 8.22).

$$\sum_{i=1}^{\infty} C_{Di} Z_0(\alpha_i r_D) = A_D + B_D ln(r_D) \tag{8.21}$$

$$C_{Di}(A_D, B_D) = \frac{(A_D/\alpha_i)[r_D Z_0'(\alpha_i r_D)]_1^{r_{De}} - (B_D/\alpha_i^2)[Z_0(\alpha_i r_D) - \alpha_i r_D ln(r_D) Z_0'(\alpha_i r_D)]_1^{r_{De}}}{\frac{1}{2} \left[r_D^2 (Z_0(\alpha_i r_D))^2 + (Z_0'(\alpha_i r_D))^2 \right]_1^{r_{De}}} \tag{8.22}$$

where, $Z_0'(\alpha_i r_D) = dZ_0(\alpha_i r_D)/d(\alpha_i r_D)$. The Bessel functions and the constants that complete Eqs. 8.17 and 8.18 are given in Fig. 8.1. For the constant rate case with no flow at the outer boundary, there is no steady-state solution and hence cannot be discussed using the general framework employed here. For interested readers, the solution to this case is discussed in Muskat (1934).

8.2.2   Laplace transformation

Using the initial condition $\Delta p_D(r_D, 0) = 0$, Laplace transformation of Eq. 8.11 is given in Eq. 8.23.

$$\frac{\partial^2}{\partial(r_D\sqrt{s})^2} \Delta\bar{p}(r_D\sqrt{s}) + \frac{1}{r_D\sqrt{s}} \frac{\partial}{\partial(r_D\sqrt{s})} \Delta\bar{p}(r_D\sqrt{s}) - \Delta\bar{p}(r_D\sqrt{s}) = 0 \tag{8.23}$$

The general solution to the problem can be written as a linear combination of zeroth order modified Bessel functions I_0 and K_0. In infinite reservoirs, I_0 is disregarded since $I_0(x) \to \infty$ as $x \to \infty$. In reservoirs with finite outer boundary (bounded reservoirs), the general solution is given by Eq. 8.24.

$$\Delta\bar{p}(r_D\sqrt{s}) = \bar{A}I_0(r_D\sqrt{s}) + \bar{B}K_0(r_D\sqrt{s}) \tag{8.24}$$

As before, when sandface flow rate is constant, the dimensionless pressure difference is given by Eq. 8.25. When the sandface pressure is constant, the dimensionless flow rate is given by Eq. 8.26.

$$\Delta\bar{p}_{D(Q)}(r_D\sqrt{s}) \mid_{r_D=1} = \bar{A}_D I_0(\sqrt{s}) + \bar{B}_D K_0(\sqrt{s}) \tag{8.25}$$

Constant flowrate

$$\Delta p_{D(Q)}(r_{De}, t_D) = 0$$

$$Z_0(\alpha_i r_D) = J_0(\alpha_i r_D)Y_0(\alpha_i r_{De}) - Y_0(\alpha_i r_D)J_0(\alpha_i r_{De})$$

$$Z_0'(\alpha_i r_D) = -J_1(\alpha_i r_D)Y_0(\alpha_i r_{De}) + Y_1(\alpha_i r_D)J_0(\alpha_i r_{De})$$

$$A_D = \ln(r_{De}) \qquad B_D = -1$$

$$-\frac{\partial \Delta p_{D(Q)}}{\partial r_D}(1, t_D) = 1$$

$$Z_0'(\alpha_i) = 0$$

Not possible to solve for A and B
since steady state is never
reached.

$$\frac{\partial \Delta p_{D(Q)}}{\partial r_D}(r_{De}, t_D) = 0$$

Constant pressure

$$\Delta p_{D(P)}(r_{De}, t_D) = 0$$

$$Z_0(\alpha_i r_D) = J_0(\alpha_i r_D)Y_0(\alpha_i r_{De}) - Y_0(\alpha_i r_D)J_0(\alpha_i r_{De})$$

$$Z_0'(\alpha_i r_D) = -J_1(\alpha_i r_D)Y_0(\alpha_i r_{De}) + Y_1(\alpha_i r_D)J_0(\alpha_i r_{De})$$

$$A_D = 1 \qquad B_D = -1/\ln(r_{De})$$

$$\Delta p_{D(P)}(1, t_D) = 1$$

$$Z_0(\alpha_i) = 0$$

$$Z_0(\alpha_i r_D) = J_0(\alpha_i r_D)Y_1(\alpha_i r_{De}) - Y_0(\alpha_i r_D)J_1(\alpha_i r_{De})$$

$$\frac{\partial \Delta p_{D(P)}}{\partial r_D}(r_{De}, t_D) = 0$$

$$Z_0'(\alpha_i r_D) = -J_1(\alpha_i r_D)Y_1(\alpha_i r_{De}) + Y_1(\alpha_i r_D)J_1(\alpha_i r_{De})$$

$$A_D = 1 \qquad B_D = 0$$

Figure 8.1: Bessel-Fourier solution for homogeneous reservoir — Bessel functions and steady-state constants for different boundary conditions.

$$\bar{Q}_{D(P)}(r_D\sqrt{s}) \mid_{r_D=1} = -\bar{A}_D\sqrt{s}I_1(\sqrt{s}) + \bar{B}_D\sqrt{s}K_1(\sqrt{s}) \tag{8.26}$$

The constants $\bar{A}_D$ and $\bar{B}_D$ depend on the boundary conditions at the inner and the outer boundaries, respectively and can be computed from Eq. 8.27. The matrices $\bar{C}$ for the different boundary conditions are given in Table. 8.1. For infinite reservoirs: $\bar{A}_D = 0$; and $\bar{B}_D = 1/s\sqrt{s}K_1(\sqrt{s})$ or $1/sK_0(\sqrt{s})$ for constant rate and constant pressure cases, respectively.

$$\begin{bmatrix} \bar{C}_{11} & \bar{C}_{12} \\ \\ \bar{C}_{21} & \bar{C}_{22} \end{bmatrix} \begin{bmatrix} \bar{A}_D \\ \\ \bar{B}_D \end{bmatrix} = \begin{bmatrix} \frac{1}{s} \\ \\ 0 \end{bmatrix} \tag{8.27}$$

at $r_D = 1$	Constant flow rate $-\frac{\partial \Delta p_{D(Q)}}{\partial r_D} = 1$	
at $r_D = r_{De}$	$\Delta p_{D(Q)} = 0$	$\frac{\partial \Delta p_{D(Q)}}{\partial r_D} = 0$
$[\bar{C}]$	$\begin{bmatrix} -\sqrt{s}I_1(\sqrt{s}) & \sqrt{s}K_1(\sqrt{s}) \\ I_0(r_{De}\sqrt{s}) & K_0(r_{De}\sqrt{s}) \end{bmatrix}$	$\begin{bmatrix} -\sqrt{s}I_1(\sqrt{s}) & \sqrt{s}K_1(\sqrt{s}) \\ -\sqrt{s}I_1(r_{De}\sqrt{s}) & \sqrt{s}K_1(r_{De}\sqrt{s}) \end{bmatrix}$
at $r_D = 1$	Constant pressure $\Delta p_{D(P)} = 1$	
at $r_D = r_{De}$	$\Delta p_{D(P)} = 0$	$\frac{\partial \Delta p_{D(P)}}{\partial r_D} = 0$
$[\bar{C}]$	$\begin{bmatrix} I_0(\sqrt{s}) & K_0(\sqrt{s}) \\ I_0(r_{De}\sqrt{s}) & K_0(r_{De}\sqrt{s}) \end{bmatrix}$	$\begin{bmatrix} I_0(\sqrt{s}) & K_0(\sqrt{s}) \\ -\sqrt{s}I_1(r_{De}\sqrt{s}) & \sqrt{s}K_1(r_{De}\sqrt{s}) \end{bmatrix}$

Table 8.1: Coefficients to the Laplace transformation solution for a homogeneous reservoir

8.2.3   Results and Discussion

The similarities between the pressure derivative $d\Delta p_{D(Q)}/dln(t_D)$ and reciprocal rate derivative $d(1/Q_{D(P)})/dln(t_D)$ was discussed in detail in the chapter 3 of the thesis. The derivatives computed using Laplace transformation and Bessel-Fourier series are compared in Fig. 8.2. Inversion of Eqs. 8.25 and 8.26 from Laplace domain to the time domain is performed numerically using Stehfest (1970) algorithm. The following inferences can be made from Fig. 8.2.

- Small numerical approximations are involved in the Bessel-Fourier solution (truncation of an
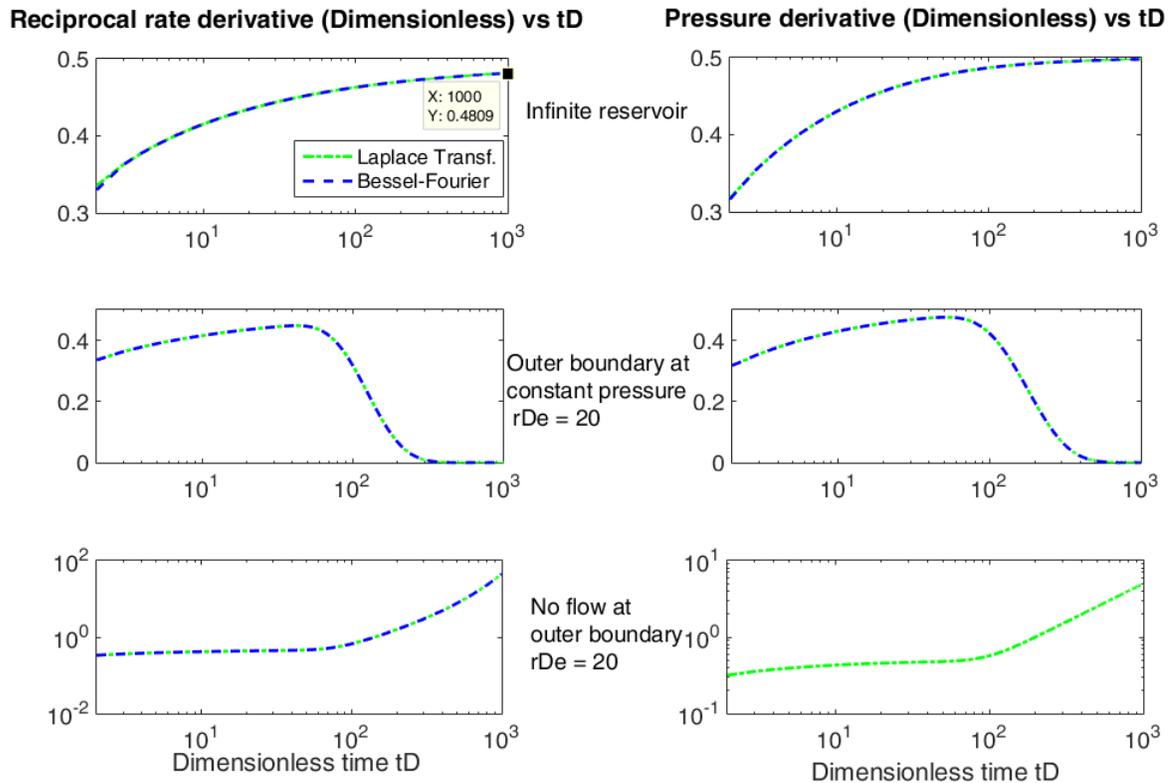
Figure 8.2: Radial flow in a homogeneous reservoir. Pressure derivative and reciprocal-rate derivative from the two solution techniques are compared.

infinite series to a finite number of terms) and Laplace transformation solution (numerical inversion). However, the two solutions show very good agreement.

- For infinite reservoirs, reciprocal rate derivative is expected to show similar behavior as the pressure derivative (Eqs. 8.9 and 8.10). Fig. 8.2 shows similar derivatives for bounded reservoirs too.

- The reciprocal rate derivative approaches the asymptotic value of 0.5 slightly slower than pressure derivative.

CPU run times for the two methods are shown in Fig. 8.3. For a computation with 1000 time steps, the run time for the Laplace solution is 15.8 seconds as against the 0.6 seconds for the Bessel-Fourier solution. In Bessel-Fourier solution, the coefficients of the series (60 terms) are computed only once (at the beginning), and thereafter, it is merely an addition of exponentially decaying terms at each time step. This makes the computation of Bessel-Fourier solution computationally faster than inversion by Stehfest algorithm.

8.3 Homogeneous reservoir with skin

In the 1950s, the early days of pressure transient analysis, several authors have noted the existence of a near-wellbore heterogeneity in the test data. This was inferred from larger pressure drops at early

Profile Summary
Generated 21-Mar-2017 09:06:51 using cpu time.

Function Name	Calls	Total Time	Self Time*	Total Time Plot (dark band = self time)
Maincode	1	16.607 s	0.020 s	
Laplace_solution	1	15.823 s	0.009 s	
Stehfest_algo	1000	15.814 s	2.011 s	
factorial	264000	12.231 s	12.231 s	
Laplace_func	16000	1.572 s	1.572 s	
BesselFourier_solution	1	0.648 s	0.147 s	
Besselroots	1	0.463 s	0.041 s	
inner_boundarycondition	5129	0.422 s	0.144 s	
besselZ0p	5309	0.295 s	0.295 s	

Figure 8.3: MATLAB run time comparison between Laplace solution and Bessel-Fourier solution

times than what was predicted by homogeneous reservoir models. This heterogeneity is attributed to various factors like damage during drilling, completion procedure, invasion of non-reservoir fluids, etc. The general practice is to model the near-wellbore zone as a cylindrical region concentric with the wellbore ($r_w < r < r_S$) with a uniform permeability k_s that is different from virgin permeability k. When the sandface flow rate is constant, steady-state is reached quickly in the skin zone due to its small dimensions. The additional pressure loss due to the skin zone is given by Eq. 8.28. Upon non-dimensionalization Eq. 8.28 yields Eq. 8.29 which quantifies the near-wellbore heterogeneity as non-dimensional skin term S.

$$\Delta p^{skin} = \frac{Q}{2\pi k_s h/\mu} ln(\frac{r_S}{r_w}) - \frac{Q}{2\pi k h/\mu} ln(\frac{r_S}{r_w}) \tag{8.28}$$

$$S = \Delta p^{skin}_{D(Q)} = (\frac{k}{k_s} - 1)ln(\frac{r_S}{r_w}) \tag{8.29}$$

Since the similarity between the reciprocal rate derivative and pressure derivative is well established in the previous section, we will focus only on constant pressure problems (and reciprocal-rate derivative) in the subsequent sections.

8.3.1 Bessel-Fourier solution - constant pressure with near-wellbore skin

When the sandface pressure is constant, the near-wellbore skin in Eq. 8.29 modifies the boundary condition at the inner reservoir boundary to Eq. 8.30. Derivation of Eq. 8.30 is discussed in detail in chapter 3. In chapter 3, the solution to this problem was given using Laplace transformation technique. Here, we will discuss the solution using Bessel-Fourier series.

$$-S\frac{\partial \Delta p_{D(P)}}{\partial r_D}(1,t_D) + \Delta p_{D(P)}(1,t_D) = 1 \tag{8.30}$$

The general Bessel-Fourier solution to this problem is same as Eq. 8.20. The Bessel functions are

at $r_D = 1$	$-S\frac{\partial \Delta p_{D(P)}}{\partial r_D}(1, t_D) + \Delta p_{D(P)}(1, t_D) = 1$	
at $r_D = r_{De}$	$\Delta p_{D(P)} = 0$	$\frac{\partial \Delta p_{D(P)}}{\partial r_D} = 0$
A_D	$-ln(r_{De})/[S + ln(r_{De})]$	1
B_D	$-1/[S + ln(r_{De})]$	0
α_i	$Z_0(\alpha_i) - S\alpha_i Z_0'(\alpha_i) = 0$	

Table 8.2: Constant sandface pressure with near-wellbore skin; coefficients A_D, B_D and α_i for Bessel-Fourier solution.

constructed using outer boundary conditions and hence take the same form as in Fig. 8.1. However, the constants A_D, B_D and roots α_i depend on the inner boundary condition (Eq. 8.30) and are recomputed (see Table 8.2).

8.3.2 Skin at the outer boundary during laboratory tests

It is uncommon to have a skin at the outer boundary and, to the best of our knowledge, this has not been discussed in the literature. The pressure loss at the outflow meters in the laboratory setup creates an additional pressure drop at the outer boundary proportional to the flow rates (Eq. 8.31). The outflow meters are exposed to the atmospheric pressure at the free end, resulting in a pressure increase at the outer radii of the samples. The corrected outer boundary condition is given in Eq. 8.32.

$$\Delta p^{loss} = mQ_{out} \tag{8.31}$$

$$\Delta p_{D(P)}(r_{De}) + r_{De}\bar{S}_{out}\frac{\partial \Delta p_{D(P)}}{\partial r_D}(r_{De}) = 0 \tag{8.32}$$

where, $\bar{S}_{out}$ is the outer skin given by Eq. 8.33.

$$\bar{S}_{out} = 2\pi mkh/\mu \tag{8.33}$$

The constants A_D and B_D, and the Bessel function Z_0 satisfying boundary conditions in Eqs. 8.30 and 8.31 are given in Eq. 8.34. As before, the coefficients α_i depend on the inner boundary condition and take the values in Table 8.2.

$$A_D = \frac{\bar{S}_{out} + ln(r_{De})}{S + \bar{S}_{out} + ln(r_{De})}$$

$$B_D = -\frac{1}{S + \bar{S}_{out} + ln(r_{De})}$$

$$(8.34)$$

$$Z_0(\alpha_i r_D) = J_0(\alpha_i r_D)Y_0(\alpha_i r_{De}) - Y_0(\alpha_i r_D)J_0(\alpha_i r_{De}) - \bar{S}_{out}r_{De}\alpha_i$$

$$[J_0(\alpha_i r_D)Y_1(\alpha_i r_{De}) - Y_0(\alpha_i r_D)J_1(\alpha_i r_{De})]$$

The Laplace transformation solution undergoes only one change to incorporate the two skins — a change in matrix $[\bar{C}]$ to reflect boundary conditions in Eqs. 8.29 and 8.31.

$$\bar{C} = \begin{bmatrix} -S\sqrt{s}I_1(\sqrt{s}) + I_0(\sqrt{s}) & S\sqrt{s}K_1(\sqrt{s}) + K_0(\sqrt{s}) \\ \\ I_0(r_{De}\sqrt{s}) + \bar{S}_{out}r_{De}\sqrt{s}I_1(r_{De}\sqrt{s}) & K_0(r_{De}\sqrt{s}) - \bar{S}_{out}r_{De}\sqrt{s}K_1(r_{De}\sqrt{s}) \end{bmatrix}$$

$$(8.35)$$

For the outflow meters used in the laboratory tests m is 0.00796 bars/(ml/h). For example, in Ohio A sample the outer skin computed using Eq. 8.33 is $\bar{S}_{out} = 1.46$. Fig. 8.4 shows the effect of outer skin, $\bar{S}_{out}$, on the reciprocal-rate derivative. The near-wellbore skin only stretches the time scale in reciprocal-rate derivative plots in Fig. 8.4. The real influence of near-wellbore skin on the derivative can be observed only in a radial composite model.

8.4 Radial composite model

In the previous section, the pressure in the near-wellbore zone was considered to have reached steady state at all times. This assumption is accurate while computing derivatives at medium and large times but at early times the pressure in the near-wellbore zone experiences transient changes. In this section, we solve the transient flow problem in both near well and virgin zone. This divides the reservoir into two composite zones of different reservoir properties, but the flow is still radial. Radial composite model for an infinite reservoir is dicussed in chapter 3. A general solution applicable to other boundary conditions at the outer boundary are discussed here.

The ratio of the mobilities of the virgin zone and the skin zone is M, i.e $(k/\mu)/(k/\mu)_s = M$; the ratio of the diffusivities are also be considered to be M, i.e $K/K_s = M$ when the storativities in the two zones are equal. The pressure evolution is given by Eqs. 8.36 and 8.37, and the boundary conditions are listed in Eqs. 8.38 to 8.41. The properties of the virgin zone is used for non-dimensionalization of these equations. As before, $r_D = r/r_w$ and $t_D = K_v t/r_w^2$.
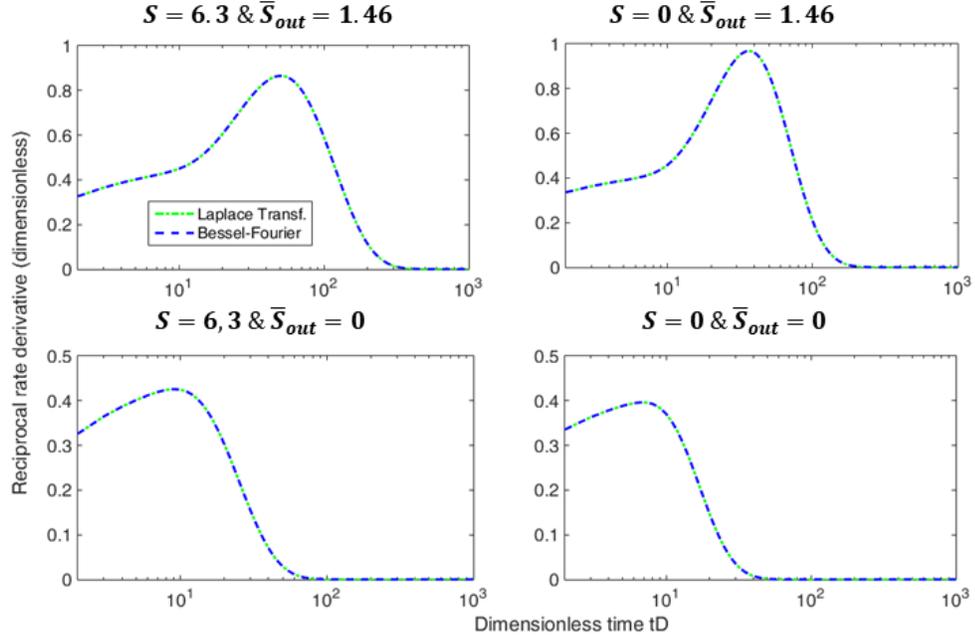
Figure 8.4: Effect of near-wellbore skin and outer skin on reciprocal-rate derivatives

In the skin zone $(1 \leq r_D < r_{Ds})$:

$$\frac{\partial^2}{\partial r_D^2} \Delta p_{D(P)}^s + \frac{1}{r_D} \frac{\partial}{\partial r_D} \Delta p_{D(P)}^s = \frac{\partial}{\partial (t_D/M)} \Delta p_{D(P)}^s \qquad (8.36)$$

In the virgin zone $(r_{Ds} \leq r_D < r_{De})$:

$$\frac{\partial^2}{\partial r_D^2} \Delta p_{D(P)}^v + \frac{1}{r_D} \frac{\partial}{\partial r_D} \Delta p_{D(P)}^v = \frac{\partial}{\partial t_D} \Delta p_{D(P)}^v \qquad (8.37)$$

The boundary conditions are:

$$\Delta p_{D(P)}^s (1, t_D) = 1 \qquad (8.38)$$

$$\Delta p_{D(P)}^s (r_{Ds}, t_D) = \Delta p_{D(P)}^v (r_{Ds}, t_D) \qquad (8.39)$$

$$\frac{\partial \Delta p_{D(P)}^s}{\partial r_D} (r_{Ds}, t_D) = M \frac{\partial \Delta p_{D(P)}^v}{\partial r_D} (r_{Ds}, t_D) \qquad (8.40)$$

$$H_1 \Delta p_{D(P)}^v (r_{De}) + r_{De} \bar{S}_{out} \frac{\partial \Delta p_{D(P)}^v}{\partial r_D} (r_{De}) = 0 \qquad (8.41)$$

Eq. 8.41 is a general boundary condition at the outer boundary. Constant pressure or no flow or mixed boundary conditions at the outer boundary can be enforced by selecting appropriate values for $H_1 (0$ or $1)$ and $\bar{S}_{out}$. The general solutions to Eqs. 8.36 and 8.37 in the Laplace domain are given in Eqs. 8.42 and 8.43.

$$\Delta \bar{p}^s_{D(P)}(r_D\sqrt{s}) = \bar{A}^s_D I_0(r_D\sqrt{Ms}) + \bar{B}^s_D K_0(r_D\sqrt{Ms}) \tag{8.42}$$

$$\Delta \bar{p}^v_{D(P)}(r_D\sqrt{s}) = \bar{A}^v_D I_0(r_D\sqrt{s}) + \bar{B}^v_D K_0(r_D\sqrt{s}) \tag{8.43}$$

The non-dimensional sandface flow rate in Laplace domain is given in Eq. 8.44. The coefficients $\bar{A}_D$ and $\bar{B}_D$ are computed using Eq. 8.45.

$$\bar{Q}_{D(P)}(r_D\sqrt{s}) = -\frac{1}{M}\frac{\partial \Delta \bar{p}^s_{D(P)}}{\partial r_D}(\sqrt{s}) = -\sqrt{s/M}\bar{A}^s_D I_1(\sqrt{Ms}) + \sqrt{s/M}\bar{B}^s_D K_1(\sqrt{Ms}) \tag{8.44}$$

$$[C]_{4\times4} \times \left\{ \begin{array}{c} \bar{A}^s_D \\[2ex] \bar{B}^s_D \\[2ex] \bar{A}^v_D \\[2ex] \bar{B}^v_D \end{array} \right\} = \left\{ \begin{array}{c} \frac{1}{s} \\[2ex] 0 \\[2ex] 0 \\[2ex] 0 \end{array} \right\} \tag{8.45}$$

where,

$$[C]_{4\times4} = \begin{bmatrix} I_0(\sqrt{Ms}) & K_0(\sqrt{Ms}) & 0 & 0 \\[2ex] I_0(r_{Ds}\sqrt{Ms}) & K_0(r_{Ds}\sqrt{Ms}) & -I_0(r_{Ds}\sqrt{s}) & -K_0(r_{Ds}\sqrt{s}) \\[2ex] -I_1(r_{Ds}\sqrt{Ms}) & K_1(r_{Ds}\sqrt{Ms}) & \sqrt{M}I_1(r_{Ds}\sqrt{s}) & -\sqrt{M}K_1(r_{Ds}\sqrt{s}) \\[2ex] 0 & 0 & \begin{array}{c}H_1 I_0(r_{De}\sqrt{s})+ \\[1ex] \bar{S}_{out}r_{De}\sqrt{s}I_1(r_{De}\sqrt{s})\end{array} & \begin{array}{c}H_1 K_0(r_{De}\sqrt{s})- \\[1ex] \bar{S}_{out}r_{De}\sqrt{s}K_1(r_{De}\sqrt{s})\end{array} \end{bmatrix} \tag{8.46}$$

The reciprocal rate derivatives for two different mobility ratios M are shown in Fig. 8.5; skin $S = (M-1)\,ln(r_s/r_w)$. For $M = 1$, the derivative is similar to that of a homogeneous reservoir, as expected. For $M = 10$ (positive skin), the initial stabilization is representative of the mobility of
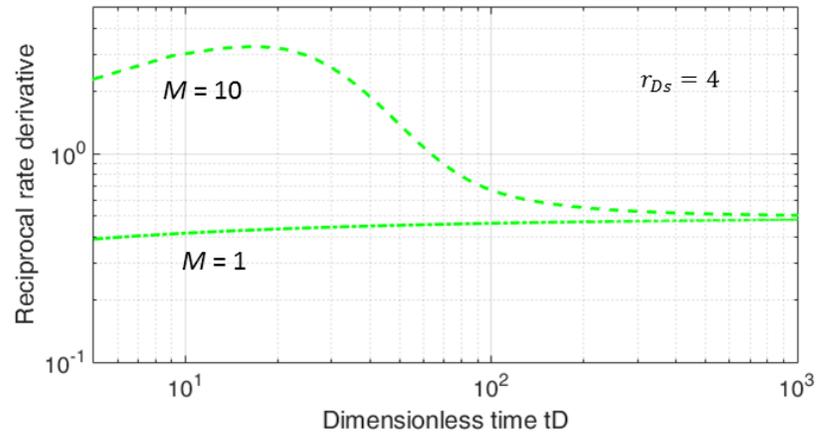
Figure 8.5: Radial composite model with in-situ parameters

the near-wellbore zone. The second stabilization that occurs after $t_D = 100$ is what will be used for interpretation of in-situ tests and this clearly is independent of the near wellbore heterogeneity.

Fig. 8.6 shows the application of radial composite model to the laboratory setup. Due to the small dimensions of the laboratory samples ($r_{De} = 8$), the boundary effects come into play even before the second stabilization is reached. For Ohio samples, this happens in less than a minute.

When the outer boundary is maintained at constant pressure, the reciprocal rate derivative is almost zero for $t_D > 30$ (Fig. 8.6 top). But, this is often not the case due to pressure losses in the outflow meter. There is a second stabilization at a later time, proportional to $\bar{S}_{out}$. Also, this stabilization is not influenced by the near-wellbore skin (Fig. 8.6 bottom).
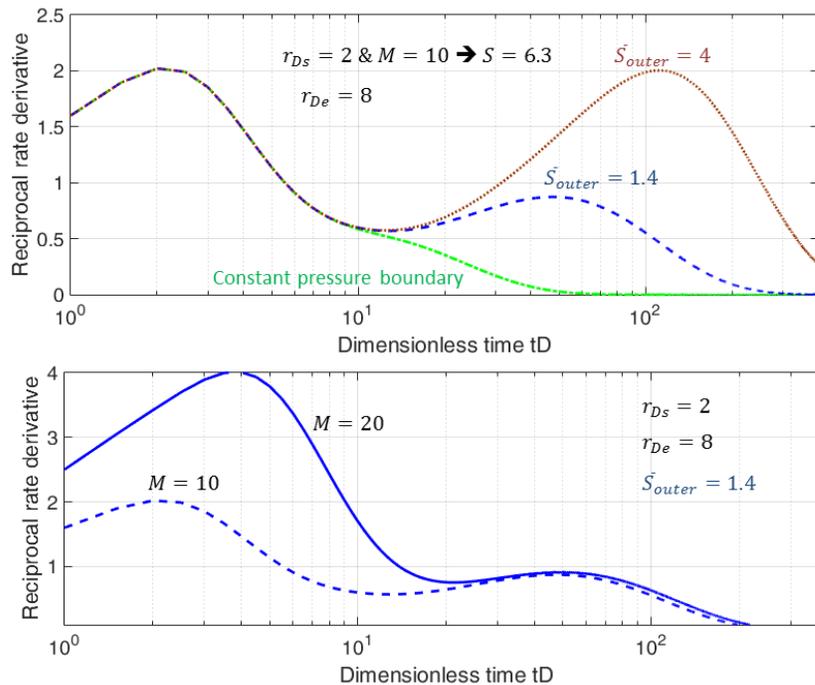
Figure 8.6: Radial composite model with parameters for laboratory setup

Nomenclature

c_f	Compressibility of reservoir fluid
c_p	Compressibility of pore volume
c_t	Total compressibility, $= s_w c_w + [1 - s_w] c_o + c_p$
e_w	Exponent in k_{rw} (Eq. 3.42)
e_o	Exponent in k_{ro} (Eq. 3.43)
f_w	Fraction of injected fluid in the flowing stream, $u_w/(u_w + u_0)$
h	Open hole thickness
h_{samp}	Thickness of the samples in laboratory setup, 16.66 cm
h_w	Interface depth in the wellbore
$\dot{h}_w$	Interface velocity
H	Well depth (measured depth)
H_{cas}	Casing shoe depth
I_0	Modified Bessel function, first kind, order zero
I_1	Modified Bessel function, first kind, first order
J_0	Bessel function, first kind, order zero
k	Single-phase permeability
k_d	Permeability in the damaged (skin) zone
$(k/\mu)_d$	Mobility of the damaged (skin) zone
k_{rw}	Relative permeability of water
k_{ro}	Relative permeability of oil
$k_{rw}(s_{orw})$	Relative permeability of water at residual oil saturation
$k_{ro}(s_{wc})$	Relative permeability of oil at connate water saturation
$\widehat{k}$	Permeability estimate from injection log
δk	Error in permeability estimate
$\langle k \rangle_{avg}$	Average permeability of central hole in laboratory setup
$\langle k \rangle^i_{samp}$	Average permeability of ith sample in laboratory setup
K_0	Modified Bessel function, second kind, order zero

K_1	Modified Bessel function, second kind, first order
K	Hydraulic diffusivity, $k/\mu\phi c_t$
M	Mobility ratio, $(k/\mu)/(k/\mu)_d$
M_r	Ratio of maximum relative mobilities, $[k_{rw}(s_{orw})/\mu_w]/[k_{ro}(s_{wc})/\mu_o]$
p	Change in pore pressure, $p - P_{ini}$
$\bar{p}$	Pore pressure in Laplace domain
p_c	Capillary pressure
p_D	Non-dimensional pressure, $\triangle p/\triangle P$
p_o	Pore pressure in oil
p_w	Pore pressure in water
P_a	Wellbore pressure in the annulus
P_{res} and P_{ini}	Initial formation pressure
P_a^{wh}	Annulus wellhead pressure
P_t^{wh}	Tubing wellhead pressure
P_{in}	Inlet pressure in the laboratory setup
P_{out}	Outlet pressure in the laboratory setup
$\triangle P$	Pressure head applied on the formation, $P_a - P_{res}$
$\triangle P^i$	Effective pressure head for i^{th} sample
$\triangle P_{res}$	Error in input reservoir pressure
q	Injection rate into the formation per unit thickness
q_{conv}	Flow rate computed through convolution
$\bar{q}_D$	Laplace transformation of $q_D(t)$ with respect to t
q_D	Non-dimensional flow rate, $q\mu/2\pi k\triangle P$
$q_{\mu+}^{wf}$	Formation injection rate of less-viscous fluid
$q_{\mu-}^{wf}$	Formation injection rate of viscous fluid
Q^i	Injection rate into i^{th} sample
Q_a^{wh}	Annulus wellhead flow rate (measured)
Q_t^{wh}	Tubing wellhead flow rate (measured)
Q_a^*	Effective circulation rate in the annulus (computed)
Q_t^*	Effective circulation rate in the tubing (computed)
Q_R^i	Outflow rate collected from the ith sample
Q_{in}	Injection rate into the laboratory setup
Q_{out}	Withdrawal rate from the laboratory setup
r	Radius measured from well axis

r_e	Outer radius of the sample
r_d	Radius of the skin zone
r_f	Radius of the saturation front
r_{inv}	Investigation radius
r_w	Wellbore radius (or sample inner radius)
r_D	Non-dimensional radius, r/r_w
s	Laplace transform variable
s_{or}	Residual oil saturation
s_{orw}	Water saturation at residual oil saturation, $1 - s_{or}$
s_w	Water saturation in the formation
s_{wf}	Water saturation at the saturation front
s_{wc}	Connate (irreducible) water saturation
s_w^{ini}	Initial water saturation in the formation
S	Skin (near-wellbore damage), $[(k/k_s) - 1] \, ln(r_d/r_w)$
S_a	Annulus cross-sectional area
S_t	Tubing cross-sectional area
$\bar{S}$	Global skin estimated by reciprocal-rate derivative analysis
δS	Local skin variations
t_{beg}	Time at the beginning of closing WTLog (laboratory tests)
t_{end}	Time at the end of closing WTLog (laboratory tests)
t_D	Non-dimensional time, $K_{hyd}t/r_w^2$
$\overrightarrow{u}$	Fluid flux per unit cross-sectional area
$\overrightarrow{u_w}$	Water flux per unit cross-sectional area
$\overrightarrow{u_o}$	Oil flux per unit cross-sectional area
Y_0	Bessel function, second kind, order zero
z	Measure depth from the wellhead

η	Ratio of hydraulic diffusivities, $(K_{hyd})/(K_{hyd})_d$
λ	Total mobility during two-phase flow, $= k\left[(k_{rw}/\mu_w) + (k_{ro}/\mu_o)\right]$
$\hat{\lambda}_o$	Mobility of the original formation fluid, $\hat{\lambda}_o$
μ	Dynamic viscosity
μ_w	Dynamic viscosity of the water in the formation
μ_o	Dynamic viscosity of the oil in the formation
ρ	Fluid density

ρ_a Fluid density in the annulus

ρ_o Oil density in the formation

ρ_t Fluid density in the central tube

ρ_w Water density in the formation

ρ_a^{wh} Fluid density at annulus wellhead

ρ_t^{wh} Fluid density at tubing wellhead

$\bar{\rho}_{oh}$ Average fluid density in the open hole

τ Time at which interface in wellbore reaches depth z

ϕ Porosity

Ω Ratio of formation injection rates: viscous fluid / less-viscous fluid

List of publications

Manivannan, S., P. Bérest, and B. Brouard (2015). "Effect of Changes in the Cavern Pressure and Wellbore Temperature during a Liquid-Liquid MIT". In: *Proc. SMRI Fall Meeting, Santander, Spain.*

Manivannan, S., A. Jacques, B. Brouard, P. Bérest, J.-L. Boutaud de la Combe, V. Jaffrezic, and M. Fleury (2017). "A Novel Injectivity and Permeability Log for Tight Reservoirs". In: *SPE Europec featured at 79th EAGE Conference and Exhibition.* doi: SPE-185860-MS

Manivannan, S. and P. Bérest (2018). "Closure of a cylindrical hole in a Norton-Hoff medium". In: *Rock Mechanics and Rock Engineering (completed 1st peer view and awaiting publication).*

Manivannan, S., J. Barottin, P. Bérest, B. Brouard, V. De Greef, and A. Jacques (2018). "In-situ permeability test in a salt formation at Marboz, France". In: *Proc. SMRI Fall Meeting, Belfast, Ireland.*

Bibliography

Abbaszadeh, M. and M. Kamal (1989). "Pressure-Transient Testing of Water-Injection Wells". In: *SPE Reservoir Engineering* 4.1, pp. 115–124. DOI: SPE-16744-PA (cit. on p. 48).

Allen, D., D. Bergt, D. Best, B. Clark, I. Falconer, J.-M. Hache, C. Kienitz, M. Lesage, J. Rasmus, C. Roulet, and P. Wraight (1989). "Logging While Drilling". In: *Oilfield review* 1 (cit. on p. 15).

Allen, D., C. Flaum, T.S. Ramakrishnan, J. Bedford, K. Castelijns, D. Fairhurst, G. Gubelin, N. Heaton, C. C. Minh, M. A. Norville, M. R. Seim, T. Pritchard, and R. Ramamoorthy (2000). "Trends in NMR Logging". In: *Oilfield Review* (cit. on pp. 15, 77).

Andersen, M. A. (2011). "Introduction to Wireline Logging". In: *Oilfield Review* 23.1 (cit. on p. 10).

Araktingi, U.G. and F.M. Orr Jr (1993). "Viscous Fingering in Heterogeneous Porous Media". In: *SPE Advanced Technology Series* 1.1, pp. 71–80. DOI: SPE-18095-PA (cit. on p. 84).

Berest, P., B. Brouard, and J. G. Durup (2001). "Tightness Tests in Salt-Cavern Wells". In: *Oil & Gas Science and Technology - Rev. IFP* 56.5, pp. 451–469. DOI: 10.2516/ogst:2001037 (cit. on pp. 16, 17).

Beretta, E., A. Tiani, G. Lo Presti, and F. Verga (2007). "Value of Injection Testing as an Alternative to Conventional Well Testing: Field Experience in a Sour-Oil Reservoir". In: *SPE Reservoir Evaluation & Engineering* 10, pp. 112–121. DOI: SPE-100283-PA (cit. on p. 48).

Bourdet, D.P., T.M. Whittle, A.A. Douglas, and Y.M. Pirard (1983). "A New Set of Type Curves Simplifies Well Test Analysis". In: *World oil* 196 (6), pp. 95–106 (cit. on pp. 24, 36, 42).

Bratvold, R.B. and R.N. Horne (1990). "Analysis of Pressure-Falloff Tests Following Cold-Water Injection". In: *SPE Formation Evaluation* 5.03, pp. 293–302. DOI: SPE-18111-PA (cit. on pp. 49, 52, 55, 57).

Bérest, P., B. Brouard, M. Karimi-Jafari, and L. Van Sambeek (2007). "Transient behavior of salt caverns. Interpretation of Mechanical Integrity Tests". In: *Int. J. Rock Mech. Min. Sc.* 44, pp. 767–786 (cit. on p. 102).

Brock, D.C. and F.M. Orr Jr (1991). "Flow Visualization of Viscous Fingering in Heterogeneous Porous Media". In: *SPE Annual Technical Conference and Exhibition, 6-9 October, Dallas, Texas.* DOI: SPE-22614-MS (cit. on pp. 84, 85).

Brouard, B. and P. Bérest (1998). "A tentative classification of salts according to their creep properties." In: *Proc. SMRI Spring Meeting, New Orleans, Louisiana*, pp. 18–38 (cit. on pp. 104, 105).

Brouard, B., P. Bérest, and G. Durup (2001). "In-situ salt permeability testing". In: *Proc. SMRI Fall Meeting, Albuquerque, New Mexico,* pp. 139–157 (cit. on pp. 94, 105, 108).

Brouard, B., P. Bérest, V. de Greef, J.F. Beraud, C. Lheur, and E. Hertz (2013). "Creep closure rate of a shallow salt cavern at Gellenoncourt, France". In: *Int. J. Rock Mech. Min. Sc.* 62, pp. 42–50 (cit. on p. 100).

Buckley, S.E. and M.C. Leverett (1941). "Mechanism of Fluid Displacement in Sands". In: *Trans., AIME*, pp. 107–16 (cit. on pp. 48, 51–53).

Cantini, S., D. Baldini, E. Beretta, D. Loi, and S. Mazzoni (2013). "Reservoir Permeability from Wireline Formation Testers". In: *EAGE Annual Conference & Exhibition incorporating SPE Europec, 10-13 June, London, UK* (cit. on pp. 13, 14).

Carslaw, H. S. and J. C. Jaeger (1946). *Conduction of Heat in Solids.* Oxford University Press (cit. on pp. 42, 120, 121).

Carslaw, H.S. (1921). *Mathematical Theory of the Conduction of Heat in Solids.* Macmillan and Co., Ltd (cit. on p. 120).

Chuoke, R. L., P. Van Meurs, and C. Van der Poel (1959). "The Instability of Slow, Immiscible, Viscous Liquid-Liquid Displacements in Permeable Media". In: *Trans. AIME* 216, pp. 188–194 (cit. on p. 83).

Chustz, M. J., J. R. May, C. Wallace, D. Reitsma, P. D. Fredericks, S. R. Dickinson, and L. D. Smith (2007). "Managed-Pressure Drilling With Dynamic Annular Pressure-Control System Proves Successful in Redevelopment Program on Auger TLP in Deepwater Gulf of Mexico". In: *Innovative Drilling* (cit. on p. 36).

Cumming, J., D.A. Wooff, T. Whittle, R. Crossman, and A. C. Gringarten (2013). "Assessing the Non-Uniqueness of the Well Test Interpretation Model Using Deconvolution". In: *EAGE Annual Conference & Exhibition incorporating SPE Europec, 10-13 June, London, UK*. DOI: SPE-164870-MS (cit. on p. 45).

Curial, A. (1986). "La sedimentation salifere et supersalifere du Palogene Bressan". PhD thesis. Université Claude Bernard Lyon l (cit. on p. 94).

Delhomme, Jean-Pierre (2007). "Aquifer systems management: Darcy's legacy in a world of impending water shortage". In: ed. by L. Chery and G. de Marsily. London: Taylor & Francis. Chap. The quest for permeability evaluation in wireline logging, pp. 55–70 (cit. on pp. 14–16).

Di, J. and J. L. Jensen (2016). "A New Approach for Permeability Prediction With NMR Measurements in Tight Formations". In: *SPE Reservoir Evaluation & Engineering* 19.03. DOI: SPE-180921-PA (cit. on p. 15).

Durup, J.G. (1994). "Long term tests for tightness evaluations with brine and gas in salt". In: *Proc. SMRI Fall Meeting, Hannover, Germany* (cit. on pp. 102, 104).

Ehlig-Economides, C.A. and H.J. Ramey Jr. (1981). "Transient Rate Decline Analysis for Wells Produced at Constant Pressure". In: *SPE Journal* 21.1, pp. 98–104. DOI: SPE-8387-PA (cit. on pp. 28, 39).

Fetkovich, M. J. (1980). "Decline Curve Analysis Using Type Curves". In: *Journal of Petroleum Technology* 32.06, pp. 1065–1077. DOI: 10.2118/4629-PA (cit. on p. 35).

Gringarten, A. C. (2008). "From Straight Lines to Deconvolution: The Evolution of the State of the Art in Well Test Analysis". In: *SPE Reservoir Evaluation & Engineering* 11.01, pp. 41–62. DOI: SPE-102079-PA (cit. on pp. 14, 35).

Gringarten, A. C. (2010). "Practical Use of Well-Test Deconvolution". In: *SPE Annual Technical Conference and Exhibition, 19-22 September, Florence, Italy.* Ed. by SPE. DOI: SPE-134534-MS (cit. on p. 45).

Hasan, A., S. Kabir, and D. Lin (2005). "Analytic Wellbore Temperature Model for Transient Gas-Well Testing". In: *SPE Reservoir Evaluation & Engineering* 8.03, pp. 240–247. DOI: 10.2118/84288-PA (cit. on p. 24).

Hawkins Jr., M. (1956). "A Note on the Skin Effect". In: *Journal of Petroleum Technology* 8, pp. 65–66 (cit. on p. 39).

Homsy, G. M. (1987). "Viscous Fingering in Porous Media". In: *Annual Review of Fluid Mechanics* 19.1, pp. 271–311. DOI: 10.1146/annurev.fl.19.010187.001415 (cit. on pp. 83, 84).

Hurst, W. (1934). "Unsteady Flow of Fluids in Oil Reservoirs". In: *Journal of Applied Physics* 5.1, pp. 20–30. DOI: 10.1063/1.1745206 (cit. on pp. 120, 123).

Izgec, B., S. Kabir, D. Zhu, and R. Hasan (2007). "Transient fluid and heat flow modeling in coupled wellbore/reservoir systems". In: *SPE Reservoir Evaluation & Engineering.* DOI: 10.2118/102070-PA (cit. on p. 24).

Jacob, C. E. and S. W. Lohman (1952). "Nonsteady flow to a well of constant drawdown in an extensive aquifer". In: *Transactions of American Geophysical Union* 33.4, pp. 559–569. DOI: 10.1029/TR033i004p00559 (cit. on pp. 36, 38, 41, 42, 121).

Jacques, A., J.-L. Boutaud de la Combe, P. Bérest, and B. Brouard (2013). "Method of estimating physical parameters of a geological formation". English. Pat. US 8,583,378 B2 (cit. on p. 17).

Kabir, C.S., A.R. Hasan, D.L. L. Jordan, and X. Wang (1996a). "A Wellbore/Reservoir Simulator for Testing Gas Wells in High-Temperature Reservoirs". In: *SPE Formation Evaluation* 11, pp. 128–134. DOI: 10.2118/28402-PA (cit. on p. 24).

Kabir, C.S., A.R. Hasan, G. E. Kouba, and M. Ameen (1996b). "Determining Circulating Fluid Temperature in Drilling, Workover, and Well Control Operations". In: *SPE Drilling & Completion* 11, pp. 74–79. DOI: 10.2118/24581-PA (cit. on pp. 25, 26).

Kamps, C. and B. Dow (2017). "Technology Update: Lowering Adoption Barriers to MPD - Land and Sea". In: *Journal of Petroleum Technology* 69, pp. 18–19 (cit. on p. 36).

Kuchuk, F. J. (2009). "Radius of Investigation for Reserve Estimation From Pressure Transient Well Tests". In: *SPE Middle East Oil and Gas Show and Conference, 15-18 March, Manama, Bahrain.* Ed. by SPE. DOI: SPE-120515-MS (cit. on p. 47).

Lampe, B. and J.L. Ratigan (2014). "Pitfalls of a Nitrogen-Brine interface Mechanical Integrity Test". In: *Proc. SMRI Spring Meeting, San Antonio, Texas*, pp. 19–30 (cit. on p. 100).

Levitan, M. (2003). "Application of Water Injection/Falloff Tests for Reservoir Appraisal: New Analytical Solution Method for Two-Phase Variable Rate Problems". In: *SPE Journal* 8.04, pp. 341–349. DOI: SPE-87332-PA (cit. on pp. 48–50, 55, 57).

Manivannan, S. and P. Bérest (2018). "Closure of a cylindrical hole in a Norton-Hoff medium". In: *Rock Mechanics and Rock Engineering (completed 1st peer view and awaiting publication)* (cit. on p. 104).

Manivannan, S., P. Bérest, and B. Brouard (2015). "Effect of Changes in the Cavern Pressure and Wellbore Temperature during a Liquid-Liquid MIT". In: *Proc. SMRI Fall Meeting, Santander, Spain,* pp. 3–19 (cit. on pp. 26, 100).

Manivannan, S., A. Jacques, B. Brouard, P. Bérest, J.-L. Boutaud de la Combe, V. Jaffrezic, and M. Fleury (2017). "A Novel Injectivity and Permeability Log for Tight Reservoirs". In: *SPE Europec featured at 79th EAGE Conference and Exhibition.* DOI: SPE-185860-MS (cit. on pp. 18–20, 95).

Mikhailov, D., N. Ryzhikov, A. Makarova, V. Shako, A. Burukhin, and B. Theuveny (2015). "A Method for Determination of Near-wellbore Zone Properties Alteration during Well Drilling, Completion and Cleanup Operations by Combination of Numerical Simulations and Special Experimental Technique". In: *SPE European Formation Damage Conference and Exhibition, 3-5 June, Budapest, Hungary.* DOI: SPE-174248-MS (cit. on p. 12).

Muskat, M. (1934). "The Flow of Compressible Fluids Through Porous Media and Some Problems in Heat Conduction". In: *Journal of Applied Physics* 5.3, pp. 71–94. DOI: 10.1063/1.1745233 (cit. on pp. 120, 123).

Nashawi, I.S. and A. Malallah (2006). "Rate Derivative Analysis of Oil Wells Intercepted by Finite Conductivity Hydraulic Fracture". In: *Canadian International Petroleum Conference, 13-15 June, Calgary, Alberta.* DOI: 10.2118/2006-121 (cit. on p. 36).

Nicholson, J. W. (1921). "A Problem in the Theory of Heat Conduction". In: *Proceedings of the Royal Society of London* 100.704, pp. 226–240. DOI: 10.1098/rspa.1921.0083 (cit. on p. 120).

Proett, M., M. Walker, D. Welshans, and C. Gray (2003). "Formation Testing While Drilling, a New Era in Formation Testing". In: *SPE Annual Technical Conference and Exhibition, 5-8 October, Denver, Colorado.* DOI: SPE-84087-MS (cit. on p. 13).

Saffman, P. G. and G. Taylor (1958). "The penetration of a fluid into a porous medium or Hele-Shaw cell containing a more viscous liquid". In: *Proceedings of the Royal Society of London A: Mathematical, Physical and Engineering Sciences* 245.1242, pp. 312–329. DOI: 10.1098/rspa.1958.0085 (cit. on p. 83).

Sánchez-Palencia, E. (1980). *Non-homogeneous media and vibration theory.* Lecture notes in physics. Springer-Verlag (cit. on pp. 9, 10).

Skaug, N.T., J.L. Ratigan, and B.C. Lampe (2011). "A critical look at the Nitrogen/Brine Interface Mechanical Integrity Test". In: *Proc. SMRI Fall Meeting, York, UK*, pp. 324–332 (cit. on p. 100).

Smith, L.P. (1937). "Heat Flow in an Infinite Solid Bounded Internally by a Cylinder". In: *Journal of Applied Physics* 8.6, pp. 441–448. DOI: 10.1063/1.1710319 (cit. on pp. 38, 120, 121).

Stehfest, H. (1970). "Numerical Inversion of Laplace Transforms". In: *Communicarions of the ACM* 13.1, pp. 47–49. DOI: 10.1145/361953.361969 (cit. on pp. 38, 119, 125).

Theis, C. V. (1935). "The relation between the lowering of the Piezometric surface and the rate and duration of discharge of a well using ground-water storage". In: *Transactions of American Geophysical Union* 16.2, pp. 519–524. DOI: 10.1029/TR016i002p00519 (cit. on pp. 47, 120).

Timur, A. (1968). "An Investigation Of Permeability, Porosity, & Residual Water Saturation Relationships For Sandstone Reservoirs". In: *The Log Analyst* 9.04 (cit. on p. 14).

Turki, L., J. A. Demski, and A. S. Grader (1989). "Decline Curve Analysis in Composite Reservoirs". In: *SPE Eastern Regional Meeting, 24-27 October, Morgantown, West Virginia*. DOI: 10.2118/SPE-19316-MS (cit. on p. 36).

Uraiet, A. A . and R. Raghavan (1980). "Unsteady Flow to a Well Producing at a Constant Pressure". In: *Journal of Petroleum Technology* 32.10, pp. 1803–1812. DOI: SPE-8768-PA (cit. on pp. 29, 36, 42).

Van Everdingen, A. F. (1953). "The Skin Effect and Its Influence on the Productive Capacity of a Well". In: *Journal of Petroleum Technology* 5.06, pp. 171–176. DOI: SPE-203-G (cit. on pp. 39, 42).

Van Everdingen, A. F. and W. Hurst (1949). "The Application of the Laplace Transformation to Flow Problems in Reservoirs". In: *Trans. AIME*, pp. 305–324. DOI: SPE-949305-G (cit. on pp. 38, 104, 121).

Varhug, M. (2016). "Basic Well Log Interpretation". In: *Oilfield Review* (cit. on p. 15).

Verga, F., D. Viberti, and E. Salina Borello (2011). "A new insight for reliable interpretation and design of injection tests". In: *Journal of Petroleum Science and Engineering* 78.1, pp. 166 –177. DOI: https://doi.org/10.1016/j.petrol.2011.05.002 (cit. on pp. 48, 49, 52).

Von Schroeter, T., F. Hollaender, and A.C. Gringarten (2004). "Deconvolution of Well-Test Data as a Nonlinear Total Least-Squares Problem". In: *SPE Journal* 9.04, pp. 375–390. DOI: SPE-77688-PA (cit. on p. 45).

Wei, D.-F., X.-P. Liu, X.-X. Hu, R. Xu, and L.-L. Zhu (2015). "Estimation of Permeability from NMR Logs Based on Formation Classification Method in Tight Gas Sands". In: *Acta Geophysica* 63.5, pp. 1316–1338. DOI: 10.1515/acgeo-2015-0042 (cit. on p. 15).

Welge, H. J. (1952). "A simplified method for computing oil recovery by gas or water drive". In: *Trans. AIME* 195, p. 91 (cit. on p. 53).

Zhang, W. and A. S. Grader (1994). "Analysis of Rate Decline Derivatives". In: *SPE Eastern Regional Meeting, 8-10 November, Charleston, West Virginia*. DOI: 10.2118/29180-MS (cit. on p. 36).

Titre : Mesure de la perméabilité fonction de la profondeur dans le découvert d'un puits en descendant une colonne composée de deux fluides distincts.

Mots clés : mesure de la perméabilité en place, problèmes inverses, évaluation pétrophysiques.

Résumé : Dans les puits de production d'eau, de pétrole, de gaz et de chaleur géothermique, ou dans les puits d'accès à un stockage d'hydrocarbures, il est précieux de connaître la perméabilité de la formation ou de sa couverture en fonction de la profondeur, soit pour améliorer le modèle de réservoir, soit pour choisir les zones dans lesquelles procéder à des opérations spéciales.

On propose une technique qui consiste à balayer la hauteur du découvert par une interface entre deux liquides de viscosités très contrastées. Le débit total qui pénètre la formation à chaque instant est ainsi une fonction de la position de l'interface et de l'historique des pressions dans le puits. On doit alors résoudre un problème inverse : rechercher la perméabilité fonction de la profondeur à partir de l'historique des débits dans le temps. Dans la pratique, le puits est équipé d'un tube central. Le balayage est effectué par injection d'un liquide à pression d'entrée constante dans le tube central et soutirage d'un autre liquide par l'espace annulaire. On mesure les débits d'injection et de soutirage dont la différence est le débit qui entre dans la formation.

Pour valider et améliorer cette technique, on a d'abord utilisé une maquette simulant un découvert multi-couches disponible au LMS. On a exploité aussi des essais en place réalisés dans la couverture peu perméable d'un stockage souterrain de gaz. Dans ces essais, un liquide visqueux placé dans le découvert était déplacé par un liquide moins visqueux (méthode dite « opening »). Les couches plus perméables étaient correctement identifiées (Manivannan et al. 2017), mais une estimation quantitative était un défi en raison des phénomènes transitoires qui affectent le voisinage immédiat des puits. De plus, le rayon investigué dans le massif était petit.

La thèse a relevé ces défis en proposant un essai légèrement différent et une nouvelle technique d'interprétation. Les essais avec une maquette modifiée ont montré la supériorité d'une méthode « closing » dans laquelle le puits est d'abord rempli du liquide le moins visqueux. On ménage une période de stabilisation avant l'injection du liquide visqueux pour réduire les effets transitoires ; elle permet aussi d'estimer la perméabilité moyenne et l'influence de la zone endommagée à la paroi (le « skin »).

Puis on conduit l'essai proprement dit. L'historique des débits mesurés en tête de puits constitue le profil d'injection dont on déduit le profil de perméabilité. Cette estimation suppose un écoulement monophasique dans chaque couche et le même « skin » pour toute la formation. Les incertitudes principales portent sur les pressions de formation et les variations possibles du « skin ». Elles sont estimées au moyen d'un calcul analytique. On a vérifié sur la maquette que les profils de perméabilité estimés présentent une bonne concordance avec les perméabilités mesurées avant les essais.

Title : Measuring permeability vs depth in the unlined section of a wellbore using the descent of a fluid column made of two distinct fluids

Keywords : in-situ permeability measurement, inverse problems, petrophysical evaluation

Abstract : In wells producing water, oil, gas or geothermal energy, or in the wells used for hydrocarbon storage, it is critical to evaluate the permeability of the formation as a function of well depth, to improve the reservoir model, and also to identify the zones where additional investigation or special completions are especially useful.

In this thesis, we propose a technique which consists of scanning the open hole (uncased section of the wellbore) with an interface between two fluids with a large viscosity contrast. The injection rate into the formation depends on interface location and pressure history in the well. An inverse problem should be solved: estimate permeability as a function of depth from the evolution of flow rates with time. The wells are usually equipped with a central tube. The scanning is done by the injection of a liquid in the central tube at constant wellhead pressure and wellhead injection and withdrawal rates are measured; the difference between these two flow rates is the formation injection rate.

To validate and improve this technique, we used a laboratory model mimicking a multi-layer formation, already available at LMS. We also made use of in-situ tests performed on an ultra-low permeable cap rock above an underground gas storage reservoir. In these tests, a viscous fluid contained in the open hole was displaced by The more permeable layers were correctly identified (Manivannan et al. 2017), but a quantitative estimation was challenging due to some transient phenomena in the vicinity of the wellbore (near-wellbore zone). In addition, the investigation radius was small.

These challenges are addressed by proposing a slightly modified test procedure and a new interpretation workflow. Laboratory tests with a modified test setup showed the advantages of the 'closing' method in which the well is filled with a less-viscous fluid at the start of the test. We also added a stabilization period before the injection of viscous fluid to reduce the transient effects; this also allows us to estimate the average permeability of the open hole and the effect of near-wellbore damage (skin).

Then the test proper is performed (closing WTLog). The injection profile of the less-viscous fluid is computed from the wellhead flow rate history. A permeability profile is estimated from the injection profile. The permeability estimation considers a monophasic flow in each layer and same skin value for all the formation layers. Major uncertainties in the permeability estimates are caused by formation pressures and heterogeneities in skin values; they are estimated using an analytical formula. We have verified on the laboratory setup that the estimated permeability profiles are well correlated to